UNIVERSITÀ
DEGLI STUDI
DI PADOVA

University of Padova

Department of Chemical Sciences

Ph.D. Course in

SCIENCE & ENGINEERING OF MATERIALS AND NANOSTRUCTURES

36° Cycle

THE PIVOTAL ROLE OF LIGANDS DETERMINING THE PROPERTIES OF ATOMICALLY PRECISE GOLD NANOCLUSTERS

Coordinator: **Prof. Stefano Agnoli**

Supervisor: **Prof. Flavio Maran**

Co-Supervisor: **Prof. Sara Bonacchi**

Ph.D. student: **Mattia Reato**

Table of Contents

1. Introduction

1.1 Atomically Precise Nanoclusters

Atomically precise nanoclusters (NCs) are molecules. Nearly three decades have passed since the groundbreaking work of 1996, titled "Nanocrystals Gold Molecule" by Professor Whetten.[1] He was the first to timidly introduce the world to a new type of chemical species, where aggregates of gold atoms, protected by alkanethiolates ligands, could be synthesized and manipulated using thiol-gold chemistry. A revolutionary aspect of these macromolecular species was their ability to retain their integrity in solution. This means they could be dissolved in common organic solvents, dried, and then resuspended, just like true molecules.[1] Today, in the year 2024, we can recognize this work as the dawn of the gold nanocluster revolution. No one in 1996 could have imagined that over time, these new chemical species would be treated as molecules in all respects.

From that day forward, the study, particularly the synthesis, of nanoclusters has intensified, aided by technological and instrumental advancements that enable us to investigate these complex systems with greater clarity. The Whetten group continued their research for nearly another decade, identifying several new species with varying masses (ranging from 5 to 30 kDa).[1–5] However, the atomic precision and molecular purity we now associate with nanoclusters had not yet been achieved. Despite this, interest within the scientific community gradually grew, fueled by evidence of novel physicochemical properties that surpassed predictions based on dimensional scaling from bulk metal counterparts. The first work to propose true nanocluster isolation was that of Tsukuda in 2005.[6] They synthesized small gold clusters (~1 nm size) protected by glutathione molecules (GSH) by reductive decomposition of Au(I)-SG polymers at low temperatures. These clusters were then separated into fractions using electrophoresis and analyzed using electrospray ionization (ESI) mass spectrometry. They identified a series of Au NCs with cores ranging from 10 to 39 gold atoms, all protected by glutathione. Among these species, for the very first time, a nanocluster composed of 25 gold atoms and protected by 18 ligands was identified.[6] This remarkable discovery marked a turning point in nanocluster research, leading to the development of methods for synthesizing, separating, and characterizing atomically precise nanoclusters (in particular

$Au_{25}(SR)_{18}$) with controlled sizes and compositions. In this scenario, Professor Jin has emerged as a pioneer in the synthesis of NCs,[7–11] developing a “one-pot method” for preparing functionalized-thiol capped Au_{25} NCs, bypassing the synthetic challenges associated with the previous two-phase approach.[8] Additionally, he developed the size-focusing methodology,[10] which further simplified this process. This advancement revolutionized the field of nanocluster research, providing a much-needed accessibility boost for these novel systems. For the first time in nearly 15 years, the synthesis of nanoclusters became remarkably more straightforward. This novel method enabled the preparation of NCs with unprecedented atomic-level precision, eliminating the need for electrophoretic or chromatographic purification of size-mixed products.

In a concurrent development, the first single-crystal structure of an atomically precise nanocluster ($Au_{102}(SR)_{44}$) was reported.[12] The resolution of the first single crystal of an Au NC, surprise and fascinate the scientific community, revealing entirely unexpected structural features of nanoclusters, particularly regarding the organization of thiolate ligands on their surfaces. Contrary to common presumptions, thiolate ligands do not merely bind to Au atoms; instead, they form an organic shell (monolayer) around the entire NC surface via bridges known as “staples,” where Au and S atoms alternate.

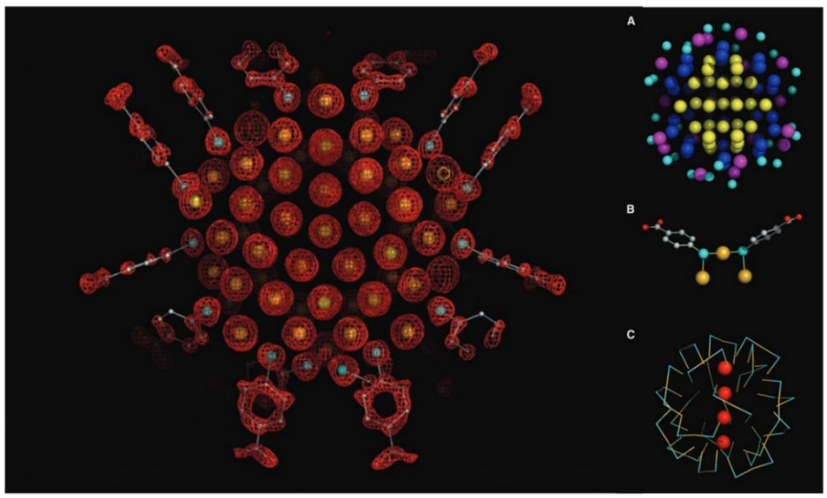

Figure 1 X-ray crystal structure determination of the Au_{102}(p-MBA)$_{44}$ nanocluster, where p-MBA stays for p-mercaptobenzoic acid. Electrondensity map(redmesh)andatomic structure (gold atoms depicted as yellow spheres, and p-MBA shown as framework and with small spheres (sulfur in cyan, carbon in gray, and oxygen in red). **A)** Successive shells of gold atoms interacting with zero (yellow), one (blue), or two (magenta) sulfur atoms. Sulfur atoms are cyan. **B)** Example of two p-MBAs interacting with three gold atoms in a bridge conformation, here termed a staple motif. Gold atoms are yellow, sulfur atoms are cyan, oxygen atoms are red, and carbon atoms are gray. **C)** Distribution of staple motifs in the surface

of the nanoparticle. Staple motifs are depicted symbolically, with gold in yellow and sulfur in cyan. Only the gold atoms on the axis of the MD are shown (in red). This was the first NC's resolved crystal structure to be published.[12]

The realization that atomically precise nanoclusters were not just intriguing but also held a wealth of potential scientific surprises sparked a surge of research activity in the following years. This led to a significant increase in the number of proposed syntheses of novel NCs and, consequently, the number of solved structures. Currently, the family of NCs has expanded to encompass various nanoclusters of different metals, such as, Ag, Cu, Pt, Pd and Ir.[13–22] The prospect of creating even more nanoclusters is immense, as new combinations can be obtained by varying the type of core (size or chemical nature) as well as the types of ligands that form the organic monolayer surrounding the NC.

Among all these nanoclusters, $Au_{25}(SR)_{18}$ holds a very special place in the nanocluster world. Probably because of the early discovery, easy preparation, high stability, and thus easy functionalization and application.[7,23,24] With time, $Au_{25}(SR)_{18}$ it has become the most exploited and studied cluster to obtain information regarding the structure-property correlation of Au NCs. Over the years, extensive research has been conducted into its physicochemical properties, including its catalytic, optical, electrochemical, chiral, and magnetic properties.[23,25–33] These investigations have fueled interest in both theoretical research and practical applications. In addition, the availability of more and more crystal structures of $Au_{25}(SR)_{18,}$[24,34–38] has enabled researchers to correlate its catalytic activity with its structure, in an increasingly accurate and precise manner.[39,40] Au_{25} is certainly the nanocluster that, in the past, defined the field of atomically precise nanoclusters and we believe it is going to continue to shape its future.

1.2 The Molecular Au_{25} Nanocluster

NCs bridge the gap between nanoparticles and molecules, where discrete electronic states form, and distinctive physicochemical properties are observed. Clusters with a core diameter smaller than about 1.6 nm show the presence of a HOMO-LUMO gap, and peculiar optical, magnetic and electrochemical properties, different from those of the massive metal.

$Au_{25}(SR)_{18}$, as we already said, is the most studied molecular NC. It is composed by 25 gold atoms, protected, and surrounded by an organic shell

(monolayer) made by 18 ligands. In this work we will talk extensively about thiolate ligands. In Figure 2, the first X-Ray resolved single structure of an Au_{25} NC, by Murray, is shown (the Jin group succeeded in crystallization[41] of $Au_{25}(SC_2H_4Ph)_{18}$ at about the same time).

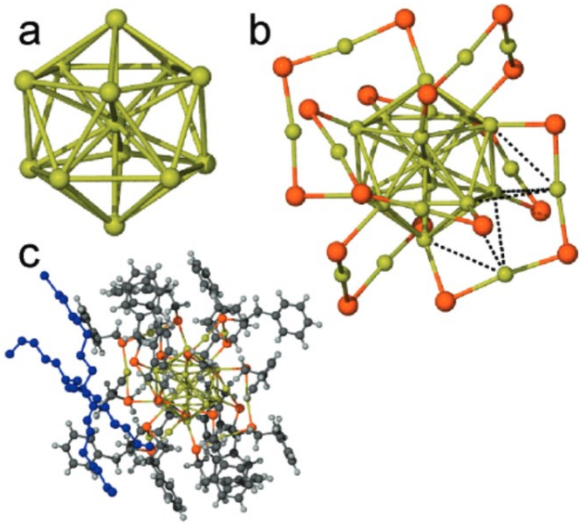

Figure 2 Breakdown of X-ray crystal structure of $[TOA][Au_{25}(SCH_2CH_2Ph)_{18}]$ as seen from [001]. **(a)** Arrangement of the Au_{13} core with 12 atoms on the vertices of an icosahedron and one in the center. **(b)** Depiction of gold and sulfur atoms, showing six orthogonal $-Au_2(SCH_2CH_2Ph)_3-$ "staples" surrounding the Au_{13} core (two examples of possible aurophilic bonding shown as dashed lines). **(c)** $[TOA][Au_{25}(SCH_2CH_2Ph)_{18}]$ structure with the ligands and TOA^+ cation (depicted in blue) (Legend: Gold) yellow; Sulfur) orange; Carbon) gray; Hydrogen) off-white; the TOA+ counterion is over two positions with one removed for clarity).[24]

The work by Murray, shows for the first time the structure of this fascinating nanoclusters (in particular $Au_{25}(SC_2Ph)_{18}^-$), revealing that the arrangement of the metal atoms consisted by an icosahedral core with 13 Au atoms, in which the 13th is inserted at the symmetric center of the structure. While, the ligands that covered the core, organized in redundant motifs of $-Au_2(SCH_2CH_2Ph)_3-$ type, which were called "staples". The NC, considering also the surrounding organic shell, has a diameter of less than 1 nm, which allows it to display molecular behavior. In the following figure a revised version (to better underline all the structure components of the cluster) of a crystal structure obtained by our group and regarding the most naked Au_{25} ever synthesized, $Au_{25}(SC_2H_5)_{18}$, at his 0-charge state so with no counterion in the structure, is presented.[37] Thanks to these crystals, more precise and targeted information regarding the structure has been acquired.

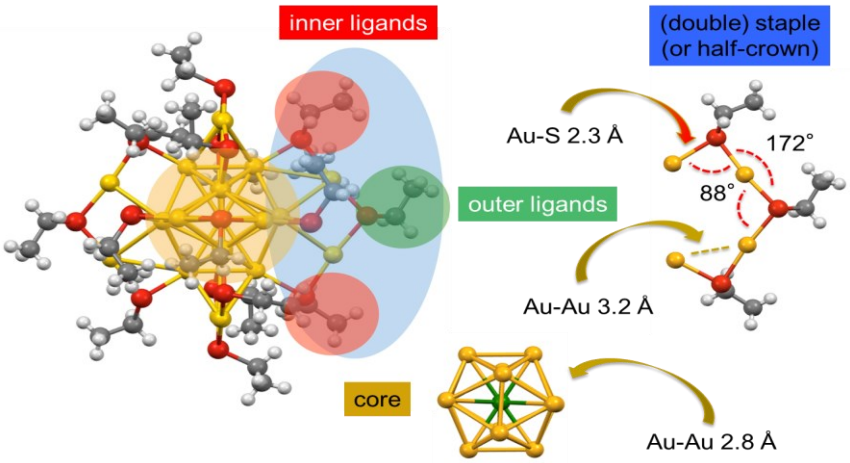

Figure 3 Projection showing the X-ray crystal structure of $Au_{25}(SEt)_{18}^{0}$. Au = yellow, S = red, C = gray, H = white, together with the staple units and the identification of inner and outer ligands.[37]

The figure above clearly illustrates that the 18 thiolated ligands forming the monolayer divide into two groups: 12 inner ligands (represented by red circles) where sulfur atoms form bonds with one Au atom of the gold core and one staple Au atom, and 6 outer ligands (represented by green circle) where the bonds are with two staple Au atoms. Each staple is composed of Au_{core}-(-SR-Au-SR-Au-SR-)-Au_{core} ($Au_2(SR)_3$ stoichiometry), featuring two Au atoms from outside the icosahedral core (underlined by yellow circle) and three thiolate ligands. Two of these ligands are directly connected to the metal core (hence referred to as inner) and one is not directly connected to the core (hence termed outer). Several properties of $Au_{25}(SR)_{18}$ have been studied in detail. For space limitations, here we do not have room enough to cover everything that has been done in this direction, but good recent reviews and books are available.[13,42–44] Regardless, in the subsequent chapter (Chapter 2), a succinct yet comprehensive evaluation of its most significant molecular traits will be provided to appropriately contextualize the discussion of the thesis findings.

1.3 Modification of the Nanocluster's Monolayer Induced by Ligand Exchange Reaction

Altering the structure or chemical composition of nanoclusters is a hot research area within the field of nanosystems science. This is driven by the potential to uncover novel chemical species that could deepen our understanding of the fundamental principles governing these fascinating molecular entities and to precisely tune their properties, paving the way for a wide range of applications in catalysis, sensing and other fields. While the focus of this research topic has traditionally centered on the

modification of their metal cores (via doping or size transformation), as these cores largely determine their chemical and physical properties,[36] the influence of ligands surrounding the metal core is often underestimated. Ligands, commonly organic molecules such as alkanethiols, actually play a crucial role in shaping the properties of nanoclusters. They not only protect the metal core from chemical degradation but also influence the stability, size, shape, and electronic properties of the NC.[45]

Our research group has consistently focused on ligands, exploring how the physicochemical properties of Au_{25} NCs vary upon surface modification, with particular emphasis on their electrochemical properties. This includes, characterization through cyclovoltammetry (CV) and Differential Pulse Voltammetry (DPV) and the study of electron transfer (ET) processes both in solution and in the solid state. In 2016, our group demonstrated for the first time, thanks to Pulse Electron Nuclear Double Resonance (ENDOR), that the orbital distribution actually spread onto the protecting alkanethiolate ligands. Indeed, ENDOR results, together with ^{1}H-NMR measurements, show that the electron-proton interaction affects atoms that can be as far as 6 Å from the icosahedral core, with a much stronger interaction for the inner ligands, because directly connected to the Au_{13} core. Interestingly, although the HOMO and LUMO orbitals of the molecular cluster span onto the first atoms of the capping ligands,[46] our group shows that the electrochemical behavior is mostly determined by the size and to some extent shape of the metal core. On the other hand, the way by which the core communicates with the surroundings is always mediated by the capping monolayer. The latter constitutes a complex interface of often-neglected importance that determines physical properties and modulates electronic coupling with other molecules. Taking advantage of previous work related to the average dielectric constant of the monolayer (ε_m) in terms of concentric-sphere-capacitor model[25,47–50], our group recently studied the electrochemical behavior of a large series of $Au_{25}(SC_nH_{2n+1})_{18}$ clusters (with n varying from 2 to 18) in the presence of different electrolytes. The experiments have demonstrated that *n* affects the position of the peaks and analysis of the data shows that ε_m is larger than usually assumed (i.e., taken as the value of alkyl chains) but yet smaller than that of the specific solvent/electrolyte system (ε_s), and is the result of contributions from ligands, solvent, and electrolyte.[51]

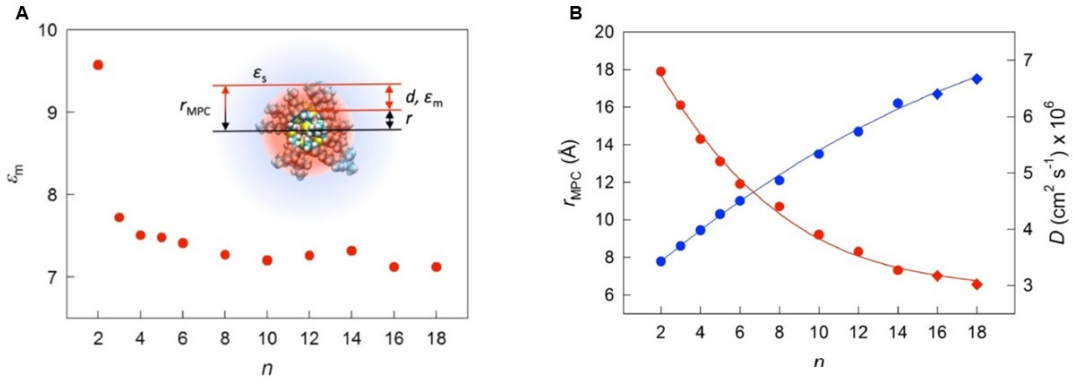

Figure 4 A) Dependence of ε_m on n, as determined in dichloromethane (DCM). The cartoon illustrates the regions with different ε values and the relevant distances. B) Dependence of the diffusion coefficient D (red circles, scale on right) and the NC (in the Figure called MPC) radius (blue circles, scale on left) on n.[51]

For n = 2 (See Figure 4A), the cluster is virtually naked. The monolayer is, therefore, quite penetrable by solvent and chemicals, and this is a very important aspect for properly framing our understanding of redox reactions of NCs. In addition, by studying the effect of n on the voltammetric reduction and oxidation of $Au_{25}(SC_nH_{2n+1})_{18}^0$ clusters (heterogeneous ET), also with the support of ^{1}H-NMR spectroscopy, IR absorption spectroscopy and molecular dynamics (MD) results,[52] in a work of 2014, our group shows that for n < 12 the ligands are quite fluid and have a monolayer thickness of only about 1/4 the (generally assumed) fully extended conformation length (d_{fec}) of the capping ligands.

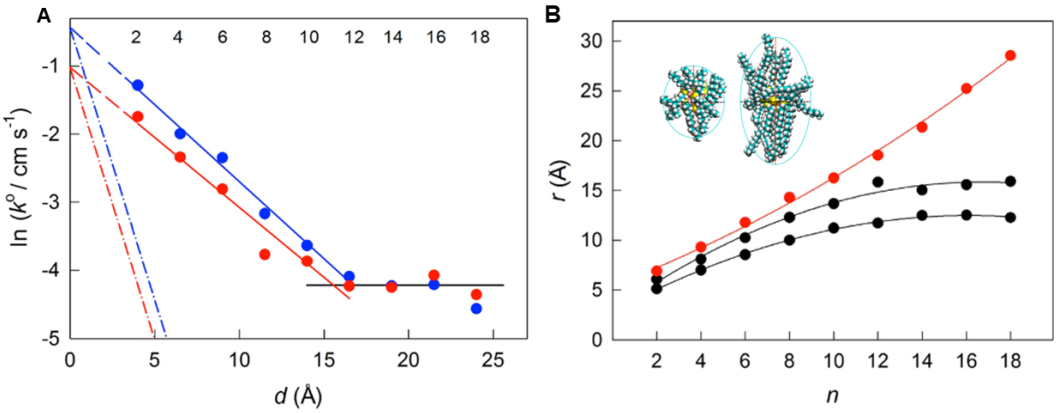

Figure 5 A) Distance effect on the heterogeneous ET rate constants for first reduction (R1, blue) and first oxidation (O1, red). The distance d corresponds to fully extended conformations of the alkyl chains. Uncertainty in ln k^0 values is 0.05-0.1. Linear regressions correspond to β = 0.23 (R1) and 0.21 Å^{-1} (O1). The two dash-dot lines and the horizontal line correspond to β = 0.8 and 0 Å^{-1}, respectively. **B)** Dependence of the semiaxis lengths a (red) and b and c (black) on the number of carbon atoms in the chain. (For calculation and interpretation of the used semiaxis, the reader is referred to the article)[52] In

the inset: representative snapshots from the molecular dynamics calculations trajectories of approximately spherical C10 (left) and elongated C18 NCs (right), in benzene at 300 K.[52]

Whereas these NCs are approximately spherical, longer alkyl chains self-organize into bundles and impart an ellipsoid shape to the Au_{25} (Figure 5B). In these clusters, ET essentially involves the ellipsoid belt, which provides the shortest distance for electronic coupling: this distance is approximately constant and, thus, ET becomes independent of the ligand length (Figure 5A). Ligand fluidity also affects the NC diffusion coefficient (D) value, and this allows assessing the NC radius (r_{NC}) as a function of n (Figure 4B).[51] The effective Stokes monolayer thickness (d_S), obtained by subtracting the core radius (r), corresponds to only 0.59 d_{fec}. All these aspects should be considered very carefully when interpreting the mechanism of redox reactions, the effective distance between reacting species, and the distance effect on the ET rate. The use of different ligands or the modification of the capping monolayer by ligand exchange reactions allows extending and controlling their electrochemistry also in terms of collective substituent effects, which is unfeasible in common molecules. From the viewpoint of ET, NCs are unique because they feature systems completely surrounded by thiolates, and this makes them the 3D equivalent of 2D self-assembled monolayers on extended gold surfaces; a 3D monolayer on a small cluster, however, is not so shielding and thus exogenous molecules may penetrate and experience the properties of a quite unique nanoenvironment, with potentially very interesting implications, especially for catalytic and sensor applications.

Researchers are now exploring ways to manipulate the ligand shell to fine-tune the properties of nanoclusters. Up to now, various strategies have been developed to modify the properties of gold nanoclusters, such as: (i) capping the metal core surface with different types of ligands to modify the protecting monolayer, such as by ligand exchange reactions (LERs) strategy;[53–57] (ii) doping the cluster with other metal atoms to modify the metallic part of the nanocluster;[36,58–63] and (iii) using transformation reaction aimed to modify the core size of nanoclusters.[45,53,64–66] The LER is certainly the key method for modifying the surfaces of the nanoclusters, and was implemented several years ago by the Murray group.[67] These reactions primarily entail the stoichiometric substitution of ligands that decorate the nanocluster surface, that is the nanocluster's organic monolayer, with ligands freely dissolved in the surrounding medium.[53,55,57,68,69] Essentially, LERs offer a dynamic avenue for replacing the incoming ligands, termed "endogenous", with new ligands, named "exogenous" (Figure 6).

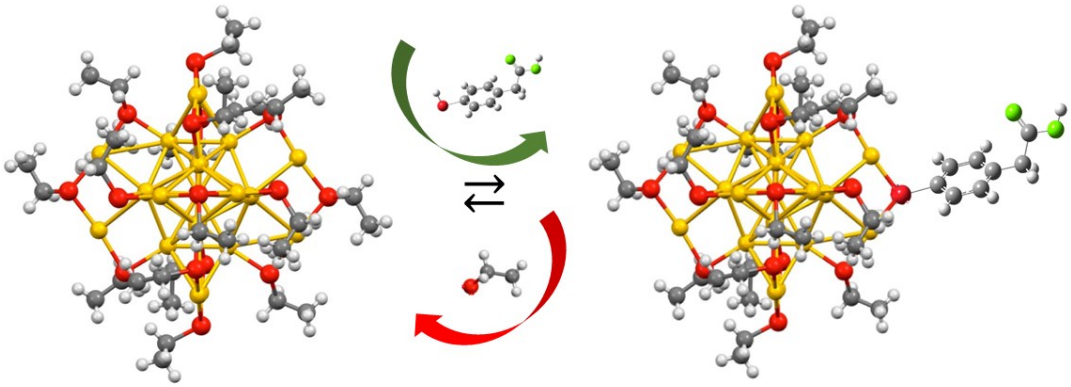

Figure 6 Example of Ligand exchange reaction in which the HSC_2H_5 ligand (endogenous) is replaced by an $HSPhCH_2COOH$ ligand (exogenous).

This transition holds the potential to engender profound alterations in the properties of the nanoclusters, which comprises their solubility in aqueous environments, reactivity towards other molecular species, and their interaction with incident light, all of which accentuate the versatility and applicability of these nanoscale materials. The mechanism of LER on NCs has not yet been elucidated and for this reason, we will not dwell much on it. Indeed, much of the scientific community in this field agreed in attributing an associative S_N2-like mechanism to LER, both thanks to experimental[70] and theoretical[68] results. However, curiously, very recently, a paper by Wu and co-workers demonstrated that a S_N2 mechanism was not possible.[71] Indeed, a single crystal structure analysis of ligand exchanged clusters showed that part of the sulfur atoms retained their configuration upon ligand exchange, which seems of course not possible for a S_N2-like process. They proposed a unimolecular nucleophilic substitution (S_N1)-like mechanism.

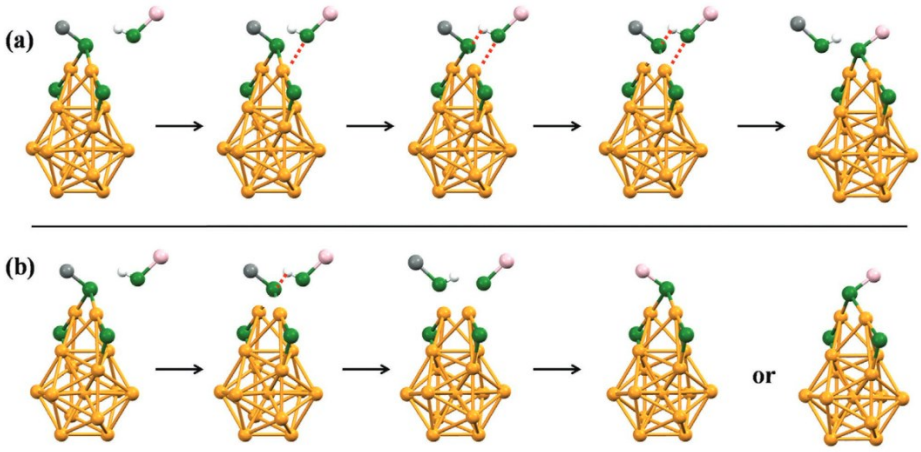

Figure 7 a) Associative S_N2-like mechanism and **b)** S_N1-like mechanism of the ligand exchange reaction. Au, yellow; S, green; the α-C atom of the outgoing thiol, gray; and the α-C atom of the incoming thiol,

pink. Only one staple and the Au_{13} core are presented. The other five staples and the rest of the C and H atoms are omitted for clarity. The red dashed lines represent the interaction between the incoming thiol and the nanocluster.

In any case, the quantity of data, because of the fast dynamics and complexity of the ligand exchange, is, to date, not enough to clarify the mechanistic details of this reaction. However, we can underline that LER is strongly based on the Au-S chemistry. Indeed, the organic shell protecting the NCs, is quite similar to the well-known Self Assembled Monolayers (SAMs). Since the SAM is not rigid, the Au-S interface on clusters is also non-static. Moreover, also in the cluster surface several processes, including thiolate migration, and thiolate desorption (with subsequent re-adsorption), can occur. Thiolate migration has been experimentally observed for both clusters and surfaces at temperatures above ambient, while thiolate desorption occurs even at room temperature for both flat surfaces and clusters.[72,73] In addition, the structural motif of the staples, on the NC's surface, certainly helps the dynamicity of the ligands. Despite the great uncertainty that still exists, thanks to experimental evidence we can say that (i) the chemical reactivity of nanoclusters was found to be largely independent of their size,[74] but the stability of the sample is a key factor determining the outcome of LER.[71] The rate and extent of LERs have been found to increase with the increase in positive electronic charge on the Au cluster core,[75] but they decrease with the increase in the size of the incoming ligand and the carbon chain length of the protecting monolayer.[76]

Here are some important examples of how LERs can be used: (i) Implementation in biology and medicine: The surface of the NC can be modified, for example, to bind cancer cells or to deliver drugs to specific parts of the body;[77–82] (ii) tuning of electronic and optical properties for developing new types of devices, such as light-emitting diodes and solar cells;[83,84] and (iii) assembly: LERs can be used to assemble nanoclusters into larger structures. Indeed, the different dimension, hindrance and chemical nature of ligands can favor the transformation of the NC's core[45,56,85–88] and the interaction with each other in diverse ways, leading, eventually, to the formation of larger superstructures.[89–92] Careful selection of ligands can thus direct NCs assembly.

Significant research has been conducted on the possibility of tuning the physicochemical properties of Au NCs by acting on the ligands. For example, there is a wealth of literature on the enhancement of photophysical properties of Au NCs functionalized with chromophore or porphyrin ligands.[33,41,46–48] Alongside the widespread interest in the properties and applications of functionalized atomically

precise gold nanoclusters (Au NCs), in the last years there has been a surge of research exploring their potential as molecular units for assembling larger superstructures. This endeavor has been fueled by the realization that Au NCs can exhibit synergistic properties and functionalities when assembled into organized structures and novel materials.[90] Indeed, NCs exhibit exceptional thermodynamic stability, enabling controlled size modulation, stoichiometry adjustment, and tailoring of their molecular surface chemistry. This opens the possibility of constructing a vast library of novel molecular units with atomically precise structures and established structure-property relationships. These unique attributes place NCs at the forefront of material science, offering the prospect of designing novel hierarchical materials with unprecedented properties. However, despite the tantalizing promise of self-assembled metal NCs, significant research is required to develop effective tools for controlling their assembly. Hakkinen and his collaborators paved the way for exploring this topic, using density functional theory (DFT) calculations.[92] Their study focused on simulating the discrete dimeric species formed by covalently linking anionic $Au_{25}(SR)_{18}$ nanoclusters with a benzene-1,4-dithiol (BDT) molecule (Figure 8).

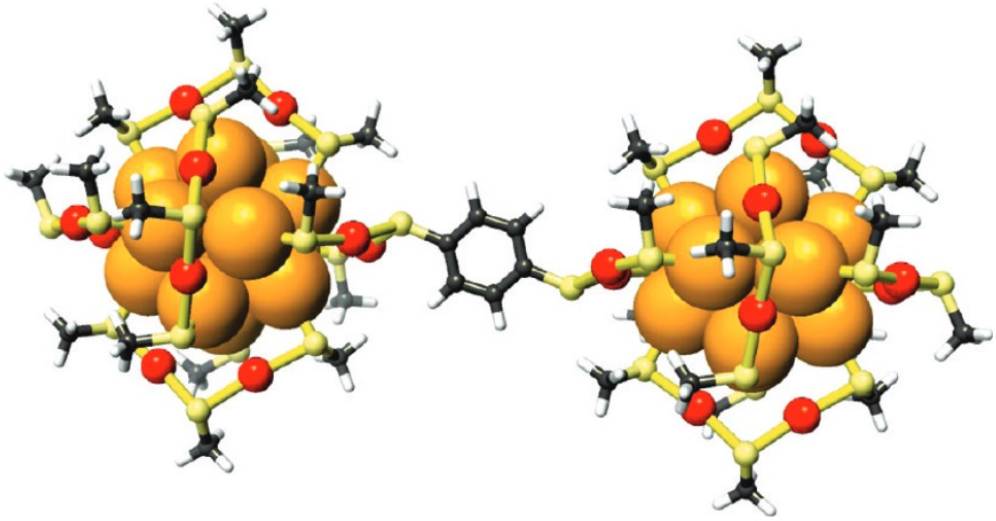

Figure 8 Structure of the relaxed $[Au_{25}(SCH_3)_{17}\text{-BDT-}(SCH_3)_{17}Au_{25}]^{2-}$ dimer. Color code: Au_{core} = orange, Au_{staple} = yellow, S = red, C = black, H = white.[92]

The optimized structure of the Au_{25} dimer revealed that Au_{25} units in the dimer retained their individual electron shell structures after linking with the dithiol ligand. In addition, calculations of the HOMO-LUMO gaps in the gas phase yielded almost identical values, while the density of states was higher for the dimers due to the individual contributions of the two Au_{25} units. This study highlighted the potential of using Au NCs as molecular units for dimers or even larger structures, provided suitable linking methods can be established. Recently, significant progress has been made in utilizing

supramolecular chemistry to manipulate the ligand interactions of Au NCs, enabling the formation of intricate and reversible superstructures.[93–95] However, the controlled assembly of Au NCs into well-defined superstructures, with a precise understanding of the atomic-level structure of the resulting materials, remained a challenging endeavor. At this regard, another pioneering study by Hakkinen and colleagues in 2016, actually starts to cover this gap, demonstrating experimentally the covalent coupling of atomically precise Au_{102} and Au_{250} nanoclusters using a dithiol ligand as molecular bridge.[90] Unlike isolated Au NCs, these multimers exhibited hybridized plasmon modes with remarkably large red-shifts, likely arising from electron tunneling through the molecular states of the disulfide bridge. Motivated by these findings, several studies have attempted to synthesize new and well-defined Au NC-based superstructures using a bottom-up approach.[89,91] Among the most important examples it is necessary to mention the works of Burgi and co-workers, but we refer the reader to the chapters concerning the results to find out more.

In conclusion, ligands, commonly organic molecules such as thiols, play a crucial role in shaping the properties of nanoclusters. They not only protect the metal core from chemical degradation but also influence the stability, size, shape, and also electronic properties of the nanocluster. Indeed, the previous paragraph highlighted how the ligand shell serves as a dielectric barrier, shielding the core from its surroundings and hindering reactivity. Moreover, it can modulate the nanocluster's electronic structure, influencing its optical, magnetic, and catalytic properties. Furthermore, the arrangement of ligands on the nanocluster's surface and their chemical nature can influence its interactions with other molecules, surfaces and NCs, or formation of larger superstructures. This can be exploited to tailor the nanocluster's properties for specific applications.

As research on nanoclusters progresses, the importance of ligands is becoming increasingly evident. Researchers are now exploring ways to manipulate the ligand shell to fine-tune the properties of nanoclusters and enable more intricate chemistry with the goal of creating novel supermolecules, opening up new possibilities for their application in various fields. It is precisely in this landscape that this doctoral thesis fits in, trying to contribute to the understanding and discovery of these fascinating molecules which are the atomically precise nanoclusters.

1.4 Aim of the Thesis

The thesis work I am about to present explores the fascinating world of atomically precise nanoclusters (NCs), investigating their properties and potential applications. NCs have gained immense scientific interest due to their promise for various applications. However, research into these intriguing systems is still active, with fundamental studies ongoing. Our research group (The Molecular Electrochemistry and Nanosystems group) has played a key role in unraveling the principles governing NCs and their connection to their structure. We have particularly emphasized the crucial role of ligands in shaping the nanoclusters' properties. Ligands have long been underestimated, often considered superficially or even incorrectly. Over the years, our research has highlighted their profound impact on the overall molecular properties of NCs. Among all NCs, Au_{25} (protected by thiolates) is the most widely studied, thanks to its practical advantages (high-yield synthesis, stability in three oxidation states, and early discovery) and unique properties. From an electrochemical perspective, NCs are remarkable in that they consist of thiolates completely surrounding the metal core, akin to a 3D analog of 2D self-assembled monolayers on extended gold surfaces. However, unlike the well-shielded monolayers on extended surfaces, the 3D monolayer on a small cluster allows exogenous molecules to penetrate and experience the properties of a unique nanoenvironment. Our group's extensive research has led to a series of publications, contributing significantly to the recognition within the scientific community that ligands are not merely ancillary components, but rather fundamental tools with profound implications. This recognition has driven my doctoral thesis.

In this thesis work, after introducing the concept of NCs (Chapter 1) and the methods and characterization techniques used (Chapter 2), I present a series of studies focused on manipulating NC ligand chemistry. These studies demonstrate that carefully tailoring the ligands on the nanocluster surface allows us to modify (Chapter 4, 5, 9) and even precisely control (Chapter 3) properties such as electron transfer in solution (Chapter 5), conductivity of nanocluster films and their associated electron transfer in the solid state (Chapters 3, 5), and overall redox properties (Chapter 9). Additionally, I explore the possibility of enabling the formation of novel species with unique properties through chemical bonding between distinct NC units, after ad-hoc surface modification, via Ligand Exchange Reaction (LER) (Chapters 6, 8). Finally, Chapters 4 and 7 showcase instances where nanocluster surface modification has facilitated their application-oriented utilization. Chapters 5 and 8

highlight two particularly groundbreaking achievements. Chapter 5 demonstrates the profound impact of the isotopic effect on the solid-state packing properties of NCs, as evidenced by the first-ever crystal structure determination of a fully deuterated cluster. Chapter 8, on the other hand, presents the synthesis of an Au_{25} dimer linked by a molecular bridge comprising a metal atom complex, which was found to be a multicomponent redox-active molecule. This achievement was made possible through a novel LER strategy that utilizes electrostatic driving forces followed by a change in product solubility, ensuring the complete absence of byproducts arising from successive exchanges. This novel synthesis approach is a significant breakthrough that could lead to the development of new complex systems with a wide range of applications.

In conclusion, we believe this thesis work makes an important contribution to scientific research on atomically precise nanoclusters and confirms the importance of ligands in determining the properties of these molecules. We believe this work can stimulate further research on modifying the properties of NCs by surface modification.

1.5 References

1. Whetten, R. L.; Khoury, J. T.; Alvarez, M. M.; Murthy, S.; Vezmar, I.; Wang, Z. L.; Stephens, P. W.; Cleveland, C. L.; Luedtke, W. D.; Landman, U. Nanocrystal Gold Molecules. *Adv. Mater.* **1996**, *8* (5), 428–433.
2. Schaaff, T. G.; Knight, G.; Shafigullin, M. N.; Borkman, R. F.; Whetten, R. L. Isolation and Selected Properties of a 10.4 kDa Gold:Glutathione Cluster Compound. *J. Phys. Chem. B* **1998**, *102* (52), 10643–10646.
3. Schaaff, T. G.; Shafigullin, M. N.; Khoury, J. T.; Vezmar, I.; Whetten, R. L. Properties of a Ubiquitous 29 kDa Au:SR Cluster Compound. *J. Phys. Chem. B* **2001**, *105* (37), 8785–8796.
4. Price, R. C.; Whetten, R. L. All-Aromatic, Nanometer-Scale, Gold-Cluster Thiolate Complexes. *J. Am. Chem. Soc.* **2005**, *127* (40), 13750–13751.
5. Wyrwas, R. B.; Alvarez, M. M.; Khoury, J. T.; Price, R. C.; Schaaff, T. G.; Whetten, R. L. The Colours of Nanometric Gold: Optical Response Functions of Selected Gold-Cluster Thiolates. *Eur. Phys. J. D* **2007**, *43* (1–3), 91–95.
6. Negishi, Y.; Nobusada, K.; Tsukuda, T. Glutathione-Protected Gold Clusters Revisited: Bridging the Gap between Gold(I)Thiolate Complexes and Thiolate-Protected Gold Nanocrystals. *J. Am. Chem. Soc.* **2005**, 127, 5261-5270.
7. Zhu, M.; Lanni, E.; Garg, N.; Bier, M. E.; Jin, R. Kinetically Controlled, High-Yield Synthesis of Au_{25} Clusters. *J. Am. Chem. Soc.* **2008**, *130* (4), 1138–1139.
8. Wu, Z.; Suhan, J.; Jin, R. One-Pot Synthesis of Atomically Monodisperse, Thiol-Functionalized Au_{25} Nanoclusters. *J Mater Chem* **2009**, *19* (5), 622–626.
9. Qian, H.; Zhu, Y.; Jin, R. Size-Focusing Synthesis, Optical and Electrochemical Properties of Monodisperse $Au_{38}(SC_2H_4Ph)_{24}$ Nanoclusters. *ACS Nano* **2009**, *3* (11), 3795–3803.
10. Jin, R.; Qian, H.; Wu, Z.; Zhu, Y.; Zhu, M.; Mohanty, A.; Garg, N. Size Focusing: A Methodology for Synthesizing Atomically Precise Gold Nanoclusters. *J. Phys. Chem. Lett.* **2010**, *1* (19), 2903–2910.
11. Qian, H.; Jin, R. Controlling Nanoparticles with Atomic Precision: The Case of $Au_{144}(SCH_2CH_2Ph)_{60}$. *Nano Lett.* **2009**, *9* (12), 4083–4087.
12. Jadzinsky, P. D.; Calero, G.; Ackerson, C. J.; Bushnell, D. A.; Kornberg, R. D. Structure of a Thiol Monolayer-Protected Gold Nanoparticle at 1.1 Å Resolution. *Science* **2007**, *318* (5849), 430–433.
13. Kang, X.; Chong, H.; Zhu, M. $Au_{25}(SR)_{18}$: The Captain of the Great Nanocluster Ship. *Nanoscale* **2018**, *10* (23), 10758–10834.
14. Dong, C.; Huang, R.-W.; Chen, C.; Chen, J.; Nematulloev, S.; Guo, X.; Ghosh, A.; Alamer, B.; Hedhili, M. N.; Isimjan, T. T.; Han, Y.; Mohammed, O. F.; Bakr,

O. M. [$Cu_{36}H_{10}(PET)_{24}(PPh_3)_6Cl_2$] Reveals Surface Vacancy Defects in Ligand-Stabilized Metal Nanoclusters. *J. Am. Chem. Soc.* **2021**, *143* (29), 11026–11035.

15. Alhilaly, M. J.; Huang, R.-W.; Naphade, R.; Alamer, B.; Hedhili, M. N.; Emwas, A.-H.; Maity, P.; Yin, J.; Shkurenko, A.; Mohammed, O. F.; Eddaoudi, M.; Bakr, O. M. Assembly of Atomically Precise Silver Nanoclusters into Nanocluster-Based Frameworks. *J. Am. Chem. Soc.* **2019**, *141* (24), 9585–9592.

16. Bootharaju, M. S.; Dey, R.; Gevers, L. E.; Hedhili, M. N.; Basset, J.-M.; Bakr, O. M. A New Class of Atomically Precise, Hydride-Rich Silver Nanoclusters Co-Protected by Phosphines. *J. Am. Chem. Soc.* **2016**, *138* (42), 13770–13773.

17. Ghosh, A.; Huang, R.-W.; Alamer, B.; Abou-Hamad, E.; Hedhili, M. N.; Mohammed, O. F.; Bakr, O. M. [$Cu_{61}(StBu)_{26}S_6Cl_6H_{14}]^+$: A Core–Shell Superatom Nanocluster with a Quasi- $J_{36}Cu_{19}$ Core and an “18-Crown-6” Metal-Sulfide-like Stabilizing Belt. *ACS Mater. Lett.* **2019**, *1* (3), 297–302.

18. Joshi, C. P.; Bootharaju, M. S.; Alhilaly, M. J.; Bakr, O. M. [$Ag_{25}(SR)_{18}]^-$: The “Golden” Silver Nanoparticle. *J. Am. Chem. Soc.* **2015**, *137* (36), 11578–11581.

19. Huang, X.; Li, Z.; Yu, Z.; Deng, X.; Xin, Y. Recent Advances in the Synthesis, Properties, and Biological Applications of Platinum Nanoclusters. *J. Nanomater.* **2019**, *2019*, 1–31.

20. Cook, A. W.; Hrobárik, P.; Damon, P. L.; Wu, G.; Hayton, T. W. A Ketimide-Stabilized Palladium Nanocluster with a Hexagonal Aromatic Pd_7 Core. *Inorg. Chem.* **2020**, *59* (2), 1471–1480.

21. Yamamoto, H.; Maity, P.; Takahata, R.; Yamazoe, S.; Koyasu, K.; Kurashige, W.; Negishi, Y.; Tsukuda, T. Monodisperse Iridium Clusters Protected by Phenylacetylene: Implication for Size-Dependent Evolution of Binding Sites. *J. Phys. Chem. C* **2017**, *121* (20), 10936–10941.

22. Medves, M.; Sementa, L.; Toffoli, D.; Fronzoni, G.; Krishnadas, K. R.; Bürgi, T.; Bonacchi, S.; Dainese, T.; Maran, F.; Fortunelli, A.; Stener, M. Predictive Optical Photoabsorption of $Ag_{24}Au(DMBT)_{18}^-$ via Efficient TDDFT Simulations. *J. Chem. Phys.* **2021**, *155* (8), 084103.

23. Parker, J. F.; Kacprzak, K. A.; Lopez-Acevedo, O.; Häkkinen, H.; Murray, R. W. Experimental and Density Functional Theory Analysis of Serial Introductions of Electron-Withdrawing Ligands into the Ligand Shell of a Thiolate-Protected Au_{25} Nanoparticle. *J. Phys. Chem. C* **2010**, *114* (18), 8276–8281.

24. Heaven, M. W.; Dass, A.; White, P. S.; Holt, K. M.; Murray, R. W. Crystal Structure of the Gold Nanoparticle [$N(C_8H_{17})_4$][$Au_{25}(SCH_2CH_2Ph)_{18}$]. *J. Am. Chem. Soc.* **2008**, *130* (12), 3754–3755.

25. Murray, R. W. Nanoelectrochemistry: Metal Nanoparticles, Nanoelectrodes, and Nanopores. *Chem. Rev.* **2008**, *108* (7), 2688–2720.

26. Jin, R. Atomically Precise Metal Nanoclusters: Stable Sizes and Optical Properties. *Nanoscale* **2015**, *7* (5), 1549–1565.

27. Agrachev, M.; Ruzzi, M.; Venzo, A.; Maran, F. Nuclear and Electron Magnetic Resonance Spectroscopies of Atomically Precise Gold Nanoclusters. *Acc. Chem. Res.* **2019**, *52* (1), 44–52.

28. Antonello, S.; Holm, A. H.; Instuli, E.; Maran, F. Molecular Electron-Transfer Properties of Au_{38} Clusters. *J. Am. Chem. Soc.* **2007**, *129* (32), 9836–9837.

29. Zeng, C.; Jin, R. Chiral Gold Nanoclusters: Atomic Level Origins of Chirality. *Chem. Asian J.* **2017**, *12* (15), 1839–1850.

30. Zhu, Y.; Guo, J.; Qiu, X.; Zhao, S.; Tang, Z. Optical Activity of Chiral Metal Nanoclusters. *Acc. Mater. Res.* **2021**, *2* (1), 21–35.

31. Li, G.; Abroshan, H.; Liu, C.; Zhuo, S.; Li, Z.; Xie, Y.; Kim, H. J.; Rosi, N. L.; Jin, R. Tailoring the Electronic and Catalytic Properties of Au_{25} Nanoclusters *via* Ligand Engineering. *ACS Nano* **2016**, *10* (8), 7998–8005.

32. Agrachev, M.; Antonello, S.; Dainese, T.; Ruzzi, M.; Zoleo, A.; Aprà, E.; Govind, N.; Fortunelli, A.; Sementa, L.; Maran, F. Magnetic Ordering in Gold Nanoclusters. *ACS Omega* **2017**, *2* (6), 2607–2617.

33. Dainese, T.; Agrachev, M.; Antonello, S.; Badocco, D.; Black, D. M.; Fortunelli, A.; Gascón, J. A.; Stener, M.; Venzo, A.; Whetten, R. L.; Maran, F. Atomically Precise $Au_{144}(SR)_{60}$ Nanoclusters (R = Et, Pr) Are Capped by 12 Distinct Ligand Types of 5-Fold Equivalence and Display Gigantic Diastereotopic Effects. *Chem. Sci.* **2018**, *9* (47), 8796–8805.

34. De Nardi, M.; Antonello, S.; Jiang, D.; Pan, F.; Rissanen, K.; Ruzzi, M.; Venzo, A.; Zoleo, A.; Maran, F. Gold Nanowired: A Linear $(Au_{25})_n$ Polymer from Au_{25} Molecular Clusters. *ACS Nano* **2014**, *8* (8), 8505–8512.

35. Antonello, S.; Dainese, T.; Pan, F.; Rissanen, K.; Maran, F. Electrocrystallization of Monolayer-Protected Gold Clusters: Opening the Door to Quality, Quantity, and New Structures. *J. Am. Chem. Soc.* **2017**, *139* (11), 4168–4174.

36. Fei, W.; Antonello, S.; Dainese, T.; Dolmella, A.; Lahtinen, M.; Rissanen, K.; Venzo, A.; Maran, F. Metal Doping of $Au_{25}(SR)_{18}^{-}$ Clusters: Insights and Hindsights. *J. Am. Chem. Soc.* **2019**, *141* (40), 16033–16045.

37. Dainese, T.; Antonello, S.; Gascón, J. A.; Pan, F.; Perera, N. V.; Ruzzi, M.; Venzo, A.; Zoleo, A.; Rissanen, K.; Maran, F. $Au_{25}(SEt)_{18}$, a Nearly Naked Thiolate-Protected Au_{25} Cluster: Structural Analysis by Single Crystal X-Ray Crystallography and Electron Nuclear Double Resonance. *ACS Nano* **2014**, *8* (4), 3904–3912.

38. Kumara, C.; Aikens, C. M.; Dass, A. X-Ray Crystal Structure and Theoretical Analysis of $Au_{25-x}Ag_x(SCH_2CH_2Ph)_{18}^-$ Alloy. *J. Phys. Chem. Lett.* **2014**, *5* (3), 461–466.

39. Li, G.; Jin, R. Atomically Precise Gold Nanoclusters as New Model Catalysts. *Acc. Chem. Res.* **2013**, *46* (8), 1749–1758.

40. Zhu, Y.; Jin, R.; Sun, Y. Atomically Monodisperse Gold Nanoclusters Catalysts with Precise Core-Shell Structure. *Catalysts* **2011**, *1* (1), 3–17.

41. Zhu, M.; Aikens, C. M.; Hollander, F. J.; Schatz, G. C.; Jin, R. Correlating the Crystal Structure of A Thiol-Protected Au_{25} Cluster and Optical Properties. *J. Am. Chem. Soc.* **2008**, *130* (18), 5883–5885.

42. Parker, J. F.; Fields-Zinna, C. A.; Murray, R. W. The Story of a Monodisperse Gold Nanoparticle: $Au_{25}L_{18}$. *Acc. Chem. Res.* **2010**, *43* (9), 1289–1296.

43. Qian, H.; Zhu, M.; Wu, Z.; Jin, R. Quantum Sized Gold Nanoclusters with Atomic Precision. *Acc. Chem. Res.* **2012**, *45* (9), 1470–1479.

44. Krishnadas, K. R.; Pradeep, T. Structure and Chemical Properties of Clusters. In *Atomically Precise Metal Nanoclusters*; Elsevier, **2023**; pp 5–49.

45. Rambukwella, M.; Sakthivel, N. A.; Delcamp, J. H.; Sementa, L.; Fortunelli, A.; Dass, A. Ligand Structure Determines Nanoparticles' Atomic Structure, Metal-Ligand Interface and Properties. *Frontiers in Chemistry*, **2018,** 6, 330.

46. Agrachev, M.; Antonello, S.; Dainese, T.; Gascón, J. A.; Pan, F.; Rissanen, K.; Ruzzi, M.; Venzo, A.; Zoleo, A.; Maran, F. A Magnetic Look into the Protecting Layer of Au_{25} Clusters. *Chem. Sci.* **2016**, *7* (12), 6910–6918.

47. Kim, J.; Lema, K.; Ukaigwe, M.; Lee, D. Facile Preparative Route to Alkanethiolate-Coated Au_{38} Nanoparticles: Postsynthesis Core Size Evolution. *Langmuir* **2007**, *23* (14), 7853–7858.

48. Su, B.; Zhang, M.; Shao, Y.; Girault, H. H. Solvent Effect on Redox Properties of Hexanethiolate Monolayer-Protected Gold Nanoclusters. *J. Phys. Chem. B* **2006**, *110* (43), 21460–21466.

49. Laaksonen, T.; Pelliniemi, O.; Quinn, B. M. Ion Permeability of SAMs on Nanoparticle Surfaces. *J. Am. Chem. Soc.* **2006**, *128* (44), 14341–14346.

50. Garcia-Morales, V.; Mafé, S. Monolayer-Protected Metallic Nanoparticles: Limitations of the Concentric Sphere Capacitor Model. *J. Phys. Chem. C* **2007**, *111* (20), 7242–7250.

51. Antonello, S.; Dainese, T.; De Nardi, M.; Perotti, L.; Maran, F. Insights into the Interface Between the Electrolytic Solution and the Gold Core in Molecular Au_{25} Clusters. *ChemElectroChem* **2016**, *3* (8), 1237–1244.

52. Antonello, S.; Arrigoni, G.; Dainese, T.; De Nardi, M.; Parisio, G.; Perotti, L.; René, A.; Venzo, A.; Maran, F. Electron Transfer through 3D Monolayers on Au_{25} Clusters. *ACS Nano* **2014**, *8* (3), 2788–2795.

53. Kang, X.; Zhu, M. Transformation of Atomically Precise Nanoclusters by Ligand-Exchange. *Chem. Mater.* **2019**, *31* (24), 9939–9969.

54. Hossain, S.; Kurashige, W.; Wakayama, S.; Kumar, B.; Nair, L. V.; Niihori, Y.; Negishi, Y. Ligand Exchange Reactions in Thiolate-Protected Au_{25} Nanoclusters with Selenolates or Tellurolates: Preferential Exchange Sites and Effects on Electronic Structure. *J. Phys. Chem. C* **2016**, *120* (45), 25861–25869.

55. Niihori, Y.; Kikuchi, Y.; Kato, A.; Matsuzaki, M.; Negishi, Y. Understanding Ligand-Exchange Reactions on Thiolate-Protected Gold Clusters by Probing Isomer Distributions Using Reversed-Phase High-Performance Liquid Chromatography. *ACS Nano* **2015**, *9* (9), 9347–9356.

56. Shichibu, Y.; Negishi, Y.; Tsukuda, T.; Teranishi, T. Large-Scale Synthesis of Thiolated Au_{25} Clusters via Ligand Exchange Reactions of Phosphine-Stabilized Au_{11} Clusters. *J. Am. Chem. Soc.* **2005**, *127* (39), 13464–13465.

57. Wang, Y.; Bürgi, T. Ligand Exchange Reactions on Thiolate-Protected Gold Nanoclusters. *Nanoscale Adv.* **2021**, *3* (10), 2710–2727.

58. Ding, M.; Tang, L.; Ma, X.; Song, C.; Wang, S. Effects of Ligand Tuning and Core Doping of Atomically Precise Copper Nanoclusters on CO_2 Electroreduction Selectivity. *Commun. Chem.* **2022**, *5* (1), 172.

59. Ghosh, A.; Mohammed, O. F.; Bakr, O. M. Atomic-Level Doping of Metal Clusters. *Acc. Chem. Res.* **2018**, *51* (12), 3094–3103.

60. Li, Y.; Biswas, S.; Luo, T.-Y.; Juarez-Mosqueda, R.; Taylor, M. G.; Mpourmpakis, G.; Rosi, N. L.; Hendrich, M. P.; Jin, R. Doping Effect on the Magnetism of Thiolate-Capped 25-Atom Alloy Nanoclusters. *Chem. Mater.* **2020**, *32* (21), 9238–9244.

61. Maity, S.; Kolay, S.; Ghosh, S.; Chakraborty, S.; Bain, D.; Patra, A. Unraveling the Effect of Single Atom Doping on the Carrier Relaxation Dynamics of Mag_{24}^{n-} Nanoclusters. *J. Phys. Chem. Lett.* **2022**, 5581–5588.

62. Walter, M.; Moseler, M. Ligand-Protected Gold Alloy Clusters: Doping the Superatom. *J. Phys. Chem. C* **2009**, *113* (36), 15834–15837.

63. Kang, X.; Li, Y.; Zhu, M.; Jin, R. Atomically Precise Alloy Nanoclusters: Syntheses, Structures, and Properties. *Chem. Soc. Rev.* **2020**, *49* (17), 6443–6514.

64. Chen, Y.; Zhou, M.; Li, Q.; Gronlund, H.; Jin, R. Isomerization-Induced Enhancement of Luminescence in $Au_{28}(SR)_{20}$ Nanoclusters. *Chem. Sci.* **2020**, *11* (31), 8176–8183.

65. Zeng, C.; Chen, Y.; Das, A.; Jin, R. Transformation Chemistry of Gold Nanoclusters: From One Stable Size to Another. *J. Phys. Chem. Lett.* **2015**, *6* (15), 2976–2986.

66. Dainese, T.; Antonello, S.; Bogialli, S.; Fei, W.; Venzo, A.; Maran, F. Gold Fusion: From $Au_{25}(SR)_{18}$ to $Au_{38}(SR)_{24}$, the Most Unexpected Transformation of a Very Stable Nanocluster. *ACS Nano* **2018**, 12(7), 7057-7066.

67. Templeton, A. C.; Wuelfing, W. P.; Murray, R. W. Monolayer-Protected Cluster Molecules. *Acc. Chem. Res.* **2000**, *33* (1), 27–36.

68. Heinecke, C. L.; Ni, T. W.; Malola, S.; Mäkinen, V.; Wong, O. A.; Häkkinen, H.; Ackerson, C. J. Structural and Theoretical Basis for Ligand Exchange on Thiolate Monolayer Protected Gold Nanoclusters. *J. Am. Chem. Soc.* **2012**, *134* (32), 13316–13322.

69. Zhao, J.; Ziarati, A.; Rosspeintner, A.; Wang, Y.; Bürgi, T. Engineering Ligand Chemistry on Au_{25} Nanoclusters: From Unique Ligand Addition to Precisely Controllable Ligand Exchange. *Chem. Sci.* **2023**, *14* (28), 7665–7674.

70. Salassa, G.; Sels, A.; Mancin, F.; Bürgi, T. Dynamic Nature of Thiolate Monolayer in $Au_{25}(SR)_{18}$ Nanoclusters. *ACS Nano* **2017**, *11* (12), 12609–12614.

71. Yan, N.; Xia, N.; Wu, Z. Metal Nanoparticles Confronted with Foreign Ligands: Mere Ligand Exchange or Further Structural Transformation? *Small* **2021**, *17* (27), 2000609.

72. Bürgi, T. Properties of the Gold–Sulphur Interface: From Self-Assembled Monolayers to Clusters. *Nanoscale* **2015**, *7* (38), 15553–15567.

73. Pensa, E.; Cortés, E.; Corthey, G.; Carro, P.; Vericat, C.; Fonticelli, M. H.; Benítez, G.; Rubert, A. A.; Salvarezza, R. C. The Chemistry of the Sulfur–Gold Interface: In Search of a Unified Model. *Acc. Chem. Res.* **2012**, *45* (8), 1183–1192.

74. Guo, R.; Murray, R. W. Substituent Effects on Redox Potentials and Optical Gap Energies of Molecule-like $Au_{38}(SPhX)_{24}$ Nanoparticles. *J. Am. Chem. Soc.* **2005**, *127* (34), 12140–12143.

75. Song, Y.; Murray, R. W. Dynamics and Extent of Ligand Exchange Depend on Electronic Charge of Metal Nanoparticles. *J. Am. Chem. Soc.* **2002**, *124* (24), 7096–7102.

76. Hostetler, M. J.; Templeton, A. C.; Murray, R. W. Dynamics of Place-Exchange Reactions on Monolayer-Protected Gold Cluster Molecules. *Langmuir* **1999**, *15* (11), 3782–3789.

77. Chen, L.-Y.; Wang, C.-W.; Yuan, Z.; Chang, H.-T. Fluorescent Gold Nanoclusters: Recent Advances in Sensing and Imaging. *Anal Chem* **2015**, 87(1), 216-229.

78. Gao, P.; Chang, X.; Zhang, D.; Cai, Y.; Chen, G.; Wang, H.; Wang, T. Synergistic Integration of Metal Nanoclusters and Biomolecules as Hybrid Systems for Therapeutic Applications. *Acta Pharm. Sin. B* **2021**, *11* (5), 1175–1199.

79. Tao, Y.; Li, M.; Ren, J.; Qu, X. Metal Nanoclusters: Novel Probes for Diagnostic and Therapeutic Applications. *Chem. Soc. Rev.* **2015**, *44* (23), 8636–8663.

80. Zan, X.; Li, Q.; Pan, Y.; Morris, D. J.; Zhang, P.; Li, P.; Yu, H.; Zhu, M. Versatile Ligand-Exchange Method for the Synthesis of Water-Soluble Monodisperse AuAg Nanoclusters for Cancer Therapy. *ACS Appl. Nano Mater.* **2018**, *1* (12), 6773–6781.

81. Zhu, H.; Zhou, Y.; Wang, Y.; Xu, S.; James, T. D.; Wang, L. Stepwise-Enhanced Tumor Targeting of Near-Infrared Emissive Au Nanoclusters with High Quantum Yields and Long-Term Stability. *Anal. Chem.* **2022**, 94(38), 13189-13196.

82. Lin, C.-A. J.; Yang, T.-Y.; Lee, C.-H.; Huang, S. H.; Sperling, R. A.; Zanella, M.; Li, J. K.; Shen, J.-L.; Wang, H.-H.; Yeh, H.-I.; Parak, W. J.; Chang, W. H. Synthesis, Characterization, and Bioconjugation of Fluorescent Gold Nanoclusters toward Biological Labeling Applications. *ACS Nano* **2009**, *3* (2), 395–401.

83. Chen, L.; Black, A.; Parak, W. J.; Klinke, C.; Chakraborty, I. Metal Nanocluster-based Devices: Challenges and Opportunities. *Aggregate* **2021**, 3(4), e132.

84. Chen, Y.-S.; Choi, H.; Kamat, P. V. Metal-Cluster-Sensitized Solar Cells. A New Class of Thiolated Gold Sensitizers Delivering Efficiency Greater Than 2%. *J. Am. Chem. Soc.* **2013**, *135* (24), 8822–8825.

85. Zeng, C.; Liu, C.; Pei, Y.; Jin, R. Thiol Ligand-Induced Transformation of $Au_{38}(SC_2H_4Ph)_{24}$ to $Au_{36}(SPh\text{-}t\text{-}Bu)_{24}$. *ACS Nano* **2013**, *7* (7), 6138–6145.

86. Dass, A.; Jones, T. C.; Theivendran, S.; Sementa, L.; Fortunelli, A. Core Size Interconversions of $Au_{30}(S\text{-}t\text{Bu})_{18}$ and $Au_{36}(SPhX)_{24}$. *J. Phys. Chem. C* **2017**, *121* (27), 14914–14919.

87. Das, A.; Li, T.; Li, G.; Nobusada, K.; Zeng, C.; Rosi, N. L.; Jin, R. Crystal Structure and Electronic Properties of a Thiolate-Protected Au_{24} Nanocluster. *Nanoscale* **2014**, *6* (12), 6458.

88. Maman, M. P.; Nair, A. S.; Cheraparambil, H.; Pathak, B.; Mandal, S. Size Evolution Dynamics of Gold Nanoclusters at an Atom-Precision Level: Ligand Exchange, Growth Mechanism, Electrochemical, and Photophysical Properties. *J. Phys. Chem. Lett.* **2020**, *11* (5), 1781–1788.

89. Ho-Wu, R.; Sun, K.; Goodson, T. Synthesis and Enhanced Linear and Nonlinear Optical Properties of Chromophore–Au Metal Cluster Oligomers. *J. Phys. Chem. C* **2018**, *122* (4), 2315–2329.

90. Lahtinen, T.; Hulkko, E.; Sokołowska, K.; Tero, T.-R.; Saarnio, V.; Lindgren, J.; Pettersson, M.; Häkkinen, H.; Lehtovaara, L. Covalently Linked Multimers of Gold Nanoclusters $Au_{102}(p\text{-}MBA)_{44}$ and $Au_{\sim 250}(p\text{-}MBA)_n$. *Nanoscale* **2016**, *8* (44), 18665–18674.

91. Sokolowska, K.; Hulkko, E.; Lehtovaara, L.; Lahtinen, T. Dithiol-Induced Oligomerization of Thiol-Protected Gold Nanoclusters. *J. Phys. Chem. C* **2018**, *122* (23), 12524–12533.

92. Akola, J.; Kacprzak, K. A.; Lopez-Acevedo, O.; Walter, M.; Grönbeck, H.; Häkkinen, H. Thiolate-Protected Au_{25} Superatoms as Building Blocks: Dimers and Crystals. *J. Phys. Chem. C* **2010**, *114* (38), 15986–15994.

93. Rival, J. V.; Nonappa; Shibu, E. S. Light-Triggered Reversible Supracolloidal Self-Assembly of Precision Gold Nanoclusters. *ACS Appl. Mater. Interfaces* **2020**, *12* (12), 14569–14577.

94. Nag, A.; Pradeep, T. Assembling Atomically Precise Noble Metal Nanoclusters Using Supramolecular Interactions. *ACS Nanosci. Au* **2022**, 2, 3, 160–178.

95. Qin, Z.; Zhang, J.; Wan, C.; Liu, S.; Abroshan, H.; Jin, R.; Li, G. Atomically Precise Nanoclusters with Reversible Isomeric Transformation for Rotary Nanomotors. *Nat. Commun.* **2020**, *11* (1), 6019.

2. Experimental Methods and Techniques

2.1 Mass Spectrometry

Mass spectrometry (usually MALDI or ESI) is undoubtedly one of the most important characterization techniques in the world of atomically precise metal nanoclusters world. Indeed, Mass spectrometry provides direct information on the molecular weight of the NC being analyzed, offering crucial insights onto its structure and stoichiometry. Indeed, once the chemical composition of the metal core is known (most of the time easily determined by the UV-Vis spectrum of the molecule), the mass spectra can provide information about the number and type of ligands composing the organic monolayer. This information helps, in the absence of X-ray crystals, to reconstruct the structure and possibly the stoichiometry of the studied nanocluster. Since the initial use of mass spectrometry to characterize the very first examples of nanoclusters, in an outstanding work of Whetten, in 1996,[1] significant time has passed and a profound awareness of the importance of this technique has grown. Currently, modern mass spectrometers are widely used in the nanocluster's community.[2–5]

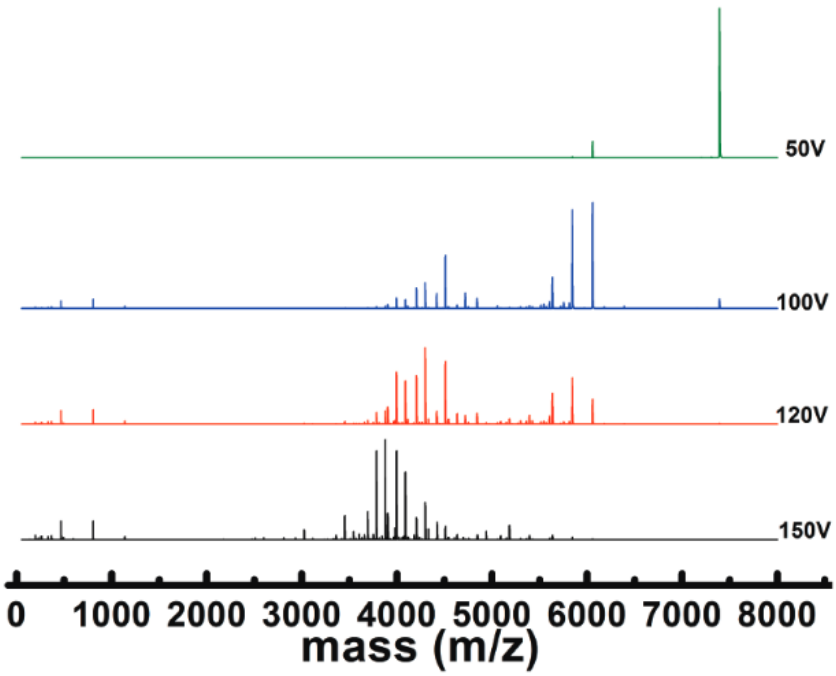

Figure 1 MS/MS of $Au_{25}(SCH_2CH_2Ph)_{18}^-$ at the different collision energies as shown in the figure.[2]

Figure 1 shows a typical MALDI mass spectrum of $Au_{25}(SR)_{18}$, at different collision energies. Increasing the energy, the birth of new signals is observed due to greater fragmentation of the cluster and their aggregates, with the disappearing of the molecular ion (dominant peak at 50 V). Going more in depth in the mass spectra of $Au_{25}(SR)_{18}$ NCs: when the collision energy is low enough, the typical mass spectra is presented in Figure 2.

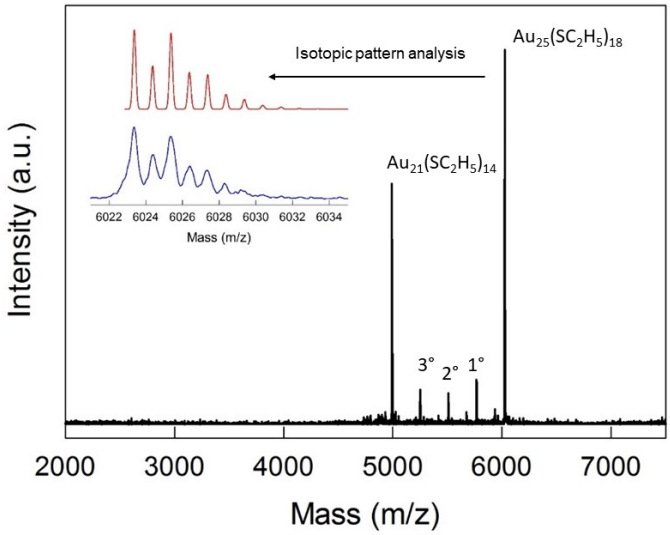

Figure 2 Typical MALDI mass spectrum of $Au_{25}(SC_2H_5)_{18}$. The loss of four Au-thiolated ligand complexes produces a stable species clearly visible in the spectrum ($Au_{21}(SC_2H_5)_{14}$). 1°, 2°, and 3° are fragmentations related to the loss of one (1°), two (2°), and three (3°) Au-SR units from the Au_{25} NC. Isotopic pattern, both experimental (blue line) and simulated (red line) of molecular ion peak are shown in the inset.

In addition to the molecular peak, the signals due to the fragmentation loss of 4 gold atoms and 4 ligands is clearly visible. This is a characteristic fragmentation pattern of these clusters. The inset shows the experimental (blue) and simulated (red) isotopic pattern of the molecular peak. All the Au_{25} NCs present the same fragmentations pattern just described. Of course, the m/z signals depend on the ligands used to protect the NC's core. Indeed, mass spectrometry is also particularly useful for the characterization of the products of ligand exchange reactions. In these reactions, the number of exchanged ligands is usually not unique, spanning a range dependent on the ligands and reaction conditions. The mass spectrum is the only tool that rapidly provides this information. In conclusion, due to its high accuracy and resolution capabilities, mass spectrometry allows for ‘‘confident’’ nanocluster assignment. Furthermore, mass spectrometry could be of tremendously helpful in mechanistic

studies, revealing reaction intermediates and playing a crucial role in advancing our understanding of reaction mechanisms involving NCs, such as ligand exchange reaction (LER).[4]

2.2 Optical Spectroscopy

UV-Vis spectroscopy is a powerful tool for the characterization of Au NCs. The absorption spectra of atomically precise nanoclusters exhibit a series of characteristic features that depend, principally, on the number of gold atoms, the cluster structure, and its redox state. In contrast to larger nanoparticles, which typically exhibit a single plasmonic band, the absorption spectrum of NCs is more complex and can be used to distinguish between different NCs.

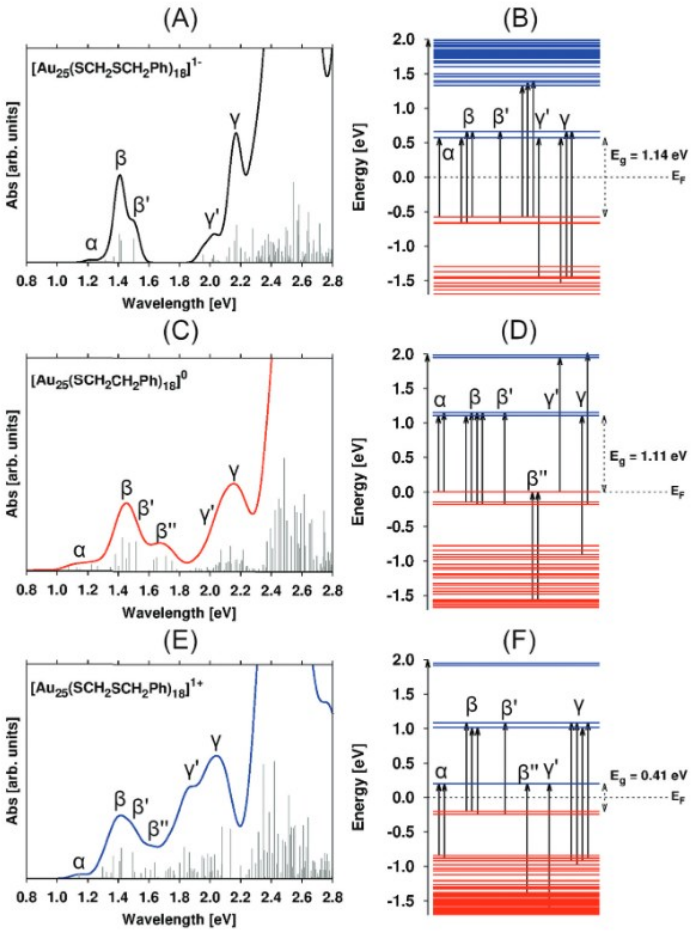

Figure 3 Absorption spectrum of (A) $[Au_{25}(SCH_2CH_2Ph)_{18}]^-$, (C) $[Au_{25}(SCH_2CH_2Ph)_{18}]^0$ and (E) $[Au_{25}(SCH_2CH_2Ph)_{18}]^{1+}$ nanoclusters along with their corresponding (B, D, and F) energy diagram of frontier molecular orbitals. In (A, C, and E), the vertical gray lines correspond to the single oscillator strengths relative to individual electronic transitions. In (B, D, and F), the occupied and unoccupied molecular orbitals are drawn in red and blue, respectively. Some of the main electronic transitions

contributing to the main absorption peaks (labeled as α, β, β', β'', γ, and γ') are depicted in the energy diagrams. The HOMO–LUMO energy gap (E_g) is indicated for each nanocluster.

For sure, UV-Vis spectroscopy is the easier and faster way to identified the charge state of a NC, in particular of Au_{25}. Figure 3 shows the differences in the UV-Vis absorption (together with the frontier molecular orbitals), of the same Au_{25}, but at different charge state (-1, 0, and +1). Contrary, UV-Vis absorption is not very sensitive to the type of ligand used (Figure 4)

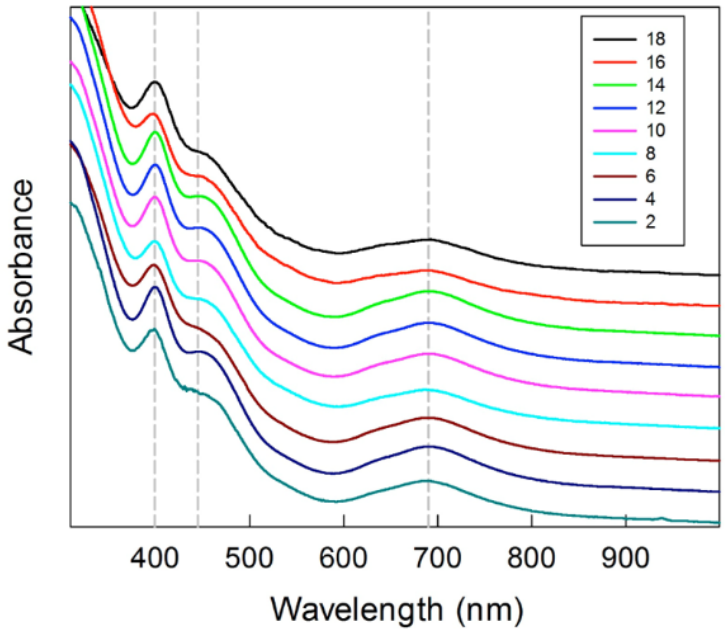

Figure 4 Comparison of the UV-Vis absorption spectra of $Au_{25}(SC_n)_{18}^0$. For clarity, the spectra have been vertically shifted. Dashed lines mark the main spectral features.[6]

Since, Au_{25} is a "molecular" cluster (d < 1.6 nm), it displays UV-Vis absorption spectra containing several fine features. Going more in depth about the absorption features: The UV-vis spectra of $Au_{25}(SC_n)_{18}^0$ (Figure 5) show the presence of a peak at 400 nm (plateau when is in its -1-charge state), a shoulder at ca. 445 nm (peak when is in its -1-charge state), and a broad peak at 690 nm (the same, but blue shifted, when is in its -1-charge state).[7] For n = 2-14, the average molar extinction coefficient at 400 nm is 5.5 x 10^4 M^{-1} cm^{-1}, that is, essentially the same as that of $Au_{25}(SC_2H_4Ph)_{18}$, 5.38 x 10^4 M^{-1} cm^{-1}, which nicely points to the optical behavior of $Au_{25}(SR)_{18}$ clusters (SR = generic thiolated ligand) as virtually only determined by the structure of the gold core.[6]

In conclusion, the UV-Vis absorption spectra of molecular $Au_{25}(SR)_{18}$ clusters not only exhibit genuine molecular features but are also highly sensitive to the actual charge

state. Moreover, they therefore provide an ideal means of evaluating the purity, monodispersity, and charge state of the cluster, as well as its concentration by molar extinction coefficient, which is not only independent by the solvent but also remains constant with the alkyl group used as protective ligands on the NC system.[6]

As for the absorption properties, emission properties of NCs also seems to arise specifically from the core of the clusters and be almost independent from the ligands protecting the NC itself. In addition, size dependence emission was observed.[8] However, a systematic and in-depth study on this topic has not yet been undertaken.

2.3 Nuclear Magnetic Resonance Spectroscopy

Nuclear Magnetic Resonance Spectroscopy (NMR) is one of the most powerful tools in characterizations of atomically precise nanoclusters.[9–12] However, it is not yet used much in this field, and has the potential to become a key technique complementary to mass spectrometry and X-ray structure determination. Indeed, the ligands composing the organic monolayer of the clusters are gaining more and more attention in the recent years, and NMR spectroscopy is one of the key technique in the analysis of ligands, and their dynamicity.[12] This was true also for gaining insight about the staples organizing in the Au_{25} NC's surface. Indeed, analysis of the NMR spectra of $[TOA][Au_{25}(SC_2H_4Ph)_{18}^-]$ led to evidence, quantitatively, the presence of the two families of inner and outer ligands, in agreement with the x-ray crystallography structure.[13] Similar outcome was verified for its oxidized form, $Au_{25}(SC_2H_4Ph)_{18}^0$. In this case, however, a series of remarkable chemical-shift differences, caused by the paramagnetism of this Au_{25} charge state, are observed. As expected because of the singly occupied molecular orbital (SOMO) is mostly localized onto the gold core, the inner ligands are heavily affected by the unpaired electron. This is particularly true for the $(\alpha\text{-}CH_2)_{in}$ peak that undergoes a dramatic downfield shift toward ca. 25 ppm.

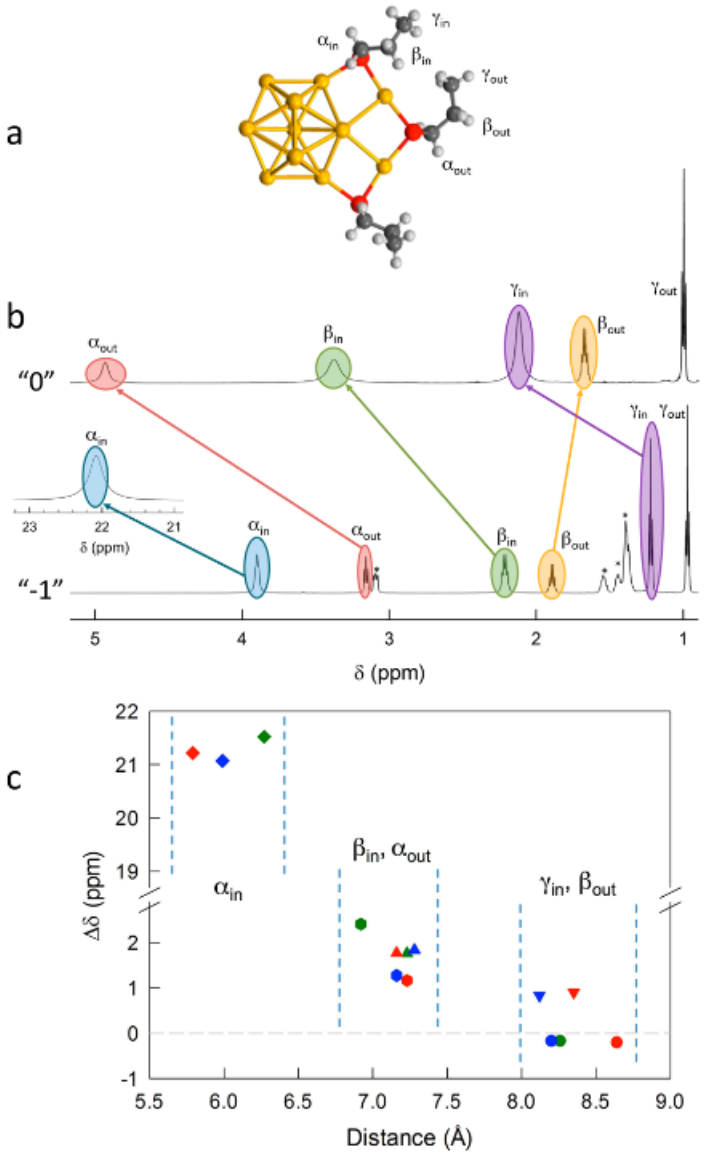

Figure 5 (a) Structure of $Au_{25}(SC_3H_7)_{18}^0$, where five staples have been removed for clarity. **(b)** ^{1}H-NMR spectra of 1 mM $Au_{25}(SC_3H_7)_{18}^0$ and $Au_{25}(SC_3H_7)_{18}^-$ (the asterisks mark the Oct_4N+ countercation) in C_6D_6 at 25 °C; the $(\alpha\text{-CH})_{in}$ signal (at 70 °C) is offset and enlarged. **(c)** Δδ values against distance: C2 (green), C3 (red), C4 (blue); $(\alpha CH)_{in}$, ◆;$(\beta\text{-CH})_{in}$, ⬢;$(\alpha\text{-CH})_{out}$, ▲;$(\gamma\text{-CH})_{in}$, ▼;$(\beta\text{-CH})_{out}$, ●. Vertical dashed lines group the protons at similar distances.[14]

Figure 5B, cleverly shows the differences between the NMR spectra of two charge state of the same Au_{25}, because of the paramagnetism. Again, as was for the UV-Vis absorption measurements, the technique could be a very useful tool for demonstrating and confirm the charge state of the studied Au_{25} NC (Please see the position in the spectra of the $(\alpha\text{-CH})_{in}$. Figure 5C shows that the positive chemical-shift difference ($\Delta\delta = \delta_{radical} - \delta_{anion}$) correlates nearly exponentially with the average distance between the central Au atom and the hydrogen atoms along the thiolate chain. These Δδ values

are a measure of how far the spin density spreads outside the Au_{13} core. The fact that it is sensitive to the position of the ligand in the staple, whether in or out, and the possibility of obtaining quantitative information about them, make NMR spectroscopy one of the most important techniques for studying the selectivity of LER in objects such as Au_{25} which offer different attack sites. Together with mass spectrometry it can become a fundamental tool for studying the kinetics and gaining insight about the mechanisms of ligand exchange reactions.

2.4 Electrochemistry and ET studies

Another tool, not used enough yet in the atomically precise nanoclusters world, is electrochemistry. Au NCs and more in general metal NCs with a diameter of less than 1.6 nm are known to exhibit molecular behaviors. They bridge the gap between nanoparticles and molecules, where discrete electronic states form, and distinctive physicochemical properties are observed. Moreover, from the electrochemical point of view, they behave just like a complex redox system.[13,15] Molecular Au NCs exhibit well-defined, characteristic peaks in their cyclic voltammetry (CV) and differential pulse voltammetry (DPV) patterns. Two of the most notable examples are (i) $Au_{144}(SR)_{60}$, which displays quantized double-layer (QDL) charging behavior (in QDL charging, each peak corresponds to a single-electron charging event that not necessarily involve orbital at different energy), and (ii) $Au_{25}(SR)_{18}$, which exhibits a well-defined HOMO-LUMO gap.[6,15,16] Electron-transfer characterization of the $Au_{25}(SR)_{18}$ native cluster shows that Au_{25} behaves in all regards as a simple molecular redox species.[17–19]

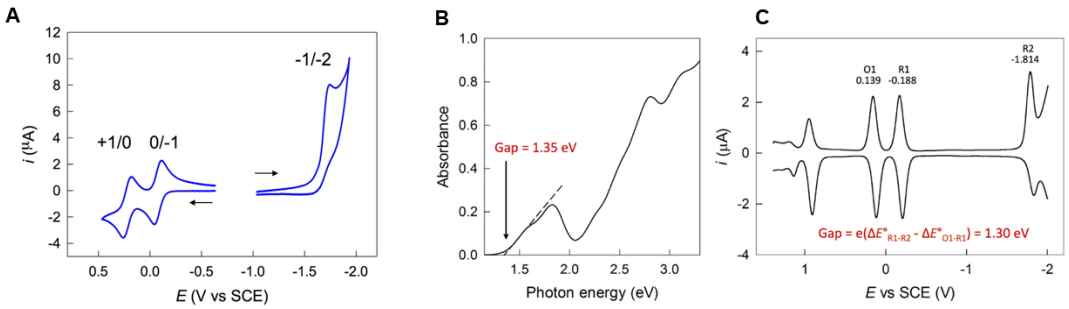

Figure 6 A) Background-subtracted CVs of 1 mM $Au_{25}(SC_2H_4Ph)_{18}^-$ in DCM/0.1 M $TBAPF_6$. v = 0.2 V s^{-1}, glassy carbon electrode, 25 °C; Comparison between the **(B)** optically and **(C)** electrochemically determined HOMO-LUMO gaps. The UV-vis absorption spectrum pertains to 0.10 mM $Au_{25}(SBu)_{18}^-$ in DCM (quartz cuvette with a 2 mm optical-path length; 22 °C), and the gap is estimated from the onset of optical absorption. The differential pulse voltammetry curve is for 0.42 mM $Au_{25}(SBu)_{18}^0$ in DCM/0.1 M

$TBAPF_6$, as obtained at 25 °C using a glassy carbon microelectrode. The peaks are labeled according to progressive electron uptake or release by the neutral cluster; the E° values (in Volt) refer to the corresponding formal potentials, as determined by cyclic voltammetry analysis.[17]

Figure 6B and 6C demonstrate the potential of electrochemical analysis for quantitative analysis of the HOMO-LUMO gap. The electrochemical gap can be corrected by the charging energy (subtracting the contribution), which is the electrostatic energy involved in the charge modification of a molecule/system in solution and is essentially due to the reorganization of the electrolyte ions and solvent dipoles around the emerging charged state. This correction results in energy-gap values that are in good agreement with the optical ones.[18] The CV (Figure 6A) shows the first two oxidations (the actual cluster is in its anionic form) and first reduction. At low scan rate (v) values and for the two most positive peaks, the separation between the anodic and the cathodic peak potentials (ΔE_p) is typical of a full reversible process. ΔE_p increases only for sufficiently high v values. The peak for the reduction to the dianion is irreversible, in agreement with a fast ET followed by chemical reaction/s. Voltammetric analysis and digital simulation showed that initial ET triggers a cascade of chemical and electrochemical steps corresponding to a sequence of stepwise dissociative ETs.

The redox formal potential (E°) values of Au_{25} clusters can be varied by proper substitution of the capping ligands.[20–22] In is worth noticing that whereas very basic electrochemical information (such as E° values and E° differences) has been reported for some molecule-like clusters and under different environment conditions (solvents, electrolytes, temperature), studies focusing on their actual ET properties, such as intrinsic barriers, activation parameters, and ET rate constants, are still very scarce. Our Group was the first to assess the ET properties of $Au_{25}(SR)_{18}^{-}$,[17] albeit in this and most of former papers (before 2008) this cluster was believed to be Au_{38} instead of Au_{25}. ET characterization showed that Au_{25} behaves in all regards as a molecular redox species whose redox potentials can be varied by proper substitution of the capping ligands.[23] Heterogeneous ET kinetics revealed that the intrinsic barrier for the oxidation of $Au_{25}(SR)_{18}^{-}$ is predominantly in the form of inner reorganization rather than solvent reorganization as usually is verified with common organic donors or acceptors. This unusually large heterogeneous ET inner reorganization result is in agreement with ET self-exchange measurements (0 and -1 forms) in the solid state[24] and in solution.[25]

2.5 General Experimental Methods Information

2.5.1 Synthesis of $Au_{25}(SR)_{18}$ Nanoclusters

A typical synthesis of $Au_{25}(SR)_{18}$ (or eventually $[TOA][Au_{25}(SR)_{18}^{-}]$) was carried out as follows:[26] To give an example, for the synthesis of the Au_{25} protected by butanethiols ($Au_{25}(SC_4H_9)_{18}$): 6 equiv of butanethiol (816 µl, 7.62 mmol) were added dropwise, under stirring and at room temperature, to a tetrahydrofuran (THF) solution (50 ml) of $HAuCl_4 \cdot 3H_2O$ (500 mg, 1.27 mmol) and tetra-n-octylammonium bromide (779 mg, 1.425 mmol). After 1 h, or in any case when the solution was colorless, a freshly prepared ice-cold solution of $NaBH_4$ (480 mg, 12.7 mmol) in water (10 ml) was rapidly added under vigorous stirring. The resulting black mixture was stirred for ca. 2 days (1 day for Au_{25} protected by phenyetanethiols) and then filtered on paper. THF was removed by rotary evaporation to leave a red-brownish oil covered by an aqueous phase. The latter was removed by dissolving the product in 50 ml of toluene followed by washing the solution with water (3 x 50 ml), using a separating funnel. The solution was filtered to remove residual white polymer-like material, and the solvent evaporated. By this procedure, the cluster is obtained as $[nOct_4N^+][Au_{25}(SC_4H_9)_{18}^-]$. The product was then further purified (i) or oxidized (ii). In the first case (i), the solid was washed with acetonitrile (3 x 15 ml), to remove possible free thiols and disulfides, and then dried. Then, the solid was further washed with icy cold MetOH (3 x 15 mL) to remove the remaining disulfides and salt. In conclusion, the solid was carefully dried by rotary evaporation and stored at 4 °C, in the solid state, in the dark. Since the -1-charge state of the Au_{25} NC is very sensitive to air, especially in the presence of light, it is best to extract it with acetonitrile (orange/red solution) before each use, to remove any oxidized residue (Au_{25}^0 is not soluble in MeCN). While, if you need the oxidated, paramagnetic species (ii) of the Au_{25} (Au_{25} at its 0-charge state) you need to perform a silica-gel chromatographic column, under aerobic conditions. More precisely, the produced Au_{25}^{-} has to be solubilized and left to age for about 2-2.5 hours. The solution was filtered to remove the possible residual white polymer-like material, and the solvent evaporated. Then the solid is solubilized in 10 mL of toluene and is filtered on a silicagel, using toluene as eluent and compressed air as the pushing gas. The orange solution of the anionic cluster in toluene was injected into the column and soon turned green while passing through the column (Figure 1, inset). After evaporation of the so-treated toluene solution, the oxidized clusters appeared as a black-brownish powder. The clusters were further purified by washing them thrice with acetonitrile. The $Au_{25}(SR)_{18}^0$ was dried (to obtain a black powder) and stored at 4 °C in the dark.

The UV-vis spectra of the anionic and neutral forms of $Au_{25}(SR)_{18}$ are compared in Figure 1, together with pictures of (A) the silica-gel column just before and during the passage of the NC solution, and (B) the two cuvettes used to take the optical spectra.

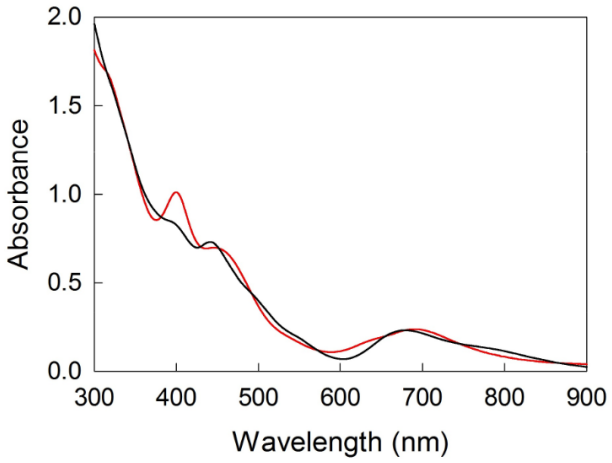

Figure 7 Comparison of the UV-Vis absorption spectra of $Au_{25}(SR)_{18}^{0}$ (red curve) and $Au_{25}(SR)_{18}^{-}$ (black curve), in DCM. Both spectra were obtained using a quartz cuvette with a 2 mm optical-path length, at room temperature, and at 0.10 mM concentration.

All the syntheses of Au_{25} NCs present in this thesis work were performed in the same way just described. The UV-Vis spectrum depends very slightly on the type of ligands[6] and therefore the same outcome is expected with all the clusters that will be presented.

Below are the experimental characterizations of one of the clusters, in particular the one protected by butanethiols at its 0-charge state ($Au_{25}(SC_4H_9)_{18}^{0}$), which are commonly used to check the success of the synthesis and to evaluate the degree of purity and quality of the synthesized NC.

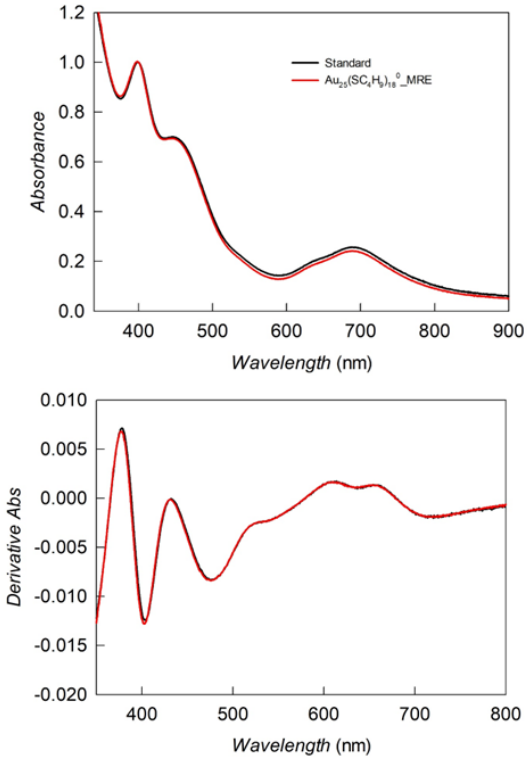

Figure 8 UV-Vis spectrum of Au_{25} NC (in this case $Au_{25}(SC_4H_9)_{18}^0$) and his derivative (bottom part) both compared with a standard absorption behavior. UV-vis characterization is the first characterization we performed after the synthesis because is fast, but provided important information such as the nature of the compound features of the Au_{25} NC), its charge state, its monodispersity and the quality of the purification, by check the comparison between the derivative abs spectra.

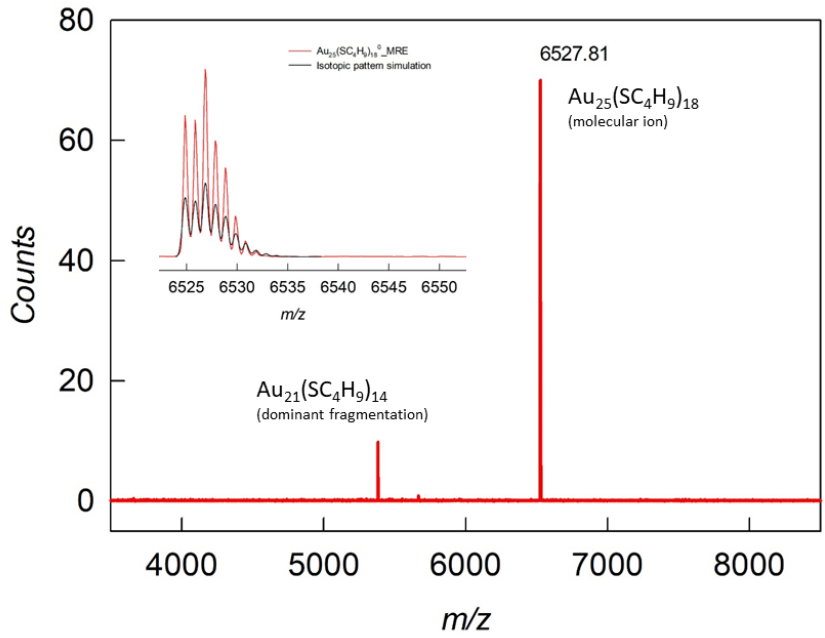

Figure 9 Negative-mode MALDI-TOF spectrum (2300 of l.i.) of Au_{25} NC (in this case $Au_{25}(SC_4H_9)_{18}^0$). Mass spectrometry is always employed to have the certainty of the monodispersion of the synthesized

cluster. In this case just the molecular ion and the fourth fragmentation are observed (Please see 2.1 paragrapgh of this Chapter for details). In the inset the magnification of the molecular ion signal, together with the simulation (by EnviPat software) of its isotopic pattern.

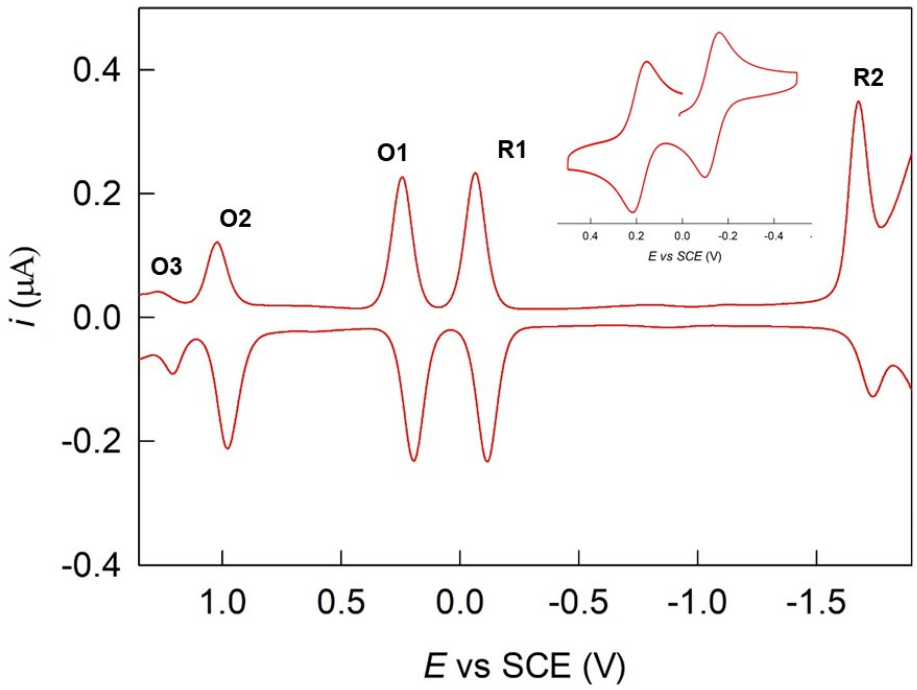

Figure 10 DPV measurements of Au_{25} NC (in this case $Au_{25}(SC_4H_9)_{18}^0$), in DCM/0.1 M $TBAPF_6$, using a GC disk electrode. Electrochemistry is a fundamental characterization tool for NCs as it is very sensitive to impurities coming from the synthesis. In the inset the magnification of the CV curve of the first reduction (R1) and first oxidation (O1) of the cluster, both reversible processes.

2.5.2 Chemicals

Hydrogen tetrachloroaurate trihydrate (99.9%), tetra-n-octylammonium bromide (98%), sodium borohydride (99%), 1-propanethiol (99%), 1-buthanethiol (99%), 1-pentanethiol (98%), 1-hexanethiol (95%), 1octanethiol (> 98.5%), 1-decanethiol (96%), 4-mercaptophenylacetic acid (97%), m-dPEG$_4$-thiol (> 95%), EDC (1-ethyl-3-(3-dimethylaminopropyl)carbodiimide hydrochloride, 5,5′-dimethyl-2,2′bipyridine (> 95%), tris(2,2′-bipyridine)ruthenium(II) hexafluorophosphate (97%), Tetrabutylammonium chloride (> 99.0%), potassium tetrakis(perfluorophenyl)borate (> 98%) methane sufonyl chloride (>99.7%), potassium thioacetate (98%), trimethylamine (≥99%), ammonia solution (7 M) in methanol, tetrahydrofuran (THF, 99.9%), toluene (99.7%), diethyl ether (99.8%), acetonitrile (≥99.9%), ethanol (≥99.8%), pentane (≥99%), cyclohexane (≥ 99.7%), methanol (≥99.8%) N,N-

dimethylformamide (99.8%), benzene (99.8%), ethylbenzene (99%), acetonitrile-d_3 (99.8%, d_3), benzene-d_6 (99.6%, d_6), dichloromethane (99.5%, d_2), N,N-Dimethylformamide-d7 (99.5%, d_7) and trans-2-[3-(4-tert-butylphenyl)-2-methyl-2-propenylidene] malononitrile (DCTB, > 98%) were purchase by Merck and used as received. 2-Methyl1-butanethiol was purchased by Alfa Aesar (99%) and used as received. 1-butane-d_9-thiol-d_9 was purchased by CDN Isotopes (98.8%) and used as received. For electrochemistry, dichloromethane (DCM, Merck, > 99.8%) was used as received. Tetra-n-butylammonium hexafluorophosphate (Fluka, 99%) was recrystallized from ethanol. Low conductivity water was milliQ Water pro analysis (Merck). Column chromatography was carried out using silica gel from Macherey-Nagel (MNKieselgel 60 M, 230-400 mesh).

2.5.3 Methods and Instrumentations

The UV-Vis spectra were obtained at 0.1 mM concentration in DCM (unless otherwise stated), with 10 mm cuvettes. We used a Thermo Scientific Evolution 60S spectrophotometer or, during syntheses, an Ocean Optics QE65000 spectrophotometer equipped with a DH-2000-BAL light source. The spectra resolution was 0.5 or 0.8 nm, respectively.

MALDI-TOF mass spectra were obtained with an Applied Biosystems 4800 MALDI-TOF/TOF spectrometer equipped with a Nd:YAG laser operating at 355 nm. The laser firing rate was 200 Hz and the accelerating voltage was 25 kV. The laser pulse intensity was kept at threshold values and then progressively increased. $Au_{25}(SR)_{18}^0$ was dissolved in DCM containing the matrix, DCTB, to obtain 0.2 mM solutions with a 1:400 MPC/matrix ratio. 2 µL of solution were dropcasted onto the sample plate and air-dried before loading into MALDI-TOF. The spectra were recorded using the reflectron positive- or negative-ion mode. As a standard, we used $Au_{25}(SC_2H_4Ph)_{18}$, which has a MW of 7394.

Electrochemical CVs experiments were carried out in DCM (MeCN) containing 0.1 M $TBAPF_6$, under an Ar atmosphere, in a glass cell thermostatted at $25\ (\pm 1)$ °C (unless otherwise specified). A 0.22 mm-radius glassy carbon disk prepared and activated as already described,[27] was the working electrode, whereas a Pt wire was the counter electrode. An Ag wire was used as the quasi-reference electrode. At the end of each experiment, the potential of the latter was calibrated against the ferricenium/ferrocene redox couple (in DCM/0.1 M TBAH, E0 = 0.460 V against the KCl saturated calomel

electrode, SCE). To minimize the ohmic drop between the working and the reference electrodes, careful feedback correction was applied.

DPV experiments were carried out under the same conditions. The experimental parameters were a peak amplitude of 50 mV, pulse width of 0.025 s, 4 mV increments per cycle, and pulse period of 0.05 s.

^{1}H-NMR spectra were obtained in DCM-d with a Bruker Avance DMX-600 MHz spectrometer equipped with a 5 mm TX-1 x,y,z-gradient powered, tripleresonance inverse probe operating at 599.90 MHz. The temperature was controlled at 25 $\pm$ 0.1 °C, with a Bruker BVT-300 automatic temperature controller. Chemical shifts are in ppm (δ units with reference to tetramethylsilane used as an internal standard). The proton assignments were performed by standard chemical shift correlations as well, eventually, as by 2D correlation spectroscopy (COSY).

Any other techniques, less used, such as HR ESI-MS, emission measurements, solid state conductivity measurements, Langmuir-Blodgett tecnique... will be described in the "Experimental section" of each chapter.

2.6 References

1. Whetten, R. L.; Khoury, J. T.; Alvarez, M. M.; Murthy, S.; Vezmar, I.; Wang, Z. L.; Stephens, P. W.; Cleveland, C. L.; Luedtke, W. D.; Landman, U. Nanocrystal Gold Molecules. *Adv. Mater.* **1996**, *8* (5), 428–433.

2. Angel, L. A.; Majors, L. T.; Dharmaratne, A. C.; Dass, A. Ion Mobility Mass Spectrometry of $Au_{25}(SCH_2CH_2Ph)_{18}$ Nanoclusters. *ACS Nano* **2010**, *4* (8), 4691–4700.

3. Chakraborty, P.; Pradeep, T. Mass Spectrometry of Atomically Precise Clusters. In *Atomically Precise Metal Nanoclusters*; Elsevier, 2023; pp 203–227.

4. Comby-Zerbino, C.; Dagany, X.; Chirot, F.; Dugourd, P.; Antoine, R. The Emergence of Mass Spectrometry for Characterizing Nanomaterials. Atomically Precise Nanoclusters and Beyond. *Mater. Adv.* **2021**, *2* (15), 4896–4913.

5. Harkness, K. M.; Cliffel, D. E.; McLean, J. A. Characterization of Thiolate-Protected Gold Nanoparticles by Mass Spectrometry. *The Analyst* **2010**, *135* (5), 868.

6. Antonello, S.; Arrigoni, G.; Dainese, T.; De Nardi, M.; Parisio, G.; Perotti, L.; René, A.; Venzo, A.; Maran, F. Electron Transfer through 3D Monolayers on Au_{25} Clusters. *ACS Nano* **2014**, *8* (3), 2788–2795.

7. Venzo, A.; Antonello, S.; Gascón, J. A.; Guryanov, I.; Leapman, R. D.; Perera, N. V.; Sousa, A.; Zamuner, M.; Zanella, A.; Maran, F. Effect of the Charge State (z = −1, 0, +1) on the Nuclear Magnetic Resonance of Monodisperse $Au_{25}[S(CH_2)_2Ph]_{18}^z$ Clusters. *Anal. Chem.* **2011**, *83* (16), 6355–6362.

8. Yang, T.-Q.; Peng, B.; Shan, B.-Q.; Zong, Y.-X.; Jiang, J.-G.; Wu, P.; Zhang, K. Origin of the Photoluminescence of Metal Nanoclusters: From Metal-Centered Emission to Ligand-Centered Emission. *Nanomaterials* **2020**, *10* (2), 261.

9. Mallissery, S. K.; Gudat, D. Solid-State ^{31}P NMR Characterisation of Phosphinine-Stabilised Gold Nanoparticles and a Phosphinine-Gold Complex. *Dalton Trans.* **2010**, *39* (18), 4280.

10. Qian, H.; Zhu, M.; Gayathri, C.; Gil, R. R.; Jin, R. Chirality in Gold Nanoclusters Probed by NMR Spectroscopy. *ACS Nano* **2011**, *5* (11), 8935–8942.

11. Salassa, G.; Bürgi, T. NMR Spectroscopy: A Potent Tool for Studying Monolayer-Protected Metal Nanoclusters. *Nanoscale Horiz.* **2018**, *3* (5), 457–463..

12. Rosa-Gastaldo, D.; Pupier, M.; Meshvildishvili, G.; Viger-Gravel, J.; Bürgi, T. Intracluster Ligand Rearrangement: An NMR-Based Thermodynamic Study. *Nanoscale* **2023**, *15* (14), 6838–6843.

13. Agrachev, M.; Ruzzi, M.; Venzo, A.; Maran, F. Nuclear and Electron Magnetic Resonance Spectroscopies of Atomically Precise Gold Nanoclusters. *Acc. Chem. Res.* **2019**, *52* (1), 44–52.

14. Agrachev, M.; Antonello, S.; Dainese, T.; Gascón, J. A.; Pan, F.; Rissanen, K.; Ruzzi, M.; Venzo, A.; Zoleo, A.; Maran, F. A Magnetic Look into the Protecting Layer of Au_{25} Clusters. *Chem. Sci.* **2016**, *7* (12), 6910–6918.

15. Antonello, S.; Maran, F. Molecular Electrochemistry of Monolayer-Protected Clusters. *Curr. Opin. Electrochem.* **2017**, *2* (1), 18–25.

16. Antonello, S.; Dainese, T.; De Nardi, M.; Perotti, L.; Maran, F. Insights into the Interface Between the Electrolytic Solution and the Gold Core in Molecular Au_{25} Clusters. *ChemElectroChem* **2016**, *3* (8), 1237–1244.

17. Antonello, S.; Holm, A. H.; Instuli, E.; Maran, F. Molecular Electron-Transfer Properties of Au_{38} Clusters. *J. Am. Chem. Soc.* **2007**, *129* (32), 9836–9837.

18. Lee, D.; Donkers, R. L.; Wang, G.; Harper, A. S.; Murray, R. W. Electrochemistry and Optical Absorbance and Luminescence of Molecule-like Au_{38} Nanoparticles. *J. Am. Chem. Soc.* **2004**, *126* (19), 6193–6199.

19. Antonello, S.; Perera, N. V.; Ruzzi, M.; Gascón, J. A.; Maran, F. Interplay of Charge State, Lability, and Magnetism in the Molecule-like $Au_{25}(SR)_{18}$ Cluster. *J. Am. Chem. Soc.* **2013**, *135* (41), 15585–15594.

20. Holm, A. H.; Ceccato, M.; Donkers, R. L.; Fabris, L.; Pace, G.; Maran, F. Effect of Peptide Ligand Dipole Moments on the Redox Potentials of Au_{38} and Au_{140} Nanoparticles. *Langmuir* **2006**, *22* (25), 10584–10589.

21. Guo, R.; Murray, R. W. Substituent Effects on Redox Potentials and Optical Gap Energies of Molecule-like $Au_{38}(SPhX)_{24}$ Nanoparticles. *J. Am. Chem. Soc.* **2005**, *127* (34), 12140–12143.

22. Aikens, C. M. Geometric and Electronic Structure of $Au_{25}(SPhX)_{18}^{-}$ (X = H, F, Cl, Br, CH_3, and OCH_3). *J. Phys. Chem. Lett.* **2010**, *1* (17), 2594–2599.

23. Antonello, S.; Maran, F. Intramolecular Dissociative Electron Transfer. *Chem. Soc. Rev.* **2005**, *34* (5), 418.

24. Choi, J.-P.; Murray, R. W. Electron Self-Exchange between $Au_{140}^{+/0}$ Nanoparticles Is Faster Than That between $Au_{38}^{+/0}$ in Solid-State, Mixed-Valent Films. *J. Am. Chem. Soc.* **2006**, *128* (32), 10496–10502.

25. Parker, J. F.; Choi, J.-P.; Wang, W.; Murray, R. W. Electron Self-Exchange Dynamics of the Nanoparticle Couple $[Au_{25}(SC2Ph)_{18}]^{0/1-}$ By Nuclear Magnetic Resonance Line-Broadening. *J. Phys. Chem. C* **2008**, *112* (36), 13976–13981.

26. De Nardi, M.; Antonello, S.; Jiang, D.; Pan, F.; Rissanen, K.; Ruzzi, M.; Venzo, A.; Zoleo, A.; Maran, F. Gold Nanowired: A Linear $(Au_{25})_n$ Polymer from Au_{25} Molecular Clusters. *ACS Nano* **2014**, *8* (8), 8505–8512.

27. Meneses, B. A.; Antonello, S.; Arévalo, M. C.; Maran, F. Double-Layer Correction for Electron-Transfer Kinetics at Glassy Carbon and Mercury Electrodes in N,N-Dimethylformamide. *Electroanalysis*, **2006**, *18*(4), 363-370.

3. Electron Transfer in Films of Atomically Precise Gold Nanoclusters*

* Published: Reato, M., Dainese, T., Antonello, S., & Maran, F. Electron transfer in films of atomically precise gold nanoclusters. *Chemistry of Materials*, **2021**, *33*(11), 4177-4187.

3.1 Abstract

In applications of monolayer-protected gold clusters, assessing the dynamic behavior of the capping monolayer is crucial, as this determines the cluster's effective size and electron transfer (ET) properties. Here we describe a systematic study on the effect of the monolayer thickness on the ET between molecular $Au_{25}(SR)_{18}^0$ nanoclusters in films. The length of the ligands protecting the Au core was varied by using a series of linear-chain thiolate (SC_nH_{2n+1}) protected Au_{25} clusters where n = 3, 4, 5, 6, 7, 8 and 10. The effect of branching was assessed by using the 2-methyl-1-butanethiolate protected Au_{25} cluster. Conductivity measurements were carried out on dry films obtained by drop casting $Au_{25}(SR)_{18}^0$ solutions onto interdigitated gold electrodes. Changing the alkyl chain from C3 to C10 induces a smooth decrease in the film conductivity of 3.5 orders of magnitude. By using electrochemically determined Stokes radii, the conductivity results were transformed into the corresponding ET rate constant (k_{ET}) between neighboring clusters. k_{ET} depends exponentially on distance, and the data show that the average Au center-to-center distance in the film is not larger than the sum of two Stokes radii. This indicates that linear alkyl chains hold a detectable degree of fluidity in films, although not as much as in solution, as shown by the trend of the corresponding heterogeneous k_{ET} values. For both physical states, these conclusions are precisely confirmed by the much slower ET rate determined for the Au_{25} cluster protected by the hindered thiolate. ET in films was also studied as a function of temperature and the results analyzed in the framework of the ET theory. We found that the outer and inner reorganization energies increase with n. For these ETs, the electronic coupling resonance between the reactant and product states, H_{RP}, ranges from 12 (n = 3) to 0.7 cm^{-1} (n = 10), and therefore, ETs are nonadiabatic. The data also show that 3/4 of the effect of distance on k_{ET} is related to H_{RP}, while the rest is associated with the intrinsic barrier, and thus, the distance dependence of the outer and inner reorganization energies.

3.2 Introduction

Monolayer-protected gold clusters (MPCs) are promising materials in areas such as catalysis, electrocatalysis, sensing, and biomedicine.[1-9] Their chemical and physicochemical properties are determined by a subtle combination of structural and electronic factors related to the core and capping ligands. When the intercluster distance is sufficiently small, specific interactions between MPCs may occur and further properties emerge. This may happen in the solid state, such as crystals and films, and assemblies. These interactions may affect the magnetic behavior, the optical properties, or the charge state.[4,10,11] For example, in single crystals, paramagnetic Au_{25}(S-*n*-butyl)$_{18}^0$ forms linear wires in which the odd electrons of individual clusters pair up to generate an antiferromagnetic system,[12] whereas the use of the phenylethanethiolate ligand cause the Au_{25} clusters to display ferromagnetism and superparamagnetism depending on the physical state and temperature.[13] For MPCs sufficiently large to display a localized surface plasmon resonance (SPR) band, the latter can be affected when the intercluster distance is sufficiently small to cause interaction between the conduction electrons of neighboring MPCs.[14,15] For smaller, atomically precise clusters, proximity between cores affects the MPC absorption and emission properties.[16-21] Importantly, electronic coupling between the relevant orbitals of clusters and nearby species implies the possibility of observing electron transfer (ET) reactions. For species in solution, this issue has been addressed for ETs involving clusters, a cluster and an electrode, or a cluster and other redox species.[22-32]

ET occurs between a donor (D) and an acceptor (A) that may be at contact distance or separated by a molecular bridge.[33-37] The bridge (B) may mediate ET according to the superexchange mechanism and/or provide orbitals where the electron can be transiently localized on its way to A (hopping mechanism).[38] For bridges that do not offer orbitals sufficiently close in energy to those localized on either D or A, such as saturated alkyl chains, only the first mechanism is operative. In the superexchange mechanism, the electron tunnels directly from D to A[34,39] and the distance dependence of the ET rate constant (k_{ET}) is described according as in eq 1:

$$k_{ET} = k_0 \exp(-\beta r_{DA}) \quad \textbf{(1)}$$

where β (Å^{-1}) is the exponential factor describing the rate drop, r_{DA} (Å) is the distance between D and A, and k_0 is the rate constant when D and A are at van der Waals distance. The dominant contribution to the distance dependence of k_{ET} is the electronic coupling between the reactant and product states at the ET transition state,

H_{RP}. In intramolecular systems, the bridge controls the D/A distance and relative orientation. If D and A are freely diffusing species, instead, the observed ET rate constant is the result of contributions from all possible relative distances and orientations of the caged D/A system.[33,40]

The distance effect on the ET rate is thus best addressed by using robust D-B-A systems. Different strategies have been implemented, ranging from studies based on the use of freely diffusing D-B-A,[34,39-43] to the electrochemical determination of the ET rate in systems where D or A are separated from the electrode by a SAM (self-assembled monolayer of thiolates on extended gold surfaces)[37,39,44,45] to metal-molecule-metal junction systems, in which ET occurs between two electrodes separated through the given bridge.[46-48] These studies have provided sound quantitative information for a variety of molecular bridges.[34,36,37-51] A saturated alkyl chain in its *all-trans* conformation is characterized by β values spanning from 0.8 to 1.0 $Å^{-1}$.[34,44,49] For this type of bridge, these are thus the minimum β values experimentally observable: the presence of *cis* 'kinks' along the bridge would increase β and, consequently, decrease the through-bond electronic coupling.[34]

ETs through SAMs have been focused on the use of thiols carrying a redox group,[44,45] and only rarely studies have been carried out with solution-dissolved redox species, although the results are correlated.[52] In this general context, MPCs provide the unique case of molecular systems completely surrounded by the same bridge, *i.e.*, a 3D thiolate monolayer, as illustrated in Figure 1 in comparison with the analogous 2D SAM.

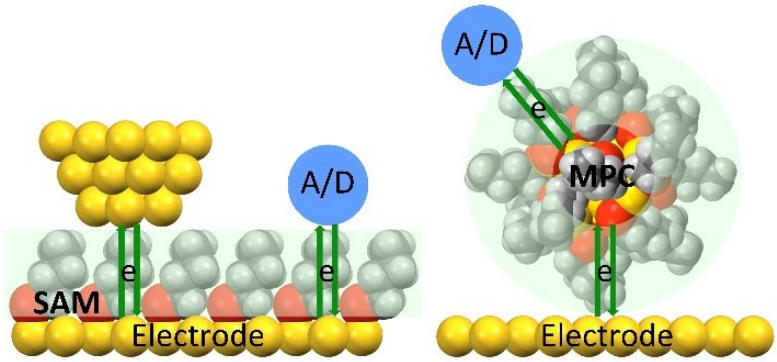

Figure 1 Cartoons of ET (left) at a thiolate SAM modified electrode, whether involving a molecular redox species or in a metal-molecule-metal junction (such as an STM tip), and (right) homogeneous or heterogeneous (electrode) ET through a thiolate monolayer capping a gold cluster. The monolayers have been highlighted in light green. Au = yellow, S = red, C = gray, H = white.

If the MPC is spherical or nearly spherical, the orientation factor is, thus, of no concern and the effect of the monolayer thickness on the electron tunneling between the gold

core and an electrode can be performed directly using freely diffusing MPCs. Moreover, whereas the study of ET through 2D-SAMs with solution-dissolved species is affected by SAM defects, and thus, possible penetration of the redox species into the monolayer, in MPCs the monolayer is *on* the redox center and, for heterogeneous ETs, the ET partner is an electrode: therefore, there is no need of tethering the cluster to the electrode surface. Recently,[30] we studied the distance effect on the standard heterogeneous ET rate constant with a series of $Au_{25}(SC_nH_{2n+1})_{18}$ clusters (n = 2, 4, 6, 8, 10, 12, 14, 16, 18) and the data indicated that in these MPCs: (i) the alkyl chains are quite folded and thus the protecting monolayer is dynamically much thinner than generally assumed; (ii) short ligands (typically, n < 12) form a quite fluid monolayer and the resulting MPCs are approximately spherical, whereas longer alkyl chains self-organize into bundles and the MPCs attain a more ellipsoidal shape (one of the three principal axes is significantly longer).

If understanding the redox properties of MPCs in solution is of special interest in areas such as redox catalysis[1,3,25,27] obtaining insights into how MPCs transfer electrons in the solid state is fundamental to tailor properties of electronic devices.[53,54] MPC films are particularly interesting as sensors for the detection of vapor-phase analytes, whose sorption affects the conductivity of the film.[5,55] MPC films are conveniently prepared on interdigitated electrode arrays (IDAs). Application of a potential difference between the two sets of electrodes causes a current to flow through the film. Conductivity depends on the cluster's size, charge state or relative population of different oxidation states, the distance between the metallic cores, which is determined by the ligands, and the electronic properties of the latter.[56-61] Relevant work on large MPCs (core > 2 nm) has been reviewed.[5] In these systems, a precise control over the size and especially charge state and associated properties cannot be achieved. For example, different magnetic behaviors were observed even for samples prepared with the same procedure by the same group.[62]

Here we specifically focus on the atomically precise gold nanoclusters Au_{25}, that is, a compound whose molecular formula and crystallographic parameters are well-defined.[63] Previous research on the conductivity of amorphous films formed of Au_{25} and slightly larger molecular MPCs has provided useful information regarding several aspects. In studies of mixed-valence $Au_{140}(SC_6H_{13})_{53}$,[58] a cluster whose stoichiometry was presumably $Au_{144}(SR)_{60}$,[64] Wuelfing and Murray observed that the conductivity depends on the charge state, reaching a maximum for a 1:1 ratio between the 0 and the +1 charge states. The bimolecular rate constant for the exchange reaction between the two redox forms was found to be 1.7 orders of magnitude

smaller for Au_{25} (earlier misidentified as Au_{38})[53] with respect to Au_{144}, which was attributed mostly to a difference in the corresponding activation energies;[60,61] it should be stressed, however, that different ligands were employed. As to mixtures of charge states, Carducci and Murray found that for $Au_{25}(SC_2H_4Ph)_{18}$ the ET rate in a film composed of the +1 and 0 charge states is smaller by ca. one order of magnitude than for a 0/-1 mixture.[61] This difference was attributed to a larger reorganization energy involved in the formation of the positively charged nanocluster, as we also observed in solution.[25,28] Conductivity measurements based on charged clusters, however, include the effect of counterions whose presence may complicate the analysis. The effect of changing the ligand length has been addressed by Wuelfing et al. using larger nanoclusters of average stoichiometry $Au_{309}(SC_nH_{2n+1})_{92}$, with n = 4, 5, 6, 7, 8, 10, 12, 16.[57] The results pointed to an exponential decrease of the rate with an increase in the ligand length. A decay exponential factor β of 0.8 $Å^{-1}$ could be calculated by assuming extensive intercalation, or bundling, of chains in neighboring MPCs.

A determination of the distance effect on the ET rates in films composed of atomically precise Au clusters and a comparison of such rates with those determined in solution for identical clusters is still missing. In this framework, molecular $Au_{25}(SR)_{18}$ clusters are ideal systems because: (i) can be prepared with atomic precision[63] independently of the ligand length;[30] (ii) have a well-established structure, as determined by single-crystal X-ray crystallography of their neutral forms for various linear alkanethiolate ligands (n = 2, 3, 4, 5);[12,65-67] (iii) their charge state can be modulated and controlled precisely;[27,28,68] (iv) the dynamic structure of the monolayer in solution has been assessed;[30] (v) their hydrodynamic radii have been determined.[69]

The objectives of this study are: (a) assess how the electron hopping between neighboring neutral Au_{25} clusters in the film state depends on the ligand length and effective monolayer rigidity in the film state; (b) compare the ET properties of films with the heterogeneous ET parameters determined for the same clusters in solution; (c) use the semiclassical two-state model to gain further insights into the distance dependence of these ET processes in terms of adiabatic versus nonadiabatic regimes.

All clusters were prepared in their zero-charge state. In this state, they are radicals[13,28,65-68,70] and the singly occupied molecular orbital (SOMO) offers the interesting situation of an orbital that can either donate or accept one electron. For the sake of better comparison of the results, we focused on $Au_{25}(SC_nH_{2n+1})_{18}^0$ clusters (hereafter indicated simply as $Au_{25}(SC\mathit{n})_{18}^0$) in which $n \leq 10$, which avoids the

aforementioned transition toward the more ellipsoid ligand arrangement.[30] We used *n* = 3, 4, 5, 6, 7, 8, and 10. To tune the monolayer thickness, we also studied the ET behavior of $Au_{25}(SMeC4)_{18}^0$, where SMeC*4* stands for 2-methyl-1-butanethiolate: in this cluster, the monolayer fluidity is diminished through introduction of a branched alkyl chain. The ET results in films could thus be analyzed in detail, leading to a self-consistent picture of the rates, activation parameters, and reorganization energies.

3.3 Results and Discussion

3.3.1 Heterogeneous ET Kinetics

The electrode kinetics for the oxidation and reduction of a series of neutral clusters was previously studied on a glassy-carbon microdisk electrode in dichloromethane (DCM) containing 0.1 M tetra-*n*-butylammonium hexafluorophosphate (TBAH), at 25 °C.[30] Here we extended the study to $Au_{25}(SC_3)_{18}^0$, $Au_{25}(SC_5)_{18}^0$, and $Au_{25}(SC_7)_{18}^0$, and carried out further checks of the previous data. At low potential scan rate (v) values, both the oxidation and reduction of $Au_{25}(SR)_{18}^0$ show chemically and electrochemically reversible cyclic voltammetries (CVs), as exemplified by the CV for the reduction of $Au_{25}(SC_7)_{18}^0$ in the inset to Figure 2. For $n > 5$, the separation between the cathodic and anodic peaks (ΔE_p) at 0.1 V s^{-1} is already slightly larger than the theoretical value of 59 mV at 25 °C.[71] For all clusters, ΔE_p increases when v increases, indicating that the process becomes quasi-reversible. The standard heterogeneous ET rate constant $k°$ (cm s^{-1}), which is the rate constant when the applied potential corresponds to the formal potential $E°'$,[72,73] was determined by studying the scan-rate dependence of ΔE_p (from 0.1 to 50 V s^{-1}) according to both the Nicholson method[74] and digital simulation of the experimental curves.[30] Figure 2 shows the ln$k°$ values for the reduction of $Au_{25}(SC3)_{18}^0$, $Au_{25}(SC5)_{18}^0$ and $Au_{25}(SC7)_{18}^0$ together with those obtained previously for clusters with other n values,[30] in which the data for n = 2 and 6 were refined with further experiments.

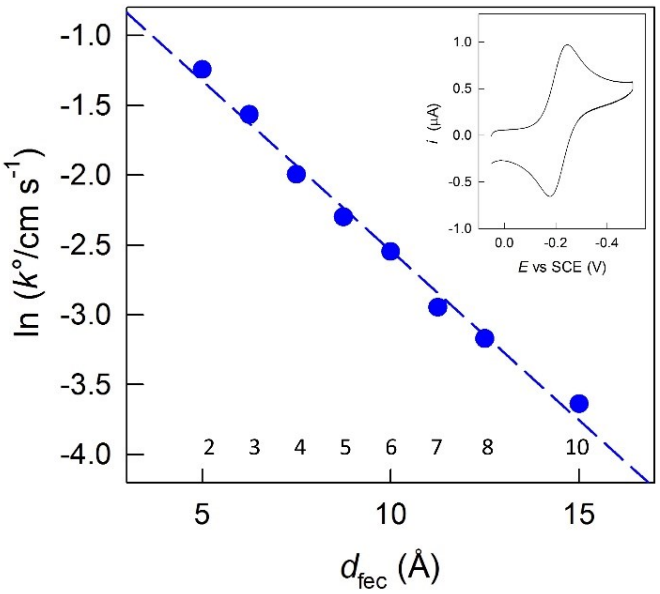

Figure 2 Distance effect on the standard ET rate constants for the 0/-1 redox couple. The *n* values are indicated at the bottom. Uncertainty in ln*k*° values is 0.05-0.1. The dashed line, with a slope of 0.24 Å^{-1}, is the linear fit to the data. The inset shows a typical CV (reversible reduction of $Au_{25}(SC7)_{18}^0$ at 0.1 V s^{-1}).

The plot shows that ln*k*° decreases linearly (r^2 = 0.991) when the ligand length increases. The abscissa is arbitrarily taken as the fully extended conformation distance of the alkyl chains (d_{fec}, from sulfur to the farthest H atom), as usually done for 2D-SAMs and often assumed for MPC systems. The slope was analyzed according to the superexchange mechanism (eq 1) to yield an apparent β value in solution, $(\beta_{sol})_{fec}$, of 0.24 Å^{-1}. A very similar plot is obtained for the $Au_{25}(SCn)_{18}^0$ oxidation.

3.3.2 Conductivity of $Au_{25}(SC_nH_{2n+1})_{18}^0$ Films (n = 3, 4, 5, 6, 7, 8 and 10)

The conductivity measurements were carried out by drop casting concentrated solutions of the $Au_{25}(SR)_{18}^0$ molecules onto IDA gold electrodes. This is an approach extensively employed to test the conductivity of MPC films.[5,56-61] We used IDAs consisting of 65 interdigitated Au fingers: length = 2 mm, width = 10 μm, interfinger width = 5 μm, thickness = 0.96 nm. Conductivity measurements were carried out on carefully dried films, by linearly scanning the bias potential (*E*) across the IDA finger pairs between +1 and -1 V. For all samples, the current *i* is linear in *E* (Figure 3), in agreement with films displaying ohmic behavior.

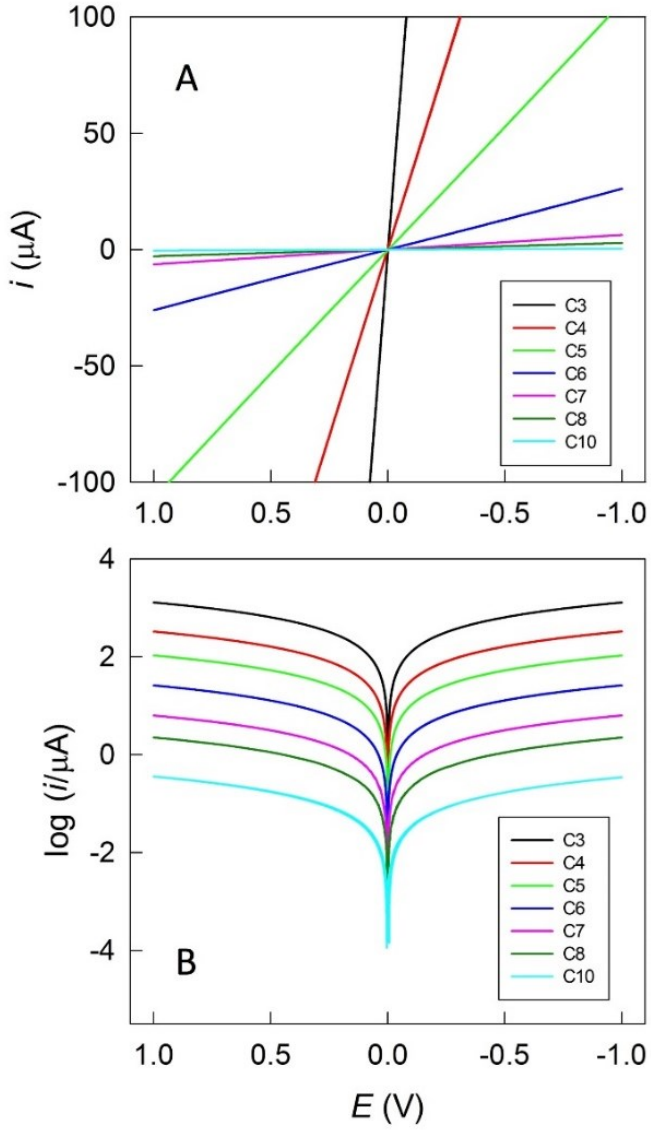

Figure 3 Plots of (A) the current *i* obtained for the $Au_{25}(SCn)_{18}^{0}$ samples (*n* = 3, 4, 5, 6, 7, 8, 10) as a function of the potential bias between the two comb gold electrodes. The corresponding logarithmic plot is shown in graph (B), where *i* is now the absolute current.

No differences were detected by running the experiments in vacuum or under an argon atmosphere. Importantly, no hysteresis effects, usually attributed to ion mobility within the film,[57] were observed. The current response did not depend on *v* (as already noted for similar MPCs[60]), which was varied from 0.1 to 40 V s^{-1} (Figure 4).

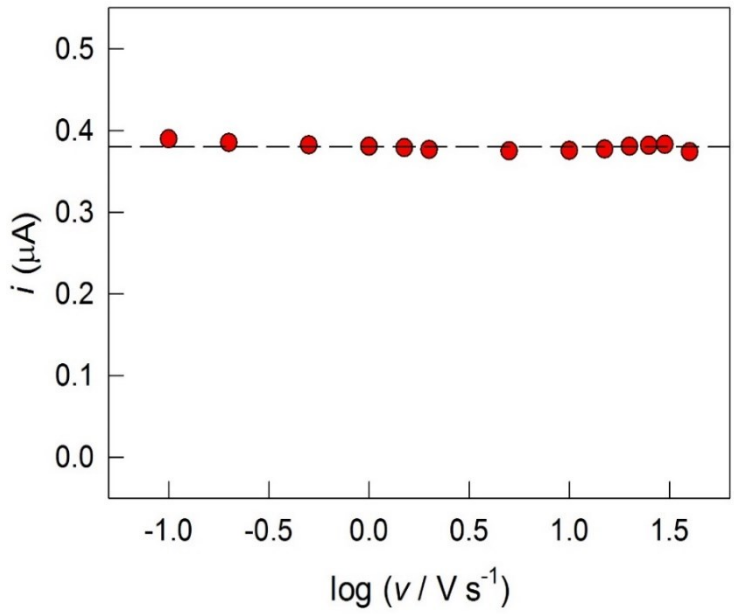

Figure 4 Typical plot (specific case: $Au_{25}(SC10)_{18}^0$ film) of the current measured with a potential bias of 1 V (between the IDA combs) as a function of the logarithm of the potential scan rate. The dashed line marks the average value.

After experiments, the MPC film could be easily removed from the IDA with DCM, yielding a solution exhibiting the same UV-vis absorption spectrum of the original MPC sample. Drop casting the same solution onto an IDA led to observe unchanged *i* - *E* behavior and conductivity, thereby confirming full stability of the MPCs.

Figure 3 shows that the ligand length affects the *i-E* plot very significantly. This behavior can be directly related to a different conductivity (σ) of the films. σ (Ω^{-1} cm^{-1}) can be calculated with eq 2:[60]

$$\sigma = \frac{l}{A_{tot}} \frac{i}{E} = C_{cell} \frac{i}{E} \quad \textbf{(2)}$$

where l is the IDA interfinger length and A_{tot} is the total area of the electrode/film interface. The cell constant $C_{cell} = l/A_{tot}$ was calculated, as described by Choi and Murray,[60] to be 0.194 cm^{-1} (see Experimental Section). The σ values are gathered in Table 1.

Table 1 Electronic conductivity data, size parameters, concentrations in films, and ET rate constants.

	σ	r_{MPC}	d_S	d_{fec}	C_{film}	k_{ET}
	(Ω^{-1} cm^{-1})	(Å)	(Å)	(Å)	(M)	(s^{-1})
C*3*	2.3×10^{-4}	8.6[a]	3.7[a]	6.25	0.44	2.9×10^{7}
C*4*	6.8×10^{-5}	9.4[a]	4.5[a]	7.5	0.33	9.2×10^{6}
C*5*	1.9×10^{-5}	10.3[a]	5.4[a]	8.75	0.25	2.9×10^{6}
C*6*	5.8×10^{-6}	11.0[a]	6.1[a]	10.0	0.21	9.2×10^{5}
C*7*	1.2×10^{-6}	11.5	6.6	11.25	0.18	1.9×10^{5}
C*8*	5.8×10^{-7}	12.1[a]	7.2[a]	12.5	0.16	1.0×10^{5}
C*10*	7.8×10^{-8}	13.5[a]	8.6[a]	15.0	0.11	1.5×10^{4}
MeC*4*	2.3×10^{-5}	10.4	5.5	7.50	0.25	3.5×10^{6}

[a] Values from reference 69.

For consistency with Figure 2, Figure 5 shows $ln\sigma$ as a function of a hypothetical edge-to-edge intercore distance assumed to correspond to the thickness of two monolayers formed of *all-trans* alkyl chains ($2d_{fec}$). The linearity of the plot (r^2 = 0.987) is in excellent agreement with a cluster-to-cluster ET hopping mechanism inside the film, in which each individual ET step occurs by superexchange tunneling through the monolayers of neighboring clusters. From the slope of the plot in Figure 5, we calculate an apparent exponential factor $(\beta_{film,\sigma})_{fec}$ of 0.46 Å^{-1} (r^2 = 0.992).

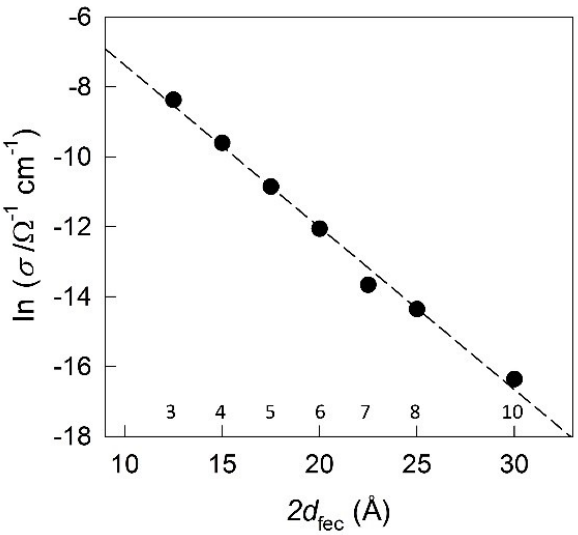

Figure 5 Dependence of the film conductivity σ (the n values are indicated at the bottom) as a function of twice the length d_{fec}. Linear regression yields a slope of 0.46 Å^{-1}.

This value is twice the value observed for $k°$ in solution but is still much smaller than the usual values observed for alkyl chains. This difference clearly shows that the effective bridge length is significantly shorter than $2d_{fec}$.

A more realistic estimate of the monolayer thickness is obtained from the diffusion coefficient (D) values. Precise D values of most of the investigated Au_{25} clusters were previously obtained from the CV peak currents at low scan rates.[69] Measurements could take advantage of the knowledge of the electrode area and the MPC concentration, which was determined accurately also by taking advantage of the constancy of the molar extinction coefficient for these clusters (at 400 nm, ε = 5.5 x 10^4 M^{-1} cm^{-1}).[30] The same approach was used for the remaining clusters. The MPC radius (r_{MPC}) is calculated with the Stokes-Einstein equation $D = k_B T/6\pi\eta r_{MPC}$, where k_B is the Boltzmann constant and η is the viscosity of the solvent; due to the approximately spherical shape and large size (with respect to the solvent molecules) of the MPCs, the use of this equation is particularly valid, and therefore, the results particularly accurate. Table 1 shows the results.

From the r_{MPC} value, the corresponding Stokes monolayer thickness (d_S) is obtained by subtracting the distance between the outermost and the central Au atoms (r_{core}), 4.9 Å.[56-58] Whereas for the much larger Au nanoparticles, in which ligand-chain packing tends to that of thiolates in 2D SAMs, the use of d_{fec} may not introduce a severe approximation, for $Au_{25}(SR)_{18}^0$ the d_S values reveal a substantial dynamic monolayer contraction, *i.e.,* $d_S = (0.59 \pm 0.02) \times d_{fec}$ (in particular, while for n = 3-5 the value increases, for n = 5-10, d_S/d_{fec} decreases from 0.617 to 0.573). This result is in line with the conclusion reached for larger MPCs in the seminal paper by Terrill et al.[56] The d_S here obtained refers to the linear thiolates: for the constrained SMeC*4* monolayer, contraction is appreciably less pronounced (d_S = 0.73 d_{fec}). It is finally worth mentioning that for the short ligands, whose $Au_{25}(SR)_{18}^0$ structures are known,[12,66,67] the r_{MPC} values are on average 5% smaller than in the crystals. This suggests that in solution the ligands are, at least from a hydrodynamic viewpoint, slightly more folded than in single crystals.

The conductivity depends on the effective *edge-to-edge* intercore distance $2d_{eff}$ through eq 3:[56]

$$\sigma = \sigma_0 [\exp(-2d_{eff}\, \beta_{film,\sigma})] \exp(-E_A/RT) \qquad \textbf{(3)}$$

where E_A is the activation energy, R is the gas constant, T is the temperature, and σ_0 is the hypothetical conductivity for cluster cores at contact distance and infinite T. In eq 3, the *effective* distance $2d_{eff}$ indicates the actual thickness of two monolayers in

the film. We assume $2d_{eff} = 2d_S$. When the $ln\sigma$ values are plotted against the $2d_S$ values, a linear plot (r^2 = 0.990) similar to that of Figure 5 is obtained, but the exponential factor, $(\beta_{film,\sigma})_S$, now is 0.84 Å^{-1} (Figure 6).

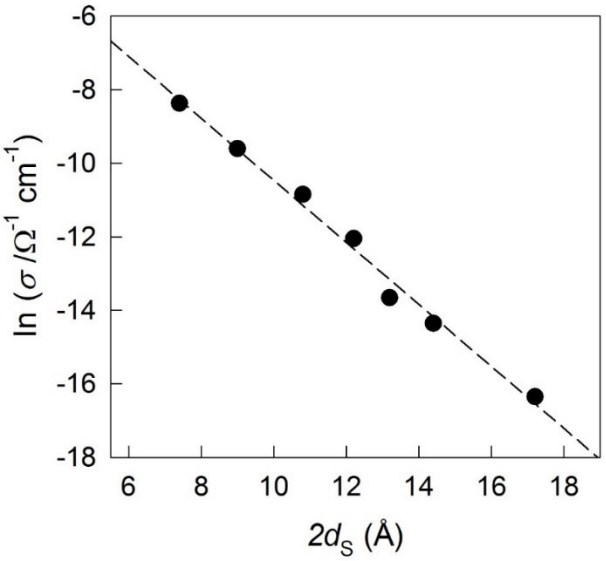

Figure 6 Dependence of the film conductivity σ (left to right, n = 3, 4, 5, 6, 7, 8, and 10) as a function of twice the length d_S. Linear regression yields $(\beta_{film,\sigma})_S$ = 0.84 Å^{-1}.

3.3.3 Comparison between Solution and Solid-State ETs

To compare the solid-state and solution-phase exponential factors, the conductivity results require transformation into ET rate-constant values, k_{ET} (s^{-1}) and thus an adjustment for the actual molar concentration of the cluster in the film C_{film} (M). This is because for the bulkier ligands less hopping sites (that is, the clusters' cores) are available between the IDA fingers. C_{film}(M) can be calculated with eq 4:

$$C_{\text{film}} = \frac{\Phi\left(10^{27}\right)}{\frac{4}{3}\pi\left(r_{\text{core}} + d_S\right)^3 N_A} \qquad \textbf{(4)}$$

where N_A is the Avogadro number and both r_{core} and d_S are in Å. The volume fraction Φ represents the fill factor, *i.e.*, the fraction of the whole volume effectively occupied by the particles. Φ depends on ordering and shape. For a collection of spherical particles, the highest average density is obtained for the hexagonal close-packed (hcp) and face-centered cubic (fcc) arrangements, with Φ = 0.74. In these geometries, each particle has twelve neighbors and in all cases the distance between two MPC centers corresponds to the sum of their effective radii. MPC films, however, are not expected to be fully ordered assemblies, and random packing of hard spherical objects is characterized by the smaller Φ value of 0.64.[75] Uneven packing and ligand

flexibility imply that the distance between neighboring MPCs can span values also slightly longer or shorter than their hydrodynamic radii. Also, in our analysis, we assume that the MPCs are spheres, but, in fact, when *n* increases, particularly for 8 and 10, $Au_{25}(SR)_{18}^0$ tends to become less spherical.[30] For ellipsoids, random packing actually generates better packing, with a Φ value of 0.74.[76] Given the nature of the investigated systems, we account for these combined effects by using an average Φ value of 0.7. The C_{film} values of Table 1 were calculated by using the d_S values.

Assuming a simple cubic-lattice model[77-79] to describe the assembly of MPCs in films,[57,58,60,61,80,81] the conductivity data can be used to estimate the corresponding first-order ET rate constants k_{ET} (s^{-1}) between neighboring clusters (eq 5):

$$k_{ET} = \frac{6RT}{10^{-3} F^2 \delta^2 C_{film}} \sigma \qquad \textbf{(5)}$$

where δ (in cm) is the *center-to-center* separation between two MPCs, taken as $2r_{MPC}$. The reaction is considered a first-order reaction as ET involves spatially fixed species where, given the symmetry of the MPC, orientation is of no concern. In eq 5, the charge-carrier and MPC concentrations are the same. For $Au_{25}(SR_{18})^0$ clusters this is an especially valid assumption because the same orbital, the SOMO, may either accept or donate one electron. The resulting k_{ET} values are in Table 1. By plotting the lnk_{ET} values against $2d_S$, we obtain a linear plot (r^2 = 0.989) corresponding to a film β value (β_{film}) of 0.80 $Å^{-1}$ (Figure 7); C_{film} decreasing with *n* is responsible for a smaller β_{film} relative to $(\beta_{film,\sigma})_S$.

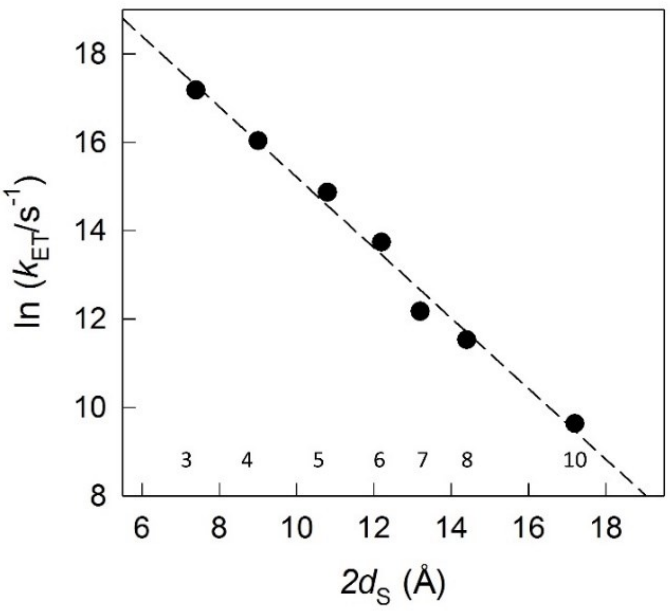

Figure 7 Dependence of the ET rate constant between MPCs inside the film (the n values are indicated at the bottom) as a function of twice the length d_S. Linear regression corresponds to β_{film} = 0.80 $Å^{-1}$.

This β_{film} is thus *apparently* in agreement with the minimum value β = 0.8 Å^{-1} expected for alkyl chains in their *all-trans* conformation; in fact, a range of β values as large as 1.0 Å^{-1} has been reported.[34,36,49] In our experimental systems, however, the chains cannot be in their fully extended conformation, and thus the observed β_{film} of 0.8 Å^{-1} is indeed only an apparent value. According to the *D* values the ligand length is on average ~59% of the fully extended conformation value, and the presence of kinks is known to increase the β value. Moreover, the ligands of neighboring monolayers must forcefully communicate via nonbonding coupling. This through-space or, in MPCs, interchain coupling (which might also involve ligands of the same cluster) is less effective than through-bond coupling in alkyl chains. Using the precise hanging mercury dropping electrode technique developed by Guidelli and co-workers,[82] Slowinski et al. found that for the same alkyl chain systems through-bond coupling has β = 0.91 Å^{-1}, whereas interchain coupling yields a β of 1.31 Å^{-1}.[83] Similar conclusions were reached, e.g., by studying electron tunneling through organic molecules in frozen glasses.[84] These considerations thus indicate that the observed β_{film} value is just too small to be reasonable. In fact, this apparent value provides a quite clear indication that the ligands are partially interdigitated especially for the longer chains, whose d_S/d_{fec} decreases with *n*. Partial interdigitation would make the actual tunneling distance *progressively* smaller than given by the sum of two Stokes radii with the result of increasing β. For instance, if we arbitrarily input a distance shorter by 80 or 67% of $2d_S$, β increases to 1.0 or 1.2 Å^{-1}, respectively. The above considerations suggest that this range of values could provide a better estimate of the actual average β and, thus, intercluster distance.

Regardless, the results show that the MPCs have a monolayer thickness that at least from the point of view of electron exchange resembles (or is limited by) that determined from the Stokes radii in solution, which is much smaller than calculated for the fully extended conformation. As from C*3* to C*10* the average d_S/d_{fec} is ~0.59, the core edge-to-edge separation corresponds to $2 \times 0.59 \times d_{fec} = 1.2\ d_{fec}$. Previous research, carried out with larger clusters of average composition $Au_{309}(SC_nH_{2n+1})_{92}$, concluded that the core edge-to-edge separation is constant and corresponds to approximately 1.2 d_{fec}.[57] For Au_{144} clusters capped with 2:3 mixtures of 1-mercaptoundecanoic acid and C*4*, C*8*, or C*10*, Zamborini et al. estimated variable degrees of interdigitation, corresponding to *edge-to-edge* separations varying from 1.1 d_{fec} to 1.7d_{fec}.[85] More recently, Carducci and Murray concluded that whereas for $Au_{144}(SC6)_{60}$ an almost complete interdigitation occurs, for $Au_{25}(SCH_2CH_2Ph)_{18}$ there is no interdigitation.[61]

It is now interesting to check the effect of d_S on the heterogeneous ET kinetics. By plotting the solution ln$k°$ values against d_S (Figure 8), β_{sol} becomes 0.43 Å^{-1} (r^2 = 0.993) that is, a value that is still about one half of that calculated for the films.

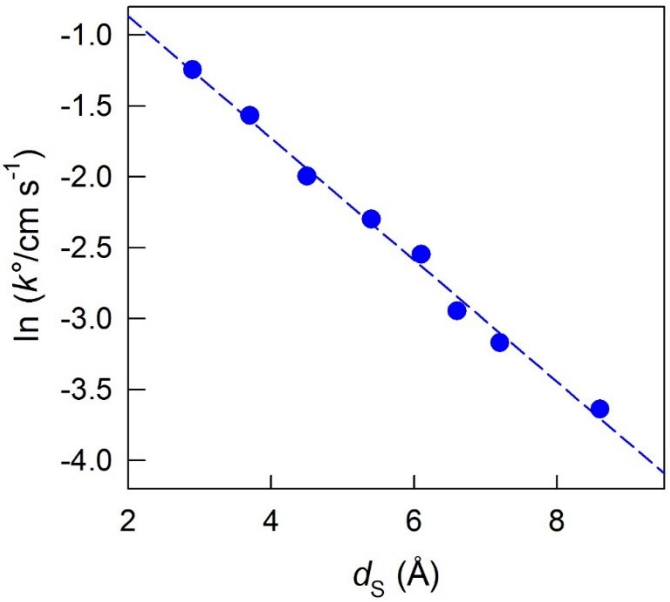

Figure 8 Dependence of the standard ET rate constant for the reduction of Au_{25} MPCs (DCM/0.1 M TBAH at 25 °C) on the distance d_S. Left to right, n = 3, 4, 5, 6, 7, 8, and 10. β_{sol} = 0.43 Å^{-1}.

This shows that although use of the Stokes radius improves β_{sol}, it does not yet provide an accurate descriptor of the effective distance at which the ET takes place. Obviously, in heterogeneous ETs interdigitation cannot be invoked. As opposed to 'normal' molecules, which are 'hard' objects, ligand-protected gold clusters can be considered as 'hard-soft' molecules where a hard metal core is surrounded by a soft molecular monolayer.[86] In other words, the alkyl chains are quite fluid and time-dependent contractions of the monolayer (or parts of it) and the effect of the collision with the electrode surface allow for the electron to tunnel between the electrode and the Au core also at distances that can be substantially shorter than those estimated from the hydrodynamic radii. The weight of these short-distance contributions to the observed ET rate constant is progressively more important for MPCs with longer, more flexible chains, with the consequence of significantly decreasing β_{sol}.

3.3.4 Further Insights: $Au_{25}(SMeC4)_{18}^0$

The analysis of the ET to/from molecular gold clusters in solid state and solution is deeply based on considering the dynamic nature of the alkanethiolate monolayer. We tested the general validity of our conclusions with a Au_{25} cluster bringing a more rigid

monolayer as an additional factor. The 2-methyl-1-butanethiolate ligand (SMeC*4*) has the same fully extended length of butanethiolate but carries a methyl group in the position β to sulfur. Its differential pulse voltammetry (DPV) behavior is quite similar to that of $Au_{25}(SC4)_{18}^0$ (Figure 9), and so is its optical behavior (Figure 10).

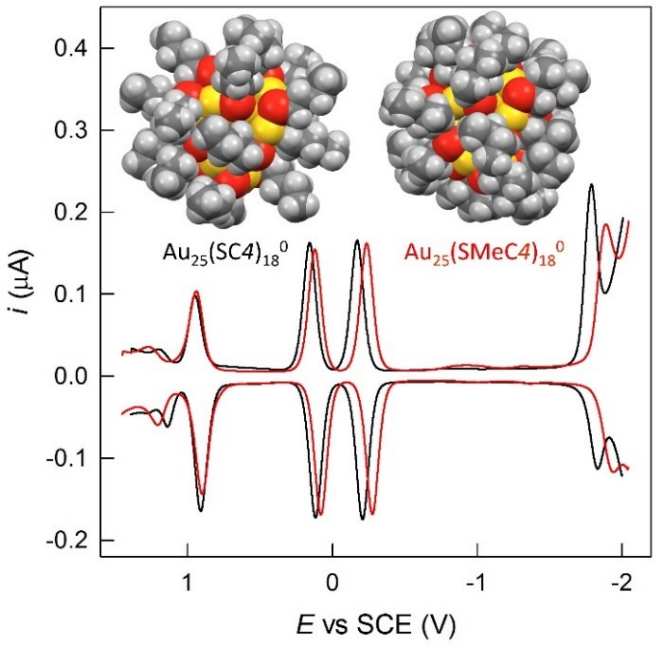

Figure 9 DPVs of 1 mM $Au_{25}(SMeC4)_{18}^0$ (red) and $Au_{25}(SC4)_{18}^0$ (black) in DCM/0.1 M TBAH. Glassy-carbon electrode, 25 °C. Inset shows models of (left) $Au_{25}(SC4)_{18}^0$ and (right) $Au_{25}(SMeC4)_{18}^0$. Au = yellow, S = red, C = gray, H = white.

Still, however, some differences can be noticed. The two reversible peaks near 0 V are less positive than those observed for the reference $Au_{25}(SC4)_{18}^0$ cluster, which can be attributed to the inductive effect of the methyl group at the β position and thus to stabilization of a positive charge (easier oxidation) and destabilization of a negative charge (more difficult reduction). For $Au_{25}(SMeC4)_{18}^0$, the peak for the formation of the dianion (just below -2 V) is less irreversible, which can be attributed to a stiffer monolayer and, therefore, a slower release of thiolates upon dianion formation.[87]

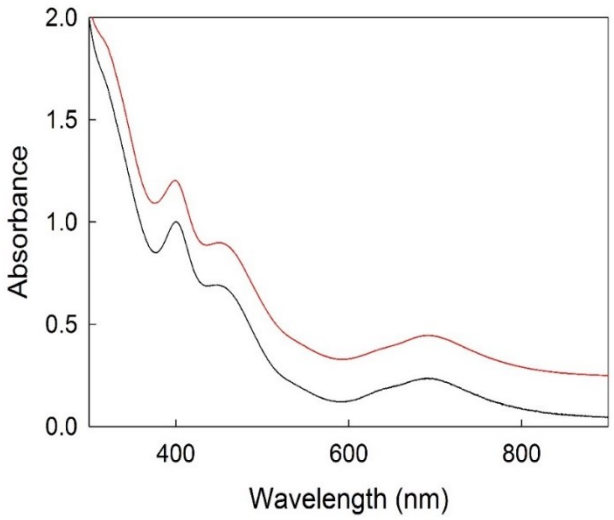

Figure 10 UV-vis absorption spectra of 0.1 mM $Au_{25}(SMeC4)_{18}^0$ (red) and $Au_{25}(SC4)_{18}^0$ (black) in hexane in a 2 mm cuvette. For the sake of better comparison, the curve of $Au_{25}(SMeC4)_{18}^0$ has been shifted vertically.

The inset of Figure 9 compares models of these two clusters and highlights an evident difference in possible penetrability of the two monolayers. We measured the film conductivity (and k_{ET}), the *D* value, and *k*° as done for the other clusters. The results are in Table 1.

Figure 11 shows the two plots pertaining to the solid-state and solution phase ET results, respectively, as a function of d_S. From these plots and Table 1 it is possible to draw some interesting conclusions. (i) The hydrodynamic radius of $Au_{25}(SMeC\mathit{4})_{18}^0$ is similar to that of $Au_{25}(SC\mathit{5})_{18}^0$ and this shows that the 2-methyl-1-butanethiolate ligands are indeed more elongated than the corresponding C*4* thiolates. (ii) In the solid state, the k_{ET} of $Au_{25}(SMeC\mathit{4})_{18}^0$ virtually lays on the correlation line; however, a larger $2d_S$ and smaller k_{ET} make it display a behavior similar to that of $Au_{25}(SC\mathit{5})_{18}^0$. (iii) In solution, $Au_{25}(SMeC\mathit{4})_{18}^0$ behaves very differently from the clusters capped by linear-chain ligands, as *k*° now falls quite below the correlation line; this is due to a much less freely folding monolayer, an effect that does not show up in the solid state. (iv) Although the Stokes radius is comparable to that of $Au_{25}(SC\mathit{5})_{18}^0$, from the viewpoint of solution ET the effective tunneling thickness in $Au_{25}(SMeC\mathit{4})_{18}^0$ is comparable to that of $Au_{25}(SC\mathit{7})_{18}^0$, once again stressing the importance of the conformational degrees of freedom in the dynamic monolayer capping MPCs. (v) Importantly, the results obtained for $Au_{25}(SMeC\mathit{4})_{18}^0$ provide a valuable support to the conclusions reached for the series of $Au_{25}(SC\mathit{n})_{18}^0$ clusters.

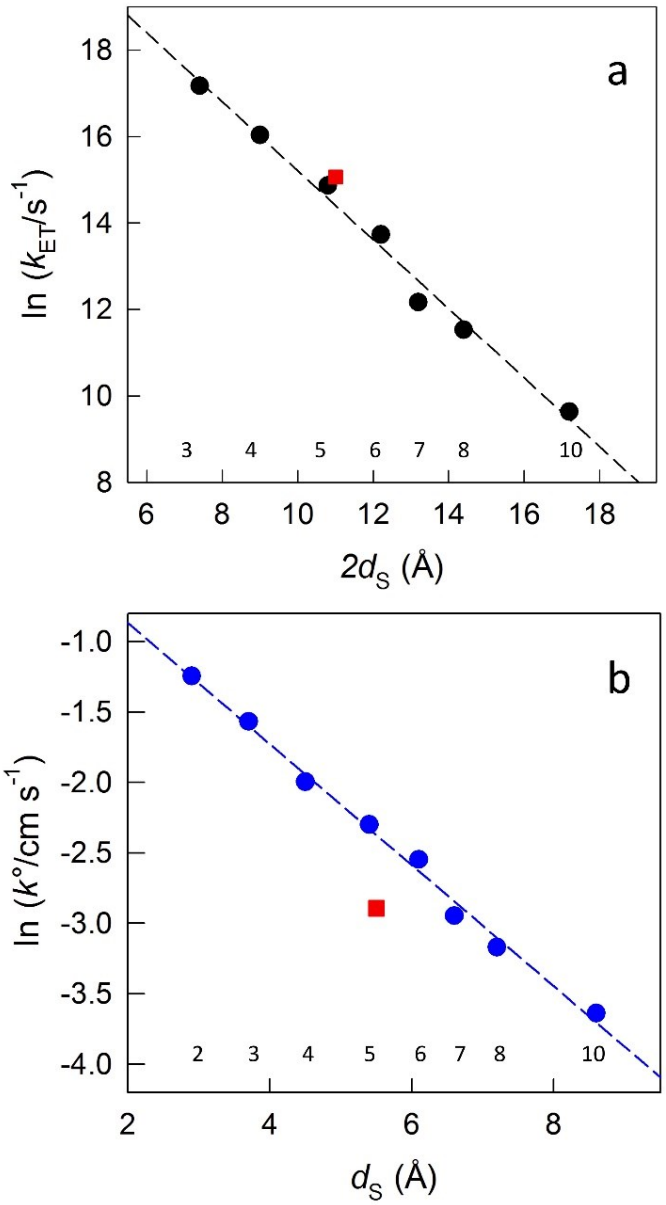

Figure 11 (a) Dependence of ET rate constant between Au_{25} MPCs inside the film (black circles; the *n* values are indicated at the bottom) together with the result obtained for $Au_{25}(SMeC4)_{18}^0$ (red square). **(b)** Distance dependence of the standard ET rate constant for the reduction of Au_{25} MPCs (DCM/0.1 M TBAH at 25 °C) capped by linear thiolates (blue circles) together with the result obtained for $Au_{25}(SMeC4)_{18}^0$ (red square). In both plots, the linear fits (dashed line: β_{film} = 0.80 Å^{-1}; β_{sol} = 0.43 Å^{-1}) do not include the $Au_{25}(SMeC4)_{18}^0$ data point.

3.3.5 Analysis of the Electron Transfer Kinetics in Films

We determined the temperature dependence of lnk_{ET} for several Au_{25} MPC films, typically in the range from 25 to -40 °C. The lnk_{ET} values were obtained from the experimental lnσ data through eq 5. For each compound, linear fit to the rate-constant

values according to eq 6 was very good (r^2 = 0.997 - 1.000), yielding the Arrhenius parameters gathered in Table 2.

$$\ln k_{ET} = \ln A - E_A/RT \quad \textbf{(6)}$$

Table 2 Kinetic parameters for ET in films.

	E_A (kJ mol^{-1})	A (s^{-1})	$\Delta G_{0,out}^{\neq}$ (kJ mol^{-1})	$\Delta G_{0,in}^{\neq}$ (kJ mol^{-1})
C*3*	18.0	4.1×10^{10}	7.2	10.8
C*4*	18.2	1.4×10^{10}	7.5	10.7
C*6*	19.4	2.4×10^{9}	7.9	11.5
C*8*	21.6	5.9×10^{8}	8.1	13.5
C*10*	22.4	1.2×10^{8}	8.3	14.1

In films, electrons hop from cluster to cluster on their way from the negative to the positive electrode combs forming the IDA. In the negative electrode region, electrons are injected into the nearby neutral clusters and are then transferred to progressively more distant clusters; in these layers, therefore, the contribution to conductivity is through sequential hopping ETs from a negatively charged to a neutral cluster. In the positive electrode region, electrons are removed from the nearby clusters and this triggers the opposite ET sequence. Only in the most central layers of the film (between the IDA fingers) the charged clusters react in a comproportionation reaction to yield two neutral clusters. Our model, therefore, differs from that seeing electronic conductivity in a sample of neutral MPCs as the result of forming charge carriers by a thermally activated disproportionation.[61] Most of the electron-hopping events, therefore, correspond to self-exchange ETs (that is, ETs at $\Delta G° = 0$). The ET activation free energy is, therefore, the intrinsic barrier, $\Delta G_0^{\neq}$. As there are no thermodynamic changes, the activation entropy should be zero, and therefore, $\Delta G_0^{\neq}$ can be taken as equal to E_A. $\Delta G_0^{\neq}$ has contributions from both the outer (solvent) and inner reorganizations.[33] Regarding this aspect, previous research based on phenylethanethiolate-protected Au_{25} clusters in films[60,61] and solution[25,26,28] concluded that the inner reorganization ($\Delta G_{0,i}^{\neq}$) can be even larger than the solvent reorganization ($\Delta G_{0,s}^{\neq}$), whereas in outer-sphere ETs involving common molecules $\Delta G_{0,i}^{\neq}$ is normally ~20% of the whole barrier.[88]

As in films $\Delta G_0^{\neq} = E_A$, the observed increase with *n* (from C*3* to C*10*, by 24%) can be attributed to $\Delta G_{0,s}^{\neq}$ and/or $\Delta G_{0,i,}^{\neq}$. We assume that the 'solvent' reorganization energy $\Delta G_{0,s}^{\neq}$ is associated with the dynamic ligands.[60] Thus, $\Delta G_{0,s}^{\neq}$ can be calculated with eq 7:

$$\Delta G_{0,S}^{\neq} = \frac{N_A e^2}{16\pi\varepsilon_0}\left(\frac{1}{\varepsilon_{op}} - \frac{1}{\varepsilon_s}\right)\left(\frac{1}{2r_1} + \frac{1}{2r_2} - \frac{1}{r_{12}}\right) \quad \textbf{(7)}$$

where *e* is the charge of the electron, ε_0 is the permittivity of vacuum, and ε_{op} and ε_s are the optical and static dielectric constants of the solvent. For ε_{op} and ε_s, we follow the same approach described by Choi and Murray,[60] who used 2.1 (taken as the square of the average refractive index of the thiols) and 3.0, respectively. As to r_1 and r_2, they correspond to the radius of the electron-exchanging gold cores, 4.9 Å. Instead, r_{12} is the MPC center-to-center distance, which is taken as $2r_{MPC}$; $2r_{12}$ is thus longer than $2r_{core}$ by $2d_S$. This difference makes $\Delta G_{0,s}^{\neq}$ (Table 2) an increasing function of *n*, with an overall increase (from C*3* to C*10*) of 15%.

$\Delta G_{0,i}^{\neq}$ is obtained by subtracting $\Delta G_{0,s}^{\neq}$ from E_A. Table 2 shows that $\Delta G_{0,i}^{\neq}$ provides a pretty important contribution to E_A (60-70%). Importantly, it is the main cause of the increase of E_a with *n*, as $\Delta G_{0,i}^{\neq}$ undergoes an overall variation of 31% (from C*3* to C*10*). We should stress that the $\Delta G_{0,i}^{\neq}$ values result from the assumption made about $\Delta G_{0,s}^{\neq}$. For example, if the ε_{op} and ε_s of thiols are replaced by the data pertaining to alkanes, the two values become smaller *and* virtually identical, with the consequence of making the solvent reorganization vanish.[33] Under these conditions, $E_A \approx \Delta G_{0,i}^{\neq}$. In either limiting case, however, $\Delta G_{0,i}^{\neq}$ would still increase with *n*. Given the different MPCs used and possible dispersity issues, this increase could not be clearly detected and rationalized before.[57] Generally speaking, inner reorganization is related to the variations in bond length and angles that the electron exchanging system undergoes on its way to the ET transition state. Regarding clusters, Raman spectroscopy evidence, obtained by studying the phenylethanethiolate-protected Au_{25} cluster in its -1 and 0 charge states, pointed to $\Delta G_{0,i}$ as associated with a collective variation of the Au-S bonds lengths upon ET.[26] It has been also shown that the Raman spectra of $Au_{25}(SCn)_{18}^0$ exhibit a strong chain length dependence.[89] Our present results would, therefore, indicate that the relative change in Au-S bond lengths undergone upon ET is also a function of *n.* It cannot be excluded that inner reorganization could also involve ligand modes, which may be affected by *n*.

Table 2 shows that ET kinetics is affected by the ligand length through both the preexponential A and E_A, which we have just discussed. Figure 12 shows the excellent linear correlation (r^2 = 0.999) of ln$A$ against 2d_S.

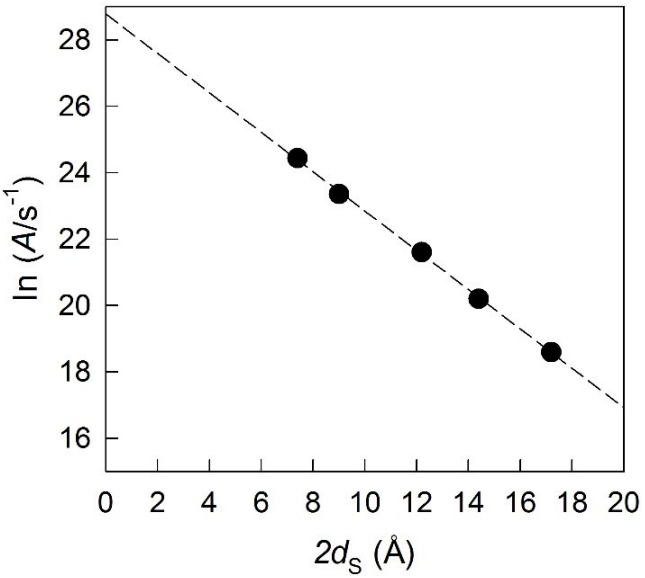

Figure 12 Dependence of the Arrhenius preexponential factor on twice the Stokes monolayer thickness. The linear fit has r^2 = 0.999

In the high-temperature limit of the semi-classical Marcus expression,[90] the first-order self-exchange ET rate constant for the film is given by eq 8:

$$k_{ET} = \frac{2\pi}{\hbar} H_{RP}^2 \frac{1}{\left(16\pi\Delta G_0^{\neq} RT\right)^{1/2}} \exp\left(-\Delta G_0^{\neq} / RT\right) \quad \textbf{(8)}$$

where H_{RP} is the electronic coupling between the reactant and product states. H_{RP} can be calculated from the preexponential term using the experimental A and, therefore, $\Delta G_0^{\neq}$ values. H_{RP} has an exponential distance dependence (eq 9):

$$H_{RP} = H_{RP}^0 \exp\left[-0.5\beta_{el}(r - r_0)\right] \quad \textbf{(9)}$$

where H_{RP}^0 is the electronic coupling at contact distance, r_0, and β_{el} is the exponential factor for electron tunneling. Eq 10 is the corresponding experimental equation (lnH_{RP} vs 2d_S, r^2 = 0.992), with $r - r_0 = 2d_S$ and H_{RP} in cm^{-1}.

$$H_{RP} = 98 \exp\left[-0.5 \times 0.58\ (2d_S)\right] \quad \textbf{(10)}$$

As already discussed, the actual intercluster distance is conceivably shorter than 2d_S, and accordingly, the β_{el} value is underestimated. Indeed, decreasing 2d_S by 67% (which makes β_{film} = 1.2 Å^{-1}) would increase β_{el} to the more reasonable value of 0.87 Å^{-1}. Regardless, the data show that 3/4 of the effect of distance on k_{ET} is related to β_{el}, while the rest is associated with $\Delta G_0^{\neq}$, and thus, a combination of $\Delta G_{0,s}^{\neq}$ and $\Delta G_{0,i}^{\neq}$ effects.

From C*3* to C*10*, H_{RP} goes from 12 to 0.7 cm^{-1}, which indicates that all these ETs proceed nonadiabatically (approximately, nonadiabatic behavior is when H_{RP} < 10 cm^{-1}). Instead, at the hypothetical core-to-core contact distance (H_{RP}^0 = 98 cm^{-1}), ET would be nearly adiabatic (the adiabatic-to-nonadiabatic transition zone roughly corresponds to 200 < H_{RP} < 10 cm^{-1}). The same conclusions can be reached in an alternative way. An ET rate constant can be written in a general form as $k_{ET} = \kappa_{el} Z \exp(-\Delta G^{\neq}/RT)$, where κ_{el} is the electronic transmission coefficients. For the MPCs investigated, use of the Landau-Zener expression[91-93] and frequency factor $Z = k_B T/h$ from transition state theory yields κ_{el} values much smaller than the adiabatic value (κ_{el} = 1). In particular, from C*3* to C*10* we calculate that κ_{el} goes from 6.6 x 10^{-3} to 1.9 x 10^{-5}. This range of values is indeed expected for nonadiabatic ETs (κ_{el} << 1). At the hypothetical core-to-core contact distance, κ_{el} = 0.3, that is, ET is somewhat nonadiabatic but not far from adiabatic.

3.4 Conclusions

This is the first systematic study on the effect of the monolayer length and branching on the ET rate between atomically precise molecular Au_{25} MPCs in the solid state. We show that the conductivity of MPC films can be tuned very finely by proper choice of both the length and/or the structure of the ligands protecting the Au core. Changing the alkyl chain from C3 to C10 induces a decrease in the film conductivity of 3.5 orders of magnitude. In terms of ET rate constant, this corresponds to a decrease $\Delta \log k_{ET}$ = 3.3, a figure much larger than that observed in solution, $\Delta \log k^{\circ}$ = 0.9. The experimental β_{film} values allow concluding that the average Au core-to-core distance in the film is at least comparable to (if not smaller than) twice the MPC hydrodynamic radius determined in solution, which already evidences a quite folded monolayer. The β_{film} value is in keeping with some interdigitation between ligands of neighboring clusters, although not as extensively as often assumed. Compared to the solution ET results, the film ET rates point to much less fluid alkyl chains. These conclusions are nicely confirmed by the results obtained for $Au_{25}(SMeC\mathit{4})_{18}^{0}$, where steric hindrance in the ligands translates into a thicker but also less mobile monolayer. Analysis of the ET kinetics in films leads to three important conclusions. (i) The length of the ligand affects both solvent and (especially) inner reorganization energies; whereas the former was predictable, the latter was not. (ii) The distance effect is mostly related to the electronic coupling between the reactant and product states. (iii) ETs are at the onset of full nonadiabatic behavior. These results and conclusions, which were made possible by the use of truly controlled molecular systems, are expected to be of relevance in applications of molecular clusters, such as vapor sensing, catalysis, and electrocatalysis.

3.5 Experimental

The syntheses of most of the $Au_{25}(SCn)_{18}^0$ clusters employed have already been described,[12,30,66,67] and the other syntheses were carried out along similar lines. All clusters were initially obtained as anions, $Au_{25}(SR)_{18}^-$, and then oxidized to form the corresponding neutral $Au_{25}(SR)_{18}^0$ clusters by using the silica-gel column chromatography method that we developed.[30,65] All clusters gave the expected optical spectrum and had the correct molecular mass, as verified by matrix-assisted laser desorption ionization time-of-flight (MALDI-TOF) mass spectrometry, and the typical ^{1}H NMR spectrum of paramagnetic clusters.[30,66,68]

The electrochemical experiments were carried out in DCM containing 0.1 M TBAH, under an Ar atmosphere at 25 °C. A 0.55 mm glassy carbon disk, prepared and activated as already described,[73] was the working electrode, whereas a Pt wire was the counter electrode. An Ag wire was the quasi-reference electrode. For the electrode kinetics experiments we used an EG&G-PARC 173/179 potentiostat-digital coulometer, an EG&G-PARC 175 universal programmer, and a Nicolet 3091 12-bit resolution digital oscilloscope. Careful feedback correction was applied to the kinetic experiments. The kinetic results were analyzed according to the Nicholson's method and double checked by digital simulation, used the DigiSim 3.03 package, a stepsize of 1 mV, and an exponential expansion factor of 0.5. The DPV experiments were carried out in the same conditions, but for using a 0.17 mm glassy carbon disk as the working electrode. The experimental parameters were: peak amplitude of 50 mV, pulse width of 0.05 s, 2 mV increments per cycle, and pulse period of 0.1 s.

For the conductivity measurements, we used Au interdigitated array (IDA) electrodes manufactured by ALS and consisting of a quartz plate supporting 65 interdigitated Au fingers (length = 2 mm, width = 10 μm, interfinger width = 5 μm, thickness = 0.96 nm). 5 μl of a concentrated DCM solution of the MPC (10 mg/0.1 mL) was drop cast and left to evaporate onto the IDA. The films were very carefully dried in vacuum for 30 min: increasing the drying time up to several hours did not affect the measured conductivity values. The use of a highly concentrated solutions guarantees formation of a film much thicker than the height of the Au fingers and this allows working under reproducible conditions. The cell constant $C_{cell} = l/A_{total}$ was calculated as described by Choi and Murray,[60] that is, by using for l the IDA gap and for A_{total} the product of the maximum useful conductive MPC film thickness (1 μm)[60] and the finger length (2 mm) times $N - 1$, where N is the total number of fingers (130). Thus, C_{cell} = 0.194 cm^{-1}. The bias potential across the IDA fingers was controlled with a CHI 660c

electrochemical workstation. The conductivity measurements were carried out at 22(1) °C by scanning the potential between +1 and -1 V, with an initial and final potential of 0 V, at scan rates in the range from 0.1 to 40 V s^{-1}. The IDA set up was inside a cell that could allow working under an argon atmosphere or *in vacuo*. For the temperature studies, the conductivity measurements were carried out inside a cell thermostated at temperature values ranging from 25 to -40 °C. To check the reproducibility of the measurements, the temperature was progressively decreased down to -40 °C and then increased back to 25 °C. In both runs, the *i* - *E* curves were collected with 5-degree increments, after allowing 20 min to let the system reach thermal equilibrium.

3.6 References

1. Du, Y.; Sheng, H.; Astruc, D.; Zhu, M. Atomically Precise Noble Metal Nanoclusters as Efficient Catalysts: A Bridge between Structure and Properties. *Chem. Rev.* **2020**, *120*, 526–622.

2. Hirai, H.; Ito, S.; Takano, S.; Koyasu, K.; Tsukuda, T. Ligand-protected gold silver superatoms: current status and emerging trends. *Chem. Sci.* **2020**, *11*, 12233-12248.

3. Kumar, B.; Kawawaki, T.; Shimizu, N.; Imai, Y.; Suzuki, D.; Hossain, S.; Naira, L. V.; Negishi, Y. Gold nanoclusters as electrocatalysts: size, ligands, heteroatom doping, and charge dependences. *Nanoscale* **2020**, *12*, 9969-9979.

4. Bonacchi, S.; Antonello, S.; Dainese, T.; Maran, F. Atomically Precise Metal Nanoclusters: Novel Building Blocks for Hierarchical Structures. *Chem. Eur. J.* **2021**, 27, 30–38.

5. Ibañez, F. J.; Zamborini, F. P. Chemiresistive Sensing with Chemically Modified Metal and Alloy Nanoparticles. *Small* **2012**, *8*, 174–202.

6. Jin, R.; Zeng, C.; Zhou, M.; Chen, Y. Atomically precise colloidal metal nanoclusters and nanoparticles: fundamentals and opportunities. *Chem. Rev*. **2016**, *116*, 10346–10413.

7. Chakraborty, I.; Pradeep, T. Atomically precise clusters of noble metals: emerging link between atoms and nanoparticles. *Chem. Rev.* **2017**, *117*, 8208–8271.

8. Howes, P. D.; Chandrawati, R.; Stevens, M. M. Colloidal Nanoparticles as Advanced Biological Sensors. *Science* **2014**, *346*, 1247390-1-10.

9. Tao, Y.; Li, M., Ren, J.; Qu, X. Metal Nanoclusters: Novel Probes for Diagnostic and Therapeutic Applications. *Chem. Soc. Rev.* **2015**, *44*, 8636-8663.

10. Ebina, A.; Hossain, S.; Horihata, H.; Ozaki, S.; Kato, S.; Kawawaki, T.; Negishi, Y. One-, Two-, and Three-Dimensional Self-Assembly of Atomically Precise Metal Nanoclusters. *Nanomaterials* **2020**, *10*, 1105.

11. Kang, X.; Zhu, M. Intra-cluster growth meets inter-cluster assembly: The molecular and supramolecular chemistry of atomically precise nanoclusters. *Coord. Chem. Rev.* **2019**, *394*, 1-38.

12. De Nardi, M.; Antonello, S.; Jiang, D.; Pan, F.; Rissanen, K.; Ruzzi, M.; Venzo, A.; Zoleo, A.; Maran, F. Gold Nanowired: A Linear $(Au_{25})_n$ Polymer from Au_{25} Molecular Clusters. *ACS Nano* **2014**, *8*, 8505-8512.

13. Agrachev, M.; Antonello, S.; Dainese, T.; Ruzzi, M.; Zoleo, A.; Aprà, E.; Govind, N.; Fortunelli, A.; Sementa, L.; Maran, F. Magnetic Ordering in Gold Nanoclusters. *ACS Omega* **2017**, *2*, 2607−2617.

14. Daniel, M.-C.; Astruc, D. Gold Nanoparticles: Assembly, Supramolecular Chemistry, Quantum-Size-Related Properties, and Applications toward Biology, Catalysis, and Nanotechnology. *Chem Rev.* **2004**, *104*, 293-346.

15. Lahtinen, T.; Hulkko, E.; Sokołowska, K.; Tero, T.-R.; Saarnio, V.; Lindgren, J.; Pettersson, M.; Häkkinen, H.; Lehtovaara, L. Covalently linked multimers of gold nanoclusters Au_{102}(*p*-MBA)$_{44}$ and $Au_{\sim 250}$(*p*-MBA)$_n$. *Nanoscale* **2016**, *8*, 18665-18674.

16. Green, T. D.; Yi, C.; Zeng, C.; Jin, R.; McGill, S.; Knappenberger, K. L., Jr Temperature-Dependent Photoluminescence of Structurally-Precise Quantum-Confined $Au_{25}(SC_8H_9)_{18}$ and $Au_{38}(SC_{12}H_{25})_{24}$ Metal Nanoparticles. *J. Phys. Chem. A* **2014**, *118*, 10611−10621.

17. Negishi, Y.; Nakazaki, T.; Malola, S.; Takano, S.; Niihori, Y.; Kurashige, W.; Yamazoe, S.; Tsukuda, T.; Häkkinen, H. A Critical Size for Emergence of Nonbulk Electronic and Geometric Structures in Dodecanethiolate-Protected Au Clusters. *J. Am. Chem. Soc.* **2015**, *137*, 1206−1212.

18. Ho-Wu, R.; Yau, S. H.; Goodson, T., III Linear and Nonlinear Optical Properties of Monolayer-Protected Gold Nanocluster Films. *ACS Nano* **2016**, *10*, 562-572.

19. Wu, Z.; Du, Y.; Liu, J.; Yao, Q.; Chen, T.; Cao, Y.; Zhang, H.; Xie, J. Aurophilic Interactions in the Self-Assembly of Gold Nanoclusters into Nanoribbons with Enhanced Luminescence. *Angew. Chem. Int. Ed*. **2019**, *58*, 8139-8144.

20. Rad, A. T.; Bao, Y.; Jang, H.-S.; Xia, Y.; Sharma, H.; Dormidontova, E. E.; Zhao, J.; Arora, J.; John, V. T.; Tang, B. Z.; Dainese, T.; Hariri, A.; Jokerst, J. V.; Maran, F.; Nieh, M.-P. Aggregation-Enhanced Photoluminescence and Photoacoustics of Atomically Precise Gold Nanoclusters in Lipid Nanodiscs ($NANO^2$). *Adv. Funct. Mater*. https://doi.org/10.1002/adfm.202009750**.**

21. Wu, Z.; Yao, Q.; Chai, J. O. H.; Ding, N.; Xu, W.; Zang, S.; Xie, J. Unraveling the Impact of Gold(I)-Thiolate Motifs on the Aggregation-Induced Emission of Gold Nanoclusters. *Angew. Chem. Int. Ed*. **2020**, *59*, 9934–9939.

22. Quinn, B. M.; Liljeroth, P.; Kontturi, K. Interfacial Reactivity of Monolayer-Protected Clusters Studied by Scanning Electrochemical Microscopy. *J. Am. Chem. Soc.* **2002**, *124*, 12915-12921.

23. Georganopoulou, D. G.; Mirkin, M. V.; Murray, R. W. SECM Measurement of the Fast Electron Transfer Dynamics between Au_{38}^{1+} Nanoparticles and Aqueous Redox Species at a Liquid/Liquid Interface. *Nano Lett.* **2004**, *4*, 1763-1767.

24. Peterson, R. R.; Cliffel, D. E. Scanning Electrochemical Microscopy Determination of Organic Soluble MPC Electron-Transfer Rates. *Langmuir* **2006**, *22*, 10307-10314.

25. Antonello, S.; Holm, A. H.; Instuli, E.; Maran, F. Molecular Electron-Transfer Properties of Au_{38} Clusters. *J. Am. Chem. Soc.* **2007**, *129*, 9836–9837.

26. Parker, J. F.; Choi, J.-P.; Wang, W.; Murray, R. W. Electron Self-Exchange Dynamics of the Nanoparticle Couple $[Au_{25}(SC_2Ph)18]^{0/1-}$ by Nuclear Magnetic Resonance Line-Broadening. *J. Phys. Chem. C* **2008**, *112*, 13976–13981.

27. Antonello, S.; Hesari, M.; Polo, F.; Maran, F. Electron Transfer Catalysis with Monolayer Protected Au_{25} Clusters. *Nanoscale* **2012**, *4*, 5333-5342.

28. Antonello, S.; Perera, N. V.; Ruzzi, M.; Gascón, J. A.; Maran, F. Interplay of Charge State, Lability, and Magnetism in the Molecule-like $Au_{25}(SR)_{18}$ Cluster. *J. Am. Chem. Soc.* **2013**, *135*, 15585-15594.

29. Liu, Z.; Xu, Q.; Jin, S.; Wang, S.; Xu, G.; Zhu, M. Electron transfer reaction between Au_{25} nanocluster and phenothiazine-tetrachloro-p-benzoquinone complex. *Int. J. Hydrogen Energy*. **2013**, *38*, 16722-16726.

30. Antonello, S.; Arrigoni, G.; Dainese, T.; De Nardi, M.; Parisio, G.; Perotti, L.; René, A.; Venzo, A.; Maran, F. Electron Transfer through 3D Monolayers on Au_{25} Clusters. *ACS Nano* **2014**, *8*, 2788–2795.

31. Lu, Y.; Jiang, Y.; Gao, X.; Chen, W. Charge state-dependent catalytic activity of $[Au_{25}(SC_{12}H_{25})_{18}]$ nanoclusters for the two-electron reduction of dioxygen to hydrogen peroxide. *Chem. Commun.* **2014**, *50*, 8464-8467.

32. Wang, D.; Yu, Y.; Sun, T.; Mirkin, M. V. Kinetics of Quantized Charging of Au_{144} Nanoclusters. *Electroanal.* **2016**, *28*, 2288-2292.

33. Marcus, R. A.; Sutin, N. Electron transfers in chemistry and biology. *Biochim. Biophys. Acta* **1985**, *811*, 265-322.

34. Paddon-Row, M. N. Superexchange-Mediated Charge Separation and Charge Recombination in Covalently Linked Donor–Bridge–Acceptor Systems. *Aus. J. Chem*. **2003**, *56*, 729–748.

35. Antonello, S.; Maran, F. Intramolecular Dissociative Electron Transfer. *Chem. Soc. Rev.* **2005**, *34*, 418-428.

36. Gray, H. B.; Winkler, J. R. Long-range Electron Transfer. *Proc. Natl. Acad. Sci. U.S.A*. **2005**, *102*, 3534**–**3539.

37. Shah, A.; Adhikari, B.; Martic, S.; Munir, A.; Shahzad, S.; Ahmade, K.; Kraatz, H.-B. Electron Transfer in Peptides *Chem. Soc. Rev.* **2015**, *44*, 1015-1027.

38. Bixon, M.; Jortner, J. Charge Transport in DNA Via Thermally Induced Hopping. *J. Am. Chem. Soc.* **2001**, *123*, 12556-12567.

39. Adams, D. M.; Brus, L.; Chidsey, C. E. D.; Creager, S.; Creutz, C.; Kagan, C. R.; Kamat, P. V.; Lieberman, M.; Lindsay, S.; Marcus, R. A.; Metzger, R. M.; Michel-Beyerle, M. E.; Miller, J. R.; Newton, M. D.; Rolison, D. R.; Sankey, O.; Schanze, K. S.; Yardley, J.; Zhu, X. Charge Transfer on the Nanoscale: Current Status. *J. Phys. Chem. B* **2003**, *107*, 6668**-**6697.

40. Antonello, S.; Crisma, M.; Formaggio, F.; Moretto, A.; Taddei, F.; Toniolo, C.; Maran, F. Insights into the Free Energy Dependence of Intramolecular Dissociative Electron Transfers. *J. Am. Chem. Soc.* **2002**, *124*, 11503-11513.

41. Closs, G. L.; Miller, J. R. Intramolecular Long-Distance Electron Transfer in Organic Molecules. *Science* **1988**, *240*, 440–447.

42. Natali, M.; Campagna, S.; Scandola, F. Photoinduced electron transfer across molecular bridges: electron- and hole-transfer superexchange pathways. *Chem. Soc. Rev.* **2014**,***43***, 4005-4018.

43. Morales-Martinez, D.; Polo, F.; Antonello, S.; Maran, F. Electrochemically Induced Electron Transfer Through Molecular Bridges. *Curr. Opinion Electrochem.* **2021**, *28*, 100700**.**

44. Smalley, J. F.; Finklea, H. O.; Chidsey, C. E. D.; Linford, M. R.; Creager, S. E.; Ferraris, J. P.; Chalfant, K.; Zawodzinsk, T.; Feldberg, S. W.; Newton, M. D. Heterogeneous Electron-Transfer Kinetics for Ruthenium and Ferrocene Redox Moieties through Alkanethiol Monolayers on Gold. *J. Am. Chem. Soc.* **2003**, *125*, 2004-2013.

45. Eckermann, A. L.; Feld, D. J.; Shaw, J. A.; Meade, T. J. Electrochemistry of Redox-active Self-assembled Monolayers. *Coord. Chem. Rev.* **2010**, *254*, 1769-1802.

46. Rampi, M. A.; Whitesides, G. M. A versatile experimental approach for understanding electron transport through organic materials. *Chem. Phys.* **2002**, *281*, 373-391.

47. Sek, S. Review: Peptides and Proteins Wired into the Electrical Circuits: An SPM-Based Approach. *Biopolymders (Pept. Sci.)* **2013**, *100*, 71-81.

48. McCreery, R. L.; Yana, H.; Bergren, A. J. A Critical Perspective on Molecular Electronic Junctions: There is Plenty of Room in the Middle. *Phys. Chem. Chem. Phys.* **2013**, *15*, 1065-1081.

49. Holmlin R. E.; Ismagilov, R. F.; Haag, R.; Mujica, V.; Ratner, M. A.; Rampi, M. A.; Whitesides, G. M. Correlating Electron Transport and Molecular Structure in Organic Thin Films. *Angew. Chem. Int. Ed.* **2001**, *40*, 2316-2320.

50. Antonello, S.; Venzo, A.; Maran, F. Dependence of Nonadiabatic Intramolecular Dissociative Electron Transfers on Stereochemistry and Driving Force. *J. Electroanal. Chem.* **2011**, *660*, 234-242.

51. Zuliani, C.; Formaggio, F.; Scipionato, L.; Toniolo, C.; Antonello, S.; Maran, F. Insights into the Distance Dependence of Electron Transfer through Conformationally Constrained Peptides. *ChemElectroChem* **2020**, *7*, 1225-1237.

52. Smalley, J. F.; Newton, M. D.; Feldberg, S. W. A simple comparison of interfacial electron-transfer rates for surface-attached and bulk solution-dissolved redox moieties. *J. Electroanal. Chem.* **2006**, *589*, 1-6.

53. Murray, R. W. Nanoelectrochemistry: Metal Nanoparticles, Nanoelectrodes, and Nanopores. *Chem. Rev.* **2008**, *108*, 2688–2720.

54. Zabet-Khosousi, A.; Dhirani, A.-A. Charge Transport in Nanoparticle Assemblies. *Chem. Rev.* **2008**, *108,* 4072–4124.

55. Yan, Y.; Warren, C. S.; Fuller, P.; Grzybowski, B. A. Chemoelectronic circuits based on metal nanoparticles. *Nature Nanotech* **2016**, *11*, 603-608.

56. Terrill, R. H.; Postlethwaite, T. A.; Chen, C.-H.; Poon, C.-D.; Terzis, A.; Chen, A.; Hutchison, J. E.; Clark, M. R.; Wignall, G.; Londono, J. D.; Superfine, R.; Falvo, M.; Johnson Jr, C. S.; Samulski, E. T.; Murray, R. W. Monolayers in Three Dimensions: NMR, SAXS, Thermal, and Electron Hopping Studies of Alkanethiol Stabilized Gold Clusters. *J. Am. Chem. Soc.* **1995**, *117*, 12537-12548.

57. Wuelfing, W. P.; Green, S. J.; Pietron, J. J.; Cliffel, D. E.; Murray, R. W. Electronic Conductivity of Solid-State, Mixed-Valent, Monolayer-Protected Au Clusters. *J. Am. Chem. Soc.* **2000**, *122*, 11465-11472.

58. Wuelfing, W. P.; Murray, R. W. Electron Hopping Through Films of Arenethiolate Monolayer-Protected Gold Clusters. *J. Phys. Chem. B* **2002**, *106*, 3139-3145.

59. Zamborini, F. P.; Leopold, M. C.; Hicks, J. F.; Kulesza, P. J.; Malik, M. A.; Murray, R. W. Electron Hopping Conductivity and Vapor Sensing Properties of Flexible Network Polymer Films of Metal Nanoparticles. *J. Am. Chem. Soc.* **2002**, *124*, 8958-8964.

60. Choi, J.-P.; Murray, R. W. Electron Self-Exchange between $Au_{140}^{+/0}$ Nanoparticles is Faster than that between $Au_{38}^{+/0}$ in Solid-State, Mixed-Valent Films. *J. Am. Chem. Soc.* **2006**, *128*, 10496-10502.

61. Carducci, T. M.; Murray, R. W. Kinetics and Low Temperature Studies of Electron Transfers in Films of Small (<2 nm) Au Monolayer Protected Clusters. *J. Am. Chem. Soc.* **2013**, *135*, 11351-11356.

62. Nealon, G. L.; Donnio, B.; Greget, R.; Kappler, J.-P.; Terazzi, E.; Gallani, J.-L. Magnetism in Gold Nanoparticles. *Nanoscale* **2012**, *4*, 5244−5258.

63. Kang, X.; Chong, H.; Zhu, M. $Au_{25}(SR)_{18}$: the captain of the great nanocluster ship. *Nanoscale* **2018**, *10*, 10758– 10834.

64. Chaki, N. K.; Negishi, Y.; Tsunoyama, H.; Shichibu, Y.; Tsukuda, T. Ubiquitous 8 and 29 kDa Gold:Alkanethiolate Cluster Compounds: Mass-Spectrometric Determination of Molecular Formulas and Structural Implications. *J. Am. Chem. Soc*. **2008**, *130*, 8608–8610.

65. Dainese, T.; Antonello, S.; Gascón, J. A.; Pan, F.; Perera, N. V.; Ruzzi, M.; Venzo, A.; Zoleo, A.; Rissanen, K.; Maran, F. $Au_{25}(SEt)_{18}$, a Nearly Naked Thiolate-Protected Au_{25} Cluster: Structural Analysis by Single Crystal X-ray Crystallography and Electron Nuclear Double Resonance. *ACS Nano* **2014**, *8*, 3904-3912.

66. Agrachev, M., Antonello, S., Dainese, T., Gascón, J. A., Pan, F., Rissanen, K., Ruzzi, M., Venzo, A., Zoleo, A.; Maran F. A Magnetic Look into the Protecting Layer of Au_{25} Clusters. *Chem. Sci.* **2016**, *7*, 6910-6918.

67. Antonello, S.; Dainese, T.; Pan, F.; Rissanen, K.; Maran, F. Electrocrystallization of monolayer-protected gold clusters: opening the door to quality, quantity, and new structures. *J. Am. Chem. Soc*. **2017**, *139*, 4168−4174.

68. Venzo, A.; Antonello, S.; Gascón, J. A.; Guryanov, I.; Leapman, R. D.; Perera, N. V.; Sousa, A.; Zamuner, M.; Zanella, A.; Maran, F. Effect of the Charge State (z = -1, 0, +1) on the Nuclear Magnetic Resonance of Monodisperse $Au_{25}[S(CH_2)_2Ph]_{18}^{z}$ Clusters. *Anal. Chem.* **2011**, *83*, 6355**–**6362.

69. Antonello, S.; Dainese, T.; De Nardi, M.; Perotti, L.; Maran, F. Insights into the Interface Between Electrolytic Solution and Gold Core in Molecular $Au_{25}(SR)_{18}$ Clusters. *ChemElectroChem.* **2016**, *3*, 1237**–**1244.

70. Zhu, M.; Eckenhoff, W. T.; Pintauer, T.; Jin, R. Conversion of Anionic $[Au_{25}(SCH_2CH_2Ph)_{18}]^{-}$ Cluster to Charge Neutral Cluster via Air Oxidation. *J. Phys. Chem. C* **2008**, *112*, 14221–14224.

71. Nicholson, R. S.; Shain, I. Theory of Stationary Electrode Polarography. *Anal. Chem.* **1964**, *36*, 706-723.

72. The heterogeneous ET rate constant is, in principle, affected by the double-layer effect, which is related to the potential Φ_S at the reaction site (distance of the center of the electroactive species to the electrode surface) relative to the potential of the bulk. Generally, Φ_S is equated to the potential of the outer Helmholtz plane, Φ_2 (here, the distance of the charged nitrogen center of TBA^+ to the electrode surface). For DCM, CV curves obtained at different TBAH concentrations show a dip at ca. 0.08 V SCE that could be associated with the

point of zero charge of glassy carbon in DCM. In analogy with previous results obtained in DMF,[73] at the reduction potentials of the clusters Φ_2 is estimated to be on the order of 0.08 - 0.09 V. However, MPCs are substantially larger than common molecules, and this makes Φ_S much smaller, if any at all, and thus negligible.

73. Meneses, A. B.; Antonello, S.; Arévalo, M.-C.; Maran, F. Double-Layer Correction for Electron-Transfer KInetics at Glassy Carbon and Mercury Electrodes in *N,N*-Dimethylformamide. *Electroanalysis* **2006**, *18*, 363-370.

74. Nicholson, R. S. Theory and Application of Cyclic Voltammetry for Measurement of Electrode Reaction Kinetics. *Anal. Chem*. **1965**, *37*, 1351-1355.

75. Skoge, M.; Donev, A.; Stillinger, F. H.; Torquato, S. Packing Hyperspheres in High-dimensional Euclidean Spaces*. Phys. Rev. E* **2006**, *74*, 041127.

76. Baule, A.; Makse, H. A. Fundamental Challenges in Packing Problems: from Spherical to Non-spherical Particles. *Soft Matter* **2014**, *10*, 4423-4429.

77. Andrieux, C. P.; Savéant, J.-M. Electron transfer through redox polymer films. *J. Electroanal. Chem*. **1980**, *111*, 377-381.

78. Laviron, E.; Roullier, L.; Degrand, C. A multilayer model for the study of space distributed redox modified electrodes: Part II. Theory and application of linear potential sweep voltammetry for a simple reaction. *J. Electroanal. Chem*. **1980**, *112*, 11-23.

79. Terrill, R. H.; Hutchison, J. E.; Murray, R. W. Solid State Electron-Hopping Transport and Frozen Concentration Gradients in a Mixed Valent Viologen-Tetraethylene Oxide Copolymer. *J. Phys. Chem. B* **1997**, *101*, 1535-1542.

80. Murray R. W. In Molecular Design of Electrode Surfaces (Techniques of Chemistry Series, vol. 22. Series editors: Weissberger, A., Saunders Jr., W. H.) Murray, R. W., Ed.; Wiley: New York, 1992, pp. 1–48.

81. Choi, J.-P.; Coble, M. M.; Branham, M. R.; DeSimone, J. M.; Murray, R. W. Dynamics of CO_2-Plasticized Electron Transport in Au Nanoparticle Films: Opposing Effects of Tunneling Distance and Local Site Mobility. *J. Phys. Chem. C* **2007**, *111*, 3778-3785.

82. Becucci, L.; Moncelli, M. R.; Guidelli, R. Surface charge density measurements on mercury electrodes covered by phospholipid monolayers. *J. Electroanal. Chem.* **1996**, *413*, 187-194.

83. Slowinski, K.; Chamberlain, R. V.; Miller, C. J.; Majda, M. Through-Bond and Chain-to-Chain Coupling. Two Pathways in Electron Tunneling through Liquid Alkanethiol Monolayers on Mercury Electrodes. *J. Am. Chem. Soc*. **1997**, *119*, 11910-11919.

84. Wenger, O. S.; Leigh, B. S.; Villahermosa, R. M.; Gray, H. B.; Winkler, J. R. Electron tunneling through organic molecules in frozen glasses. *Science* **2005**, *307*, 99-102.

85. Zamborini, F. P.; Smart, L. E.; Leopold, M. C.; Murray, R. W. Distance-dependent electron hopping conductivity and nanoscale lithography of chemically-linked gold monolayer protected cluster films. *Anal. Chim. Acta* **2003**, *496*, 3–16.

86. Agrachev, M.; Ruzzi, M.; Venzo, A.; Maran, F. Nuclear and Electron Magnetic Resonance Spectroscopies of Atomically Precise Gold Nanoclusters. *Acc. Chem. Res*. **2019**, *52*, 44−52.

87. Antonello, S.; Dainese, T.; Maran, F. Exploring Collective Substituent Effects: Dependence of the Lifetime of Charged States of $Au_{25}(SC_nH_{2n+1})_{18}$ Nanoclusters on the Length of the Thiolate Ligands. *Electroanalysis* **2016**, *28*, 2771-2776.

88. Meneses, A. M.; Antonello, S.; Arévalo, M.-C.; González, C. C.; Sharma, J.; Wallette, A. N.; Workentin, M. S.; Maran F. Electron Transfer to Sulfides and Disulfides: Intrinsic Barriers and Relationship between Heterogeneous and Homogeneous Electron-Transfer Kinetics. *Chem. Eur. J.* **2007**, *13*, 7983-7995.

89. Varnholt, B.; Guberman-Pfeffer, M. J.; Oulevey, P.; Antonello, S.; Dainese, T.; Gascón, J. A.; Bürgi, T.; Maran, F. Vibrational Coupling Modulation in n-Alkanethiolate Protected $Au_{25}(SR)_{18}^0$ Clusters. *J. Phys. Chem. C*, **2016**, *120*, 25378-25386.

90. Marcus, R.A. Nonadiabatic processes involving quantum-like and classical-like coordinates with applications to nonadiabatic electron transfers. *J. Chem. Phys*. **1984**, *81*, 4494-4500.

91. Landau, L. D. On the theory of transfer of energy at collisions II. *Phyz. Z. Sowjetunion* **1932**, *2*, 46.

92. Zener, C. Non-adiabatic crossing of energy levels. *Proc. R. Soc. London A* **1932**, *137*, 696-702.

93. Feldberg, S. W.; Sutin, N. Distance dependence of heterogeneous electron transfer through the nonadiabatic and adiabatic regimes. *Chem. Phys*. **2006**, *324*, 216–225.

4. Chemosensing with Films of Au_{25} Nanoclusters: Toward Possible Applications as Electronic Noses

4.1 Abstract

Nanoscale materials are revolutionizing the field of chemical sensing. Their unique properties, such as small size and high surface-to-volume ratio, offer several advantages over traditional bulk films. In this framework, NCs are promising materials to produce interesting devices, thanks to the possibility of controlling some physicochemical properties much better than using metal nanoparticles. Within this context, we carried out an investigation about the chemosensing behavior of atomically precise gold nanocluster films. We demonstrated that these films can be used to detect a variety of volatile organic compounds (VOCs). We tested a library of Au_{25} nanoclusters protected by a series of linear-chain thiolates (SC_nH_{2n+1}), in which n = 4,5,6,7, and 8, monitoring the different response in the conductivity of the film, under the presence of the analyte vapors inside the electrochemical cell, and analyzing in detail how the absorption of similar molecules (benzene, toluene, ethylbenzene) can affect the ET process between the core of nanoclusters. We observed an unpredictable and apparently nonsense change in the conductivity response, by increasing the chain of the ligands. Our hypothesis involves a modification in the ET pathway that, in the presence of VOCs can involve not only the Au nanocluster cores and their monolayer, but also the single molecules of vapors absorbed in the film, and, how they are positioned with respect to the ET path. This work presents the chemosensor behavior of atomically precise gold nanocluster films for the first time and paves the way for the design of new advanced vapor sensors with unprecedent performance. These sensors could be used for applications in a variety of fields, including security, environment, and health.

4.2 Introduction

In recent years, amorphous films of metallic nanoparticles coated with an organic layer have shown promise as chemoresistive materials due to the substantial increase in the conductivity of such films when exposed to small organic molecules in the atmosphere.[1–6] This property opens the way to the development of simple, low-cost devices with important applications, especially in the areas of disease diagnostics through breath analysis,[7] environmental safety,[8] and atmospheric pollution controls.[9] The operation of these devices is based on monitoring the electrical current that flows through the film deposited between two polarized electrodes.

Until now, chemiresistors have been fabricated using a variety of materials, including metals, metal oxides,[10,11] conductive polymers,[12] and insulating polymers embedded with metal or carbon.[13] In recent years, there has been a growing interest in the use of nanomaterials for chemical sensing applications.[1,14,15] Their unique properties, such as small size and high surface-to-volume ratio, offer several advantages over traditional bulk films. First, nanoscale materials are highly sensitive to analytes. This is because the surface atoms dominate their electronic properties, and analyte interactions with the surface can lead to large changes in resistance. This results in lower detection limits, allowing for the detection of even the smallest amounts of analyte. Second, nanoscale materials have fast response times. This is because analyte diffusion lengths are much smaller in nanoscale materials, leading to faster equilibration with the analyte. This makes them ideal for real-time sensing applications.[5] Third, nanoscale materials are highly miniaturizable. This is due to their small size. This leads to low cost, low power consumption, and the possibility of performing fast measurements in the field. Additionally, nanoscale materials can be used to measure analytes in highly confined spaces.[5] Overall, nanoscale materials offer several advantages over traditional bulk films for chemical sensing applications. Their high sensitivity, fast response times, and miniaturizability make them ideal for a wide range of applications.

A chemoresistive sensor is a device that exploits the variation in resistance of a solid material, due to the interaction with a particular chemical species, the analyte (Figure 1). The material whose current variation is usually recorded is a film of an active material (usually a semiconductor) deposited between two polarized electrodes with the application of a constant potential.

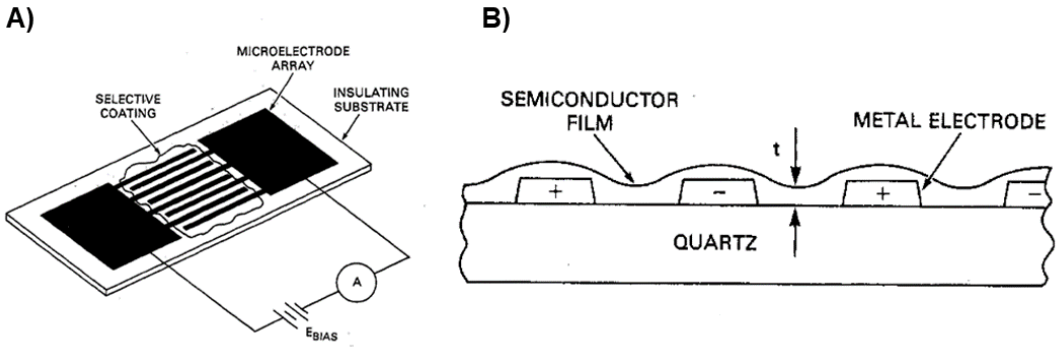

Figure 1 A) Cartoon of the chemoresistive system using IDA electrodes. **B)** A detailed side view of the planar measurement electrode.[16]

Maintaining a fixed potential (V) between the two electrodes, and consequently between alternating parallel bands, a conductivity current or resistance (R1) is recorded related to the intrinsic conductivity properties of the material used. Upon contact with a chemical environment, the film undergoes changes in its conductivity properties, which are experimentally captured as a difference in current or resistance (R2) passing between the two electrodes, before and after the interaction (Figure 2).

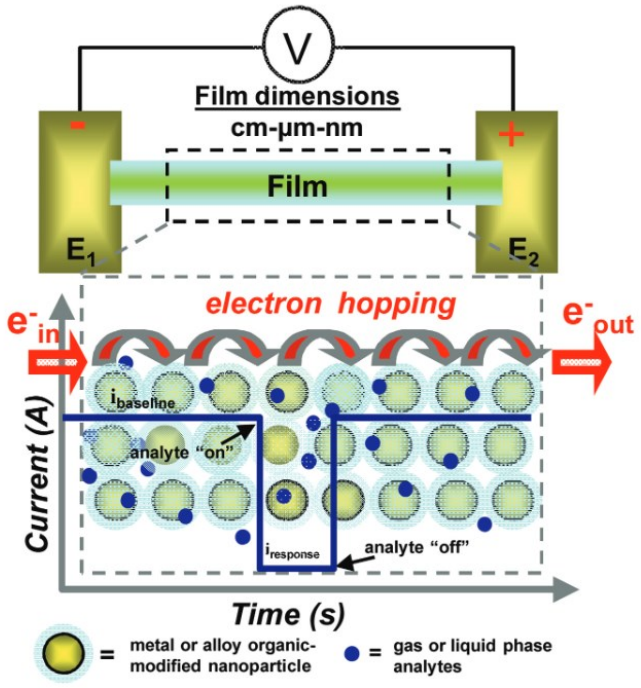

Figure 2 Schematic representation of a chemiresistive film of various dimensions of metal nanostructures separated by interdigitated SAM molecules (such as metal nanoparticles). Electron hopping occurs from core to core when a voltage (V) is applied.[5]

Sensors of this type have many positive aspects, including: (i) the speed with which the signal is acquired, (ii) the possibility of easily modifying the conducting material

used, (iii) the fact that it is completely “solvent-free”, (IV) their relatively low cost, and finally (V) the possibility of miniaturizing the device and therefore significantly increase portability and ease of use.

Numerous works describe chemoresistive systems for the detection of volatile organic compounds (VOCs) using films of gold nanoparticles of various sizes.[2–4,6,17] However, there are very few works that exploit the conductivity properties of atomically precise NCs. This is attributed to challenges in the synthesis and purification of nanoclusters, coupled with limited knowledge about the electrical properties of these nanosystems in the solid state until recently.[18] The interaction expected in a system utilizing material composed of atomically precise gold nanoclusters is associated with the absorption of volatile species within the film, specifically within the organic monolayer of the NC. VOCs, when in contact with the nanocluster film, are reversibly absorbed (partition equilibrium) by the organic monolayer that protects the NC cores. This process can induce two distinct effects in the film: (i) a structural change characterized by an increase in the average distance between the metal cores due to the physical presence of the absorbed molecular species, and (ii) a chemical change, as the presence of a new chemical species can alter the dielectric constant of the system, and of the protecting organic monolayer (Figure 3). The first of the two modifications will cause a decrease in the conductivity, due to a worse electronic coupling between the Au core. The second, however, can alter the resistance of the film in both positive and negative ways by modifying the activation energy of the ET process.

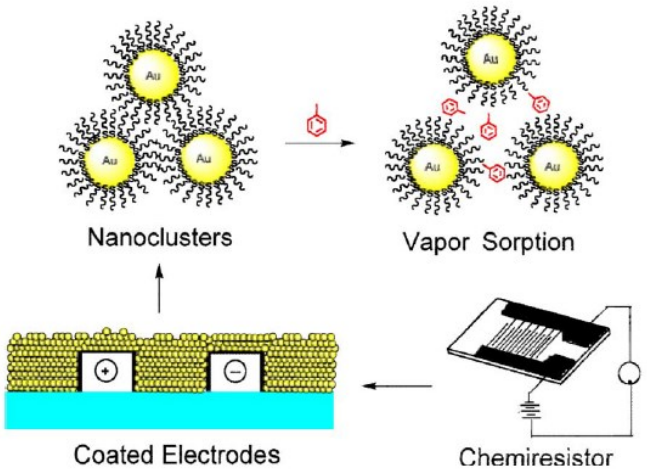

Figure 3 Cartoon illustrating the operating principle of a chemosensor using MPC. In this case in contact with toluene analyte.[19]

The peculiarity of being sensitive to two different modifications could be a plus for the realization of a sensor capable of responding to a complex matrix of vapors. By not

having a single type of response, a method of response and selective identification of a large number of species can be obtained.

Again, there is an extensive literature on chemoresistive sensors that use nanoparticles.[1–4] The results obtained with these systems are very interesting both from the point of view of sensitivity and selectivity to different VOC species. The use of atomically precise NCs in this context can bring advantages connected to the knowledge of their precise structure and to the possibility of finely modulating their properties.

4.3 Results and Discussion

For this study, we limited our analysis to the Au_{25} clusters protected by butanethiolate (C4), pentanethiolate (C5), hexanethiolate (C6), eptanethiolate (C7), and octanethiolate (C8), as they have demonstrated repeatability in the measurements.

This series of nanoclusters allowed us to also analyze the effect of the monolayer in the hopping process, in which the proposed chemosensor is based. These clusters were synthesized and characterized as detailed in Sections 2.5.1 and 2.5.3. The purity of the new clusters was assessed by UV-Vis spectroscopy, MALDI-TOF mass spectrometry, NMR spectroscopy, and electrochemistry.

4.3.1 Chemosensing Behavior of $Au_{25}(SR)_{18}^0$ Nanoclusters Films

The sensing behavior of Au NCs were monitored by evaluating the variation in the resistance of the film when in contact with an analyte vapor. The films were prepared by drop casting concentrated solutions of $Au_{25}(SR)_{18}^0$ onto IDA gold electrodes. This is an approach extensively employed to test the conductivity of NC films and is already described in Section 3.5. We used IDAs consisting of 65 interdigitated Au fingers with length = 2 mm, width = 10 um, interfinger width = 5 um, and thickness = 0.96 nm. Sensor measurements were carried out on carefully dried films, by keeping constant the bias potential (E) across the IDA finger pairs at the value of – 1 V. The absorption and desorption of vapors (generated as described in the Experimental Section) was followed by monitoring the *i* vs *time* signal. Experiments were carried out at 22(1) °C. Figure 4 shows a typical chronoamperometric experiment consisting of toluene sorption/desorption cycles.

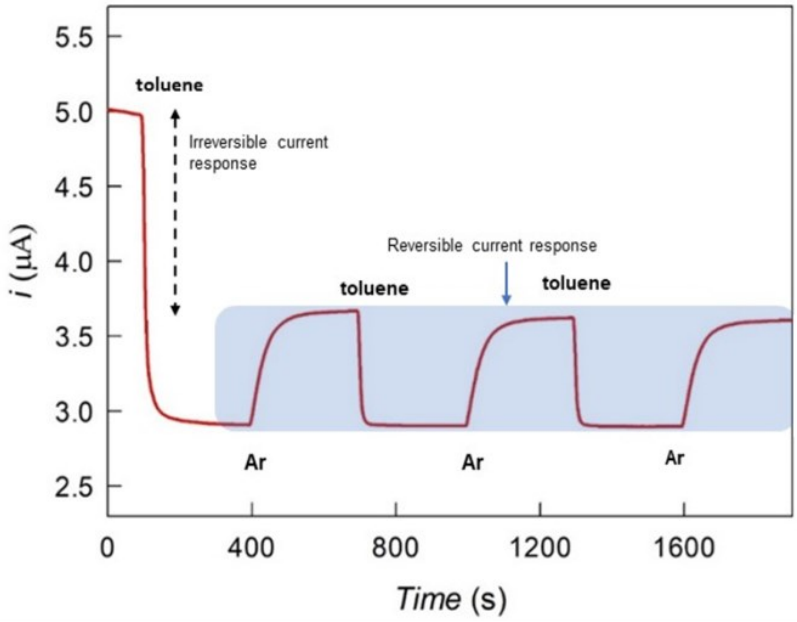

Figure 4 Typical chronoamperometric experiment consisting of consequent toluene sorption/desorption processes on $Au_{25}(SC_7H_{15})_{18}^0$ film. The applied potential was held fixed at -1 V, and Ar and toluene were alternatively flowed every 90 seconds. In blue the reversible sensor behavior is underlined.

The sensor response was also investigated by reversing the polarity between the two working electrodes (Figure 5), observing no outcome differences.

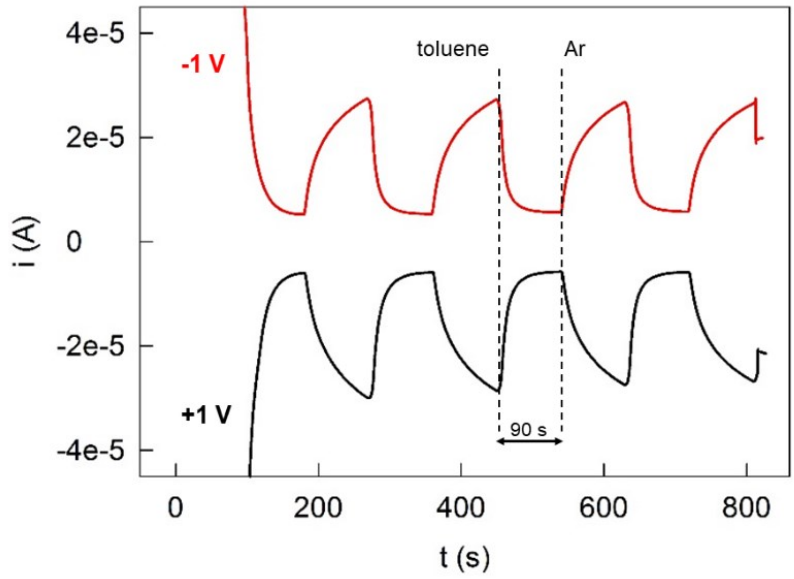

Figure 5 Typical *i* vs *t* plot of the chemosensing response of the $Au_{25}(SC_4H_9)_{18}^0$ film to toluene vapors. The applied potential was held fixed at +1 (black line) and -1 V (red line), and Ar and toluene were alternatively flowed every 90 seconds. No difference was detected.

the outcome was found to be qualitatively the same even at lower E values (Figure 6).

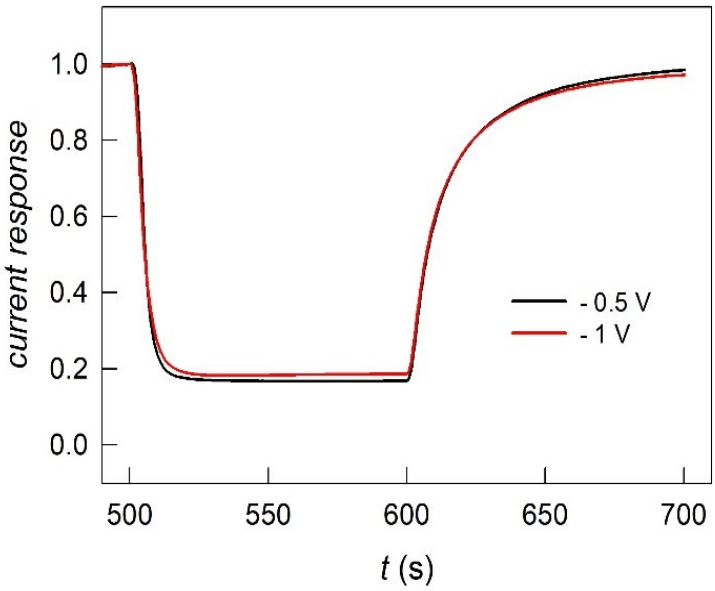

Figure 6 Chemosensing behavior as a function of the applied potential between the two working electrodes on $Au_{25}(SC_7H_{15})_{18}^0$ film.

The initial toluene sorption into the dry film causes a particularly large *i* change (Figure 4). As expected, the toluene molecules are easily absorbed on the Au_{25} nanocluster film, by his organic monolayer. The molecular absorption has the immediate effect of decreasing the conductivity current of the film, resulting in a huge and fast conductivity current drop. In the first cycle, this is always more significant, and it depends on the film thickness, as is underlined in Figure 7.

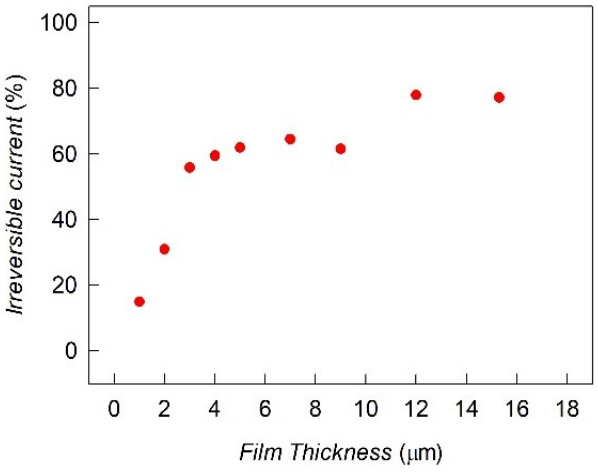

Figure 7 Current drop related to the first cycle (irreversible current response in Figure 4) as a function of the thickness of the film (Au_{25}C4) geometrically calculated as explained in the Experimental section.

From the second cycle, the sensor response turned out to be completely reversible. Concluding, the sensor outcome was observed to be fast, repeatable, and reversible.

4.3.2 Chemosensing Behavior of $Au_{25}(SC_nH_{2n+1})_{18}^0$ Films (n = 4-8) and Effect of the Ligand Length

The response to the VOC vapor can be analyzed as a relative current response (i_r, eq 1):

$$i_r = 1 - \frac{i_b - i_{VOC}}{i_b} \quad \textbf{(1)}$$

where i_b is the baseline (or reference) plateau current when no VOC vapors are present (see Figure 4), and i_{VOC} is the current response during the chronoamperometric experiment. Figure 8 shows a comparison of the sensor response related to the same Ar/toluene cycles observed for the different ligands under otherwise identical conditions.

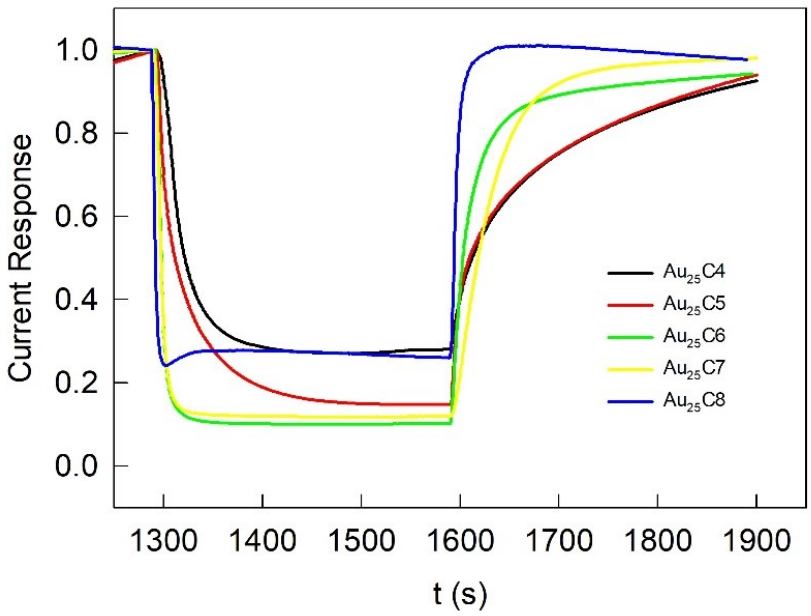

Figure 8 Study of the absorption of toluene vapors with film of Au_{25} nanoclusters with different ligand lengths ($Au_{25}Cx$, with x = 4,5,6,7, and 8). The curves are normalized at 1300 s.

Due to the smooth dependence exhibited by the ET rates as a function of n, one would intuitively expect that i_r increases with the ligand length, as the volume occupied by the ligands between the clusters provides sort of a viscous solvent for toluene. Instead, the evident decrease of i_r for n > 7 is puzzling. A very similar behavior is exhibited by ethylbenzene and benzene vapors (Figure 9).

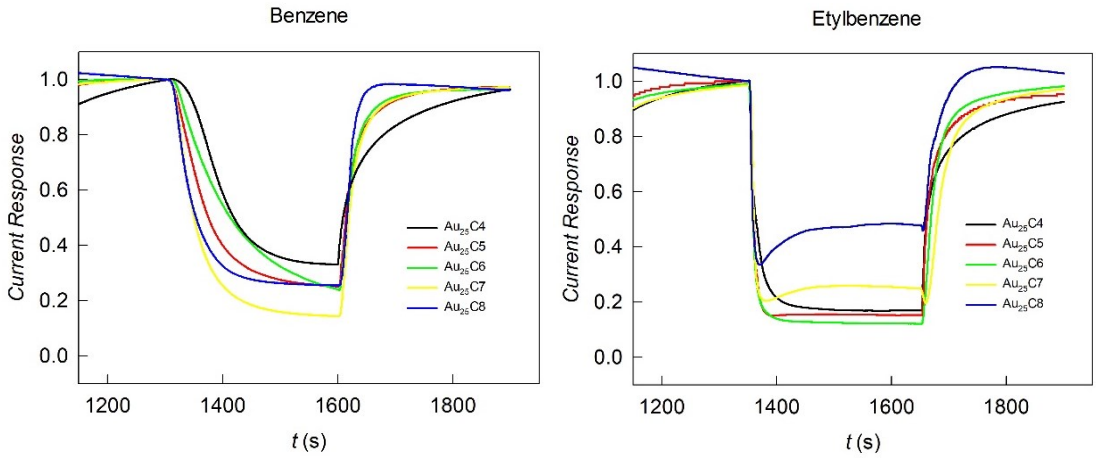

Figure 9 Study of the absorption of benzene and ethylbenzene vapors with film of Au_{25} nanocluster with different ligand length ($Au_{25}Cx$, with x = 4,5,6,7, and 8). The curves are normalized at 1300 s.

The current decrease is indeed significant, which shows that for all clusters absorption causes an evident decrease in σ (in some cases of about 60%). The resulting bell-shaped, n-dependent trend is best visualized in Figure 10.

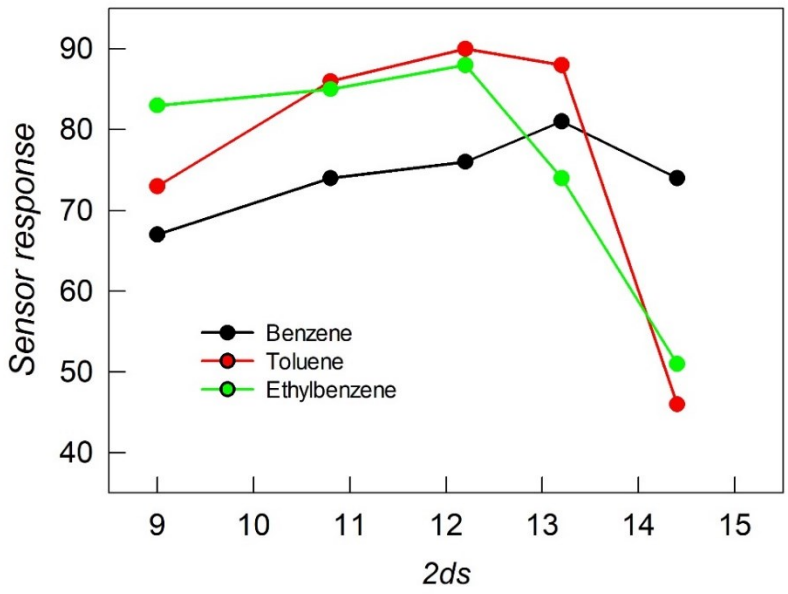

Figure 10 Current response percentage as a function of the effective distance between contiguous Au cores (approximated to *2ds*, where *ds* is the Stokes monolayer thickness, as defined in the previous chapter). The points are related to vapors of benzene, toluene, and ethylbenzene.

To better analyze the true effect on the ET process of the molecules inside the film, we proceed, as done before by many, by normalizing the data for the relative amount, in terms of volume, of organic material present in the film.[2,17] Since we are using Au_{25} with thiolates with a number of carbon atoms less than 10, we can consider them spherical[20] and then the volume occupied by the organic monolayer (f_{soft}, soft

fraction) can be calculated using the geometrical volume equation for a sphere ($V = \frac{4}{3}\pi r^3$) for the total nanocluster and then subtracting the volume of the spherical core of the nanocluster (hard part). As already done during the solid-state ET analysis presented in the previous chapter, we can access to the radius (*r*) of the core from X-ray crystallography data and to the radius of the total nanocluster using the Stokes-Einstein equation and the diffusion coefficient (D) values, previously obtained from the CV analysis.[18]

Table 1 Geometrical data of the Au_{25} nanoclusters used during the study and value of the "soft" percentage fraction needed to correct the sensor response.

N° of C atoms	r_{NC} (Å)	r_{core} (Å)	V_{tot} m^3	V_{core} m^3	V_{soft} m^3	f_{soft} %
4	9.4	4.9	3.5×10^{-27}	4.9×10^{-28}	3.0×10^{-27}	**86**
5	10.3	4.9	4.6×10^{-27}	4.9×10^{-28}	4.1×10^{-27}	**89**
6	11	4.9	5.6×10^{-27}	4.9×10^{-28}	5.1×10^{-27}	**91**
7	11.5	4.9	6.4×10^{-27}	4.9×10^{-28}	5.9×10^{-27}	**92**
8	12.1	4.9	7.4×10^{-27}	4.9×10^{-28}	6.9×10^{-27}	**93**

Figure 11 shows the same previous points after the geometrical correction (f_{soft}):

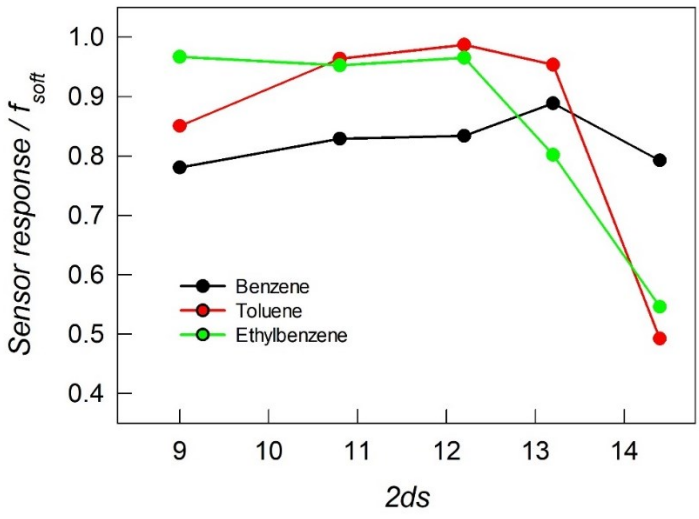

Figure 11 Dependence of the sensor response, normalized by the soft fraction, that is the organic monolayer, as a function of the effective distance between contiguous Au cores. The points are related to vapors of benzene, toluene, and ethylbenzene.

Furthermore, the correction can be enhanced by considering the response value at infinite time, thereby mitigating the influence of the kinetics associated with

the absorption process of vapor molecules. This is particularly important, as observed in Figure 8 and Figure 9, where the desorption of the VOC does not consistently reach a plateau. To address this, we employ an exponential equation to fit the absorption phase of the sensor curve, specifically the segment corresponding to the increase in conductivity. The fitted value at infinite time ($i_{b,inf}$) is then extracted. Figure 12 illustrates an example of an exponential fit, applied to the desorption of toluene in the $Au_{25}C7$ film, along with the equation employed.

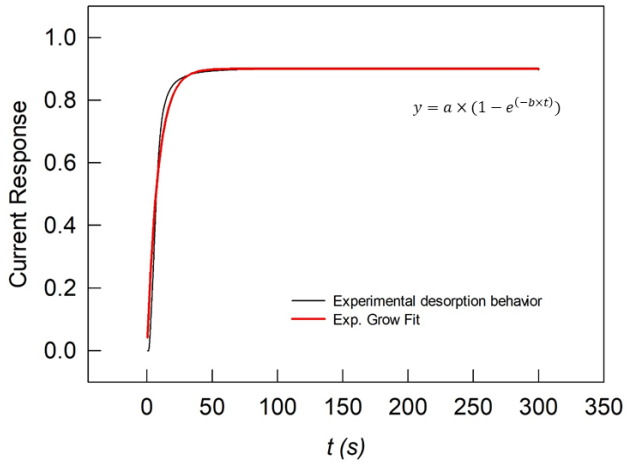

Figure 12 Example of exponential fit (red line) of the desorption of toluene vapors in $Au_{25}(SC_7H_{15})_{18}^0$ film. The equation used for the fit is shown as well.

Figure 13 shows the sensor response after both the geometrical and the exponential correction:

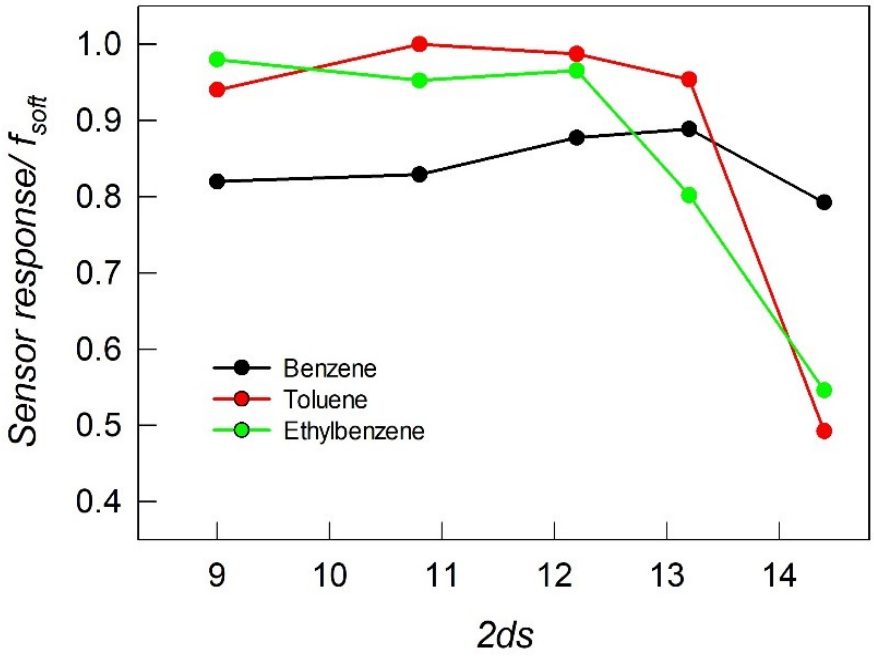

Figure 13 Dependence of the sensor response, normalized by the soft fraction, and corrected thanks to the exponential correction, as a function of the effective distance between contiguous Au cores. The points are related to vapors of benzene, toluene, and ethylbenzene.

After these corrections we can better evaluate the effect of the absorbed molecules on the ET process. As is evident in Figure 13, increasing the length of the ligand has no important effect on the sensor response for benzene as analyte and as long as the ligands are short enough. A sudden decrease of the sensor response is observed after the C7 value for the vapors of toluene and after C6 for the vapors of ethylbenzene. This response drop, corresponding to an increase in the conductivity of the film, could be attributed to a modification of the ET hopping between adjacent nanoclusters and seems to be related to the hindrance of the absorbed molecule. In the "Introduction" section of this Chapter, we explained that the swelling of the vapors in the conductive film affects the conductivity in two different ways: The first one is due to the increase in distance between the clusters core which disadvantages the hopping ET process and induces a decrease in the conductivity of the material (σ proportional to $e^{-d_{eff}}$, see eq 3 in previous Chapter), while the second one is due to the change in the dielectric constant of the material. Regarding this last point, our research group has recently evaluated electrochemically the average dielectric constant of the monolayer (ε_m) of alkanethiolated-protected Au_{25} nanoclusters in a low-polarity solvent such as DCM. They found that ε_m is the result of contributions from the ligands, the solvent, and the ions of the supporting electrolyte. For n ranging from 4 to 8 carbon atoms, ε_m has values of 7.2 - 7.5.[21] Of course we cannot consider

that a similar situation holds also in films, for the absence of the solvent and electrolyte. In the past, monolayer dielectric constant values of 3[22] and 3.6[23] were used for Au_{144} and $Au_{225,}$ both protected by hexanethiolates, that is, values not far from 2.7, the value estimated for alkanethiolate self-assembled monolayers (SAMs) on extended surfaces.[24] As the dielectric constants of benzene, toluene, and ethylbenzene are 2.28, 2.38, and 2.44, respectively, the effect of analyte absorption results to be negligible.[25] In a work by Murray, published in 2007, [26] it was proposed that, in addition to the swelling of the film that increases the average core edge-to-edge distance, there is also an effect due to the increase of the local short-range thermal motions of the unlinked donor-acceptor reaction centers (NCs cores) that is enhanced in the swelled, softened film. If these oscillating translational motions are of amplitude sufficient to shorten the separations between neighbor NCs cores at sufficient frequencies, ET can become accelerated, increasing the conductivity of films current, even though the average distance between redox centers has increased.[26] This effect should be enhanced using NCs with long ligands. However, this effect, if present, cannot explain such a big change in our sensor response (almost 60 %). For this reason, a better explanation of the phenomena can be achieved by thinking about the chemical structures of the vapors used. We hypothesize that the different behavior is related to how the aromatic ring is positioned inside the film. For the short ligands, one may expect the rings to somehow interdigitate with the ligands, so that the rings are aligned with the axis connecting two neighboring clusters. On the other hand, longer ligands allow the rings to attain other geometries, such as that perpendicular to the inter-cluster axis that is to the ET pathway. This would affect the electronic coupling extent between the cluster and the aromatic molecules and the overall efficiency of ET. Indeed, it is known that the presence of a phenyl group perpendicular to the path increases the through-space coupling.[27] Moreover, a very recent paper shows that the perpendicular conductance of a molecule bringing an aromatic ring, is about 400 times higher than that along the molecular plane.[28] In conclusion, the presence of benzene rings with the most appropriate orientation could increase the film's conductivity, thanks to a more efficient electronic coupling contribution, even though the average distance between redox centers is increasing because of the vapor's adsorption.

4.4 Conclusions

In this work, we have demonstrated that films of atomically precise Au_{25} nanoclusters can be used as fast, reversible, and stable chemoresistive sensors for the detection of a series of VOCs, including benzene, toluene, and ethylbenzene. Additionally, we have systematically investigated the effect of ligand length on sensor response. We found that increasing the ligand length has no significant effect on sensor response until a certain threshold is reached, at which a dramatic drop in current response is observed. We attribute this behavior to the arrangement of the aromatic rings of the VOCs within the film, particularly their orientation with respect to the inter-cluster direction. In the presence of longer ligands, the more dynamic environment allows the rings to adopt various geometries, including a perpendicular orientation to the electron transfer pathway. In this scenario, upon analyte absorption, two competing effects govern the conductivity current of the film: (i) the increasing distance between redox centers, leading to a decrease in conductivity, and (ii) the enhanced ET process resulting from the rearrangement of species into a favorable geometry. The balance of these two effects determines the overall sensor response. This complex interplay between the analyte and the nanocluster film highlights the importance of carefully considering the design of the sensing element. By optimizing the ligand length and other factors, it is possible to tune the sensor response to achieve the desired sensitivity and selectivity.

This work has demonstrated the potential of atomically precise gold nanoclusters as active materials for the development of fast, reversible, and stable chemoresistive sensors for VOCs. The ability to tune the properties of these nanoclusters, such as the ligand length, has enabled us to gain a deeper understanding of the underlying phenomena that govern their sensing performance. We believe that these findings pave the way for the development of next-generation chemical sensors with unprecedented sensitivity, selectivity, and robustness. The fundamental insights gained from this study can also be leveraged to design new multivariable sensing devices capable of detecting analytes in complex matrices.

4.5 Experimental

For sensing: the films were made on Au interdigitated array (IDA) electrodes manufactured by ALS and consisting of a quartz plate supporting 65 interdigitated Au fingers (length = 2 mm, width = 10 μm, interfinger width = 5 μm, thickness = 0.96 nm). 5 μl of a concentrated DCM solution of the MPC (10 mg/0.1 mL) was drop cast and left to evaporate onto the IDA. The films were very carefully dried in vacuum for 30 min. The sensing measurements were carried out with a CHI760D electrochemical workstation, by exposing the films to organic vapors and monitoring the time-evolution of film current. Measurements were carried out at room temperature and atmospheric pressure. The potential bias between the two IDA 'combs' was $\pm$ 1 V, but for some test experiments carried out at lower E. For these measurements was used a “two electrodes setup”: 1 WE electrode was connected with the reference and the counter shorted together. The film was exposed to an alternating flow of pure argon and a mixture of the VOC vapor and Ar. Benzene, toluene, and ethylbenzene vapors were generated by bubbling Ar through the analyte liquid in a bubbler, directly connected to a 25 mL, 6-neck electrochemical cell. All films show a quick response to the organic vapor, as 90% of the maximum response is reached within 15-20 s. The current returns to the baseline value i_b when exposure to the organic vapor is switched off by closing the bubbler.

For the *calculation of the film thickness:* we took advantage of the knowledge of the precise hydrodynamic radius of $Au_{25}C4$ NC (9.40 Å), to calculate the occupied volume for a unit of NC. Then, from knowing the exact amount of molecule deposited, we calculated the total volume (V_{tot}) of the sample. The thickness was then geometrically calculated as the ratio between V_{tot} and the base area of a cylinder ($A_{b,\ cylinder}$) having as its radius the drop cast radius, measured with a caliper.

4.6 References

1. Zamborini, F. P.; Leopold, M. C.; Hicks, J. F.; Kulesza, P. J.; Malik, M. A.; Murray, R. W. Electron Hopping Conductivity and Vapor Sensing Properties of Flexible Network Polymer Films of Metal Nanoparticles. *J. Am. Chem. Soc.* **2002**, *124* (30), 8958–8964.
2. García-Berríos, E.; Gao, T.; Woodka, M. D.; Maldonado, S.; Brunschwig, B. S.; Ellsworth, M. W.; Lewis, N. S. Response versus Chain Length of Alkanethiol-Capped Au Nanoparticle Chemiresistive Chemical Vapor Sensors. *J. Phys. Chem. C* **2010**, *114* (50), 21914–21920.
3. Wohltjen, H.; Snow, A. W. Colloidal Metal−Insulator−Metal Ensemble Chemiresistor Sensor. *Anal. Chem.* **1998**, *70* (14), 2856–2859.
4. Ibañez, F. J.; Zamborini, F. P. Chemiresistive Sensing of Volatile Organic Compounds with Films of Surfactant-Stabilized Gold and Gold−Silver Alloy Nanoparticles. *ACS Nano* **2008**, *2* (8), 1543–1552.
5. Ibañez, F. J.; Zamborini, F. P. Chemiresistive Sensing with Chemically Modified Metal and Alloy Nanoparticles. *Small* **2012**, *8* (2), 174–202.
6. Garg, N.; Mohanty, A.; Lazarus, N.; Schultz, L.; Rozzi, T. R.; Santhanam, S.; Weiss, L.; Snyder, J. L.; Fedder, G. K.; Jin, R. Robust Gold Nanoparticles Stabilized by Trithiol for Application in Chemiresistive Sensors. *Nanotechnology* **2010**, *21* (40), 405501.
7. Cao, W.; Duan, Y. Breath Analysis: Potential for Clinical Diagnosis and Exposure Assessment. *Clin. Chem.* **2006**, *52* (5), 800–811.
8. Mitsubayashi, Kohji.; Yokoyama, Kenji.; Takeuchi, Toshifumi.; Karube, Isao. Gas-Phase Biosensor for Ethanol. *Anal. Chem.* **1994**, *66* (20), 3297–3302.
9. Pejcic, B.; Eadington, P.; Ross, A. Environmental Monitoring of Hydrocarbons: A Chemical Sensor Perspective. *Environ. Sci. Technol.* **2007**, *41* (18), 6333–6342.
10. Franke, M. E.; Koplin, T. J.; Simon, U. Metal and Metal Oxide Nanoparticles in Chemiresistors: Does the Nanoscale Matter? *Small* **2006**, *2* (1), 36–50.
11. Albert, K. J.; Lewis, N. S.; Schauer, C. L.; Sotzing, G. A.; Stitzel, S. E.; Vaid, T. P.; Walt, D. R. Cross-Reactive Chemical Sensor Arrays. *Chem. Rev.* **2000**, 100 (7), 2595–2626.
12. Holliday, B. J.; Stanford, T. B.; Swager, T. M. Chemoresistive Gas-Phase Nitric Oxide Sensing with Cobalt-Containing Conducting Metallopolymers. *Chem. Mater.* **2006**, *18* (24), 5649–5651.
13. Lewis, N. S. Comparisons between Mammalian and Artificial Olfaction Based on Arrays of Carbon Black−Polymer Composite Vapor Detectors. *Acc. Chem. Res.* **2004**, *37* (9), 663–672.

14. Heller, I.; Janssens, A. M.; Männik, J.; Minot, E. D.; Lemay, S. G.; Dekker, C. Identifying the Mechanism of Biosensing with Carbon Nanotube Transistors. *Nano Lett.* **2008**, *8* (2), 591–595.

15. Myers, M.; Cooper, J.; Pejcic, B.; Baker, M.; Raguse, B.; Wieczorek, L. Functionalized Graphene as an Aqueous Phase Chemiresistor Sensing Material. *Sens. Actuators B Chem.* **2011**, *155* (1), 154–158.

16. Wohltjen, H.; Barger, W. R.; Snow, A. W.; Jarvis, N. L. A Vapor-Sensitive Chemiresistor Fabricated with Planar Microelectrodes and a Langmuir-Blodgett Organic Semiconductor Film. *IEEE Trans. Electron Devices* **1985**, *32* (7), 1170–1174.

17. Potyrailo, R. A. Toward High Value Sensing: Monolayer-Protected Metal Nanoparticles in Multivariable Gas and Vapor Sensors. *Chem. Soc. Rev.* **2017**, *46* (17), 5311–5346.

18. Reato, M.; Dainese, T.; Antonello, S.; Maran, F. Electron Transfer in Films of Atomically Precise Gold Nanoclusters. *Chem. Mater.* **2021**, *33* (11), 4177–4187.

19. Ancona, M. G.; Snow, A. W.; Foos, E. E.; Kruppa, W.; Bass, R. Scaling Properties of Gold Nanocluster Chemiresistor Sensors. *IEEE Sens. J.* **2006**, *6* (6), 1403–1414.

20. Antonello, S.; Arrigoni, G.; Dainese, T.; De Nardi, M.; Parisio, G.; Perotti, L.; René, A.; Venzo, A.; Maran, F. Electron Transfer through 3D Monolayers on Au_{25} Clusters. *ACS Nano* **2014**, *8* (3), 2788–2795.

21. Antonello, S.; Dainese, T.; De Nardi, M.; Perotti, L.; Maran, F. Insights into the Interface Between the Electrolytic Solution and the Gold Core in Molecular Au_{25} Clusters. *ChemElectroChem* **2016**, *3* (8), 1237–1244.

22. Hicks, J. F.; Miles, D. T.; Murray, R. W. Quantized Double-Layer Charging of Highly Monodisperse Metal Nanoparticles. *J. Am. Chem. Soc*., **2002**, 124, 13322-13328.

23. Wolfe, R. L.; Murray, R. W. Analytical Evidence for the Monolayer-Protected Cluster $Au_{225}[(S(CH_2)_5CH_3)]_{75}$. *Anal. Chem*. **2006**, 78, 1167-1173.

24. Rampi, M. A.; Schueller, O. J. A.; Whitesides, G. M. Alkanethiol Self-Assembled Monolayers as the Dielectric of Capacitors with Nanoscale Thickness. *Appl. Phys. Lett.* **1998**, *72* (14), 1781–1783.

25. Smallwood, I. M. *Handbook of Organic Solvent Properties*; Arnold; Halsted Press: London: New York, **1996**.

26. Choi, J.-P.; Coble, M. M.; Branham, M. R.; DeSimone, J. M.; Murray, R. W. Dynamics of CO_2 -Plasticized Electron Transport in Au Nanoparticle Films: Opposing Effects of Tunneling Distance and Local Site Mobility. *J. Phys. Chem. C* **2007**, *111* (9), 3778–3785.

27. Heitele, H.; Michel-Beyerle, M. E. Electron Transfer through Aromatic Spacers in Bridged Electron-Donor-Acceptor Molecules. *J. Am. Chem. Soc.* **1985**, 107, 8286-8288.

28. Afsari, S.; Yasini, P.; Peng, H.; Perdew, J. P.; Borguet, E. Anisotropic Conductivity at Single-Molecule Scale *Angew. Chem.* **2019** 131, 14413-14418.

5. Thiolate Protected Gold Nanoclusters and the Hydrogen/Deuterium Puzzle

5.1 Abstract

Electrochemical methods have been effectively employed to investigate substituent effects, a field that the late Petr Zuman pioneered. However, substituent effects have never been studied by changing a very large number of identical substituents. This type of study clearly demands the use of very special molecules in which this form of substitution is indeed feasible. Ultrasmall thiolate (SR) protected gold nanoclusters, such as $Au_{25}(SR)_{18}$, can be prepared with atomic precision and display molecular properties. Their electrochemical and, more generally, electron transfer (ET) behavior can be tailored by acting on both the metallic and organic components. $Au_{25}(SR)_{18}$ molecules, therefore, offer the chance to evaluate the combined impact of altering 18 identical ligands. We prepared the first fully deuterated gold nanocluster, $Au_{25}(SC_4D_9)_{18}$, and compared its electrochemical, ET, and solid-state behaviors with those observed for the corresponding $Au_{25}(SC_4H_9)_{18}$ cluster. The deuterated molecule displays several unexpected differences, comprising: (i) A smaller diffusion coefficient, consistent with a larger hydrodynamic radius; (ii) Lower rates of heterogeneous ET and, specifically, intercluster ET in films, pointing to a thicker monolayer; (iii) Single crystal X-ray crystallography demonstrates significant variations between the structures of $Au_{25}(SC_4D_9)_{18}$ and $Au_{25}(SC_4H_9)_{18}$. These and further findings indicate that deuterated thiolates are far from being non-innocent ligands.

5.2 Introduction

The isotope effect consists of the replacement of one substituent by one of its isotopes. The use of isotope substitution is widely regarded as one of the most fundamental and sensitive tools for deciphering reaction mechanisms.[1–4] Deuteration is the process that replaces hydrogen atoms with deuterium atoms. Deuteration has been used to study substituent effects for a variety of small molecules, including organic compounds and inorganic complexes.[2,5–10] From all the different isotope effects, one of the more interesting ones is the “steric isotope effect”. Steric isotope effects do not involve bond breaking or formation. These effects arise mainly from the varying vibrational amplitudes of different isotopologues (molecules with the same molecular formula but different isotopes). An example of a steric isotope effect is in the deslipping reaction of rotaxanes. Due to its smaller effective size, deuterium allows stoppers to pass through the macrocycle more easily, leading to faster deslipping rates for deuterated rotaxanes.[11] Among all, deuteration is one of the most used and studied, especially for the possibility of creating silent molecules at ^{1}H-NMR, which can be useful for following chemical reactions in real-time and studying their kinetics. While numerous studies have elucidated the impact of individual substituents, the simultaneous alteration of a vast number of quasi-identical substituents remains an unexplored frontier. This endeavor necessitates the utilization of unique molecular architectures that intrinsically accommodate such substitution patterns. Ultrasmall thiolate-protected gold nanoclusters ($Au_{25}(SR)_{18}$), embody ideal candidates for this groundbreaking investigation. These molecules exhibit distinct molecular characteristics, enabling the systematic manipulation of their electrochemical and (ET) properties by modulating both the metallic core and organic ligands.[12–14] However, research on the effects of altering a large number of nearly identical substituents, in metal NCs is still in its early stages. Regarding this topic, we must mention one very recent and inspiring work by Terraneo and co-workers where they reported the design, synthesis, and crystallization of a superfluorinated atomically precise Au nanocluster (Au_{25} core) even bearing 486 F atoms. The crystal structure of the aforementioned structure reveals the ability of a multi-branched superfluorinated thiol to actually drive the crystallization through F⋯F interactions.[15]

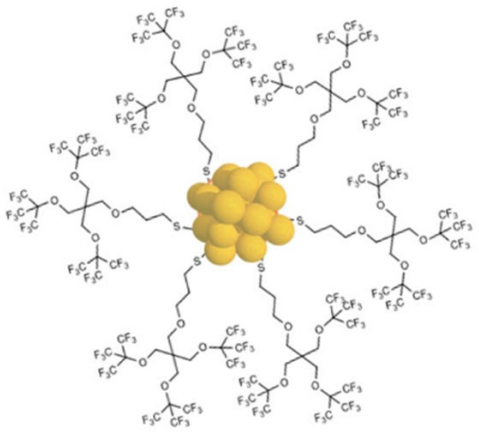

Figure 1 Cartoon representation of Au_{25} NC stabilized by $F_{27}SH$ thiol. For the sake of clarity, only 6 over 18 $F_{27}S$-ligands have been reported.[15]

Electrochemical methods have been effectively employed to investigate substituent effects, a field that the late Petr Zuman pioneered.[16] They have proven to be a powerful tool in dissecting the intricate interplay between substituents and their profound influence on molecular behavior. Our research delves into this uncharted territory by introducing the first fully deuterated gold nanocluster, $Au_{25}(SC_4D_9)_{18}$, a radical departure from the conventionally employed hydrogen-based counterparts. By meticulously comparing the electrochemical behaviors of $Au_{25}(SC_4D_9)_{18}$ (hereafter indicated simply as Au_{25}C4D) with those of its hydrogen-based counterpart, $Au_{25}(SC_4H_9)_{18}$ (hereafter indicated simply as Au_{25}C4) we unveil a wealth of unexpected phenomena. These findings shed light on the intricate interplay between deuteration and molecular properties, challenging conventional notions regarding the non-innocence of deuterated ligands. The ability to tailor the properties of molecules at the atomic scale holds immense promise for the development of novel materials with enhanced functionality and unprecedented performance. The synthesis and thorough characterization of the first fully deuterated gold nanocluster has opened the door to a paradigm shift in the study of substituent effects, offering unprecedented insights into the fundamental principles governing molecular properties.

5.3 Results and Discussion

Synthesis of $Au_{25}(SC_4D_9)_{18}^0$: The synthesis of $Au_{25}(SC_4D_9)_{18}^0$ was carried out as follows.[12] 6 equiv. of 1-butane-d_9-thiol ($CD_3(CD_2)_3SH$) (816 µl, 7.62 mmol) were added dropwise, under stirring and at room temperature, to a tetrahydrofuran (THF) solution (50 ml) of $HAuCl_4 \cdot 3H_2O$ (500 mg, 1.27 mmol) and tetra-n-octylammonium bromide

(779 mg, 1.425 mmol). After 1 h, a freshly-prepared ice-cold solution of $NaBH_4$ (480 mg, 12.7 mmol) in water (10 ml) was rapidly added under vigorous stirring. The resulting black mixture was stirred for ca. 2 days and then filtered on paper. THF was removed by rotary evaporation to leave a red-brownish oil covered by an aqueous phase. The latter was removed by dissolving the product in 50 ml of toluene followed by washing the solution with water (3 x 50 ml). The solution was filtered to remove residual white polymer-like material, and the solvent evaporated. By this procedure, the cluster is obtained as $[nOct_4N^+][Au_{25}(SC_4D_9)_{18}^-]$. The product was then further purified (for the electrocrystallization) or oxidized (for all the other physicochemical analysis). In the first case, the solid was washed with pentane (3 x 10 ml), to remove possible thiol and disulfide, and then dried. Then, the solid was washed thrice with icy cold methanol (3 x 10 mL) and acetonitrile (3 x 10 mL), to remove the remaining salt, and possible thiol and disulfide still present. Finally, the red-brownish solid was finally dried. Oxidation of $[nOct_4N^+][Au_{25}(SC_4D_9)_{18}^-]$ to its neutral form was accomplished by dissolution in DCM (5 ml) followed by passage through a silica-gel column under aerobic conditions. The DCM solution was then dried to obtain the final product as a black film/powder on the vial's wall. The composition and the monodispersity of the new cluster was assessed by UV-vis spectroscopy, MALDI-TOF mass spectrometry, and electrochemistry (Please, see "Supporting materials" section).

5.3.1 Electrochemical Behavior of $Au_{25}(SC_4D_9)_{18}$ and Similarity with his Non-deuterated Counterpart

The electrochemical behavior of Au_{25}C4D was studied in DCM/0.1 M $TBAPF_6$. The electrochemical pattern is very similar to that of his non-deuterated counterpart, Au_{25}C4. Summarily, two main reversible peaks associated with the +1/0 and 0/-1 redox couples, and further oxidation or reduction peaks corresponding to formation of higher positive or negative charge states were observed (Please see the "Supporting materials" section for the CVs). In Figure 2, the comparison of the DPV curves of deuterated and no deuterated NCs is presented.

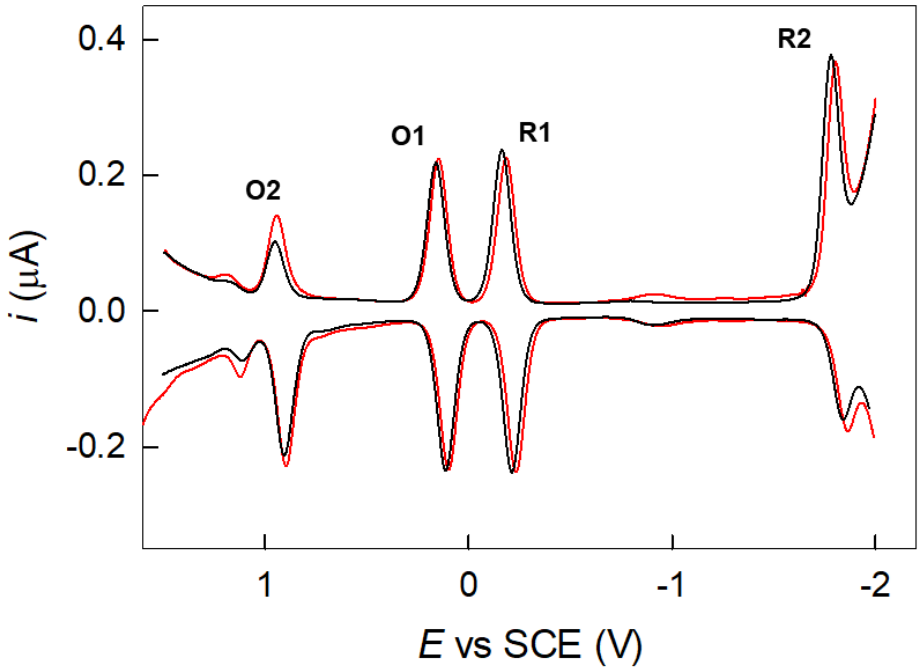

Figure 2 DPV behavior of the deuterated nanocluster, $Au_{25}(SC_4D_9)_{18}$ (red line), compared with his non-deuterated counterpart, $Au_{25}(SC_4H_9)_{18}$ (black line), both in DCM/0.1 M $TBAPF_6$, on a glassy carbon electrode.

Au_{25}C4D demonstrated a mild negative potential shift on both the reversible processes. In particular, R1 (the first reduction process, associated to 0/-1 redox couple) resulted to be shifted of about 13 mV, while O1 (the first oxidation process, associated to +1/0 redox couple) of 10 mV, resulting in a separation between the two peaks of the reversible processes of Au_{25} smaller of about 3 mV in Au_{25}C4D, respect to his non-deuterated counterpart. A deeper analysis of the CVs at low scan rates gives us the opportunity to evaluate the differences between the two NCs better, and so give an elucidation about the deuteration effect on the electrochemical properties of NCs in solution. Figure 3 shows the CVs behavior of Au_{25}C4D at different scan rates.

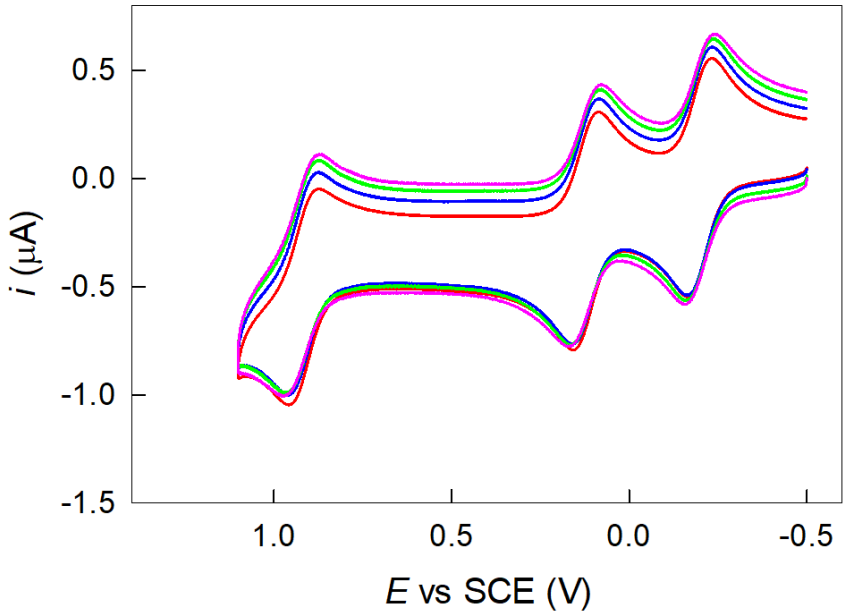

Figure 3 CV behavior of the deuterated nanocluster, $Au_{25}(SC_4D_9)_{18}$, at different scan rates (0.1 V/s red line; 0.2 V/s blue line; 0.5 V/s green line; 1 V/s purple line) obtained in DCM/0.1 M $TBAPF_6$, on a glassy carbon electrode.

From the analysis of the CV curves, we obtained some interesting electrochemical parameters. These are shown in the next table together with the same parameters of the non-deuterated NC.

Table 1 Electrochemical parameters of Au_{25}C4D compared with Au_{25}C4, obtained from low scan rates CV measurements.

	$Au_{25}(SC_4H_9)_{18}$	$Au_{25}(SC_4\mathbf{D}_9)_{18}$
E° (R1) (V)	- 0.188	- 0.201
E° (O1) (V)	0.139	0.129
ΔE° (O1-R1) (V)	0.327	0.330
D (cm^2/s)	5.60×10^{-6}	5.46×10^{-6}
r_{NC} (Å)	9.4	9.7

The previous table highlights the impact of deuteration on the kinetic properties of the electrochemical behavior of NCs in solution. However, while the ligand length remains the same, the hydrodynamic radius (r_{NC}) of Au_{25}C4D, exhibits an appreciable increase (from 9.4 Å to 9.7 Å). This finding is consistent with the calculated diffusion coefficient (D). This result, along with the increased separation between the two peaks associated with the reversible redox processes (R1 and O1), suggest a more expanded, thicker, and permeable monolayer coating the Au_{25} NCs in the deuterated system.

5.3.2 Solid-State ETs of $Au_{25}(SC_4D_9)_{18}$

The conductivity measurements were carried out by drop casting a concentrated solution of the Au_{25}C4D molecules onto IDA gold electrodes. This is an approach extensively employed to test the conductivity of NC films[17–22] and recently used by us with the goal of obtaining information about the dependence of the ET rate constant between NCs inside the films with respect to the dimension and type of the protective monolayer (Please, see Chapter 3).[23] Indeed, this type of measurement is very sensitive to the type of monolayer and above all to its organization/compactness when it is in a solid state. We used IDAs consisting of 65 interdigitated Au fingers with length = 2 mm, width = 10 μm, interfinger width = 5 μm, and thickness = 0.96 nm. Conductivity measurements were carried out on carefully dried films, by linearly scanning the bias potential (E) across the IDA finger pairs between +1 and −1 V. The current *i* is linear in E (Figure 4, red curve), in agreement with similar samples, pointing to films displaying ohmic behavior.

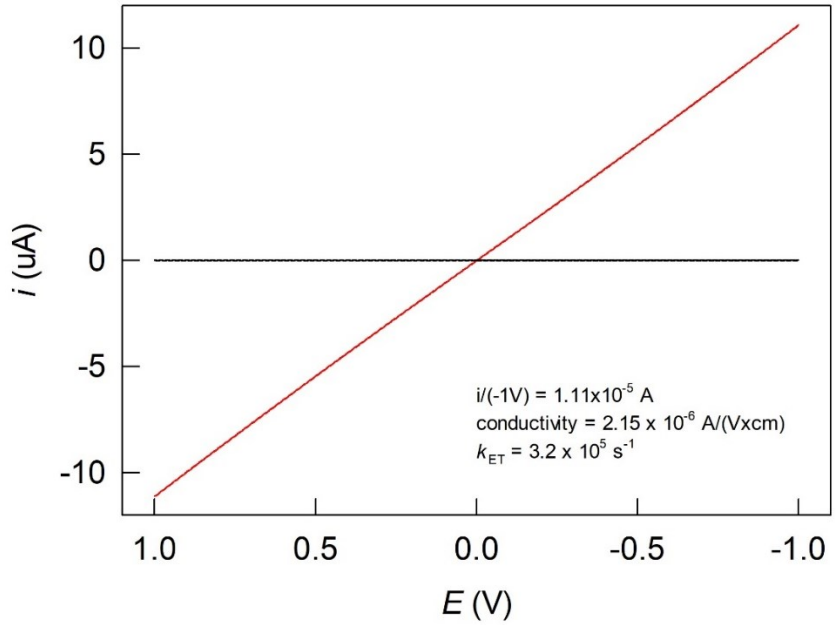

Figure 4 Plot of the current *i* obtained for the $Au_{25}(SC_4D_9)_{18}$ [0] samples as a function of the potential bias between the two comb gold electrodes.

The current response did not depend on *v*, which was varied from 0.1 to 40 V s^{-1} (*Figure S2*). After experiments, the MPC film could be easily removed from the IDA with DCM, yielding a solution exhibiting the same UV−vis absorption spectrum of the original MPC sample (*Figure S3*). Drop casting the same solution onto an IDA led to observe unchanged *i*−*E* behavior and conductivity, thereby confirming full stability of

the NCs. Figure 5 also shows the comparison between Au_{25}C4D and the same non-deuterated cluster.

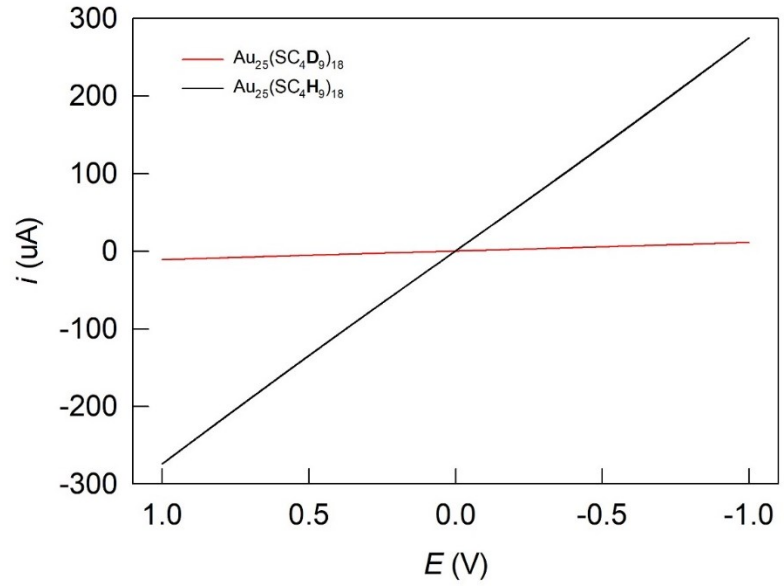

Figure 5 Plot of the current *i* obtained for the $Au_{25}(SC_4D_9)_{18}^0$ samples as a function of the potential bias between the two comb gold electrodes, compared with the non-deuterated cluster (black line).

From the above comparison, you can clearly see the drop in the conductivity current, which points to the very first, unexpected, but intriguing isotope effect on the deuterated system. It is important to emphasize again that the two clusters are identical, except for the replacement of the hydrogen atoms in the organic ligands with deuterium. While the Au_{25} core is, of course, the protagonist of the solid-state ET, these results once again demonstrate the importance of the organic shell in the ET process. To better evaluate the effect of deuterium, a series of conductivity parameters were calculated. The results are presented in *Table 2*, which also shows previous results about clusters with linear aliphatic ligands composing the monolayer. From the conductivity current, we obtained information about both the conductivity (σ) of the film and the ET rate constant (k_{ET}). Indeed, the behavior of the *i-E* plot can be directly related to the different conductivity of the film thanks to the following equation:

$$\sigma = \frac{l}{A_{tot}}\frac{i}{E} = C_{cell}\frac{i}{E} \quad \textbf{(1)}$$

Where *l* is the IDA interfinger length and A_{tot} is the total area of the electrode/film interface. The cell constant $C_{cell} = l/A_{tot}$ was calculated as described previously by Choi and Murray,[22] to be 0.194 cm^{-1}. The comparison of σ values and size parameters is gathered in Table 2.

Table 2 Electronic conductivity data, size parameters, concentrations in films, and ET rate constants.

	σ (Ω^{-1} cm^{-1})	r_{NC} (Å)	d_S (Å)	C_{film} (M)	k_{ET} (s^{-1})
C*3*[a]	2.3×10^{-4}	8.6	3.7	0.44	2.9×10^{7}
C*4*[a]	6.8×10^{-5}	9.4	4.5	0.33	9.2×10^{6}
C*5*[a]	1.9×10^{-5}	10.3	5.4	0.25	2.9×10^{6}
C*6*[a]	5.8×10^{-6}	11.0	6.1	0.21	9.2×10^{5}
C*7*[a]	1.2×10^{-6}	11.5	6.6	0.18	1.9×10^{5}
C*8*[a]	5.8×10^{-7}	12.1	7.2	0.16	1.0×10^{5}
C*10*[a]	7.8×10^{-8}	13.5	8.6	0.11	1.5×10^{4}
MeC*4*[a]	2.3×10^{-5}	10.4	5.5	0.25	3.5×10^{6}
C4D	2.2×10^{-6}	9.69	4.8	0.31	3.2×10^{5}

[a] Values from reference 22

We estimated the monolayer thickness from the diffusion coefficient (D), obtained from the CV peak currents at low scan rates, obtained in solution (Figure 3, Table 1). Measurement could take advantage of the knowledge of the electrode area and the NCs concentration, which was determined accurately also by taking advantage of the constancy of the molar extinction coefficient for these clusters (at 400 nm, ε = 5.5 × 10^4 M^{-1} cm^{-1}). The NC radius (r_{NC}) is calculated with the Stokes−Einstein equation $D = k_BT/6\pi\eta r_{MPC}$, where k_B is the Boltzmann constant and η is the viscosity of the solvent. We calculated a value of D of about $5.46 \times 10^{-10}\, m^2/s$. From the r_{NC} value, the corresponding Stokes monolayer thickness (d_S) is obtained by subtracting the distance between the outermost and the central Au atoms (r_{core}), 4.9 Å, and resulted of 4.8 Å. The conductivity depends on the effective edge-to-edge inter-core distance $2d_{eff}$ through the following equation:

$$\sigma = \sigma_0\left[\exp\left(-2d_{eff}\beta_{film,\sigma}\right)\right]\exp\left(-E_A/RT\right) \quad \textbf{(2)}$$

where E_A is the activation energy, R is the gas constant, T is the temperature, and σ_0 is the hypothetical conductivity for cluster cores at a constant distance and infinite T. In *eq. 2*, the effective distance $2d_{eff}$ indicates the actual thickness of two monolayers in the film. We assume $2d_{eff} = 2d_S$. To compare this result with the previous ones already reported, the conductivity results require transformation into ET rate-constant values, k_{ET} (s^{-1}), and thus an adjustment for the actual molar concentration of the cluster in the film C_{film} (M). We calculated this parameter as done before,[23] obtaining

a value of 0.31 M. With this, and again assuming a cubic-lattice model to describe the assembly of NCs in films, we calculated the corresponding first-order ET rate constant k_{ET} (s^{-1}) between neighboring clusters: (*eq 3*)

$$k_{ET} = \frac{6RT}{10^{-3}F^2\delta^2 C_{film}}\sigma \quad \textbf{(3)}$$

where δ (in cm) is the center-to-center separation between two NCs, taken as $2r_{NC}$. As we have extensively explained in our previous work,[23] and in Chapter 3 of this thesis, (i) the reaction is considered a first-order reaction; (ii) the ET process is so efficient because of the SOMO orbital that allows the clusters to either accept or donate one electron and (iii) the equations used are particularly valid because of the spherical shape of the investigated clusters. The k_{ET} of the completely deuterated cluster resulted to be $3.2 \times 10^{-5} s^{-1}$. It is now interesting not only to compare the deuterated and non-deuterated clusters, but also to check where the value of the deuterated one lies in the linear plot describing the dependence of k_{ET} as a function of twice the length d_S, again with the goal of better understanding the effect of the deuterium in the organization of the monolayer of the clusters, in the solid state. Figure 6 shows that the heterogeneous rate constant of the deuterated cluster deviates respects the trend line observed for the linear alkyl chains.

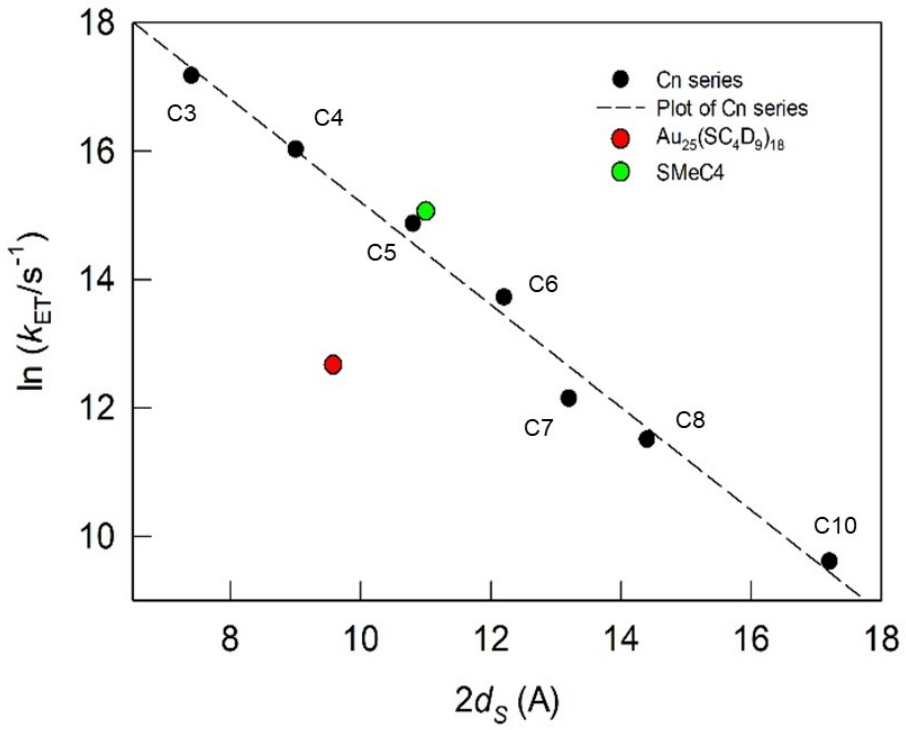

Figure 6 Dependence of the ET rate constant between Au_{25} MPCs inside the film (black circles; n values are indicated) as a function of $2d_s$ distance between cores, together with the result obtained for $Au_{25}(SMeC4)_{18}^0$ (green circle), and the new result obtained for $Au_{25}(SC_4D_9)_{18}^0$ (red circles).

These observations allow us to draw a series of conclusions: First of all, the isotope substitution has a huge effect on the solid-state ET properties of the nanoclusters. This phenomenon is not only related to changes in the ET parameters, but, most probably, involves dynamic effects of the monolayer when in the solid state (this idea will be explained better later). Furthermore, the conductivity drop, shown in Figure 5, and rationalized with the k_{ET} (Figure 6), reveals some difference in the organization of the organic monolayer or the clusters themselves, when are in the solid state.

In the literature, the isotope effect on the ET processes is typically discussed in terms of changes in ET parameters, such as the solvation time, vibrational frequencies, and the librational motion of the solvent molecules.[2,9,24,25] According to our knowledge, the ET rate constant is always reduced, but the reasons for this phenomenon are difficult to fully understand, and depends on the specific case study. However, the effect is always small, and usually authors call into question the involvement of hydrogen bonds between solvent molecules or solvent and the studied molecule. Of course, this could not be our case as we observed a significant isotope effect in the ET rate constant. For this reason, we considered that, when we investigated the solid-state ET, the major effect in the ET properties of the system was not due to changes in the ET parameters (that of course are present) but to the dynamic motion and compactness of the monolayer. In 2015, Merz et al. showed that isotope substitution can significantly affect the arrangement of molecules in the solid state.[8] Harbison first demonstrated and studied this phenomenon, showing that isotope substitution can even change the crystal structure of molecules.[26] This effect is called “isotopomeric polymorphism”.

This scenario is plausible to explain our results and is supported by the results of the electrocrystallization of Au_{25}C4D, which will be discussed in the next paragraph. Indeed, when in crystals, deuterated Au_{25} turns out to organize themselves into linear polymers with the formation of Au-Au inter-staples aurophylic bonds, just as non-deuterated one, but with some important differences. Unlike non-deuterated clusters, the polymer chains do not align parallel to each other but intersect. If we imagine that this is also true when the cluster is in film, it could affect the effective electron transfer process by creating preferential directions for the electron movement that are not parallel with each other. This could affect the cluster’s final conductivity. A more detailed description of the crystal structure will be provided later.

In conclusion, we believe that the huge effect on the electron transfer rate in the solid state is mostly due to the change in the organization/compactness of the monolayer

when it is in the solid state. The changes in the ET dynamic parameters have a negligible effect on the average final effect.

Once again, we have shown that the assumption that substituting hydrogen for deuterium does not perturb the system is not always valid.

5.3.3 Electrocrystallization and Single Crystal X-ray Crystallography of $Au_{25}(SC_4D_9)_{18}$: The Revelation of Different Solid-State Rearrangement

Our research group, in 2017, founds out that performing an electrooxidation of Au_{25}^- in MeCN, thus yields adsorbed Au_{25}^0. The oxidized nanocluster is then desorbed in the second oxidation peak (formation of the cation) or on the backward scan at potentials of the first peak (re-formation of the anion).[27] They demonstrated, by analysis of the CV behavior, that the oxidation product Au_{25}^0 does not leave the diffusion layer, while Au_{25}^- still diffuses toward the electrode, with the result of accumulating more clusters at the electrode surface. From these observations was born the idea of electrocrystallizing the nanoclusters directly on the electrode surface exploiting the change in the solubility of the two redox active species and performing a very soft and slow oxidation (macroelectrolysis) by applying a very low anode current. In this way they managed to create crystals of various $Au_{25}(SR)_{18}^0$ at very high yield. A figure of various Au_{25} crystals obtained by electrocrystallization strategy is shown here.

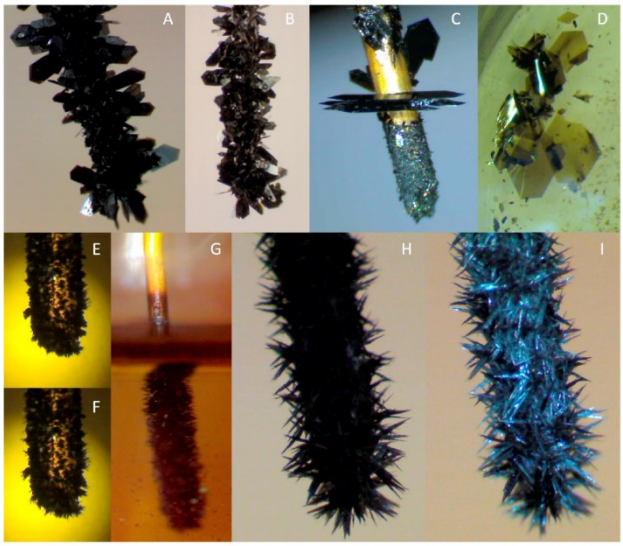

Figure 7 Crystals of various Au_{25} NCs covering the gold wire at the end of electrolysis, after extraction of the electrode from the electrochemical cell. In particular, (F,G,H, and I show needles-like crystals, typical for Au_{25} protected by butanethiols (C4) and pentanethiols (C5)).[27]

Taking advantage of the experience that the research group has accumulated regarding electrocrystallization processes, we used the same strategy to also obtain crystals of this new completely deuterated cluster with the aim of achieving information regarding its structure. Electrolysis was conducted on deoxygenated quiescent solutions of 0.03 mM (UV-vis absorption of 1.2 at 398 nm) $Au_{25}(SC_4D_9)_{18}^-$ in MeCN/0.1 M $TBAPF_6$, at room temperature. We used a two-electrode configuration in which the working electrode was a 16 mm long (8 mm immersed in solution), 0.75 mm-thick gold wire. We applied 30 nA (the first 10 days) and 50 nA (the next 7 days). To avoid the risk of causing oxidation of electrodeposited $Au_{25}(SR)_{18}^0$, which may occur because of the positive drift of the electrode potential toward the end of the controlled-current electrooxidation, we limited the extent of electrolysis to 65% of the $Au_{25}(SR)_{18}^-$ present in solution. Due to the amount of cluster employed, 4 mg, this implied electrolyzing the solutions for 17 days. Figure 8 shows that at the end of electrolysis, the crystals of deuterated NC grow on the electrode's surface.

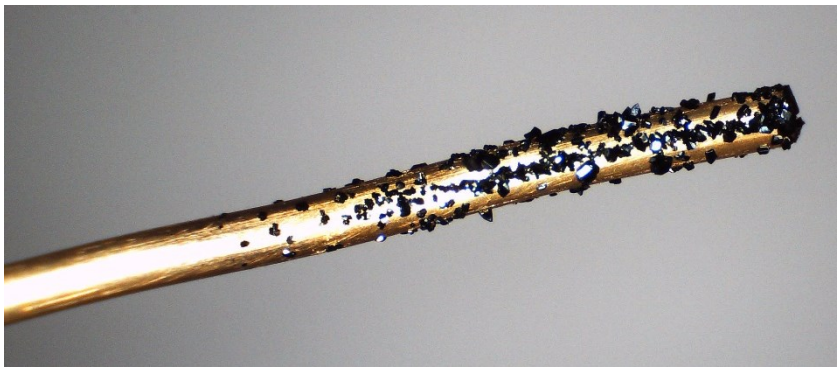

Figure 8 Crystals of completely deuterated nanocluster ($Au_{25}(SC_4D_9)_{18}$) covering the gold wire at the end of electrolysis (65% complete), after extraction of the electrode from the electrochemical cell.

As you can see from the photo (Figure 8), crystals of $Au_{25}(SC_4D_9)_{18}$ are not needle-like, but prismatic. The observation of needle-like crystals of the non-deuterated nanocluster was in keeping with finding that $Au_{25}C4$ crystallizes by forming a linear polymer of Au_{25} connected by Au−Au bonds.[12] Going more in depth: The X-Ray crystallographic analysis $Au_{25}(SC_4D_9)_{18}^0$ crystals revealed that this fully deuterated derivative is a new example of the striking polymeric structure (Figure 9A) previously documented in $Au_{25}(SC_4H_9)_{18}^0$ and $Au_{25}(SC_5H_{11})_{18}^0$. The $Au_{25}C4D$ asymmetric unit is made of two halves of two Au_{25} 'stellated' icosahedra, which are linked together by an inter-cluster Au-Au bond; the 1D chain propagates along the (1 0 0) lattice plane. However, despite what might be expected, the replacement of hydrogen for deuterium is not innocent, so the deuterated Au_{25} NC is not isostructural with the nondeuterated counterpart. A side-by-side alignment of the 1D chains of the two compounds (Figure

9B) reveals that only one NC maintains the same orientation in the two polymers, while the other one has inverted geometry and is characterized by slightly longer mean Au-Au distances in the icosahedron (among which a specially long one of 3.385 Å).

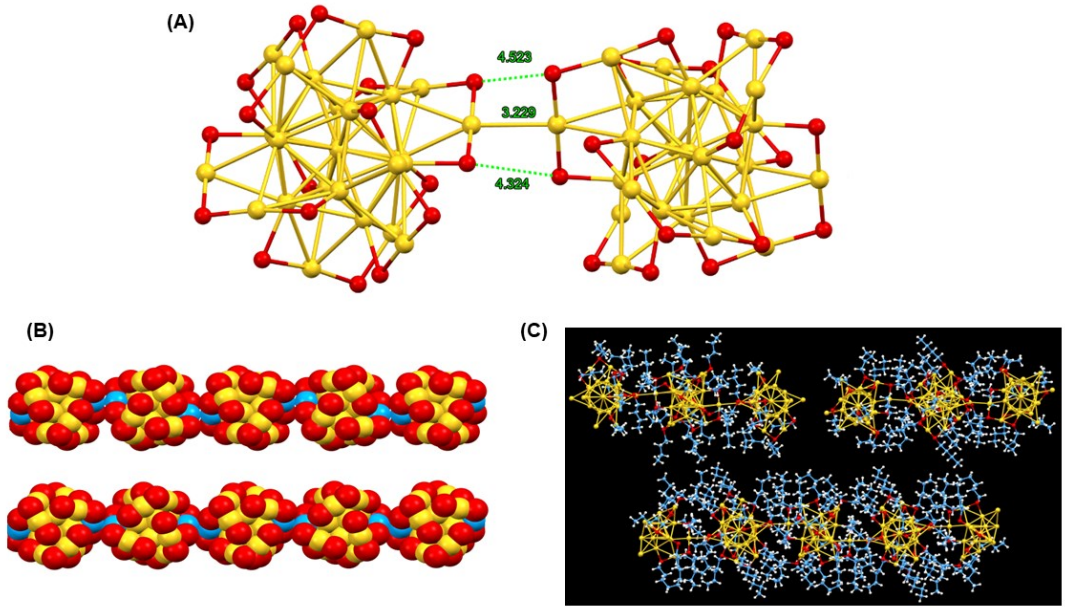

Figure 9 (A) The two distinct NCs in $Au_{25}(SC_4D_9)_{18}^0$, highlighting the intercluster Au-Au and S-S distances. (B) A side-by-side comparison of the CPK model of 1D polymeric chains of deuterated (top) and nondeuterated (bottom) Au_{25} NCs. (C) Interdigitation of the proximal alkyl side chains in $Au_{25}(SC_4D_9)_{18}^0$ (top, left), $Au_{25}(SC_4H_9)_{18}^0$ (top, right) and $Au_{25}(SC_5H_{11})_{18}^0$ (bottom). In (A) and (B) views, alkyl chains removed. Gold atoms in yellow, sulfur atoms in red, gold atoms in intercluster link (B) and carbon atoms (C) in cyan, H atoms in white.

In addition, crystals of deuterated NCs demonstrated a larger distance between two central icosahedral Au atoms, 13.017 Å. Unlike butanethiols (C4) and pentanethiols (C5) protected Au_{25}, both triclinic (*P*-1), Au_{25}C4D crystallizes in the monoclinic *C*2/*c* space group. Notably, the unit cell is four times and two times larger, respectively, than those of the C4 and C5 and the packing of the polymeric chains is markedly different. In $C4^0$ and $C5^0$ the adjacent polymeric chains run all parallel, but in C_4D^0 they describe a crisscross motif (*Figures S8*) in which neighboring rows have a limited chance to approach each other closely (shortest distance between two gold atoms in neighboring rows of 6.261 Å) and unoccupied voids remain in the unit cell. Accordingly, the alkyl side chains of adjacent rows have also a lesser opportunity to establish hydrophobic interactions to support inter-rows packing; this might also be a consequence of the different reciprocal positions assumed by the two distinct NCs in the polymeric chain. Also interesting, a visual examination of the positions assumed

by the alkyl side chains of Au_{25}C4D, C4 and C5 in the inter-cluster region (Figure 9C) shows that the interdigitation between the alkyl chains in Au_{25}C4D, is reduced if compared with C4 and C5. This evidence agrees with the results obtained about the ET in the solid state. Apparently, the replacement of deuterium for hydrogen hence introduces significant short-range modifications in the pattern of non-bonding interactions that reflect on a larger scale on the different packing of the polymeric 1D chains. A complete analysis of the crystals structure is provided in the “Supporting materials” section.

5.4 Conclusions

This work marks the first synthesis of a fully deuterated atomically precise nanocluster, $Au_{25}(SC_4D_9)_{18}$, prepared directly from deuterated butanethiol. Employing UV-Vis spectroscopy, MALDI-TOF mass spectrometry, and electrochemistry, we comprehensively characterized the novel nanocluster, and compared it with its nondeuterated counterpart, $Au_{25}(SC_4H_9)_{18}$. Our analysis revealed striking similarities in their solution behavior, as evidenced by comparable electrochemical signatures (CVs and DPVs). However, a closer examination of CVs revealed a smaller diffusion coefficient (D), consistent with a slightly larger hydrodynamic radius for the deuterated nanocluster. A more profound investigation into solid-state electron transfer (ET) between adjacent cores unveiled the most intriguing and unexpected findings. The conductivity current of fully deuterated Au_{25} films was observed to be significantly lower, accompanied by an ET rate constant (k_{ET}) nearly 30 times smaller than its nondeuterated counterpart. This discrepancy suggests a distinct solid-state arrangement, as ET efficiency is strongly influenced by the inter-core distance and monolayer configuration. To gain deeper insights into the solid-state arrangement, we successfully crystallized the novel fully deuterated nanocluster by electrocrystallization strategy. Crystallographic analysis revealed that the two nanoclusters exhibit distinct crystal structures. While the nondeuterated NC displays parallel polymer motifs (Au–Au bonds between adjacent nanoclusters), the deuterated counterpart (Au_{25}C4D) exhibits a crisscross motif, leading to a loss of directionality that could hinder solid-state ET. Furthermore, the fully deuterated nanocluster exhibits reduced interdigitation, diminished hydrophobic ligand interactions, and an increased inter-core distance compared to its nondeuterated counterpart. These factors collectively account for the significant difference in solid-state ET properties. These findings underscore the profound impact of ligands, in this case, deuterated ligands, on the physicochemical properties of atomically precise nanoclusters. These insights will undoubtedly inform future optimization and ligand design strategies for metal nanoclusters. Moreover, the availability of a fully deuterated Au nanocluster provides a unique platform for real-time kinetic studies of ligand exchange, which can be directly monitored via ^{1}H-NMR spectroscopy, as the deuterated ligands are spectrally silent. Importantly, thanks to this work we demonstrated that deuterated ligands are far from being innocent on the physicochemical properties of atomically precise metal nanoclusters. Moreover, the

innocence of isotope substitution is something that needs to be always demonstrated, not assumed.

5.5 Experimental

For the conductivity measurements we used Au interdigitated array (IDA) electrodes manufactured by ALS and consisting of a quartz plate supporting 65 interdigitated Au fingers (length = 2 mm, width = 10 μm, interfinger width = 5 μm, thickness = 0.96 nm). 5 μl of a concentrated DCM solution of the MPC (12 mg/0.12 mL) was drop cast and left to evaporate onto the IDA. The films were very carefully dried in vacuum for 30 min. The use of a highly concentrated solutions guarantees formation of a film much thicker than the height of the Au fingers and this allows to work under reproducible conditions. The cell constant $C_{cell} = l/A_{total}$ was calculated as first described by Choi and Murray,[7] and as we already did in previous works [1] that is, by using for l the IDA gap and for A_{total} the product of the maximum useful conductive MPC film thickness (1 μm)[7] and the finger length (2 mm) times $N - 1$, where N is the total number of fingers (130). Thus, $C_{cell} = 0.194$ cm^{-1}. The bias potential across the IDA fingers was controlled with a CHI 660c electrochemical workstation. The conductivity measurements were carried out at 25(1) °C by scanning the potential between +1 and -1 V, with an initial and final potential of 0 V, at scan rates in the range from 0.1 to 40 V s^{-1}. Since the comparison between the deuterated and no-deuterated clusters is very delicate, the measurements goodness was evaluated by double checking both the sample, taking advantage of the constancy of the molar emission coefficient of the cluster, and the IDA electrode, using our well-known Au_{25} non-deuterated cluster, taken as standard. To go into more detail, the UV-vis spectrum of the concentrated solution (12 mg/0.12 mL), diluting 10 uL of it in 3 mL of DCM has been analyzed before the conductivity measurement. Figure S2 shows a good agreement between the theoretical and the experimental absorption value at 401 nm. Then, studying the UV-vis absorption of the deposited film used, the amount and the purity of the deuterated cluster have been confirmed, once again. Figure S2 shows the high purity of the sample used and the good agreement between the amount of sample used and the theoretical one (the error is about 1%). Moreover, the IDA surface electrode was checked by analyzing before and after a sample of well-known Au_{25}. All these precautions allowed us to draw safe conclusions about the conductivity properties of the deuterated cluster revealing an intriguing isotopic effect affecting the solid-state electron transfer properties of the system.

The electrochemical experiments were carried out in DCM containing 0.1 M $TBAPF_6$, under an Ar atmosphere, in a glass cell thermostatted at 25 (±1) °C. A 0.22 mm radius glassy carbon disk was the working electrode, whereas a Pt wire was the counter

electrode. An Ag wire was used as the quasi-reference electrode. At the end of each experiment, the potential of the latter was calibrated against the ferricenium/ferrocene redox couple (in DCM/0.1 M $TBAPF_6$, E0 = 0.460 V against the KCl saturated calomel electrode, SCE). To minimize the ohmic drop between the working and the reference electrodes, careful feedback correction was applied. The DPV experiments were carried out under the same conditions. The experimental parameters were a peak amplitude of 50 mV, pulse width of 0.025 s, 4 mV increments per cycle, and pulse period of 0.05 s.

X-ray Crystallography: crystals of $Au_{25}(SC_4D_9)_{18}{}^0$ (for brevity, $C4D^0$) suitable for the X-ray work were grown by electrocrystallization strategy. The crystals obtained appeared as lustrous, metallic black prisms. An irregularly shaped fragment of one such prisms was chipped away, picked with a nylon loop and mounted on the goniometer head of an Oxford Diffraction Gemini diffractometer, equipped with a dual wavelength sealed–tube Enhance X–ray sources and a 2K × 2K EOS CCD area detector. Data collection was performed at 300(1) K, using graphite-monochromated Cu Kα radiation (λ = 1.54184 Å) in a 1024 × 1024 pixel mode and 2 × 2 pixel binning, through the ω–scans technique. The raw intensities were corrected for Lorentz and polarization effects; an empirical multi-scan absorption correction based on equivalent reflections was also applied by means of the scaling algorithm *SCALE3 ABSPACK*. Unit cell parameters were determined by the least-squares refinement of 37353 reflections selected during the entire data collection. Data collection, reduction and finalization were performed with the CrysAlis Pro software suit. The structure was solved by intrinsic phasing methods into the centrosymmetric *C*2/*c* space group with the SHELXT program and refined by full-matrix least-squares methods based on F_o^2 with SHELXL software, embedded into the OLEX2 program. The crystal was weakly diffracting and the final dataset is not optimal (R_{int}=0.1237). The atoms of the *n*-butylthiolate chains were located from the difference Fourier map and modeled with bond lengths restrained to 1.53 Å (esd of 0.02), except for the pivot C atoms. Additional geometric and ADP restraints (DANG, DFIX, SADI, SIMU and RIGU) were also imposed to give a chemically reasonable model. Even so, one half of the *n*-butyl chains show significant thermal motions; however, attempts to split the involved centers did not yield any better model. Three butyl chains (involved atoms: C36, C46-C47, C58-C59) are also orientationally disordered and were split into two parts, with occupancies constrained to sum to 1.0 (refined occupancies 0.57:0.43; 0.79:0.21; 0.60:0.40 for C36; C46-C47; C58-C59, respectively). Anisotropic refinement for C17 atom proved unfeasible, so only isotropic refinement was accomplished; all remaining

non-hydrogen atoms were refined anisotropically. The side chain motions also hampered the calculation of idealized positions for the deuterium atoms bound to terminal C32, C48, C60 and C72, which accordingly have not been introduced in the final model. The other deuterium atoms were placed in idealized positions and refined as riding model, with isotropic thermal factors equal to 1.2 or 1.5 (for the terminal methyl groups) times the value of the U_{eq} of the parent C atom.

The presented X-ray experimental measurement and data analyzes were performed by Prof. Alessandro Dolmella, of Department of Pharmaceutical and Pharmacological Sciences, University of Padova (PD), whom I would like to thank.

5.6 Supporting Materials

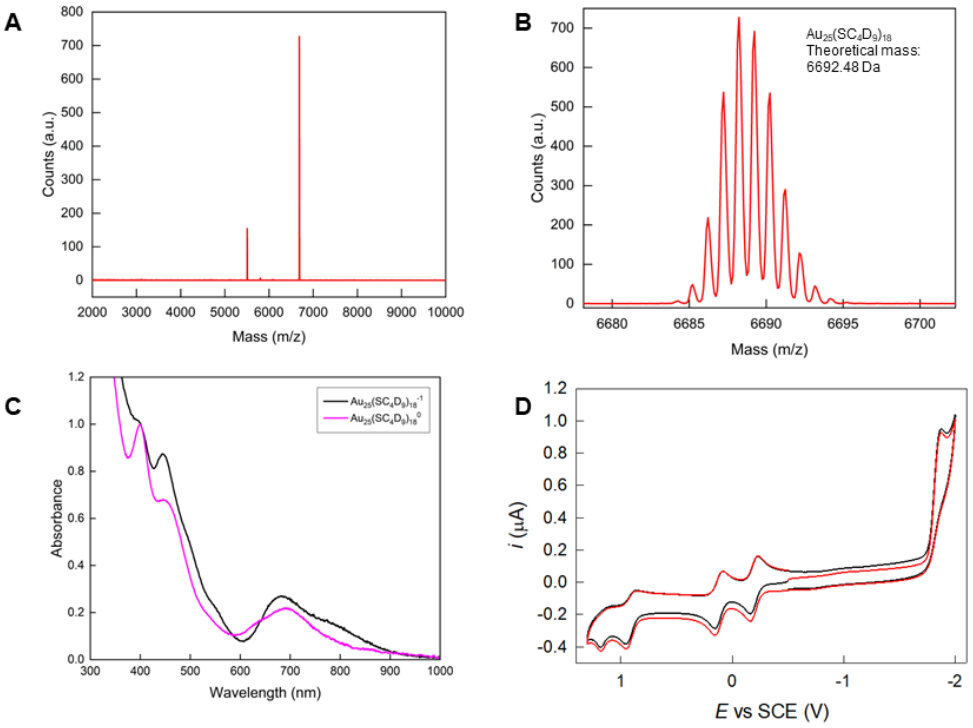

Figure S1 Characterizations of the completely deuterated Au_{25} NC. **A)** Negative mode MALDI-TOF spectrum and **(B)** the magnification of the dominant peak, referred to $Au_{25}(SC_4D_9)_{18}$, with isotopic pattern resolution. **C)** UV-Vis spectra of the same cluster at his -1 and 0 charge state. **D)** CV curves (positive and negative potentials direction), obtained in DCM/0.1 M $TBAPF_6$.

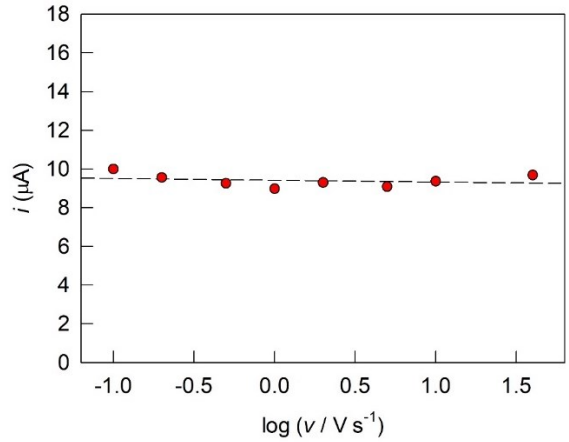

Figure S2 Plot of the current measured with a potential bias of 1 V (between the IDA combs) as a function of the logarithm of the potential scan rate. The dashed line marks the average value.

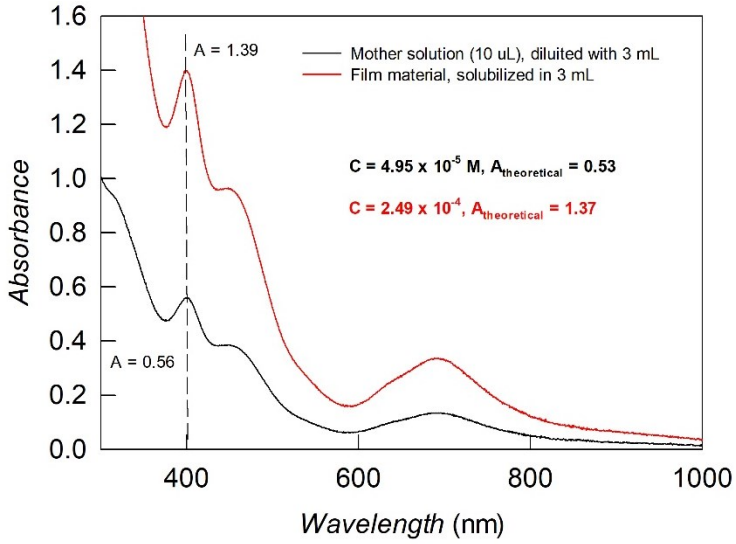

Figure S3. UV-Vis spectra of the sample used for the solid-state ET measurements, before and after the test. This result points to a very pure compound and confirms the stability of the cluster after the ET measurements.

X-ray Crystallography:

Crystals of $Au_{25}(SC_4D_9)_{18}{}^0$ (for brevity, C_4D^0) suitable for the X-ray work were grown by electrocrystallization strategy. The crystals obtained appeared as lustrous, metallic black prisms The crystallographic analysis revealed that this fully deuterated derivative is a new example of the striking polymeric structure previously documented in $Au_{25}(SBu)_{18}{}^0$ ($C4^0$) and $Au_{25}(SC_5H_{11})_{18}{}^0$ ($C5^0$).[15] The C_4D^0 asymmetric unit is made of two halves of two Au_{25} 'stellated' icosahedra (NC1 and NC2), which are linked together by an intercluster Au-Au bond; the 1D chain propagates along the (1 0 0) lattice plane. By looking at the gold atoms connectivity, the two clusters are not exactly alike, a situation resembling that of $C4^0$. However, despite what might be expected,

the replacement of hydrogen for deuterium is not innocent, so C4D^0 is not isostructural with C4^0. A side-by-side alignment of the 1D chains of the two compounds (Figure 9) reveals that only one NC maintains the same orientation in the two polymers, while the other one has inverted geometry and is characterized by slightly longer mean Au-Au distances in the icosahedron (among which a specially long one of 3.385 Å). The comparison between the 1D polymeric chain of C4D^0 with those of previously reported Au_{25} polymeric compounds shows that the distance between two central icosahedral Au atoms, 13.017 Å, is longer than in C4^0 (13.001 Å) and in C5^0, (showing the shortest contacts in polymeric compounds, 12.475/12.591 Å). Likewise, the intercluster Au-Au bond (Figure 9 and S4), 3.229 Å, is also longer (C4^0: 3.152 Å; C5^0: 2.978/3.028 Å), and the same apply to the S---S contacts among the sulfur atoms of the two closest S(R)-Au-S(R)-Au-S(R) 'staples' between neighboring NC (Figure 9 and S5). C_4D^0, C4^0 and C5^0 all have in common the up-down-up or up-up-down orientation of the alkyl side chains with respect to the S(R)-Au-S(R)-Au-S(R) mean plane, allowing the approach of the NCs close enough to trigger the 'twist-and-lock' mechanism[12] leading to polymerization. This is witnessed by an approximately orthogonal (torsional angle of 101.6/93.6°) mutual disposition of the Au-Au bonded staples (C4^0: 83.26/82.88°; Figure S6) as well as by the nearly co-linear disposition of the S-Au-S atoms of the two nearby staples (177.4 and 174.2°). Unlike C4^0 and C5^0, both triclinic (*P*-1), C_4D^0 crystallizes in the monoclinic *C*2/*c* space group. Notably, the unit cell is four times and two times larger, respectively, than those of the C4^0 and C5^0 and the packing of the polymeric chains is markedly different. In C4^0 and C5^0 the adjacent polymeric chains run all parallel, but in C_4D^0 they describe a crisscross motif in which neighboring rows have a limited chance to approach each other closely (shortest distance between two gold atoms in neighboring rows of 6.261 Å) and unoccupied voids remain in the unit cell. Accordingly, the alkyl side chains of adjacent rows have also a lesser opportunity to establish hydrophobic interactions to support inter-rows packing; this might also be a consequence of the different reciprocal positions assumed by the two distinct NCs in the polymeric chain. Also interesting, a visual examination of the positions assumed by the alkyl side chains of C_4D^0, C4^0 and C5^0 in the intercluster region (Figure 9) shows that the interdigitation between the alkyl chains in C_4D^0, is reduced if compared with C4^0 and C5^0. An investigation of nonbonding interactions in the intercluster space of C_4D^0, C4^0 using the *Mercury* software likewise shows that short interatomic contacts and non-canonical C-H---S hydrogen bonds are more represented in C4^0 than in C_4D^0 (Figure 9, S7 and S7 bis). Apparently, the replacement of deuterium for hydrogen hence introduces short-range significant modifications in the pattern of non-

bonding interactions that reflect on a larger scale on the different packing of the polymeric 1D chains.

A summary of crystal data and structure refinement compared with those of other known 1D polymers is given in Table S1. An examination of the mean distances in the two adjacent NCs compared with those found for $[Au_{25}(SBu)_{18}^0]_n$ is given in Table S2.

Table S1. Comparison of essential crystallographic data of 1D cluster-based polymers.

Compound	$[Au_{25}(SC_4)_{18}^0]_n$	$[Au_{25}(SC_5)_{18}^0]_n$	**$[Au_{25}(SC_4D_9)_{18}^0]_n$**
Reference	ACS Nano **2014**, *8*, 8505- 8512	JACS **2017**, *139*, 4168-4174	This work
CCDC number	998586	1519225	***XXXXXX***
Structural feature	Cluster-Based polymer	Cluster-Based polymer	Cluster-Based polymer
Space Group	*P*-1	*P*-1	*C*2/*c*
a, *b*, *c* (Å)	6.1305(5) 17.9824(5) 22.1697(7)	16.9880(2) 24.4379(3) 35.2401(4)	49.1438(4) 17.20520(10) 28.5730(2)
α, β, γ (°)	92.101(2) 106.955(3) 106.132(3)	69.9940(10) 80.9890(10) 88.7660(10)	90.0 93.6120(10) 90.0
Volume (Å^3)	5860.3(3)	13569.4(3)	24111.3(3)

Table S2. Mean Au-Au and Au-S bond lengths (Å) of NC1 and NC2 units of polymeric $[Au_{25}(SC_4D_9)_{18}^0]_n$ (on the left) in comparison with similar values for $[Au_{25}(SBu)_{18}^0]_n$ (on the right).

Compound	**$[Au_{25}(SC_4D_9)_{18}^0]_n$**		**$[Au_{25}(SBu)_{18}^0]_n$**	
	NC1	NC2	NC1	NC2
Au_c - Au_i (i)	2.79	2.79	2.78	2.79
Au_i - Au_i (ii)	2.98	2.97	2.95	2.97
Au_{is} - Au_{is} (iii)	2.79	2.80	2.78	2.77
Au_{st} - Au_i (iv)	3.19	3.18	3.17	3.18
Au_i - S (v)	2.38	2.37	2.38	2.37
Au_{st} - S (vi)	2.31	2.30	2.30	2.30

Legend: (i) Bonds of central Au atom towards the 12 Au atoms of the icosahedron. (ii) Bonds between icosahedral Au atoms not directly located under the staples. (iii) Bonds between the six icosahedral Au-Au pairs located just below the staples. (iv) Distance between 'stellated' Au atoms and the three icosahedron Au atoms located below it. (v) Au-S bonds involving icosahedral Au atoms. (vi) Au-S bonds involving 'stellated' gold and sulfur atoms.

As underlined from the previous table, the two adjacent independent clusters have small differences with respect to each other and resemble the corresponding units of the $[Au_{25}(SBu)_{18}^0]_n$ polymer, also with respect of the situation of the aurophilic

interactions made by the gold atoms in the staples with the Au atoms of the inner Au_{13} core. In particular, in NC1: a) in one pair of staples, one Au atom bonds to two icosahedron Au atoms and the other one bonds to only one; b) in the second pair, both staple Au atoms bond to two icosahedron Au atoms; c) in the third pair, one bonds to two and the other one to three icosahedron Au atoms. In NC2 we find the same situation seen in NC1 of $[Au_{25}(SBu)_{18}^0]_n$ that is: a) in one pair of staples, both Au atoms bond to two icosahedron Au atoms; b) both Au atoms bond to three icosahedron Au atoms; c) one Au atom bonds to two and the other one to three icosahedron Au atoms.

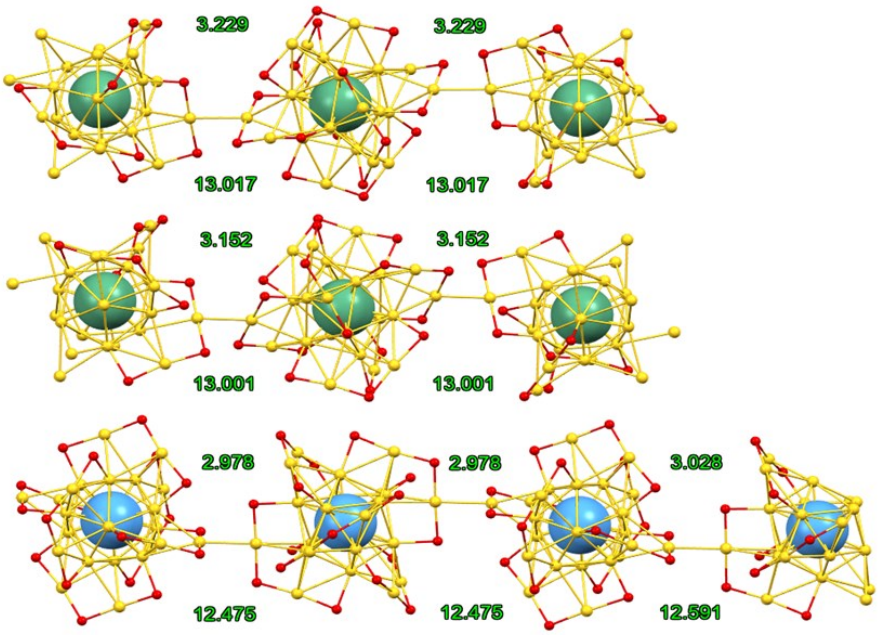

Figure S4 A comparison of Au-Au intercluster bond length (above the chain) and of the distance between the central icosahedral atoms (below the chain) of two adjacent NCs in $C4D^0$ (top), $C4^0$ (middle) and $C5^0$ (bottom). Alkyl chains removed; central icosahedral gold atom drawn as green ($C4D^0$ and $C4^0$c) or cyan ($C5^0$) cpk model.

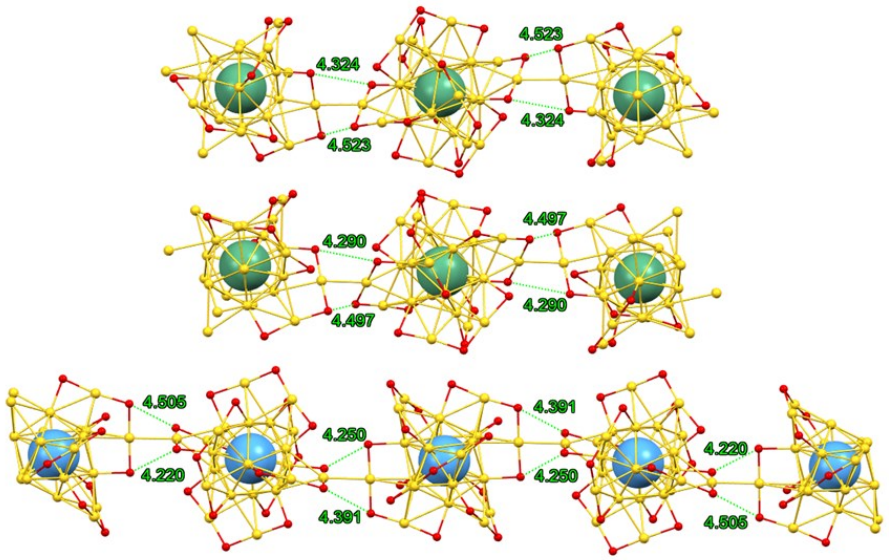

Figure S5 A comparison of S-S distances between two nearby staples at the intercluster junction in $C4D^0$ (top), $C4^0$ (middle) and $C5^0$ (bottom). Alkyl chains removed.

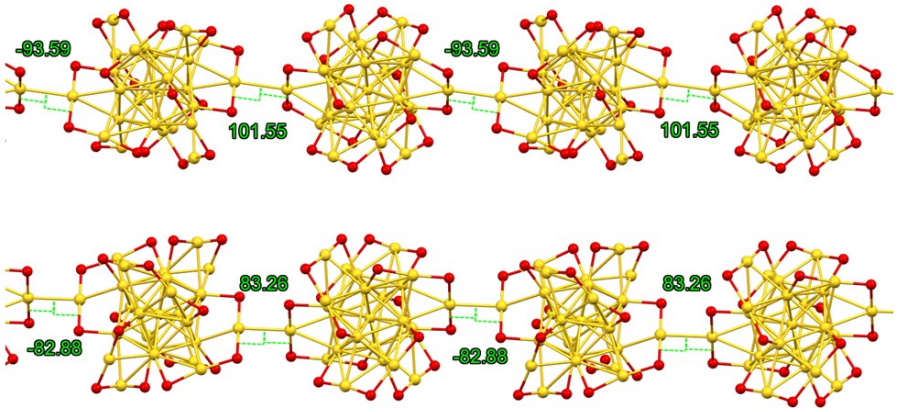

Figure S6 The torsional angles made by the two closest staples between neighboring clusters in $C4D^0$ (top) and $C4^0$ (bottom). Alkyl chains removed.

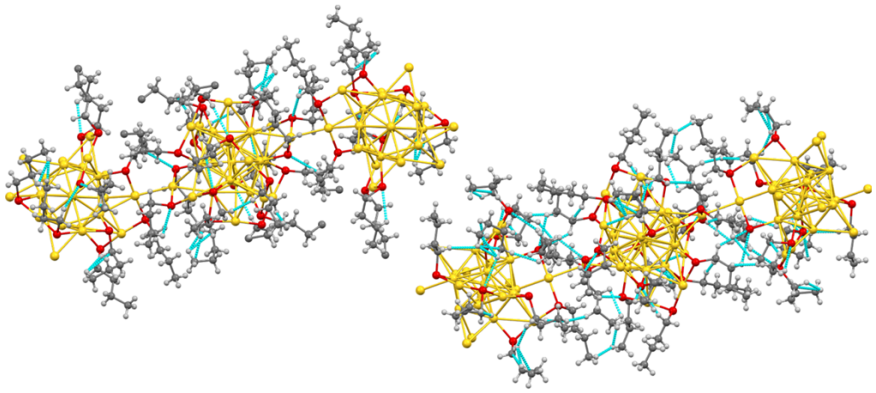

Figure S7 A view of intercluster nonbonding interactions (in cyan), including non-canonical C-H---S hydrogen bonds, in $C4D^0$ (top) and $C4^0$ (bottom).

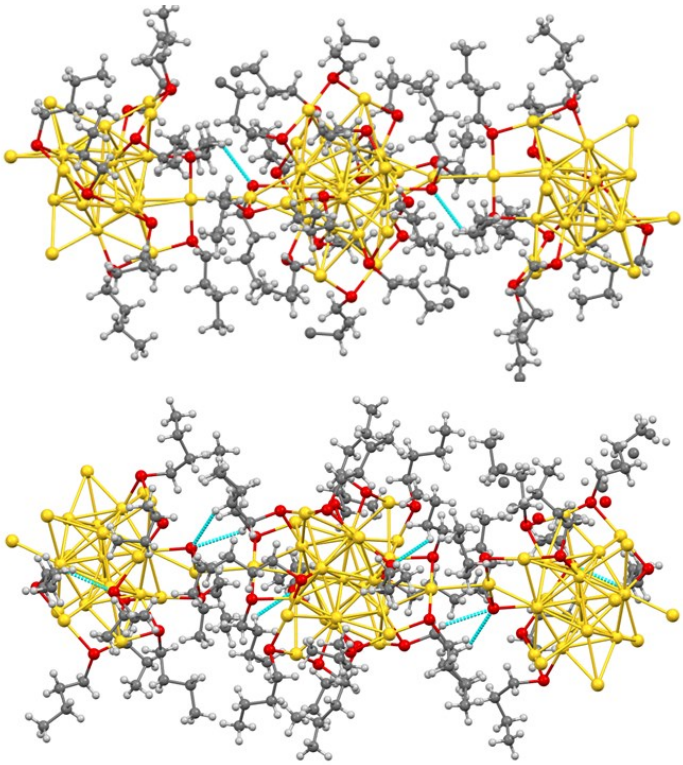

Figure S7bis A view of intercluster non-canonical C-H---S hydrogen bonds (in cyan) in $C4D^0$ (top) and $C4^0$ (bottom). Admitted contacts only if distance between H and S atoms equals the sum of vdW radia + 0,1 angstroms.

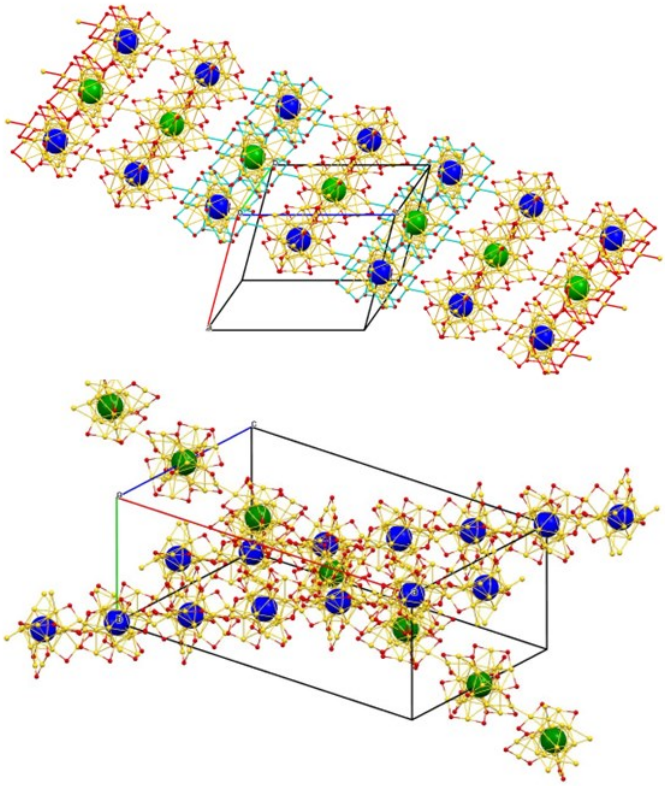

Figure S8 Packing of the polymeric chains. In $C4^0$ (top) the adjacent polymeric chains run all parallel, while in C_4D^0 (bottom) they describe a crisscross motif. Alkyl chains removed.

Figures S9 to S11 depict the crystal packing of $[Au_{25}(SC_4D_9)_{18}{}^0]_n$ along the unit cell *a, b, c* axes.

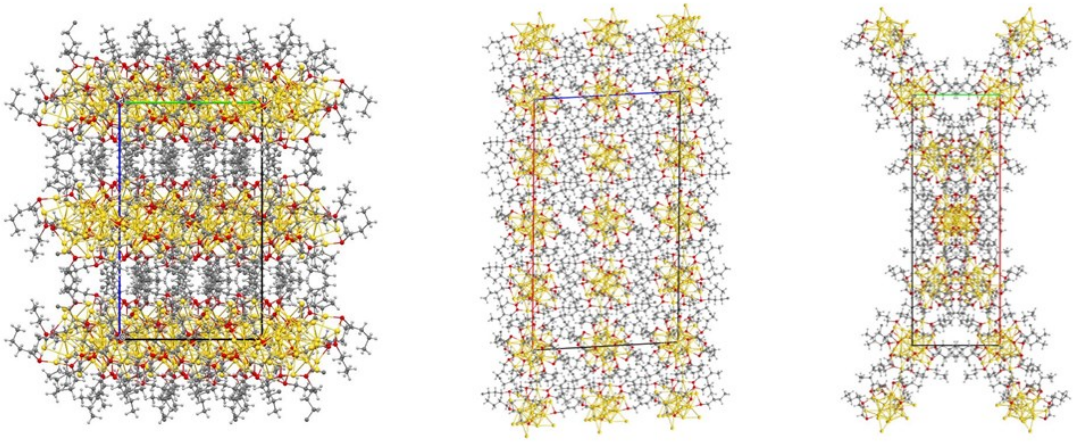

Figure S9 View of crystal packing down the crystallographic a, b and, c axis (from left to right)

5.7 References

1. Lynch, R. A.; Vincenti, S. P.; Lin, Y. T.; Smucker, L. D.; Subba Rao, S. C. Anomalous Kinetic Hydrogen Isotope Effects on the Rat of Ionization of Some Dialkyl Substituted Ketones. *J. Am. Chem. Soc.* **1972**, *94* (24), 8351–8356.
2. Sasmal, D. K.; Dey, S.; Das, D. K.; Bhattacharyya, K. Deuterium Isotope Effect on Femtosecond Solvation Dynamics in Methyl β-Cyclodextrins. *J. Chem. Phys.* **2009**, *131* (4),
3. Wiberg, K. B.; Slaugh, L. H. The Deuterium Isotope Effect in the Side Chain Halogenation of Toluene. *J. Am. Chem. Soc.* **1958**, *80* (12), 3033–3039.
4. Zi, W.; Wang, Y.-M.; Toste, F. D. An *In Situ* Directing Group Strategy for Chiral Anion Phase-Transfer Fluorination of Allylic Alcohols. *J. Am. Chem. Soc.* **2014**, *136* (37), 12864–12867.
5. Amdursky, N.; Pecht, I.; Sheves, M.; Cahen, D. Marked changes in electron transport through the blue copper protein azurin in the solid state upon deuteration. *Biophysics and computational biology* **2013**, 110(2), 507-512
6. Cerretani, C.; Palm-Henriksen, G.; Liisberg, M. B.; Vosch, T. The Effect of Deuterium on the Photophysical Properties of DNA-Stabilized Silver Nanoclusters. *Chem. Sci.* **2021**, *12* (48), 16100–16105.
7. Dresner, J.; Prochorow, J.; Sobolewski, A. Deuterium Isotope Effect on Charge-Transfer Fluorescence. *Chem. Phys. Lett.* **1978**, *54* (2), 292–294.
8. Merz, K.; Kupka, A. Deuterium Perturbs the Molecular Arrangement in the Solid State. *Cryst. Growth Des.* **2015**, *15* (4), 1553–1558.
9. Pal, H.; Nagasawa, Y.; Tominaga, K.; Yoshihara, K. Deuterium Isotope Effect on Ultrafast Intermolecular Electron Transfer. *J. Phys. Chem.* **1996**, *100* (29), 11964–11974.
10. Shirota, H.; Pal, H.; Tominaga, K.; Yoshihara, K. Substituent Effect and Deuterium Isotope Effect of Ultrafast Intermolecular Electron Transfer: Coumarin in Electron-Donating Solvent. *J. Phys. Chem. A* **1998**, *102* (18), 3089–3102.
11. Felder, T.; Schalley, C. Secondary Isotope Effects on the Deslipping Reaction of Rotaxanes: High-Precision Measurement of Steric Size. *Angew. Chem. Int. Ed.* **2003,** 42, 2258-2260.
12. De Nardi, M.; Antonello, S.; Jiang, D.; Pan, F.; Rissanen, K.; Ruzzi, M.; Venzo, A.; Zoleo, A.; Maran, F. Gold Nanowired: A Linear $(Au_{25})_n$ Polymer from Au_{25} Molecular Clusters. *ACS Nano* **2014**, *8* (8), 8505–8512.
13. Antonello, S.; Maran, F. Molecular Electrochemistry of Monolayer-Protected Clusters. *Curr. Opin. Electrochem.* **2017**, *2* (1), 18–25.

14. Agrachev, M.; Fei, W.; Antonello, S.; Bonacchi, S.; Dainese, T.; Zoleo, A.; Ruzzi, M.; Maran, F. Understanding and Controlling the Efficiency of $Au_{24}M(SR)_{18}$ Nanoclusters as Singlet-Oxygen Photosensitizers. *Chem. Sci.* **2020**, *11* (13), 3427–3440.

15. Pigliacelli, C.; Acocella, A.; Díez, I.; Moretti, L.; Dichiarante, V.; Demitri, N.; Jiang, H.; Maiuri, M.; Ras, R. H. A.; Bombelli, F. B.; Cerullo, G.; Zerbetto, F.; Metrangolo, P.; Terraneo, G. High-Resolution Crystal Structure of a 20 kDa Superfluorinated Gold Nanocluster. *Nat. Commun.* **2022**, *13* (1), 2607.

16. Zuman. P. Plenum Press, New York **1967**.

17. Ibañez, F. J.; Zamborini, F. P. Chemiresistive Sensing with Chemically Modified Metal and Alloy Nanoparticles. *Small* **2012**, *8* (2), 174–202.

18. Terrill, R. H.; Postlethwaite, T. A.; Chen, C.; Poon, C.-D.; Terzis, A.; Chen, A.; Hutchison, J. E.; Clark, M. R.; Wignall, G. Monolayers in Three Dimensions: NMR, SAXS, Thermal, and Electron Hopping Studies of Alkanethiol Stabilized Gold Clusters. *J. Am. Chem. Soc.* **1995**, *117* (50), 12537–12548.

19. Wuelfing, W. P.; Green, S. J.; Pietron, J. J.; Cliffel, D. E.; Murray, R. W. Electronic Conductivity of Solid-State, Mixed-Valent, Monolayer-Protected Au Clusters. *J. Am. Chem. Soc.* **2000**, *122* (46), 11465–11472.

20. Zamborini, F. P.; Leopold, M. C.; Hicks, J. F.; Kulesza, P. J.; Malik, M. A.; Murray, R. W. Electron Hopping Conductivity and Vapor Sensing Properties of Flexible Network Polymer Films of Metal Nanoparticles. *J. Am. Chem. Soc.* **2002**, *124* (30), 8958–8964.

21. Carducci, T. M.; Murray, R. W. Kinetics and Low Temperature Studies of Electron Transfers in Films of Small (<2 Nm) Au Monolayer Protected Clusters. *J. Am. Chem. Soc.* **2013**, *135* (30),

22. Choi, J.-P.; Murray, R. W. Electron Self-Exchange between $Au_{140}^{+/0}$ Nanoparticles Is Faster Than That between $Au_{38}^{+/0}$ in Solid-State, Mixed-Valent Films. *J. Am. Chem. Soc.* **2006**, *128* (32), 10496–10502.

23. Reato, M.; Dainese, T.; Antonello, S.; Maran, F. Electron Transfer in Films of Atomically Precise Gold Nanoclusters. *Chem. Mater.* **2021**, *33* (11), 4177–4187.

24. Schwartz, B. J.; Rossky, P. J. The Isotope Effect in Solvation Dynamics and Nonadiabatic Relaxation: A Quantum Simulation Study of the Photoexcited Solvated Electron in D2O. *J. Chem. Phys.* **1996**, *105* (16), 6997–7010.

25. Reid, P. J.; Barbara, P. F. Dynamic Solvent Effect on Betaine-30 Electron-Transfer Kinetics in Alcohols. *J. Phys. Chem.* **1995**, *99* (11), 3554–3565.

26. Zhou, J.; Kye, Y.-S.; Harbison, G. S. Isotopomeric Polymorphism. *J. Am. Chem. Soc.* **2004**, *126* (27), 8392–8393.

27. Antonello, S.; Dainese, T.; Pan, F.; Rissanen, K.; Maran, F. Electrocrystallization of Monolayer-Protected Gold Clusters: Opening the Door

to Quality, Quantity, and New Structures. *J. Am. Chem. Soc.* **2017**, *139* (11), 4168–4174.

6. Design and Synthesis of Novel Atomically Precise Nanoclusters Through Ligand Exchange Reaction

6.1 Abstract

Functionalizing the monolayer surrounding the core of atomically precise gold nanoclusters (NCs) is a powerful approach to create new nanosystems with customized electronic, electrochemical, optical, and magnetic properties for a wide range of applications. Ligand exchange reactions (LER) provide a versatile and efficient way to modify the properties of Au NCs, opening new possibilities for their applications. In this Chapter, we investigated the use of LERs to achieve two specific goals: (i) the synthesis of monofunctionalized Au_{25} nanoclusters with tailored properties and (ii) the full pegylation of Au_{144} nanoclusters for water solubility and biocompatibility. Concerning topic (i), we were successful in synthesizing monofunctionalized Au_{25} both with a carboxylic acid ending group and an amine ending group. These monofunctionalized NCs were purified and characterized, revealing slight but interesting variations in their physicochemical properties with respect to the pristine unsubstituted NC. Eventually, these units have also been used to produce dimers and other superstructures of Au_{25}. For topic (ii), we could almost completely pegylate an Au_{144} NC, thanks to a novel “step by step” LER, resulting in water-soluble and biocompatible nanoclusters. Our results demonstrate that LERs are a versatile and efficient platform for the modification and functionalization of Au NCs. This opens new possibilities for developing Au NCs-based systems with tailored properties for a wide range of applications.

6.2 Introduction

The chemical modification of nanoparticle and nanocluster surfaces is essential for their assembly,[1–5] their application in biology and medicine,[6–14] and tuning of their physical (for example, solubility), optical and electronic properties.[15–23] The LER is certainly the key method for modifying the surfaces of NCs. These reactions primarily entail the stoichiometric substitution of ligands that decorate the surface, that is the NC's organic monolayer, with ligands freely dissolved in the surrounding medium.[24–28] Essentially, LERs offer a dynamic avenue for replacing the incoming ligands, termed "endogenous", with new ligands, named "exogenous" (Figure 1). This transition holds the potential to engender profound alterations in the properties of the NCs, which comprises their solubility in aqueous environments, reactivity towards other molecular species, and their interaction with incident light, all of which accentuate the versatility and applicability of these nanoscale materials.

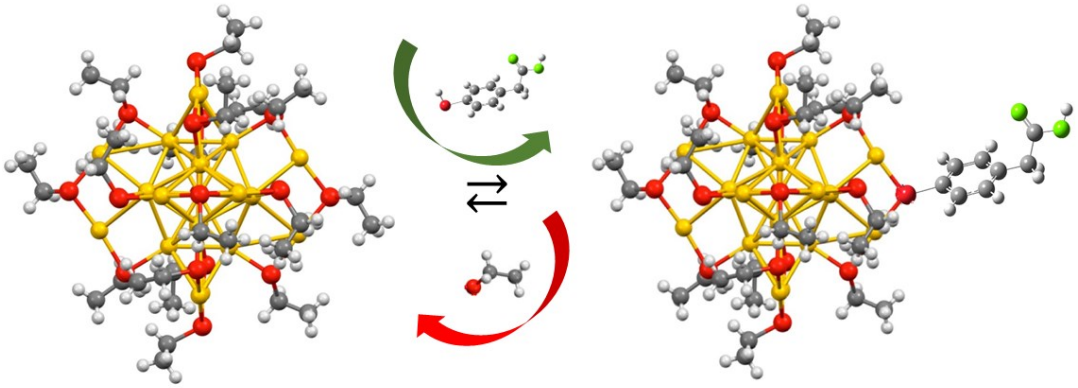

Figure 1 Example of Ligand exchange reaction in which the HSC_2H_5 ligand (endogenous) is replaced by an $HSPhCH_2COOH$ ligand (exogenous).

For decades, researchers have focused their scientific attention on the metal cores of NCs because the core largely determines their chemical and physical properties. After all, the core contains most of the frontier orbitals, and even a small change, such as doping with a single heteroatom, can cause significant differences in the properties of the NC itself.[15,19,20,29–32] In recent years, however, there has been a growing awareness of the importance of the ligands that surround the core. Ligands were once thought to have a relatively minor impact on the properties of NCs, but this is not the case. Indeed, in the previous chapters, we have shown how a simple change in the length of the ligands can have a significant impact on the conductivity and electron transfer (ET) properties (Chapters 3 and 4). Another important example is the use of deuterated ligands: as shown in Chapter 5, deuteration of the ligands can

have a profound effect on the properties of NCs, including in the solid state, as demonstrated by X-ray crystallography. For this reason, having the possibility of substituting some ligands with exogenous ones represents a powerful tool for controlling the properties of Au NCs. Moreover, LERs are relatively simple to carry out, making them a popular choice for researchers working on this topic. Here are some important examples of how LERs can be used: (i) Implementation in biology and medicine: The surface of the NC can be modified, for example, to bind cancer cells or to deliver drugs to specific parts of the body;[6,8,11,13,14,33] (ii) tuning of electronic and optical properties for developing new types of devices, such as light-emitting diodes and solar cells;[34,35] and (iii) assembly: LERs can be used to assemble nanoclusters into larger structures. Indeed, the different dimension, hindrance and chemical nature of ligands can favor the transformation of the NC's core[36–40] and the interaction with each other in diverse ways, leading, eventually, to the formation of larger superstructures.[41–44] Careful selection of ligands can thus direct NCs assembly.

Going more in depth on the last two topics, significant research has been conducted on the possibility of tuning the physicochemical properties of Au NCs by acting on the ligands. For example, there is a wealth of literature on the enhancement of photophysical properties of Au NCs functionalized with chromophore or porphyrin ligands.[33,41,45–47] However, to our knowledge, there is a scarcity of research on the effect of the monofunctionalization. This is due to the complexity of both controlling the degree of ligand exchange and purifying and separating the products with different functionalization degrees. Along with this, there has also been a great increase in interest in trying to use NCs as units to produce dimers, multimers, or larger superstructures. Within this topic, very recently, numerous studies have been published regarding the application of supramolecular chemistry to the ligands of the clusters with the goal of creating new complex and reversible systems,[46,48,49] but a small amount of work is available on the attempt to truly control the assembly of Au NCs into larger nanostructures while understanding the atomic-level structure of the newly synthesized chemical species. Hakkinen and co. in 2016 published a work in which they were able to covalently connect both Au_{102} and Au_{250}, thanks to a dithiol ligand used as a molecular bridge (Figure 2).[42] Unlike the dimers that lacked optical coupling, the multimers displayed hybridized plasmon modes with surprisingly large red-shifts, likely attributed to electron tunneling through the molecular states of the disulfide bridge. After that, some papers were published about trying to produce well-defined systems composed of Au NCs, using a bottom-up approach, with quite a few problems in the resulting products.[41,43,44] The primary challenge lies in preventing the

formation of oligomers. With each LERs, multiple reactions occurring on the same nanocluster are unavoidable, leading to poly-substitutions and the subsequent growth of unwanted superstructures (oligomers of Au NCs, as illustrated in Figure 2).

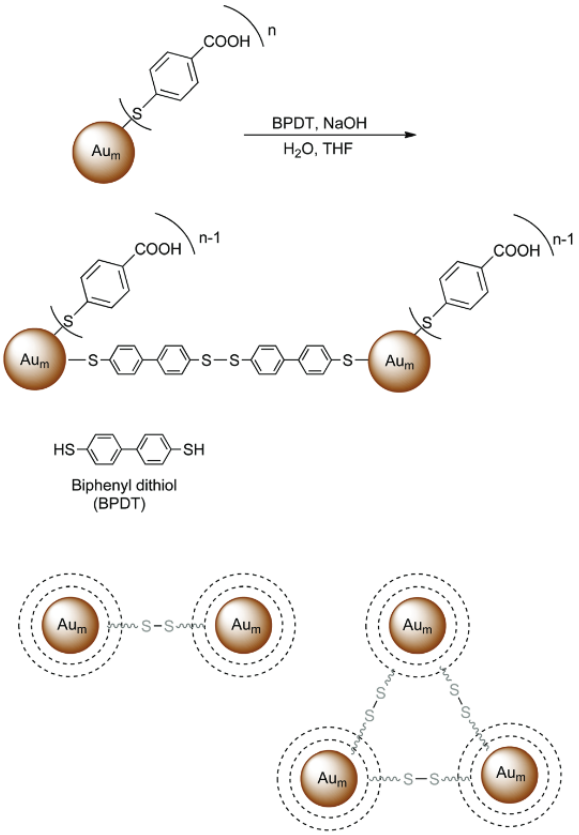

Figure 2 Schematic representation of the LER using BPDT as an exogenous ligand. The scheme shows examples of dimeric and trimeric reaction products.[42]

Oligomer yield and distributions strongly depend on the thiol used, but a trend has not been observed yet, so the design of the LER is never simple. For this reason, the production of oligomers is always expected but the distribution is not predictable. In addition, the dynamic nature of the linking reaction makes it impossible to keep isolated the non-reacted monomers, with dimers, trimers etc…Lahtinen at co. proved that with a complex system like this, disturbing the equilibrium distribution, for example by extracting one pure fraction of oligomer, has negative effects on the system that tends to the equilibrium and so converts the oligomer distribution, reaching the same original distribution as before.[42]

In conclusion, LERs are a powerful tool for modifying the surface of atomically precise gold nanoclusters, both to tune their physicochemical properties and to produce promising ad-hoc units for new functional materials assembled in

superstructures. However, the key challenge is to control LERs at a molecular level, which is essential for (i) obtaining pure functionalized nanoclusters to better understand the effect of the incoming (exogenous) ligand, and for (ii) controlling assembly to produce atomically pure superstructures.

6.3 Results and Discussion

6.3.1 Monofunctionalization

The first part of the presented work aimed to monofunctionalize the monolayer of $Au_{25}(SR)_{18}$, first with a carboxylic ending group exogenous ligand, specifically 4-Mercaptophenylacetic acid (**1**), shown below. Additionally, the second ligand chosen was an amine ending group exogenous ligand, which we designed bearing a fluorenylmethyloxy-carbonyl (Fmoc) protecting group (**2**). This last exogenous ligand was chosen to be sufficiently long to make the amino group protrude from the nanocluster's monolayer.

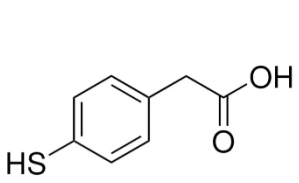

1

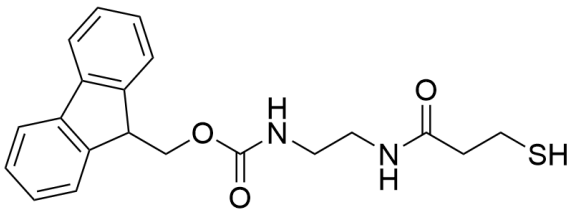

2

For this study we chose the Au_{25} protected by propanethiol in its 0-charge state, $Au_{25}(SC_3H_7)_{18}^0$, since we know it is a good reactant for the LER because of the tendency that propanethiols have to easily break the bond with the metal structure and also because of the small size that the monolayer of the cluster itself possessed, thus making the attack sites more accessible.[25] The cluster was synthesized and characterized as detailed in Sections 2.5.1 and 2.5.3. The purity of the cluster was assessed by UV-Vis spectroscopy, MALDI-TOF mass spectrometry, NMR spectroscopy, and electrochemistry. Two different LERs have been carried out. The extent of exchange was controlled by adjusting the experimental conditions, such as the relative concentrations of the cluster and exogenous ligand, to name the most important ones. The reaction was monitored by UV-Vis absorption spectroscopy and MALDI-TOF mass spectroscopy. After that, a new double solvent separation

procedure was used, with the goal of having a monofunctionalized nanocluster with a high purity level, with both the incoming ligands (**1** and **2**).

6.3.1.1 Synthesis and Purification of Monofunctionalized $Au_{25}C3$ with 4-Mercaptophenylacetic Acid: $Au_{25}(SC_3H_7)_{17}(SPhCH_2COOH)$

To introduce into the Au_{25} monolayer structure a monofunctionalization, we used the LER strategy. The experimental conditions of the LER were optimized to push the single-ligand exchange as much as possible, without producing too many subproducts (commonly the bifunctionalized cluster).

The LER was carried out in toluene, for 1 h, using a molar ratio of 1:1 of the thiol (**1**) and the Au_{25} nanocluster. More in detail: 16.00 mg (1 eq) of $Au_{25}(SC_3H_7)_{18}^0$ was dissolved in 2.55 mL of toluene (C = 1 mM), in a 50 mL flask. Then 0.43 mg (1 eq) of $HSPhCH_2COOH$ (**1**) was added, meanwhile, the solution was stirred at 300 rpm. After that the stirring speed was set to 500 rpm and the reaction was left to react for 1h, at room temperature (25 ± 1). No color changes or precipitation were observed during the entire reaction time. Here below is the stoichiometry of the LER:

$$Au_{25}(SC_3H_7)_{18} + HSPhCH_2COOH \leftrightarrows Au_{25}(SC_3H_7)_{18-x}(HSPhCH_2COOH)_x + HSC_3H_7$$

Where, *x = 0-18.*

After 1 h, toluene was removed with a rotary evaporator to leave a black solid/film on the bottom flask. There was an intense thiol odor attributed to propanethiol. The solid residue was washed with methanol (5 x 10 mL), with the goal of eliminating the excess of thiols, both the endogenous and exogenous ones. The product was first checked by UV-Vis spectrometry to verify the presence of intact $Au_{25}(SR)_{18}$ (Figure 3).

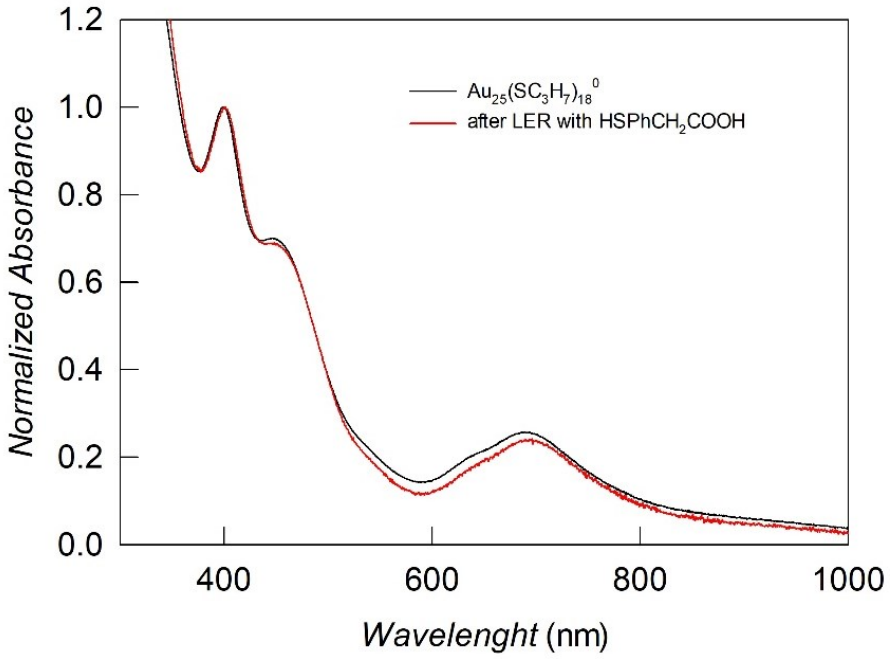

Figure 3 UV-Vis absorption spectrum of the LER with thiol (**1**) products after methanol washes, compared with the Au_{25} nanoclusters spectrum, in toluene.

The presence of the peak at ca. 400 nm, the plateau at ca. 450 nm and the large signal together with the shoulder, from 600 to 800 nm, confirm that the nanocluster survives to the LER and that the core remains intact. The shape of the signal between 600 and 800 nm is very important since it is related to the HOMO-LUMO gap of Au_{25}. To understand if the LER was successful and, eventually, how many ligands were exchanged into the cluster monolayer, MALDI-TOF mass spectrometry was employed. The mass spectra obtained after the exchange reaction (Figure 4) show different patterns ascribable to a mixture of $Au_{25}(SR)_{18}$ clusters characterized by different substitution degrees.

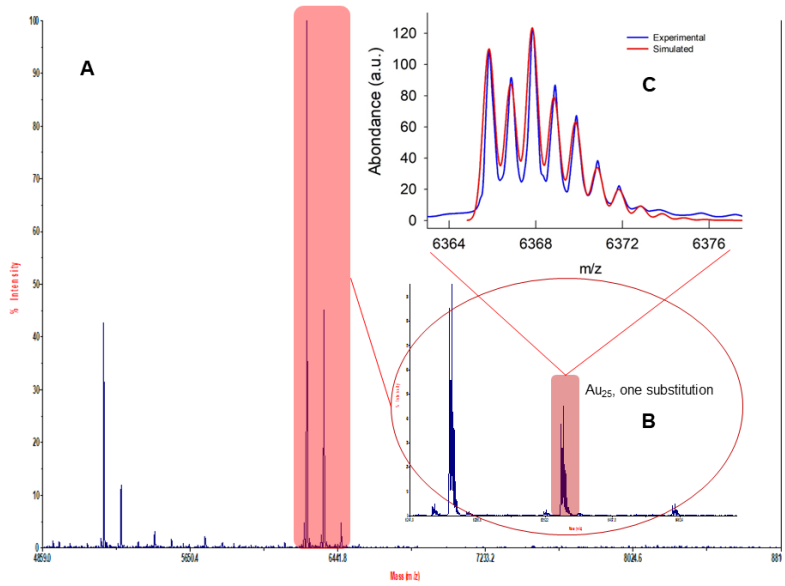

Figure 4 A) Negative-mode MALDI-TOF spectrum of the LER products; **B)** Zoom on the molecular ion's region of the MALDI-TOF spectrum; and **C)** Isotopic pattern (blue line) of the molecular ion related to the monofunctionalized Au_{25}. The red line represents the isotopic pattern simulated with EnviPat software.

Thanks to the MALDI-TOF result we could have information about the LER and the amount of substituted nanocluster. From Figure 4A we can conclude that the controlled ligand exchange reaction was successful. Moreover, the parent ion region shows at least two more signals, related to the functionalized Au_{25}. No other signals were observed at higher m/z values. From 4000 to 6000 m/z region we find the typical fragmentation signals of Au_{21}. Analyzing better the parent ion region (Figure 4B) we can say that in the product mixtures, is still present some unsubstituted cluster (6273 m/z), which is the most abundant product, and two new signals at higher m/z values and 95 m/z apart from each other. 95 Da represents the difference between the molecular weight of the exogenous ligand ($HSPhCH_2COOH$) and the endogenous one (HSC_3H_7). So, the two signals are related to the monosubstitution, (30%, calculated as reported in the "Experimentals") and the bisubstitution (less than 5%). The identity of the peak related to the monosubstituted cluster (6368 m/z) was further analyzed simulating its isotopic pattern using EnviPat free software (Figure 4C). The simulated isotopic pattern perfectly matches the experimental one, confirming the presence of 30% of the Au_{25} nanocluster with just one ligand of the 18, bringing the carboxylic acid group: $Au_{25}(SC_3H_7)_{17}(SPhCH_2COOH)$, hereafter indicated simply as Au_{25}-COOH. The next challenging step was the separation of the monofunctionalized NC from the other clusters present in the product matrix. To do this, once accumulated enough materials various strategies were tried, such as chromatographic silica

column, size exclusion chromatography (SEC) and the use of different solvents, and different pH. We found out that double solvent extraction in the presence of a phase-transfer molecule works properly. In detail, we first used hexane to dissolve all the product, and then add acetonitrile, as a second solvent able to receive the monofunctionalized cluster once few drops of toluene were added (more details were provided in the “Experimentals”). Figure 5 shows the MALDI-TOF spectra together with the UV-Vis spectra of the two separated fractions:

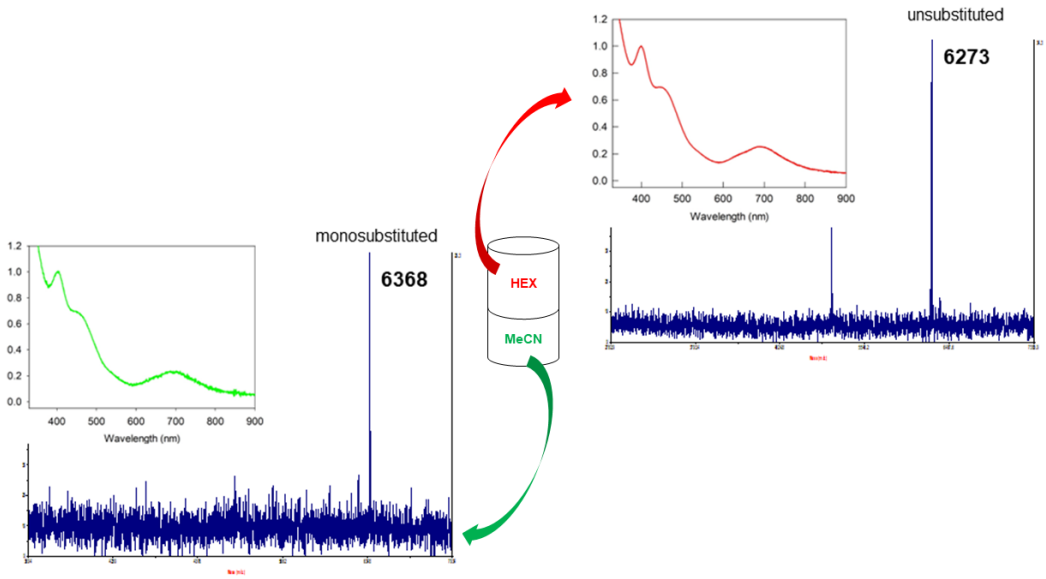

Figure 5 Negative MALDI-TOF spectra together with the UV-Vis spectra of the two fractions deriving from the double solvent extraction with phase transfer molecule. The UV-Vis characterization confirms that the nanocluster survives the extraction procedure and the MALDI-TOF experiment demonstrates that with this procedure we were able to successfully separate the monosubstituted from the unsubstituted one.

Here below (Figure 6) the MALDI-TOF spectra showing the effect of the extraction procedure is shown. On the right, the enriched monosubstituted Au_{25} sample is showed with, in the inset, the magnification of the isotopic pattern of the parent peak (6368 m/z).

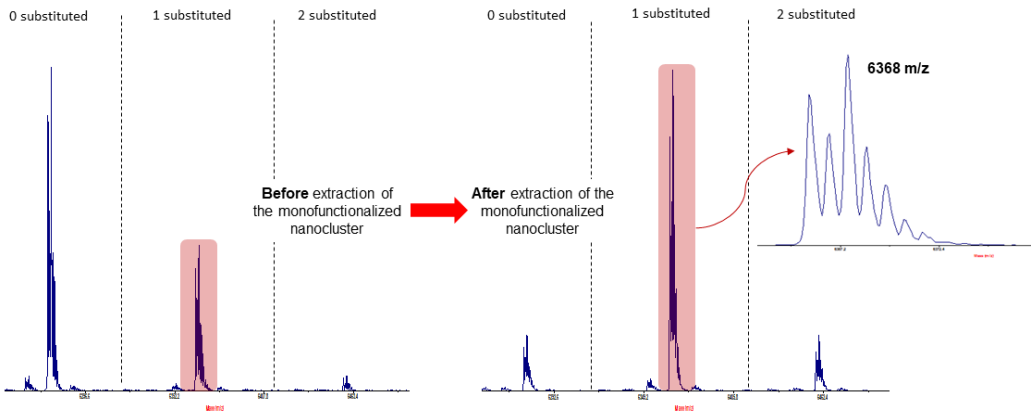

Figure 6 Negative MALDI-TOF spectra showing the LER product, before and after the extraction of the monosubstituted Au_{25} nanolcuster. The signal at 6368 m/z, related to the parental ion of $Au_{25}(SC_3H_7)_{17}(SPhCH_2COOH)$ increase and reach the 77 % of purity. In the inset the magnification of his isotopic pattern is shown.

Further purification strategies failed. Both the synthetic and separation procedures were reproducible with a final Au_{25}-COOH product relative abundance of 75 $\pm$ 5 %.

6.3.1.2 Synthesis and Purification of Monofunctionalized $Au_{25}C3$ with Amine Ending Group Ligand: $Au_{25}(SC_3H_7)_{17}(SR\text{-}NHfmoc)$

Synthesis of Exogenous Ligand 2: HS-CH_2CH_2-CO-NH-CH_2CH_2-NHFmoc

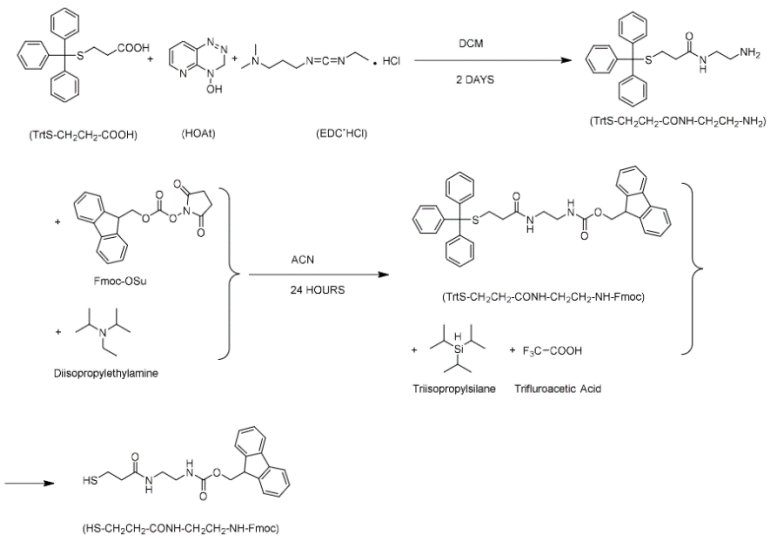

Figure 7 Synthetic route of thiol (**2**).

Synthesis of TrtS-$CH_2CH_2CONHCH_2CH_2NH_2$: TrtS-CH_2CH_2COOH (500 mg, 1.43 mmol) and HOAt (234 mg, 1.71 mmol) (Tr = trytil) was dissolved in 10 ml of CH_2Cl_2

and EDC·HCl (330 mg, 1.71 mmol) was added. The reaction mixture was stirred for 2h, and then a solution of $H_2NCH_2CH_2$-NH_2 (0.96 ml, 14.3 mmol) in 25 ml of CH_2Cl_2 was added dropwise during 1h. After 2 days the solvent was evaporated, and the crude product was purified by silica gel chromatography column using CH_2Cl_2 and then the mixture CH_2Cl_2/MeOH (v: v = 1:5) as eluents. Synthesis of TrtS-$CH_2CH_2CONHCH_2CH_2NHFmoc$: TrtS-$CH_2CH_2CONHCH_2CH_2NH_2$ (1.3 g, 3.33 mmol) was dissolved in 20 ml of MeCN, a solution of Fmoc-OSu (1.12 g, 3.33 mmol) in 20 ml of MeCN and diisopropylethylamine (0.56 ml, 3.33 mmol) were added. The reaction mixture was stirred for 24 h and concentrated to 20 ml. The white precipitate was filtered, washed with 5 ml of acetonitrile, cooled to 0 °C and dried. The organic solutions were collected, the solvent was evaporated, and the product was recrystallized from acetonitrile. 1H NMR (200 MHz, CDCl3): δ 7.55 (d, 2H, CHFmoc, J = 8 Hz), 7.51 (d, 2H, CHFmoc, J = 8 Hz), 7.20-7.50 (m, 19H; 15 H, Trt, 4H, Fmoc), 5.75 (s, 1H, NH), 5.20 (s, 1H, NH), 4.30 (d, 2H, CH_2Fmoc, J = 6 Hz), 4.15 (t, 1H, CHFmoc, J = 6 Hz), 3.26 (s, 4H, $2CH_2$), 2.50 (t, 2H, CH_2, J = 6 Hz), 2.10 (t, 2H, CH_2, J = 6 Hz). Synthesis of HS-CH_2CH_2CO-$NHCH_2CH_2NHFmoc$. TrtS-CH_2CH_2CO-$NHCH_2CH_2NHFmoc$ (0.3 g, 0.49 mmol) and 0.5 ml of triisopropylsilane (2.44 mmol) was dissolved in 8 ml of CH_2Cl_2. 1.5 ml of trifluoroacetic acid were added dropwise and the reaction mixture was stirred for 1 h. The solvent was evaporated, and 20 ml of diethyl ether were added to the white solid. The product was filtered, washed 6 × 20 ml of diethyl ether, dried, and solubilized in DCM to obtain the UV-Vis spectrum (Figure 8). ^{1}H-NMR (200 MHz, $CDCl_3$): δ 7.77 (d, 2H, CHFmoc, J = 8 Hz), 7.58 (d, 2H, CHFmoc, J = 8 Hz), 7.25-7.48 (m, 4H, Fmoc), 6.08 (s, 1H, NH), 5.19 (s, 1H, NH), 4,43 (d, 2H, CH_2Fmoc, J = 6 Hz), 4.21 (t, 1H, CHFmoc, J = 6 Hz), 3.37 (s, 4H, $2CH_2$), 2.78 (q, 2H, CH_2, J = 8 Hz), 2,46 (t, 2H, CH_2, J = 6 Hz), 1.57 (t, 1H, SH, J = 8 Hz).

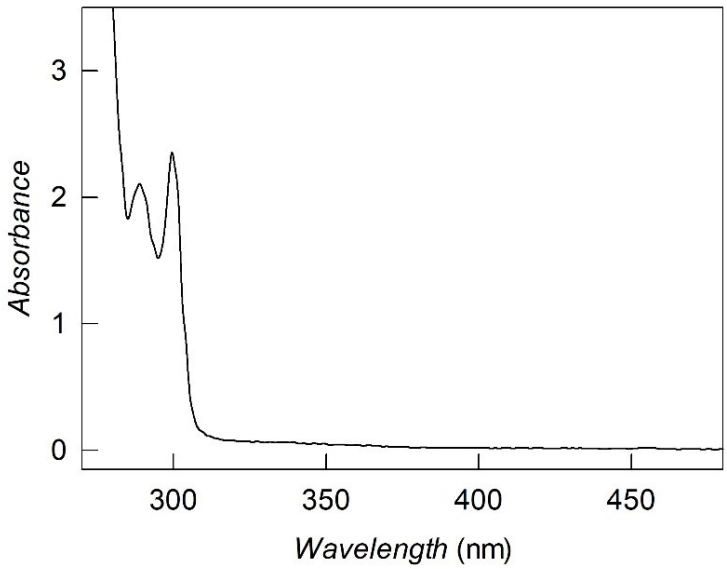

Figure 8 UV-Vis absorption spectrum of thiol **(2)** used as exogenous ligand in the presented LER, in DCM, shows the high-intensity peak (at 301 nm) of the Fmoc group.

We introduced on the nanocluster surface also an amine ending group ligand (thiol (**2**)). To this purpose, we used the same LER strategy that worked with ligand (**1**). The experimental conditions of the LER were optimized to push the single-ligand exchange as much as possible, without producing too many subproducts (commonly the bifunctionalized cluster).

The LER was carried out in dichloromethane, for 15 h, using a molar ratio of 1:1 of the thiol (**2**) and the Au_{25} nanocluster. More in detail: 23.00 mg (1 eq) of $Au_{25}(SC_3H_7)_{18}^0$ was dissolved in 8 mL of toluene (C = 0.45 mM), in a 50 mL flask. Then 1.35 mg (1 eq) of thiol (**2**) was added, meanwhile, the solution was stirred at 300 rpm. After that the stirring speed was set to 500 rpm and the reaction was left to react for 15h, at room temperature (25 ± 1). No color changes or precipitation were observed during the entire reaction time. Here below is the stoichiometry of the LER:

$$Au_{25}(SC_3H_7)_{18} + HSR - NHFmoc \leftrightarrows Au_{25}(SC_3H_7)_{18-x}(HSR - NHFmoc)_x + HSC_3H_7$$

Where, *x = 0-18.*

After 15 h, toluene was removed with a rotary evaporator to leave a black solid on the bottom flask. There was an intense thiol odor attributed to propanethiol. The solid residue was washed with methanol (5 x 10 mL), with the goal of eliminating the excess of thiols, both the endogenous and exogenous ones. The product was first checked by UV-Vis spectrometry to verify the presence of intact $Au_{25}(SR)_{18}$ (Figure 9).

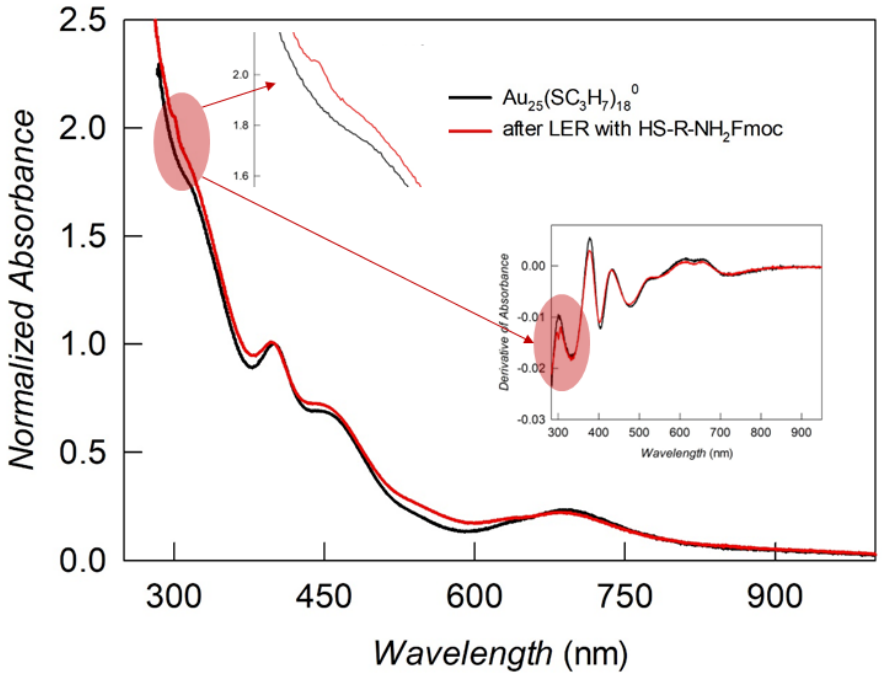

Figure 9 UV-Vis absorption spectrum of the LER with ligand (**2**) products after methanol washes, compared with the Au_{25} nanoclusters spectrum, in dichloromethane. In the inset the absorption's derivative shows the signal related to the Fmoc group.

As it was for the previous LER, the spectrum obtained after the LER shows similar features as the Au_{25} before the surface modification, confirming once again that the nanoclusters survived at the LER, especially maintaining their core structure. The introduction of the exogenous ligand (**2**) is confirmed also by the presence of the absorption signal of the Fmoc group at about 300 nm (highlighted in the inset of Figure 9 and by the derivative analysis of the absorption). The mass spectra obtained after the exchange reaction (Figure 10) show a number of signals ascribable to a mixture of $Au_{25}(SR)_{18}$ clusters characterized by different substitution degrees.

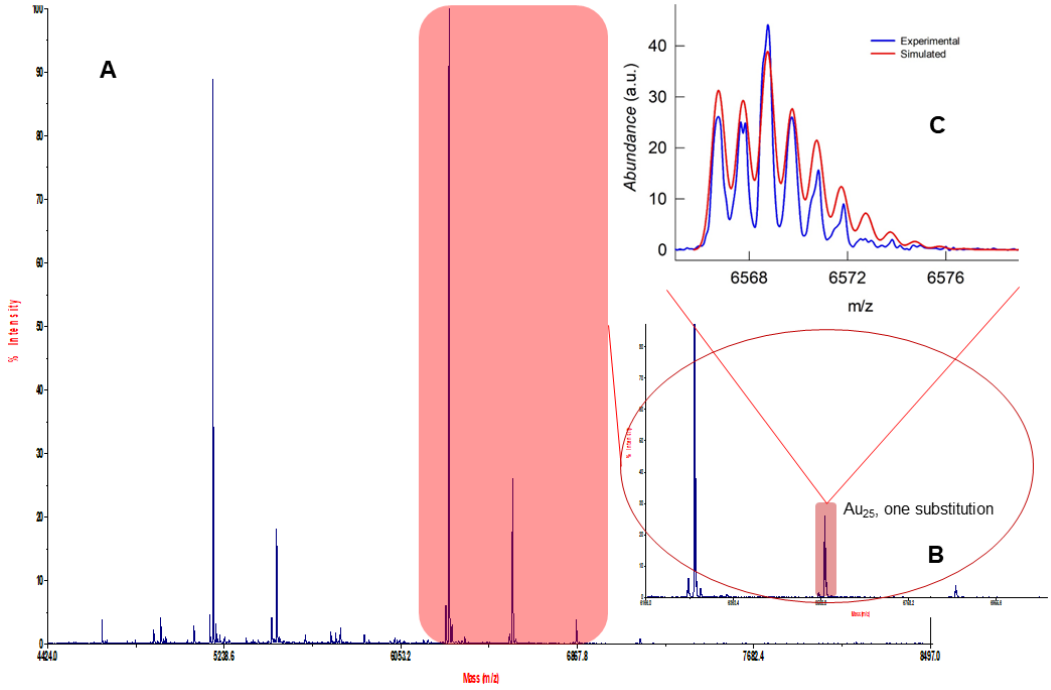

Figure 10 A) Complete negative-mode MALDI-TOF spectrum of the LER products; **B)** Zoom on the molecular ion's region of the MALDI-TOF spectrum; and **C)** Isotopic pattern (blue line) of the molecular ion related to the monofunctionalized Au_{25}. The red line represents the isotopic pattern simulated with EnviPat software.

Thanks to the MALDI-TOF result we could have information about the LER and the amount of substituted nanocluster. From Figure 10A we can conclude that the controlled ligand exchange reaction was successful. The parent ion region shows other signals than the starting unsubstituted cluster one (6273 m/z), in large amounts: Moreover, there are three new signals at higher m/z values and 292 m/z apart from each other. 292 Da represents the difference between the molecular weight of the exogenous ligand (**2**) and the endogenous one (HSC_3H_7). So, the three signals are related to the monosubstituted (20%, calculated as reported in the "Experimental"), the bisubstituted (less than 3%), and the trisubstituted (less than 1%) NC. The identity of the peak related to the monosubstituted cluster (6569 m/z) was further analyzed simulating his isotopic pattern using EnviPat free software. The simulated isotopic pattern matches the experimental one, confirming the presence of 20% of the Au_{25} nanocluster with just one exchanged ligand over the 18, bringing the Fmoc protected amine group: $Au_{25}(SC_3H_7)_{17}$(S-R-NHFmoc), hereafter indicated simply as Au_{25}-NHFmoc. Once again, the critical step is represented by the isolation of the product of interest. Also in this case, we found out that double solvent extraction, using a phase transfer molecule, was the best performing strategy. We used hexane as a first

solvent, and methanol as second solvent where the monofunctionalized cluster transferred thanks to the presence of few drops of toluene (more details were provided in the “Experimentals”). Figure 11 shows the MALDI-TOF spectra together with the UV-Vis spectra of the two separated fractions:

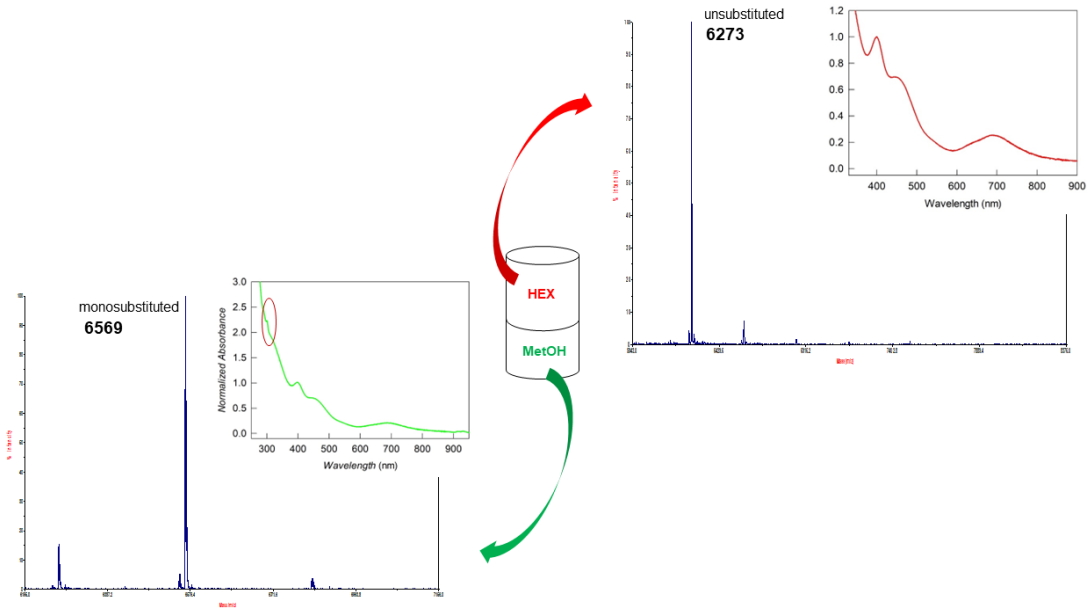

Figure 11 Negative MALDI-TOF spectra together with the UV-Vis spectra of the two fractions deriving from the double solvent extraction with phase transfer molecule. The UV-Vis characterization confirms that the nanocluster survives to the extraction procedure and the MALDI-TOF experiment demonstrates that with this procedure we were able to successfully separate the monosubstituted from the unsubstituted one.

Further purification strategies failed. The LER is repeatable and Au_{25}-NHFmoc product is always produce in a relative amount of 20 $\pm$ 5 %. However, differently from what observed with the Au_{25}-COOH, the output of the double solvent purification, with phase transfers molecule, was unpredictable. Our best result was achieving a sample with approximately 85% of Au_{25}-NHFmoc. The MALDI spectrum is shown below (Figure 12).

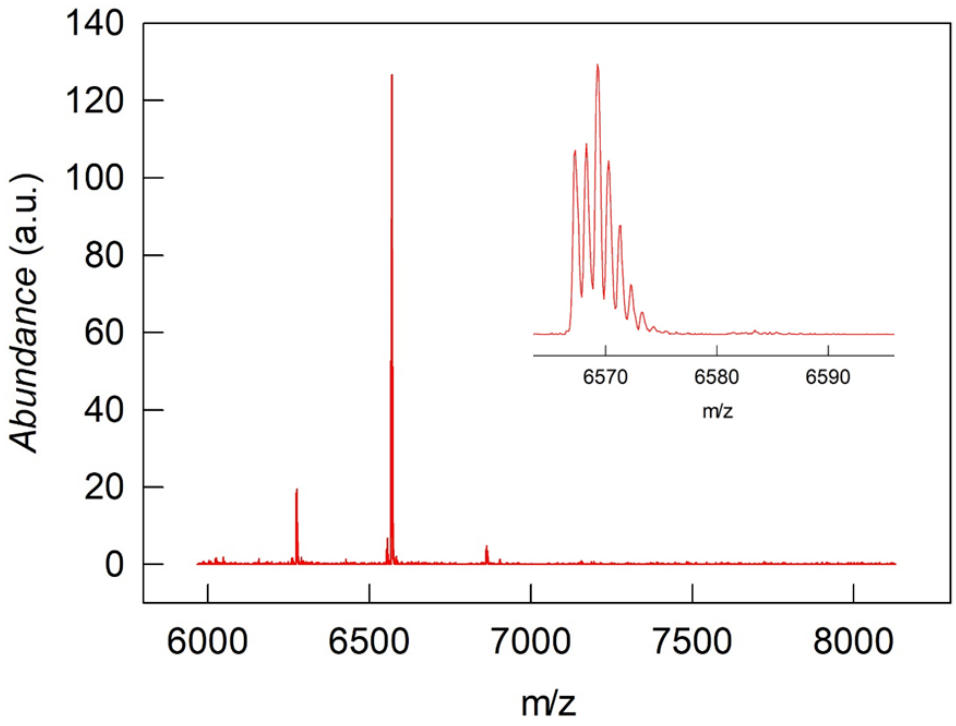

Figure 12 Negative-mode MALDI-TOF spectrum of the high purity monosubstituted $Au_{25}(SC_3H_7)_{17}$(S-R-NHFmoc). From the relative intensity, we calculated a percentage of Au_{25}-NHFmoc of about 85 %. In the inset the magnification of the parental ion related to the monofunctionalized Au_{25} signal, showing the expected isotopic pattern.

6.3.2 Physicochemical Properties of Monofunctionalized Au_{25} Nanoclusters

Although the optical and electrochemical properties of nanoclusters depend primarily on the core, the presence of a single different ligand on the surface can have an appreciable effect and the synthesized monofuncionalized clusters (Au_{25}-COOH and Au_{25}-NHFmoc) give us the opportunity to better understand their role on the complex nanocluster system.

Optical Properties and comparison between -COOH and -NHFmoc group.

Even if the absorption properties are not heavily affected by the ligands, we can analyze the different purity degrees of the amine-monosubstituted Au_{25}, thanks to the typical feature at about 301 nm of the Fmoc group of the exogenous ligand **(2)**. All the samples with different degrees of purity of Au_{25}-NHFmoc (0, 5, 30 and 85 %) were checked by UV-Vis spectroscopy. The spectra obtained before and after exchange confirm the survival of the cluster structure, showing the same fine features (peaks at 401 and 687 nm, shoulders at 455 nm) typical of $Au_{25}(SR)_{18}^0$ (Figure 13A), which is particularly evident in the derivative spectra (Figure 13B).

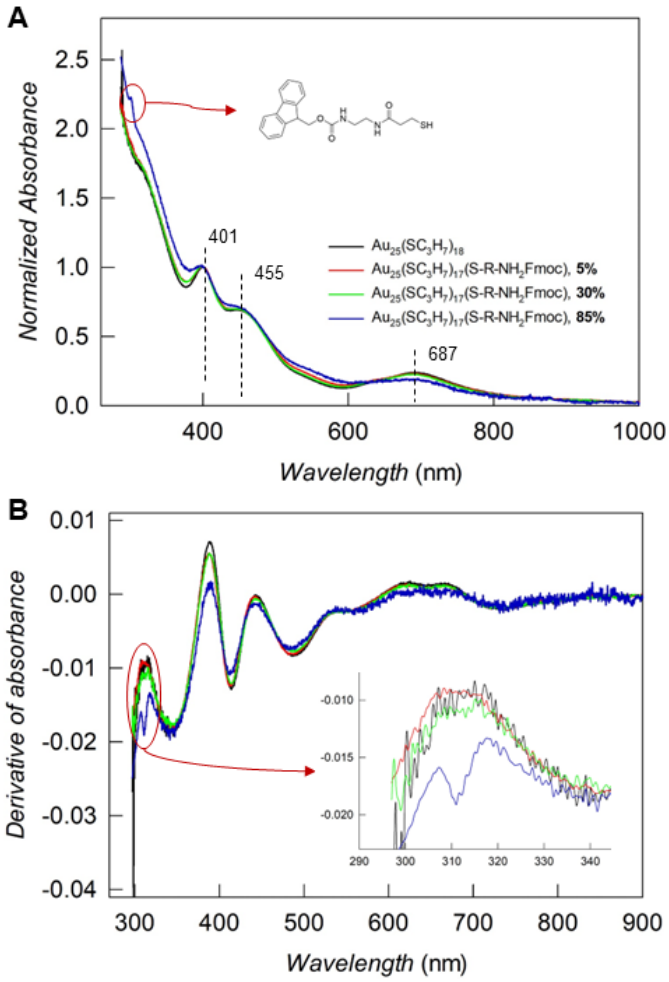

Figure 13 (A) UV-vis absorption, where the signal of the Fmoc group is underlined, and **(B)** corresponding derivative spectra (in the inset: magnification on the exogenous ligand region fingerprint) of the Au_{25} before and after modification with thiol (**2**), with different purity degrees.

Figure 13B nicely shows that increasing the relative purity of the monosubstituted nanocluster in the sample mixture leads to an increase of the height of Fmoc peaks (and inflection variation through derivative analysis) respect to Au_{25}.

The comparison between the spectra of the two different monofunctionalized nanoclusters, with similar purity degree reveals interesting features. As shown in Figure 14, the peak at 401 nm is shifted in the opposite direction depending on the functionalization inserted on the nanocluster surface.

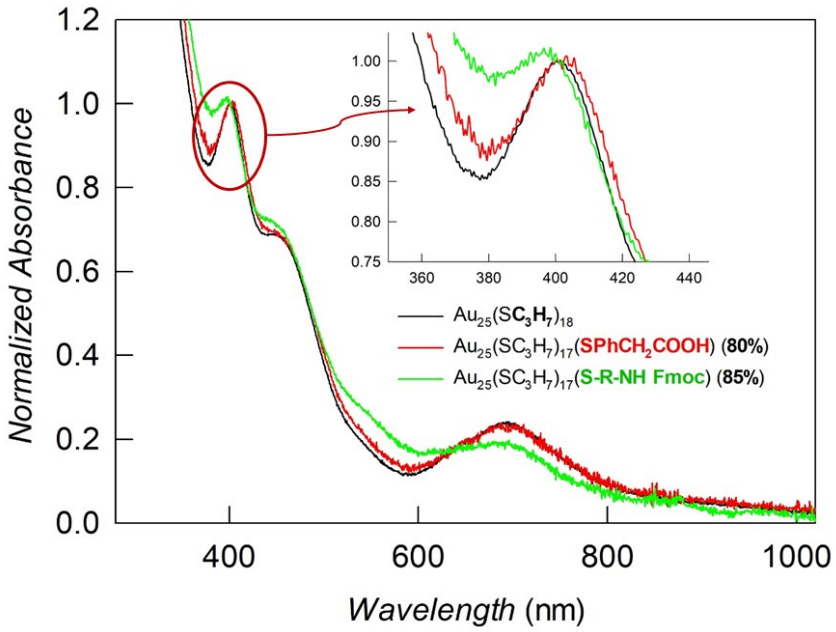

Figure 14 UV-Vis spectra of the two monofunctionalized Au_{25} nanocluster ($Au_{25}(SC_3H_7)_{17}(SPhCH_2COOH)$ in red line and $Au_{25}(SC_3H_7)_{17}$(S-R-NHFmoc) in green line) with similar degree of purity (80-85 %), in toluene. In the inset the magnification of the 401 nm signal, showing the different shift form the two samples.

In 2008, Jin and coworkers demonstrated, by both experimental evidence and TD-DFT calculations, that just the first two absorption bands (lower energy) are composed almost exclusively of atomic orbital contributions from the 13 Au atoms in the icosahedral core rather than the 12 exterior Au atoms. Otherwise, the set of occupied orbitals (HOMO through HOMO-5), which are relative to the third band (peak at 400 nm), have a significant degree of sulfur character (~25-40%). They expected a blue-shift in the absorption spectrum, using more electron donating ligands.[50] This scenario could explain the optical properties of our monofunctionalized Au_{25}. Indeed, Au_{25}-COOH, shows a red-shift of about 3 nm, in agreement with the electron withdrawing character of the introduced ligand. The opposite for the blue-shift of Au_{25}-NHFmoc.

Electrochemical Properties of carboxylic acid-monosubstituted Au_{25}.

The electrochemical behavior of Au_{25}-COOH was analyzed by DPV (Figure 15) that showed the fingerprint features ($E°_{O1}$ = 0.183 eV and $E°_{R1}$ = -0.114 eV) of Au_{25} providing further evidence of the integrity of the cluster structure.

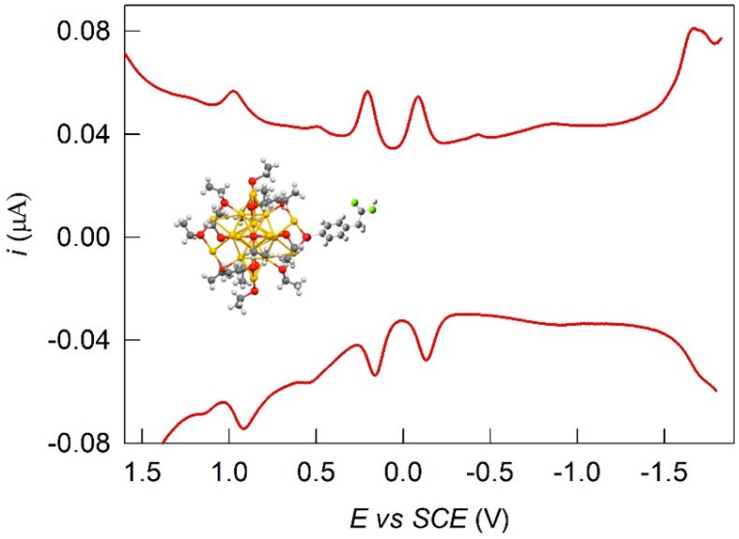

Figure 15 DPV behaviors of Au_{25} monofunctionalized with carboxylic acid ending group ligand ($Au_{25}(SC_3H_7)_{17}(SPhCH_2COOH)$), in DCM/0.1 M $TBAPF_6$.

Figure 16 shows the comparison of the electrochemical behavior of the exchanged nanocluster and the original Au_{25} in the potential region involving the first oxidation and the first reduction of the neutral cluster that is the HOMO orbital energy region.

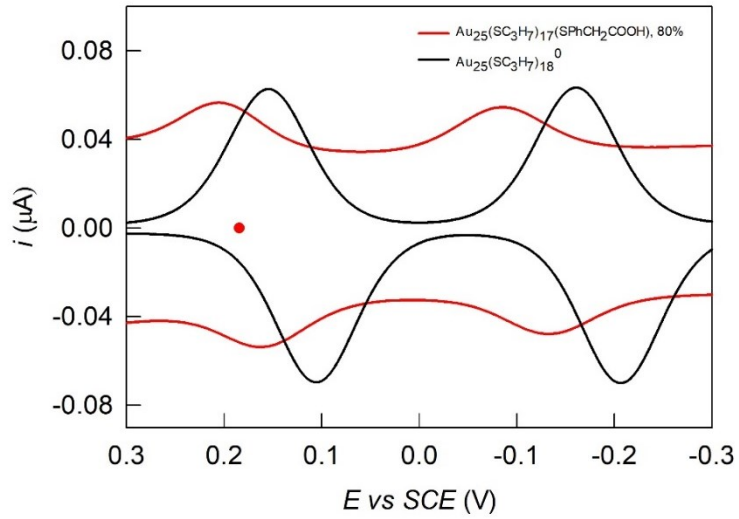

Figure 16 Comparison of the DPV behaviors of the two central reversible peaks (first reduction and first oxidation) of the Au_{25}-COOH (**1**) (red line), with the original Au_{25}^0 nanocluster (black line), in DCM/0.1 M $TBAPF_6$. The OCP of Au_{25}-COOH is shown with a red circle.

The two central peaks of the modified cluster are shifted towards positive potentials, of about 51 mV, with respect to propanethiolate-protected Au_{25}. This result confirms

that the electron-withdrawing character of a single ligand of 18 affects the orbital energy in a non-negligible way.[7]

Electrochemistry confirms the UV-Vis spectra evidence that the Au_{25} cluster structure is maintained after the LER and that the new ligand on the nanocluster surface is affecting the electronic properties of the cluster. The single-ligand modification also affects the open circuit potential (red circle in Figure 16), which reveals the partial positive charge of the system because of the carboxylic acid ending group ligand.

6.3.3 Coupling of Ad-hoc Prepared Functionalized Nanoclusters

Having two complementary functionalized Au_{25} (Au_{25}-COOH and Au_{25}-NHFmoc) with the same high level of purity (80 % for thiol (**1**) and 85 % for thiol (**2**)) gave us the opportunity to try to perform the coupling of the two Au_{25} units (Figure 17).

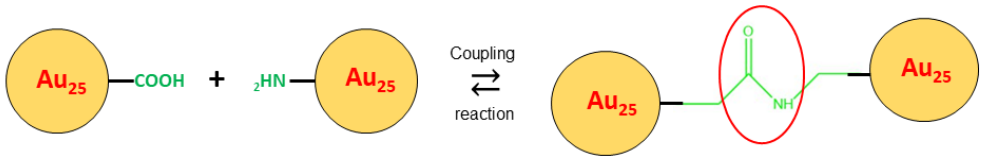

Figure 17 Cartoon representing the coupling reaction between the two monofunctionalized clusters (with thiol (**1**) and (**2**)). The proposed reaction is an amidation reaction between carboxylic acid and amine ending groups of the new ligands on the Au_{25} nanocluster's surface.

To achieve this, we started with amine *deprotection*. The Fmoc groups were removed using diethylamine, in DMF. The detailed procedure was as follows: 10 mg Au_{25}-NHFmoc was dissolved in 0.5 ml DMF with vigorous stirring. Then, 100 µL (800 eq) of diethylamine was added into the solution dropwise, under soft sonication condition. The reaction goes 15 minutes, and then was quenched by ether. The solid residue was washed with cold methanol (5 × 10 mL). After deprotection, the UV-vis spectrum and its derivative maintain the same features as those of the pristine $Au_{25}(SC_3H_7)_{18}$ cluster (Figure 18), losing the features related to fluorenyl function of the protecting group. The presence of the Au_{25} typical peaks indicates that the deprotection conditions do not affect the gold core. Some little differences in the absorption behavior are attributed to the partial reduction of the cluster in DMF.

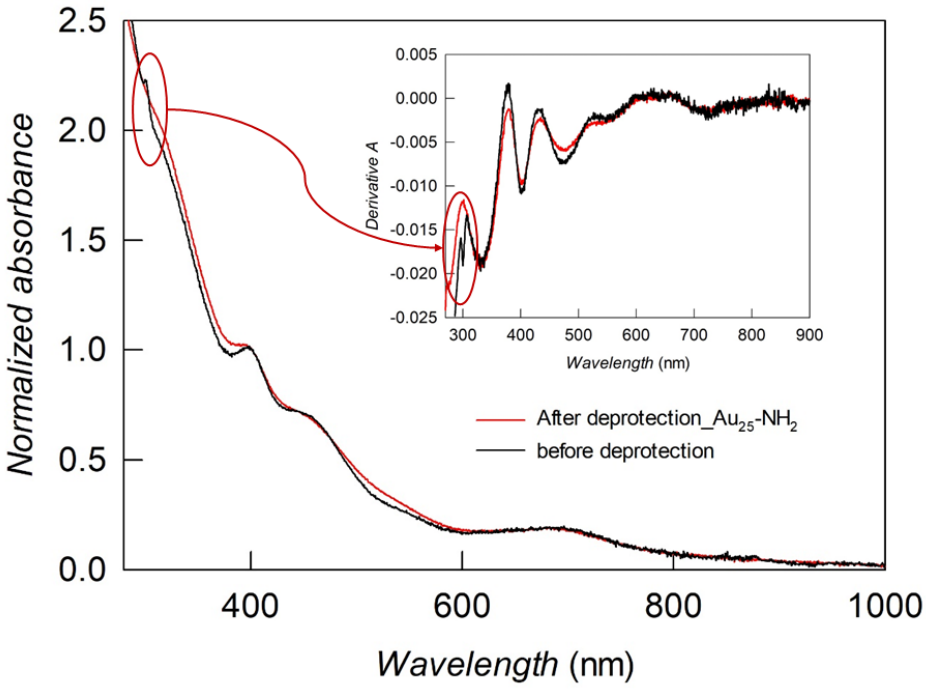

Figure 18 UV-Vis absorption of Au_{25}-NHFmoc, before (black line) and after (red line) the deprotection reaction with Et_2NH, in toluene. In the inset the corresponding derivative spectrum is shown.

The deprotected Au_{25}-NH_2 nanocluster showed low stability, most probably due to the reactivity of the ligand itself, after the deprotection. Indeed, the exogenous ligand is characterized by the presence of multiple amide groups that are known to be prone to form strong H-bonds with carbonyl groups. This could be the reason for the observed formation of a gray insoluble precipitate some minutes after the deprotection of the amine group. Anyway, we proceeded to perform the coupling reaction with Au_{25}-COOH. The coupling reaction was carried out using Et_3N (Triethylamine), and activating the carboxylic acid on the nanocluster's surface, using EDC (1-Ethyl-3-(3-dimethylaminopropyl)carbodiimide) with a modified procedure respect to the standard one, with the goal of creating a proper reaction environment for the NCs. In details, the three-steps reaction procedure has been:

1. *Activation of the Au_{25}-COOH:* 1.1 mg (1 eq) of A_{25}-COOH were put into a 2 mL vial. 0.7 mg (40 eq) of HOSu (*N*-Hydroxysuccinimide) was added. After that 150 uL of toluene were added and just the nanocluster was solubilized. The HoSu remains in powder. After that 1 mg (40 eq) of EDC was added. The reaction was left to react for 30 minutes, at room temperature ($T = 25 \pm 1$), sonicating at the maximum power.

2. *Deprotection of the Au_{25}-NH_2:* A deprotected fresh solution of Au_{25}-NH_2 was prepared using Et_2NH with the procedure described above.

3. *Coupling reaction:* 0.2 uL (10 eq) of Et_3N was added to the 2 mL vial containing the activated Au_{25}-COOH nanocluster (1.1 eq). Then the fresh produced solution of deprotected Au_{25}-NH_2 nanocluster (1 eq) was added and left to react for 2 h, stirring vigorously. After 2 h, the solvent was removed with a rotary evaporator. The solid residue was washed with methanol (5 x 1 mL).

The product was first checked by UV-Vis spectroscopy to check the NC integrity (Figure 19), and then characterized by MALDI-TOF spectrometry (Figure 20).

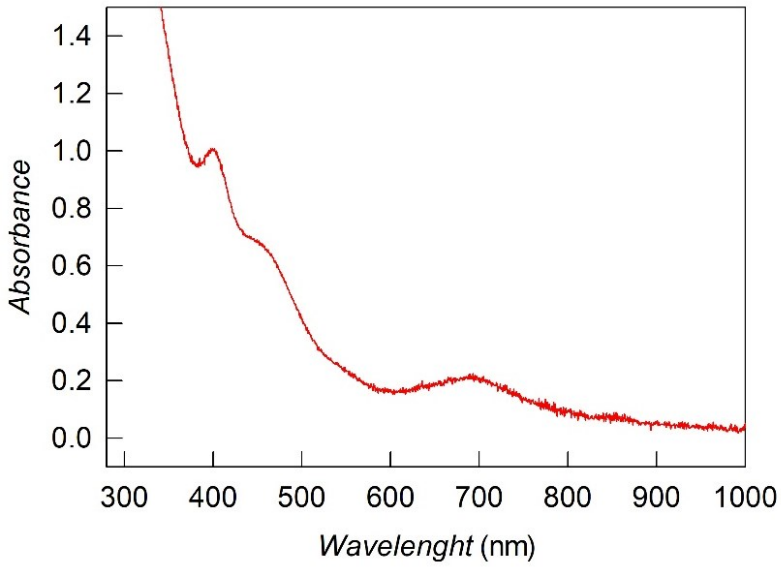

Figure 19 UV-Vis absorption of the product of the coupling reaction between Au_{25}-COOH and Au_{25}-NH_2, in toluene.

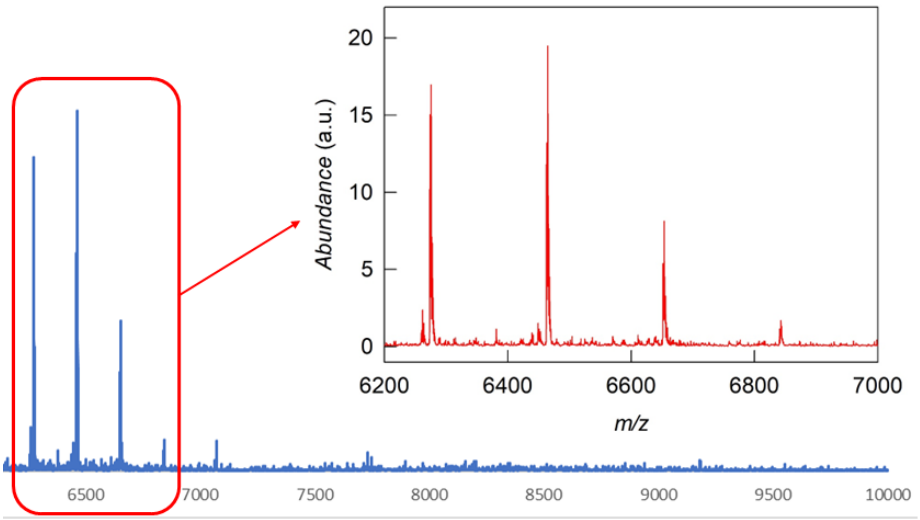

Figure 20 Negative-mode MALDI-TOF spectrum of the coupling reaction product. In the inset, the magnification on the typical nanocluster region, shows signals at m/z value higher than 6276 (MM of $Au_{25}(SC_3H_7)_{18}$) suggesting the production of bigger superstructures.

From the MALDI-TOF spectrum we didn't observe the parent ion of species related to the coupling of two or more Au_{25}, but we observed signals at m/z values higher than 6276 (mass of the original Au_{25}) probably related to the fragmentations of some bigger superstructure. Interesting, no other signal related to the two reactants were observed (no Au_{25}-COOH and no Au_{25}-NH_2 detected). Here below the analysis of the MALDI signals is shown (Figure 21).

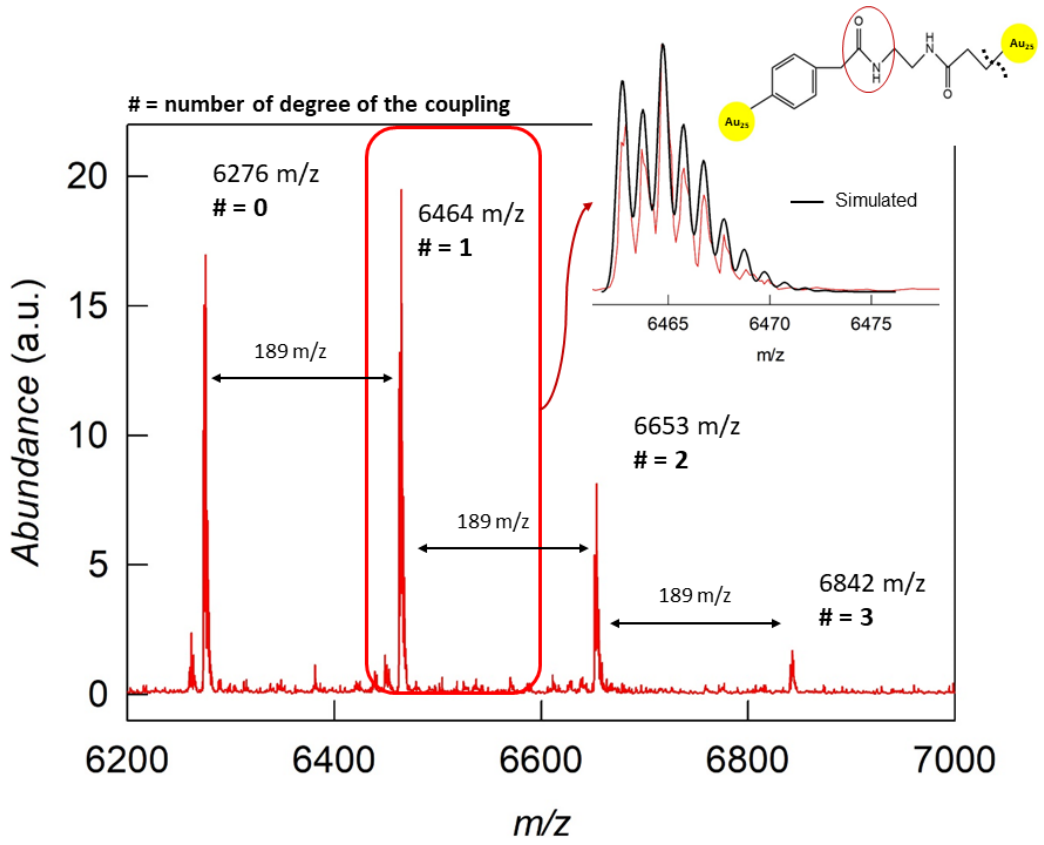

Figure 21 Negative-mode MALDI-TOF analysis of the coupling reaction product. In the inset the magnification of the underlined peak (more intense peak at 6464 m/z), related to the fragmentation of the dimer species (Au_{25}-CONH-Au_{25}), produced thanks to the amidation reaction between the two monofunctionalized Au_{25} NCs, together with the simulated isotopic pattern. Isotopic pattern simulated with EnviPat software. The nature of the verified fragmentation is shown in the same inset. The amide group formed is underlined with a red circle.

Despite the absence of the parent peak with the expected mass, the MALDI-TOF analysis proves the success of the reaction. Indeed, the mass of the peak with the highest intensity (6464 m/z), corresponds to a fragmentation expected from the dimer species (Au_{25}-CONH-Au_{25}), deriving from the coupling. Indeed, the signal is related to an Au_{25} nanocluster with 17 original ligands (6198 Da) plus one new ligand deriving from the condensation reaction between the activated carboxylic acid and the free amine group of the second nanocluster (MM of the amide bridge = 265 Da). The

proposed fragmentation is made explicit in the upper part of the inset of Figure 21. In addition to this signal, other secondary signals, at a higher m/z value of about 189 (difference between the new ligand after the amidation reaction and the original ligands, ± 1 Da), were observed. Since we started the coupling reaction with high pure samples of the monofunctionalized Au_{25}, with just a little amount of the bifunctionalized one, these signals are suggesting a reorganization of the ligands in the nanocluster's surface and between the nanoclusters themselves, with the effect of producing bigger superstructures beyond the dimer species. Indeed, according to the MALDI-TOF characterizations, the bigger superstructure produced is a tetramer of Au_{25}, as supposed in the scheme here below (Figure 22).

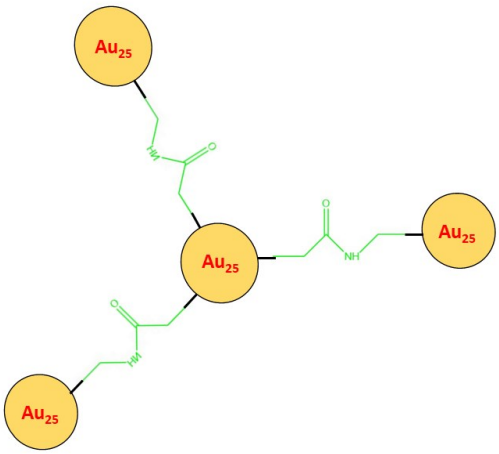

Figure 22 Cartoon showing the supposed biggest superstructure derived from the coupling reaction, according to the MALDI-TOF results.

Different strategies were tested to separate the dimer, trimer, and tetramer but unfortunately no one was successful. Indeed, the SEC was also tried with the result of separating just the non-reacted Au_{25} completely protected by propanethiolate ($Au_{25}(SC_3H_7)_{18}^0$). The product turns out to be very unstable and degrades faster when solubilized. Most probably this is due to both the lability of the amide group in solution when also a small percentage of water is present, and the flexibility of the ligand bridge, because of its length and chemical nature.

6.3.4 Heavily Substitution on $Au_{144}(SC_2H_4Ph)_{60}$ Nanocluster

(The work was carried out at the Department of Chemistry and Biochemistry, in the Northern Arizona University, in Flagstaff, Arizona, USA, at the Prof. Whetten Laboratory)

This paragraph aimed to propose a new strategy to obtain a heavy substitution on Au_{144} nanocluster. To be more precise, a new "step-by-step" LER strategy will we proposed to almost fully PEGylate an atomically precise gold nanocluster composed by 144 gold atoms (Au_{144}), using a very small amount of exogenous ligand m-PEG_4-thiol **(3)**, (hereafter indicated simply as PEG4) and show below.

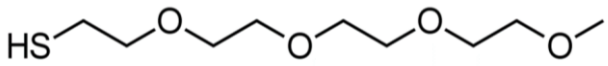

3

The LER strategy involves multiple ligand exchange reactions followed by purification of the reaction product after each step. This approach minimizes the amount of ligand reactant required and cleverly utilizes Le Chatelier's principle to drive the reaction towards the products, specifically towards the most exchanged species. Indeed, after each LER, we eliminate the byproducts, which represent the endogenous ligands generated during the reaction. This approach effectively shifts the reaction towards the more exchanged products (Le Chatelier's principle) without the need for excess equivalents.

For this study, we chose the Au_{144} protected by phenylethanethiol in its 0-charge state, $Au_{144}(SC_2H_4Ph)_{60}^0$ (hereafter indicated simply as Au_{144}PET), a very well-known NC. The synthesis of Au_{144}PET was performed following a literature procedure,[51] with minor modifications. In detail: 0.10 g (0.254 mmol, 1 equiv) of $HAuCl_4 \cdot 3H_2O$ was dissolved in 2.54 mL of methanol, and then 0.166 g of tetra-n-octylammonium bromide (0.305 mmol, 1.2 equiv) was added. The resulting red suspension was stirred for 20 min at 20 °C until complete dissolution of the reagents. The stirring speed was set to 100 rpm and 0.206 ml (1.524 mmol, 6 equiv) of phenylethanethiol, dissolved in 2 mL methanol was added dropwise over a period of ~3 min. The solution quickly became a milky-white suspension. The stirring speed was increased to 600 rpm and a freshly prepared icy-cold aqueous solution (2 mL) of $NaBH_4$ (0.096 g, 2.54 mmol, 10 equiv) was quickly added to the reaction mixture. The suspension immediately became black and plenty of gas evolved. The cup of the flask was closed after 2-3 minutes, after a brown/orange suspension appeared. The reaction was stopped after ~15 h. The black precipitate was washed 4 times with cold methanol (5 mL) and 3 times with acetonitrile (5 mL) to fully remove the Au_{25}^-clusters.

The purified product $Au_{144}(SC_2H_4Ph)_{60}$ was finally extracted with toluene (55 % of yield). The purity of the cluster was assessed by UV-Vis spectroscopy (Figure 23) and HR ESI-MS mass spectrometry (Figure 24).

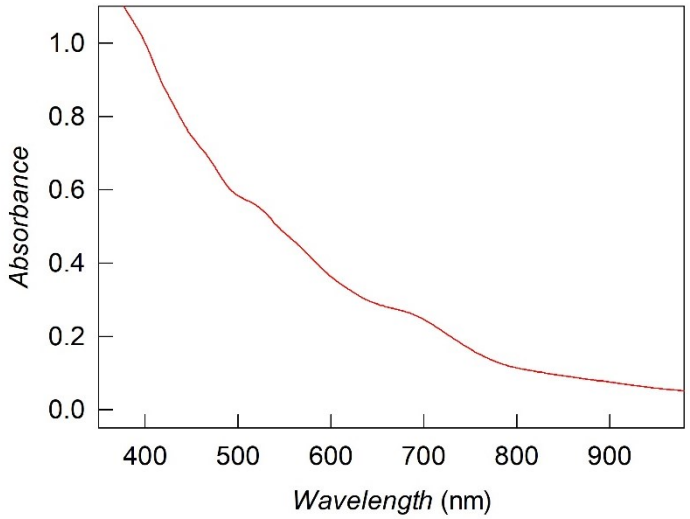

Figure 23 UV-Vis absorption of Au_{144}PET, in toluene.

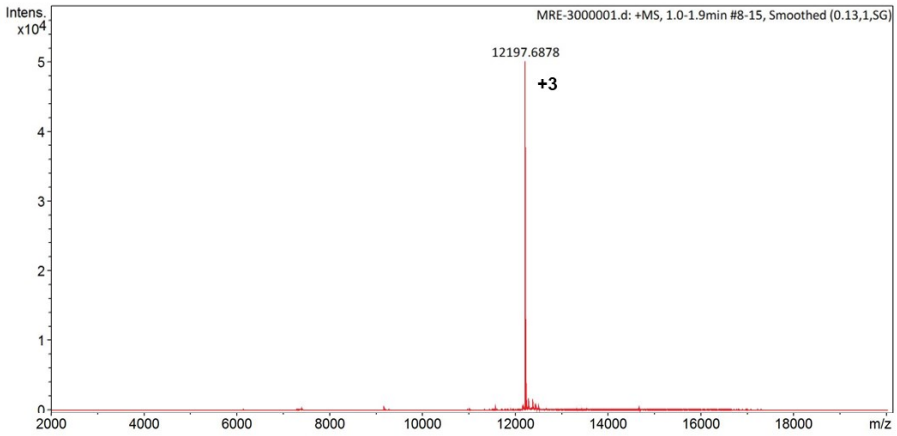

Figure 24 HR ESI-MS Mass spectrum providing direct evidence for the desired NC. The charge states 3+ (dominant), is assigned in agreement with the molecular formula (mass ~ 36596 Da) of $Au_{144}(SC_2H_4Ph)_{60}$.

The “step-by-step” LER was optimized over time, and the optimized procedure is presented here:

1. 6 mg of Au_{144}PET was dissolved in 0.8 mL of deoxygenated THF, in a 25 mL flask. The solution was kept stirred at 300 rpm, in the dark. 1 µL (32 equiv) of PEG4, solubilized in 0.2 mL of THF, was slowly added to the flask. The reaction was stopped after 24 hours. After the reaction was stopped a lot of smell of phenylethanethiol was detected, proving the success of the LER. The

product was dried and washed several times with MetOH, until no more smell of free thiols was detected.

2. The product of step 1. was dissolved in 0.8 mL of deoxygenated THF, in a 25 mL flask. The solution was kept stirred at 300 rpm, in the dark. 1 µL (32 equiv) of PEG4, solubilized in 0.2 mL of THF, was slowly added to the flask. After 5 hours, the flask was put in hot oil-bath, connected to the refluxing glass, and left to react to reflux (T = 70 °C) for 18 hours. Then After the reaction was stopped a lot of smell of phenylethanethiol was detected, proving the further success of the LER. The product was dried, and the solubility checked. The step 2. LER's product was found to be soluble in MetOH. Moreover, to eliminate the excess of thiols present, several washes with a mixture of DCM and H_2O/MetOH were done. More in detail: The product was first solubilized in 1 mL of DCM, then 0.5 mL of H_2O were added, forming two phases. In addition, 0.5 mL of MetOH were added. After handshaking, the cluster moved in DCM and the H_2O/MetOH phase became cloudy (presence of free thiols). The washing process was done until the water phase was clear.
3. 6 mg of product of step 2. was dissolved in 0.6 mL of deoxygenated MetOH, in a 25 mL flask. The solution was kept stirred at 300 rpm, in the dark. 3 µL (96 equiv) of PEG4, solubilized in 0.4 mL of MetOH was slowly added to the flask, and left to react to reflux (T = 90 °C) for 5 hours. After that several washes with the same mixture of the previous step (DCM and H_2O/MetOH) were performed.
4. 6 mg of product of step 3. was dissolved in 0.6 mL of deoxygenated MetOH, in a 25 mL flask. The solution was kept stirred at 300 rpm, in the dark. 2 µL (64 equiv) of PEG4, solubilized in 0.4 mL of MetOH was slowly added to the flask, and left to react to reflux (T = 90 °C) for 5 hours. After that several washes with the same mixture of the previous step (DCM and H_2O/MetOH) were performed.

Here below, the UV-Vis spectra of the Au_{144} NC during the "step by step" LER.

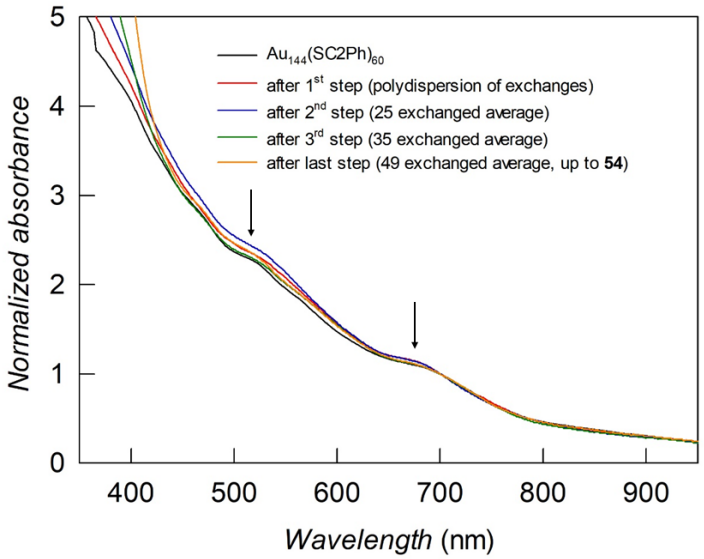

Figure 25 UV-Vis absorption of the purified products of the "step-by-step" LER, in toluene.

The presence of all the features (more evident ones at ca. 660 nm, and ca. 510 nm) of the original NC ($Au_{144}(SC_2H_4Ph)_{60}$), in all the purified products of the different steps, confirms that the nanocluster survives the LER and that the cores remain intact. Importantly, no other signals referring to the plasmon absorption band of Au NPs, at 530 nm, were detected. This is important to evaluate whether the reaction is destructive for the clusters. To understand if the LER was successful and, eventually, how many ligands were exchanged into the cluster monolayer during the "step-by-step" LER, HR ESI-MS mass spectrometry was employed. The mass spectra obtained after step 3 and 4 (Figure 26) show the success of the proposed LER and the obtaining of an almost completely exchanged Au_{144} (inset Figure 26).

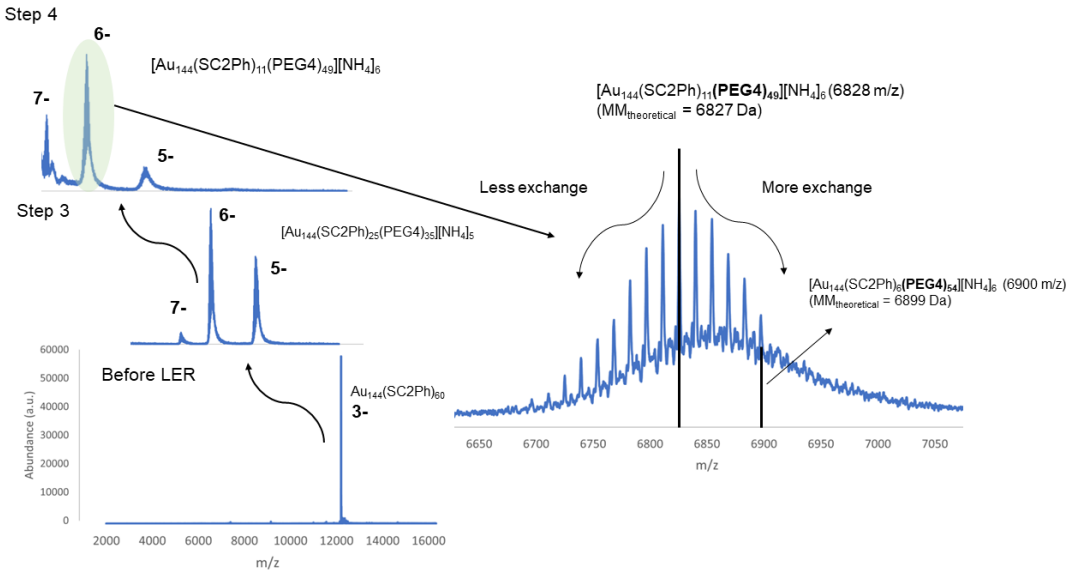

Figure 26 Negative mode HR ESI-MS Mass spectra (obtained adding the 10% in weight of ammonium formate) providing direct evidence of the success of the "step-by-step" LER. In the figure, the behavior of the mass spectra of Au_{144} NC is underlined. In the inset, the magnification of the -6-charge state signal related to the purified products of the last step of the LER is presented. The signal shown a gaussian distribution of exchanged cluster, pointed to 49 exchanges (dominant) over 60. The signal related to 54 exchanges, is also clear visible and underlined in the same inset. This proof the synthesis of a Au_{144} that introduced 54 novel ligands over the 60: $[Au_{144}(SC2Ph)_6(PEG4)_{54}][NH_4]_6$.

From the ESI spectra, we obtained information about the degree of exchange at every step-by-step LER. In particular, it is interesting to focus on the mass spectra of the purified product after the last step (top of the figure). It presents a Gaussian signal that refers to different exchanged clusters, centered at "value", corresponding to an Au_{144} that undergoes to 49 exchanges over the 60 possible. Moreover, the signal at a higher m/z value refers to a species composed of Au_{144} with 54 novel ligands and just 6 original ones. This last one refers to a species with a stoichiometry of $Au_{144}(SC_2H_4Ph)_6(PEG4)_{54}[NH_4]_6$, pointing to an almost completely PEGylated nanocluster. Interestingly, the sample with more PEG4 on the structure, showed more propensity towards ionization. Indeed, the ratio between the peaks of different charges changes (See left part of Figure 26), with a propensity to form more stable, more highly charged species the more advanced LER is, as expected having introduced a series of ligands that can easily accommodate negative charges, facilitating the ionization process of the ESI-MS experiment.

Thanks to this novel "step-by-step" LER we almost peghylated an Au_{144} NC, using a very small amount of exogenous ligands (approximately 60 times less, with more repeatable and safer results) by cleverly exploiting Le Chatelier's principle.

Going into more detail about the synthesis: we used the strategy of moving away the HSC2Ph (endogenous ligand) from the reaction environment, with the goal of pushing more the reaction toward the products (more exchanged clusters); we changed solvent, using MetOH, from step 3, with the goal of stabilized better the more polar products, that are the clusters with a higher exchanged degree. This was necessary from the second step onwards, as no success was obtained, just increasing the number of equivalents. During the LER, we had to change the washing and purification procedures, to cope with the different types of products we were producing, which are different degrees of exchange. Indeed, from step 2 we used a double phases extraction procedure, with which we moved all the free thiols away. The change in the procedure was needed because of the solubility of the Au_{144} when having at least 20-25 PEG4 ligands over 60. After reaching the 50 exchange (step 4) the extraction process becomes trickier as the Au_{144} starts to be quite soluble also in water.

6.4 Conclusions

In this work, through the strategic application of Ligand Exchange Reactions (LER), we have successfully achieved our dual objectives: (i) controlling the substitution on the Au_{25} nanocluster surface to produce monofunctionalized clusters with tailored properties for specific applications, and (ii) pushing the substitution degree on the Au_{144} nanocluster surface to synthesize novel nanoclusters that are otherwise inaccessible by direct synthesis, offering promising avenues for biological applications.

Addressing this last topic, we introduced a novel "step-by-step" LER strategy that effectively utilizes Le Chatelier's principle. This strategy involves continuously removing the free thiols (endogenous ones) generated by the LER from the reaction environment, thereby driving the reaction toward the production of more exchanged nanoclusters. In addition, we optimized the reaction conditions based on the product obtained at each step, changing times, temperatures, reaction solvent, and product purification procedures during the reaction. This novel strategy allowed us to produce an almost completely PEGylated Au_{144} cluster (Au_{144} protected by 54 PEG4 ligands over 60), by minimizing the amount of ligand reactants required (using approximately 30 times less respect to precedent procedures, with an astonishing ratio between the endogenous and the exogenous ligands of about just 1 over 3.5, with even more repeatable and safer results). The possibility of having an HR ESI-MS in the laboratory was fundamental for the success and optimization of the ligand exchange procedure. Regarding the first topic (i), we have implemented LER on $Au_{25}(SR)_{18}^{0}$, achieving single-ligand substitution on the nanocluster surface for the first time. This was accomplished using two distinct exogenous ligands: one bearing a carboxylic acid ending group and the other carrying a Fmoc-protected amine ending group. To maximize the yield of monofunctionalized Au_{25} nanoclusters while minimizing the production of higher substitution degrees, the experimental conditions of both LERs were meticulously optimized. Subsequently, we devised a novel strategy for extracting the monofunctionalized nanoclusters, resulting in samples of exceptional purity. The introduction of a single exogenous ligand among the eighteen ligands on the Au_{25}, coupled with the attainment of such high purity, presents a remarkable opportunity to meticulously investigate the impact of single functionalization on the nanocluster surface. Electrochemical characterization of Au_{25}-COOH by DPV revealed a potential shift towards more positive potentials, consistent with the electron-withdrawing nature of the carboxylic acid ending group. Furthermore, we

proposed a coupling reaction between the two monofunctionalized Au_{25} (Au_{25}-COOH and Au_{25}-NH_2), utilizing a modified amidation/condensation reaction to connect the two Au_{25} units via an amide bond.

These strategies pave the way for the design of novel LERs that enable precise molecular-level control over the functionalization of ligands within the monolayer of atomically precise metal nanoclusters. This opens up a vast array of possibilities, including the development of tailored units for constructing novel superstructures with applications in advanced materials design.

6.5 Experimental

MALDI-TOF mass spectrometry measurement:

Experiments were carried out with an Applied Biosystems 4800 MALDITOF/TOF spectrometer equipped with a Nd: YAG laser operating at 355 nm, with a laser firing rate of 200 Hz and an accelerating voltage of 25 kV. DCTB (trans-2[3-(4-tert-butylphenyl)-2-methyl-2-propenylidene] malononitrile, Sigma -Aldrich, ≥98%) was used as the matrix. The instrument was calibrated with $Au_{25}(SC_2Ph)_{25}$. The clusters were dissolved in DCM containing DCTB to obtain 0.2 mM solutions with a 1:400 nanocluster/matrix ratio. A 3 μL solution was drop cast onto the sample plate and air-dried. All spectra were recorded using the reflector negative-ion mode.

Calculation of the percentage of substituted species, from the MALDI-TOF spectra.

The relative percentage of different degrees of substituted Au_{25} nanoclusters was calculated considering the relative abundance of all the signals related to the nanoclusters, both of the parental ion species and of the Au_{21} fragmentation. This is done supposing a similar ionization activity and ease fragmentation between original Au_{25} nanocluster and cluster after undergoing to LER. This is a commonly used approximation for this type of evaluation.

Double solvent extraction using a phase transfer molecule.

The double solvent extraction was found to be successful on the separation of the monosubstituted Au_{25} nanoclusters, on the non-reacted one. The procedure for the extraction after LER with thiol (**1**) (and with thiol (**2**)) was as follows: The solid product was solubilized in Hexane (1 mL every 3 mg), in a 20 mL vial. Then 3-5 toluene drops were added and finally the MeCN (MetOH regarding thiol (**2**)) was added (1 mL every 3 mg). The vial was hand shacked, and 2 phases were formed: in the bottom the MeCN (MetOH) was pale yellow colored, while in the top the HEX was strong green coloreled. We eventually extracted the monofunctionalized Au_{25} nanoclusters from the bottom phase, using a 250 μL HAMILTON syringe. Not using the toluene drops, no phase transfer was observed.

HR ESI-MS measurements

Electrospray ionization mass spectra were acquired on Bruker time-of-flight (micrOTOF) mass spectrometer or Bruker maXis plus instruments (Bruker Daltronics), operated in the positiveion mode, with the mass-range typically set for m/z 3000–20 000. All spectra were acquired by direct infusion out of the neat DCM

solution of each sample, diluted to a concentration of 0.1 mg mL^{-1}, with further addition of ammonium formate (10% in weight). The flow rate was 10 µL min^{-1}, and typical data acquisition times were 0.5 min, such that each spectrum shown consumed ~5 µL of the solution, containing ~0.5 µg or ~15 pmol of dry sample. Mass spectrometer source conditions include: electrospray emitter −5 kV, endplate offset −500, capillary exit −100 V, skimmer 1–40 V, hexapole 1–23 V, hexapole rf 800 V, skimmer 2–23 V, lens 1 transfer time 300 µs, and prepulse storage 50 µs; MCP detector voltage 2400 V; nebulizer pressure, sheath gas, and dry temperature set usually at 1.5 bar and 0.0 L min^{-1} (no flow), and 30 °C, respectively. For the in-source collision-induced dissociation, the conditions were: electrospray emitter −5 kV, end plate offset −500, capillary exit −350 V, skimmer 1–33 V, hexapole 1–23 V, hexapole rf 800 V, skimmer 2–28.1 V, lens 1 transfer, and prepulse time 300 and 60 µs; MCP detector voltage 2500 V; nebulizer pressure and sheath gas set usually at 4 bar and 4 L min^{-1}, respectively

6.6 References

1. Dong, A.; Chen, J.; Vora, P. M.; Kikkawa, J. M.; Murray, C. B. Binary Nanocrystal Superlattice Membranes Self-Assembled at the Liquid–Air Interface. *Nature* **2010**, *466* (7305), 474–477.
2. Sánchez-Iglesias, A.; Rivas-Murias, B.; Grzelczak, M.; Pérez-Juste, J.; Liz-Marzán, L. M.; Rivadulla, F.; Correa-Duarte, M. A. Highly Transparent and Conductive Films of Densely Aligned Ultrathin Au Nanowire Monolayers. *Nano Lett.* **2012**, *12* (12), 6066–6070.
3. Cademartiri, L.; Bishop, K. J. M. Programmable Self-Assembly. *Nat. Mater.* **2015**, *14* (1), 2–9.
4. Zhou, B.; Shi, B.; Jin, D.; Liu, X. Controlling Upconversion Nanocrystals for Emerging Applications. *Nat. Nanotechnol.* **2015**, *10* (11), 924–936.
5. Lin, Q.-Y.; Mason, J. A.; Li, Z.; Zhou, W.; O'Brien, M. N.; Brown, K. A.; Jones, M. R.; Butun, S.; Lee, B.; Dravid, V. P.; Aydin, K.; Mirkin, C. A. Building Superlattices from Individual Nanoparticles via Template-Confined DNA-Mediated Assembly. *Science* **2018**, *359* (6376), 669–672.
6. Chen, L.-Y.; Wang, C.-W.; Yuan, Z.; Chang, H.-T. Fluorescent Gold Nanoclusters: Recent Advances in Sensing and Imaging. *Anal Chem* **2015**, 87, 216-229.
7. Parker, J. F.; Kacprzak, K. A.; Lopez-Acevedo, O.; Häkkinen, H.; Murray, R. W. Experimental and Density Functional Theory Analysis of Serial Introductions of Electron-Withdrawing Ligands into the Ligand Shell of a Thiolate-Protected Au $_{25}$ Nanoparticle. *J. Phys. Chem. C* **2010**, *114* (18), 8276–8281.
8. Gao, P.; Chang, X.; Zhang, D.; Cai, Y.; Chen, G.; Wang, H.; Wang, T. Synergistic Integration of Metal Nanoclusters and Biomolecules as Hybrid Systems for Therapeutic Applications. *Acta Pharm. Sin. B* **2021**, *11* (5), 1175–1199.
9. Gao, P.; Wu, S.; Chang, X.; Liu, F.; Zhang, T.; Wang, B.; Zhang, K.-Q. Aprotinin Encapsulated Gold Nanoclusters: A Fluorescent Bioprobe with Dynamic Nuclear Targeting and Selective Detection of Trypsin and Heavy Metal. *Bioconjug. Chem.* **2018**, *29* (12), 4140–4148.
10. Howes, P. D.; Chandrawati, R.; Stevens, M. M. Colloidal Nanoparticles as Advanced Biological Sensors. *Science* **2014**, *346* (6205), 1247390.
11. Tao, Y.; Li, M.; Ren, J.; Qu, X. Metal Nanoclusters: Novel Probes for Diagnostic and Therapeutic Applications. *Chem. Soc. Rev.* **2015**, *44* (23), 8636–8663.
12. Wu, J.; Wu, Y.; Bian, H.; Peng, Z.; Liu, Y.; Yin, Y.; Du, J.; Lu, X. Fabrication of a Ratiometric Electrochemiluminescence Biosensor Using Single Self-

Enhanced Nanoluminophores for the Detection of Spermine. *Talanta* **2023**, *253*, 123880.

13. Zan, X.; Li, Q.; Pan, Y.; Morris, D. J.; Zhang, P.; Li, P.; Yu, H.; Zhu, M. Versatile Ligand-Exchange Method for the Synthesis of Water-Soluble Monodisperse AuAg Nanoclusters for Cancer Therapy. *ACS Appl. Nano Mater.* **2018**, *1* (12), 6773–6781.

14. Zhu, H.; Zhou, Y.; Wang, Y.; Xu, S.; James, T. D.; Wang, L. Stepwise-Enhanced Tumor Targeting of Near-Infrared Emissive Au Nanoclusters with High Quantum Yields and Long-Term Stability. *Anal. Chem.* **2022**, 94, 38, 13189–13196.

15. Fei, W.; Antonello, S.; Dainese, T.; Dolmella, A.; Lahtinen, M.; Rissanen, K.; Venzo, A.; Maran, F. Metal Doping of $Au_{25}(SR)_{18}^{-}$ Clusters: Insights and Hindsights. *J. Am. Chem. Soc.* **2019**, *141* (40), 16033–16045.

16. Gunawardene, P.; Martin, J.; Wong, J.; Ding, Z.; Corrigan, J.; Workentin, M. Controlling the Structure, Properties and Surface Reactivity of Clickable Azide-Functionalized $Au_{25}(SR)_{18}$ Nanocluster Platforms Through Regioisomeric Ligand Modifications. *Angew. Chem. Int.* **2022**, 61.

17. Hossain, S.; Kurashige, W.; Wakayama, S.; Kumar, B.; Nair, L. V.; Niihori, Y.; Negishi, Y. Ligand Exchange Reactions in Thiolate-Protected Au_{25} Nanoclusters with Selenolates or Tellurolates: Preferential Exchange Sites and Effects on Electronic Structure. *J. Phys. Chem. C* **2016**, *120* (45), 25861–25869.

18. Jiang, D.; Dai, S. From Superatomic $Au_{25}(SR)_{18}^{-}$ to Superatomic $M@Au_{24}(SR)_{18}^{q}$ Core−Shell Clusters. *Inorg. Chem.* **2009**, *48* (7), 2720–2722.

19. Li, Y.; Biswas, S.; Luo, T.-Y.; Juarez-Mosqueda, R.; Taylor, M. G.; Mpourmpakis, G.; Rosi, N. L.; Hendrich, M. P.; Jin, R. Doping Effect on the Magnetism of Thiolate-Capped 25-Atom Alloy Nanoclusters. *Chem. Mater.* **2020**, *32* (21), 9238–9244.

20. Walter, M.; Moseler, M. Ligand-Protected Gold Alloy Clusters: Doping the Superatom. *J. Phys. Chem. C* **2009**, *113* (36), 15834–15837.

21. Wang, S.; Li, Q.; Kang, X.; Zhu, M. Customizing the Structure, Composition, and Properties of Alloy Nanoclusters by Metal Exchange. *Acc. Chem. Res.* **2018**, *51* (11), 2784–2792.

22. Agrachev, M.; Fei, W.; Antonello, S.; Bonacchi, S.; Dainese, T.; Zoleo, A.; Ruzzi, M.; Maran, F. Understanding and Controlling the Efficiency of $Au_{24}M(SR)_{18}$ Nanoclusters as Singlet-Oxygen Photosensitizers. *Chem. Sci.* **2020**, *11* (13), 3427–3440.

23. Antonello, S.; Maran, F. Molecular Electrochemistry of Monolayer-Protected Clusters. *Curr. Opin. Electrochem.* **2017**, *2* (1), 18–25.

24. Heinecke, C. L.; Ni, T. W.; Malola, S.; Mäkinen, V.; Wong, O. A.; Häkkinen, H.; Ackerson, C. J. Structural and Theoretical Basis for Ligand Exchange on

Thiolate Monolayer Protected Gold Nanoclusters. *J. Am. Chem. Soc.* **2012**, *134* (32), 13316–13322.

25. Wang, Y.; Bürgi, T. Ligand Exchange Reactions on Thiolate-Protected Gold Nanoclusters. *Nanoscale Adv.* **2021**, *3* (10), 2710–2727.

26. Kang, X.; Zhu, M. Transformation of Atomically Precise Nanoclusters by Ligand-Exchange. *Chem. Mater.* **2019**, *31* (24), 9939–9969.

27. Niihori, Y.; Kikuchi, Y.; Kato, A.; Matsuzaki, M.; Negishi, Y. Understanding Ligand-Exchange Reactions on Thiolate-Protected Gold Clusters by Probing Isomer Distributions Using Reversed-Phase High-Performance Liquid Chromatography. *ACS Nano* **2015**, *9* (9), 9347–9356.

28. Zhao, J.; Ziarati, A.; Rosspeintner, A.; Wang, Y.; Bürgi, T. Engineering Ligand Chemistry on Au_{25} Nanoclusters: From Unique Ligand Addition to Precisely Controllable Ligand Exchange. *Chem. Sci.* **2023**, *14* (28), 7665–7674.

29. Ding, M.; Tang, L.; Ma, X.; Song, C.; Wang, S. Effects of Ligand Tuning and Core Doping of Atomically Precise Copper Nanoclusters on CO_2 Electroreduction Selectivity. *Commun. Chem.* **2022**, *5* (1), 172.

30. Maity, S.; Kolay, S.; Ghosh, S.; Chakraborty, S.; Bain, D.; Patra, A. Unraveling the Effect of Single Atom Doping on the Carrier Relaxation Dynamics of MAg_{24}^{n-} Nanoclusters. *J. Phys. Chem. Lett.* **2022**, 5581–5588.

31. Kang, X.; Li, Y.; Zhu, M.; Jin, R. Atomically Precise Alloy Nanoclusters: Syntheses, Structures, and Properties. *Chem. Soc. Rev.* **2020**, *49* (17), 6443–6514.

32. Ghosh, A.; Mohammed, O. F.; Bakr, O. M. Atomic-Level Doping of Metal Clusters. *Acc. Chem. Res.* **2018**, *51* (12), 3094–3103.

33. Lin, C.-A. J.; Yang, T.-Y.; Lee, C.-H.; Huang, S. H.; Sperling, R. A.; Zanella, M.; Li, J. K.; Shen, J.-L.; Wang, H.-H.; Yeh, H.-I.; Parak, W. J.; Chang, W. H. Synthesis, Characterization, and Bioconjugation of Fluorescent Gold Nanoclusters toward Biological Labeling Applications. *ACS Nano* **2009**, *3* (2), 395–401.

34. Chen, L.; Black, A.; Parak, W. J.; Klinke, C.; Chakraborty, I. Metal Nanocluster-based Devices: Challenges and Opportunities. *Aggregate* **2021,** 3.

35. Chen, Y.-S.; Choi, H.; Kamat, P. V. Metal-Cluster-Sensitized Solar Cells. A New Class of Thiolated Gold Sensitizers Delivering Efficiency Greater Than 2%. *J. Am. Chem. Soc.* **2013**, *135* (24), 8822–8825.

36. Zeng, C.; Liu, C.; Pei, Y.; Jin, R. Thiol Ligand-Induced Transformation of $Au_{38}(SC_2H_4Ph)_{24}$ to $Au_{36}(SPh\text{-}t\text{-}Bu)_{24}$. *ACS Nano* **2013**, *7* (7), 6138–6145.

37. Dass, A.; Jones, T. C.; Theivendran, S.; Sementa, L.; Fortunelli, A. Core Size Interconversions of $Au_{30}(S\text{-}t\text{Bu})_{18}$ and $Au_{36}(SPhX)_{24}$. *J. Phys. Chem. C* **2017**, *121* (27), 14914–14919.

38. Shichibu, Y.; Negishi, Y.; Tsukuda, T.; Teranishi, T. Large-Scale Synthesis of Thiolated Au $_{25}$ Clusters via Ligand Exchange Reactions of Phosphine-Stabilized Au_{11} Clusters. *J. Am. Chem. Soc.* **2005**, *127* (39), 13464–13465.

39. Das, A.; Li, T.; Li, G.; Nobusada, K.; Zeng, C.; Rosi, N. L.; Jin, R. Crystal Structure and Electronic Properties of a Thiolate-Protected Au_{24} Nanocluster. *Nanoscale* **2014**, *6* (12), 6458.

40. Maman, M. P.; Nair, A. S.; Cheraparambil, H.; Pathak, B.; Mandal, S. Size Evolution Dynamics of Gold Nanoclusters at an Atom-Precision Level: Ligand Exchange, Growth Mechanism, Electrochemical, and Photophysical Properties. *J. Phys. Chem. Lett.* **2020**, *11* (5), 1781–1788.

41. Ho-Wu, R.; Sun, K.; Goodson, T. Synthesis and Enhanced Linear and Nonlinear Optical Properties of Chromophore–Au Metal Cluster Oligomers. *J. Phys. Chem. C* **2018**, *122* (4), 2315–2329.

42. Lahtinen, T.; Hulkko, E.; Sokołowska, K.; Tero, T.-R.; Saarnio, V.; Lindgren, J.; Pettersson, M.; Häkkinen, H.; Lehtovaara, L. Covalently Linked Multimers of Gold Nanoclusters Au_{102}(p-MBA)$_{44}$ and $Au_{\sim 250}$(p-MBA)$_n$. *Nanoscale* **2016**, *8* (44), 18665–18674.

43. Sokolowska, K.; Hulkko, E.; Lehtovaara, L.; Lahtinen, T. Dithiol-Induced Oligomerization of Thiol-Protected Gold Nanoclusters. *J. Phys. Chem. C* **2018**, *122* (23), 12524–12533.

44. Akola, J.; Kacprzak, K. A.; Lopez-Acevedo, O.; Walter, M.; Grönbeck, H.; Häkkinen, H. Thiolate-Protected Au_{25} Superatoms as Building Blocks: Dimers and Crystals. *J. Phys. Chem. C* **2010**, *114* (38), 15986–15994.

45. Hu, X.; Zheng, Y.; Zhou, J.; Fang, D.; Jiang, H.; Wang, X. Silver-Assisted Thiolate Ligand Exchange Induced Photoluminescent Boost of Gold Nanoclusters for Selective Imaging of Intracellular Glutathione. *Chem. Mater.* **2018**, *30* (6), 1947–1955.

46. Rival, J. V.; Nonappa; Shibu, E. S. Light-Triggered Reversible Supracolloidal Self-Assembly of Precision Gold Nanoclusters. *ACS Appl. Mater. Interfaces* **2020**, *12* (12), 14569–14577.

47. Kito, N.; Takano, S.; Masuda, S.; Harano, K.; Tsukuda, T. Au_{13} Superatom Bearing Two Terpyridines at Coaxial Positions: Photoluminescence Quenching via Complexation with 3d Metal Ions. *Bull. Chem. Soc. Jpn.* **2023**, *96* (9), 1045–1051.

48. Nag, A.; Pradeep, T. Assembling Atomically Precise Noble Metal Nanoclusters Using Supramolecular Interactions. *ACS Nanosci. Au* **2022**, 2, 3, 160-178.

49. Qin, Z.; Zhang, J.; Wan, C.; Liu, S.; Abroshan, H.; Jin, R.; Li, G. Atomically Precise Nanoclusters with Reversible Isomeric Transformation for Rotary Nanomotors. *Nat. Commun.* **2020**, *11* (1), 6019.

50. Zhu, M.; Aikens, C. M.; Hollander, F. J.; Schatz, G. C.; Jin, R. Correlating the Crystal Structure of A Thiol-Protected Au_{25} Cluster and Optical Properties. *J. Am. Chem. Soc.* **2008**, *130* (18), 5883–5885.

51. Dainese, T.; Antonello, S.; Bonacchi, S.; Morales-Martinez, D.; Venzo, A.; Black, D. M.; Hoque, M. M.; Whetten, R. L.; Maran, F. Isolation of the $Au_{145}(SR)_{60}X$ compound (R= n-butyl, n-pentyl; X= Br, Cl): novel gold nanoclusters that exhibit properties subtly distinct from the ubiquitous icosahedral $Au_{144}(SR)_{60}$ compound. *Nanoscale* **2021***, 13*(36), 15394-15402.

7. Langmuir Blodgett with ad-hoc Functionalized Nanocluster: Overcoming the Hydrophobic Barrier

7.1 Abstract

Atomically precise metal nanoclusters (NCs) are revolutionizing the field of nanomaterials, opening up unprecedented opportunities to fine-tune their properties for a wide range of applications. One of the most promising directions is the controlled assembly of NCs into functional films and materials. While Langmuir-Blodgett (LB) technique has proven to be highly effective for generating precise monolayers of amphiphilic molecules, it has remained almost elusive for NCs due to their intrinsic hydrophobicity or hydrophilicity, rendering them incompatible with the LB strategy. In this work, we present the first successful example of a real monolayer of molecular NCs achieved using the LB technique. This breakthrough was enabled by a novel surface modification strategy, introducing a single hydrophilic ligand onto the hydrophobic organic monolayer of an $Au_{25}(SC_3H_7)_{18}$ NC, effectively anchoring the NCs to the water phases of the LB. This innovative approach enabled the formation of the first single layer of atomically precise metal nanoclusters on water surfaces. The successful fabrication of this monolayer opens a new era in the development of functional materials based on these fascinating nanomaterials. These materials hold immense potential for applications in advanced nanoelectronics, sensors, and catalysis, paving the way for transformative technological advancements.

7.2 Introduction

The systematic study of Langmuir monolayers traces its roots to the pioneering work of Agnes Pockels and Irving Langmuir in the late 19th and early 20th centuries. Their investigations into the behavior of oil molecules at the water surface laid the foundation for this remarkable technique. Langmuir, in collaboration with Katherine Blodgett, further advanced the technique, demonstrating the ability to deposit well-defined multilayers of amphiphilic molecules onto solid substrates through a sequential immersion and extraction process.[1] This technique, now known as the Langmuir-Blodgett (LB) technique, has revolutionized the field of materials science, and opened up new avenues for the fabrication of functional materials with tailored properties.

Summarizing: The Langmuir-Blodgett (LB) technique stands as a renowned method for fabricating well-defined layered structures with molecular precision. It involves spreading amphiphilic molecules onto the surface of a water phase, known as the subphase, and compressing them into a highly condensed state (Figure 1).

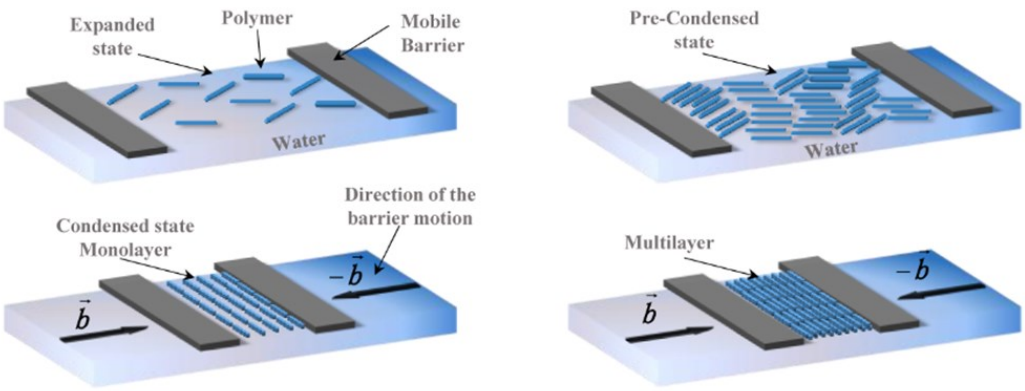

Figure 1 Schematic showing Langmuir compression and merging of monolayer (and eventually multilayers).[2]

Langmuir monolayers have emerged as a versatile platform for the fabrication of functional materials with tailored properties. These unique structures, meticulously controlled at the molecular level, exhibit exceptional properties, making them valuable for a wide range of applications.[3–9]

The preparation of Langmuir monolayers typically involves spreading solutions of water-insoluble amphiphiles in volatile organic solvents onto the surface of an aqueous subphase. Specialized Langmuir troughs equipped with movable barriers

allow for precise compression of the monolayer, effectively altering the area occupied by individual amphiphile molecules. In situ monitoring of surface pressure changes using a surface balance, typically of the Wilhelmy type, provides real-time insights into the monolayer's structural and thermodynamic transitions (Figure 2).

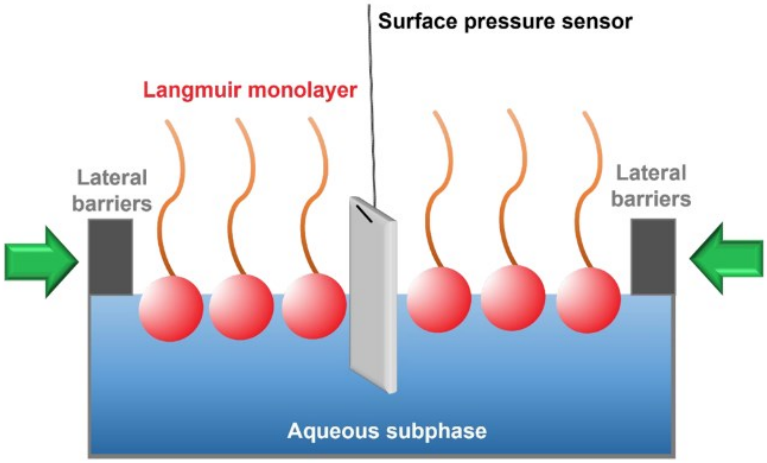

Figure 2 Typical Langmuir trough with lateral barriers to compress the monolayer laterally and a sensor (Wilhelmy type) to measure the surface pressure.[1]

One of the most common methods for evaluating Langmuir monolayers is through the surface pressure-molecular area (π-A) isotherm measurements. These isotherms, obtained by plotting surface pressure (π) as a function of molecular area (A) at constant temperature, provide valuable information about the monolayer's phase behavior, structural transitions, and from which the main molecular area can be calculated which is linked to the quality of the film produced. While the exact shape of π-A isotherms varies depending on the amphiphile's structure and the temperature, a typical isotherm exhibits distinct phases: Two-dimensional gaseous (G) phase: At large molecular area, monolayers exist in a disordered, gas-like state. Liquid-expanded (LE) phase: Compression of the monolayer results in a phase transition to the LE phase, characterized by increased order and mobility of amphiphile molecules. Liquid-condensed (LC) phase: Further compression induces a transition to the LC phase, where amphiphile molecules are tightly packed and exhibit long-range order. Eventually a two-dimensional solid-condensed phase (S) can merge: At the highest achievable surface pressures, the monolayer can eventually undergo a phase transition to the S phase, forming a crystalline structure with high rigidity.

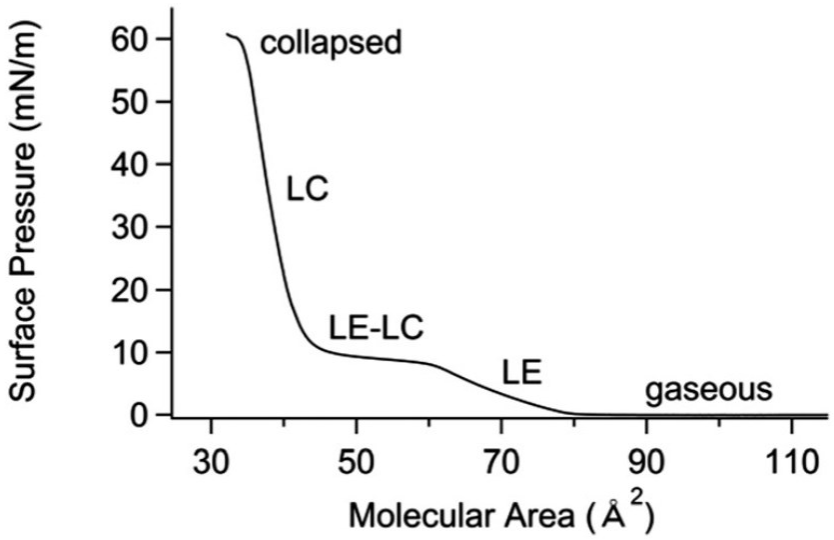

Figure 3 Typical surface pressure isotherm for a Langmuir monolayer of amphiphilic molecules.[10]

The maximum surface pressure, known as the collapse pressure, marks the limit beyond which the monolayer can no longer withstand compression and collapses into three-dimensional microcrystals. This information is critical for optimizing monolayer properties and ensuring their stability under specific conditions.[5]

The success of the LB technique hinges on the use of amphiphilic molecules with an appropriate hydrophilic-hydrophobic balance. For this reason, the majority of LB research has focused on molecules like fatty acids and phospholipids. However, recent advancements have expanded the scope of the technique to include unconventional materials, including metal nanoparticles[3,11,12] and atomically precise metal nanoclusters (NCs).[6,7,13–16] These nanoclusters, with a diameter of less than 1.6 nm, exhibit unique properties that can be exploited to create novel LB films with enhanced functionalities. Right now, there are very few works that have used molecular nanoclusters in a Langmuir Blodgett experiment. Among them, we must take into consideration the works of Burgi and his group. In the work of 2021 called "Deposition of Extended Ordered Ultrathin Films of $Au_{38}(SC_2H_4Ph)_{24}$ Nanocluster using Langmuir–Blodgett Technique",[13] they study for the very first time in our knowledge, in a systematic way, the deposition of ultra-thin films of molecular nanocluster, in particular of Au_{38} NC. They finely evaluated the effect of gradually increasing the surface pressures applied by the teflon barriers and following various lengths of time spent by the NCs on the water surface under constant compression before the deposition, by fast AFM measurements. They found, thanks also to XRR and GIWAXS experiments, a certain degree of vertical and in-plane re-organization of NCs within the film as well as the degree of interdigitation between the ligands of

neighboring molecules. The relevant factors controlling the assembly of these NCs include (i) π···π and C-H···π interactions between phenyl rings of adjacent molecules,[17] which increase in strength with the degree of interdigitation between ligands of the cluster within the 2D assembly, and in our opinion also (ii) the prolate shape of the considered molecules.[18] However, the prolate shape can have the disadvantage of making the calculation of the theoretical area of one Au_{38} NC in a 2D lattice (needed to evaluate the success of the formation of a single layer of molecules on the surface) very complicated, due to the different orientations that the molecule can have within the 2D material. Later in time, less than one year ago, they published another interesting study about ultra-thin films of Au_{38} NC made by LB strategy. In this work, they assessed information on the structural and nanomechanical properties of the produced film by bimodal atomic force microscopy and X-ray reflectivity. They demonstrated that Au_{38} NCs have a particular propensity to form trilayers, with LB technique.[19]

In conclusion, NCs hold immense promise as building blocks for the formation of ultrathin films with exceptional properties. However, despite their remarkable potential, the direct formation of a single monolayer of Au NCs using the Langmuir-Blodgett technique remains elusive. This challenge stems from the inherent hydrophobicity of Au NCs, which hinders their interaction with the aqueous subphase required for monolayer formation. To address this roadblock, we propose a novel strategy that involves functionalizing the Au NC surface with hydrophilic group.

7.3 Results and Discussion

Early experiments were conducted to investigate the formation of Langmuir films using unfunctionalized alkanethiolated-protected Au_{25} nanoclusters (NCs) with different ligand lengths (3, 4, and 10 number of C atoms). However, these attempts were unsuccessful, as the isotherms obtained for each cluster indicated a main molecular area far below the theoretical values. This finding can be attributed to the inherent hydrophobicity of the Au_{25} NCs, which are completely surrounded by a hydrophobic shell, rendering them incompatible with the water subphase. This hydrophobicity hinders the formation of a stable monolayer, leading to the initial formation of islands that grow into large structures as the solvent evaporates over time. These observations align with previous studies on similar systems.[3,12] (Please, see the “Supporting materials” section for the isotherms).

These preliminary results highlight the challenge of utilizing unfunctionalized Au_{25} NCs for LB assembly due to their hydrophobic nature. To overcome this limitation, we propose a strategy involving surface functionalization to introduce hydrophilic group onto the NC surface, enabling their effective interaction with the water subphase and facilitating the formation of well-defined monolayers. This approach holds the potential to significantly expand the range of nanomaterials amenable to LB techniques, opening new avenues for the fabrication of advanced functional materials.

7.3.1 Langmuir films of Au_{25} Nanoclusters: The Benefits of Having a Hydrophilic Component on the Hydrophobic Organic Shell

As already said in the previous paragraph, the formation of a single layer on the water-air interface was never achieved using hydrophobic NCs. Here above the isotherm obtained for the Au_{25} NC protected by propanethiols is shown.

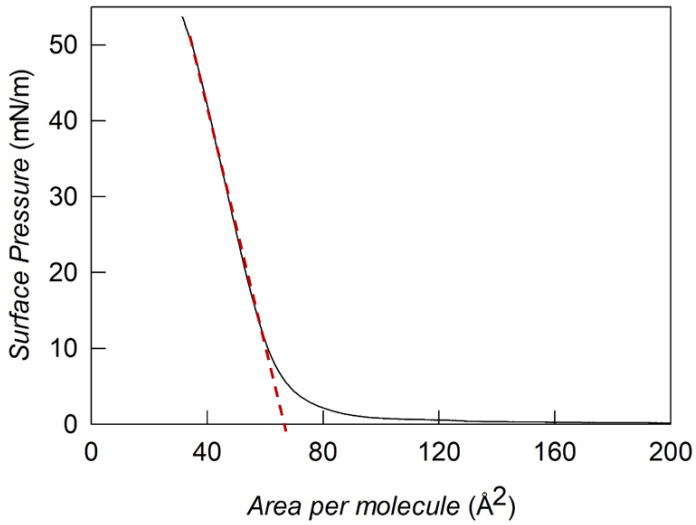

Figure 4 Surface pressure/area isotherm of $Au_{25}(SC_3H_7)_{18}$ film. Dashed line determines the main molecular area of the molecule at ≈ 66 Å^2.

Experimentally, 90 µL of a high concentrated solution of Au_{25} NC in DCM (2.3 mg/mL) were gently deposited on the water surface of the Langmuir bath (150 x 507 mm), by a Hamilton syringe. The speed of the barriers was set constant at 1 mm/m. From the obtained isotherm we calculated the main molecular area, obtained as the intersection point of the linear plot describing the maximum slope of the curve, with the x-axis (linear plot: $y = 104.41 - 1.57x$). The isotherm shape is as expected and very similar to already published isotherms of metal NCs,[13] but the obtained main molecular area (≈ 66 Å^2) is too low for the description of this type of molecule. The thus delayed

increase in surface area is certainly due to the formation of islands of Au NCs on the water surface, because of the hydrophobic nature of the molecules and the very small area per molecule point to a multilayers structure due to overlapping layers of nanoclusters. So, what would happen if we try to create a Langmuir film using a modified Au_{25} NC, to have a hydrophilic part able to better interact with the water phase?

We perform the same Langmuir experiment, using a monofunctionalized Au_{25} NC, bringing just one (over the 18 ligands) carboxylic acid ending group. In particular, we took advantage of the experience acquired in the control over the ligand exchange reaction (LER) using es exogenous ligand the 4-mercaptophenylacetic acid. The LER and the purification of the product has already been extensively explained in Chapter 6. Summarizing, we left the original Au_{25} nanocluster, protected by eighteen propanethiols, to react, for 1h, in toluene, with 1 eq of $HSPhCH_2COOH$. After that the solvent was removed with a rotary evaporator obtaining a sample with 30% of monosubstituted nanoclusters. Then we performed a double solvent extraction using a phase transfer molecule. With this purification strategy we were able to obtain a very high pure (over 80 %) monofunctionalized sample: $Au_{25}(SC_3H_7)_{17}(SPhCH_2COOH)$. Please see Chapter 6 for more information about the LER, purification procedures and characterizations. Having a sample bringing one hydrophilic group in the organic shell, represents, of course, a very interesting change to try to form a molecular monolayer by Langmuir-Blodgett procedure. The same amount of mol was used for the LB experiment. More in detail, we spread 200 µL of 1 mg/mL in DCM of sample, in the same LB bath (150 x 507 mm). The speed of the barriers was set constant at 1 mm/m. As for the previous experiment, we recorded the surface pressure as a function of the area per molecule. Here below the resulted isotherm, together with the one obtained for the original nanocluster before the LER, is shown (Figure 5).

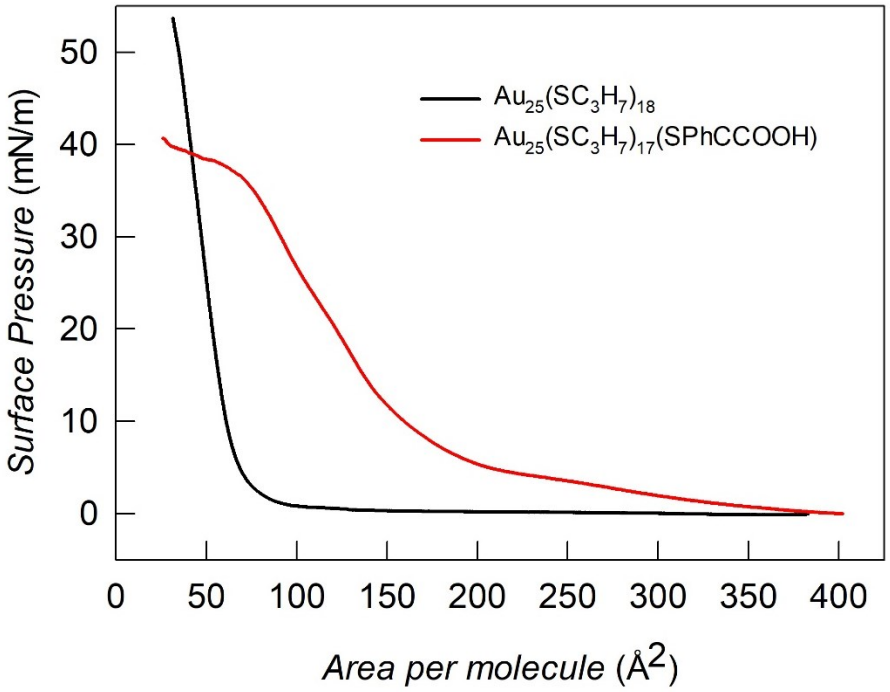

Figure 5 Surface pressure/area isotherm of the original and completely hydrophobic NC film (black line) compared with the one obtained after the monofunctionalization with the carboxylic ending group (red line).

The effect of the hydrophilic group, in the organic shell of the nanocluster, really changed the resulting isotherm that now starts to increase early and point to a larger main molecular area than before (with the original nanocluster). The fast increase of the surface area, contrary to what happens with non-functionalized nanoclusters, is consistent with the good spreading of the molecules on the water surface (no formation of islands). This is because of the chemical nature of the functionalization that resulted in being a good anchoring point for the NCs on the water surface, minimizing the possibility of multilayer structures. Looking more carefully to the isotherm (red line) you can also note the various phases described in the introduction to this chapter.

7.3.2 Analysis of the Langmuir Films of $Au_{25}(SC_3H_7)_{17}(SPhCH_2COOH)$: Calculation of the Geometrical Parameters

Now, focusing on the isotherm obtained using the monofunctionalized Au_{25} nanocluster, we can evaluate the main molecular area to compare it with the area per molecule (nanocluster). Here below the isotherm, with the maximum slope of the

curve (referred to the transition from liquid to solid phase) underlined by a dashed line.

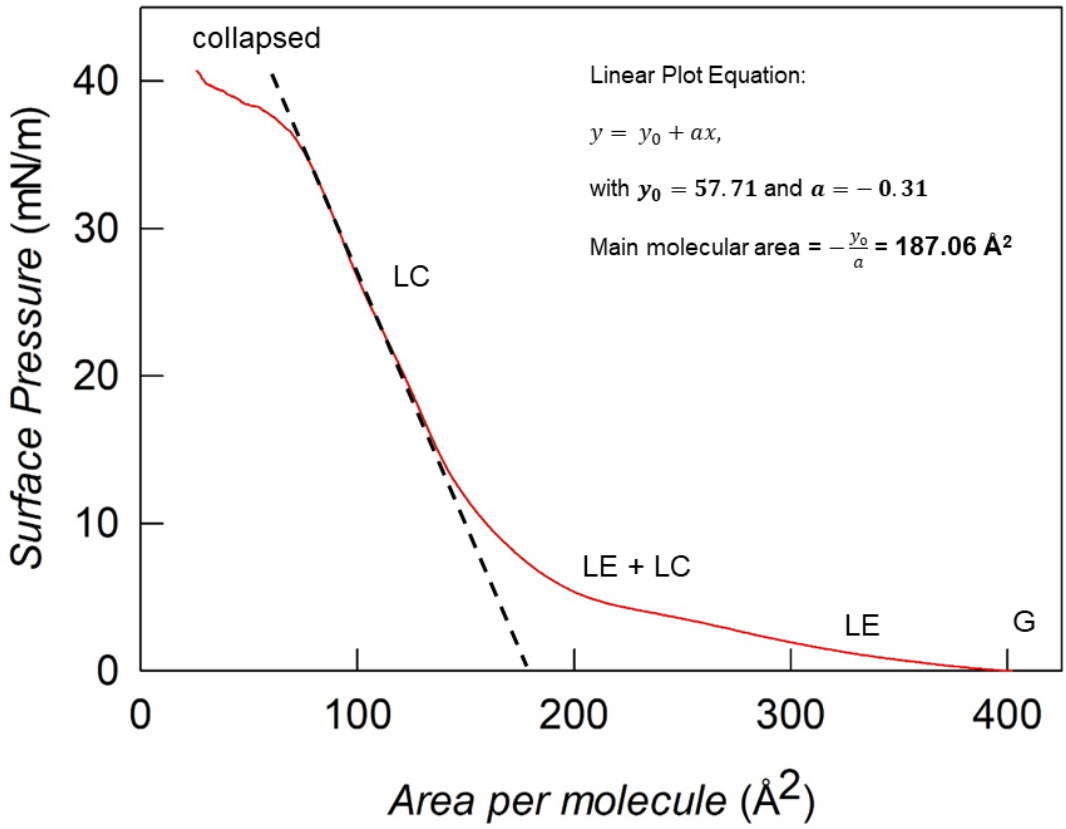

Figure 6 Surface pressure/area isotherm of $Au_{25}(SC_3H_7)_{17}(SPhCH_2COOH)$ film. Dashed line determines the main molecular area of the molecule at ≈ 187 Å^2. The various stages of the film's formation which are recognizable have been indicated (G = gaseous, LE = liquid-expanded, LC = liquid-condensed phases).

From the linear plot referred to the region where there is the maximum variation of the surface pression as a function of the area per molecule (transition from liquid to solid phase), we fit the data with a linear equation of $y = y_0 + ax$ type. From the inverse of the ration between y_0 and a we obtained the value of the main molecular area that represent the area occupied by each molecule (in this case nanocluster) on the water surface, inside his lattice structure. The obtained value is around 187 Å^2. To evaluate the quality of the obtained main molecular area we calculated the theoretical area per molecule when a monolayer of NCs is formed. For a collection of spherical particles, the highest average density is obtained for the hexagonal close-packed (hcp) arrangement. This is the approximation commonly used for this calculation.[13] Having just one anchoring group (the only one ligand bringing the carboxylic acid), and the remaining part (the one that must interact) perfectly spherical, there are no arrangement problems to take into consideration. However, interdigitation between

ligands can occur, resulting in lowering the expected main molecular area. For this reason, we have to take into account this phenomenon, as was previously done by Burgi and co.[13]

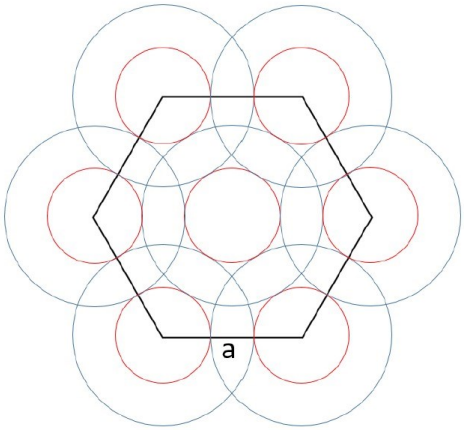

Figure 7 Top view of a hexagonal close packed arrangement. Red ovals represent the gold core, blue ovals represent the cluster size including the ligand shell. Here the full interdigitation scenario is represented.[13]

One unit cell accommodates three cluster molecules in an hcp arrangement, and therefore, area needed for one molecule in the lattice is calculated from $A = \frac{3\sqrt{3}a^2}{2}$, where a is the length of the side of the hexagon and it depends on the interdigitation degree between nanoclusters. We can distinguish two limit cases: (i) no interdigitation and (ii) full interdigitation between ligands. For the estimation of *a* we used the experimental hydrodynamic radius of the Au_{25} nanocluster. The radius is about 8.6 Å (4.9 Å from the core + 3.7 Å referred to the Stokes monolayer thickness).[20] So, *a* can have the values of (i) 17.2 Å (no interdigitation between ligands) or (ii) 13.5 Å (full interdigitation). From these we can calculate the two limiting cases regarding the main molecular areas, that resulted to be: (i) 256 and (ii) 158 $Å^2$. The experimental result about the main molecular area (187 $Å^2$) is therefore in agreement since it lies within the theoretical range expected from the formation of a perfect monolayer. More interesting, we found out that the value is perfectly in agreement with the interdigitation degree estimated from the analysis of the electron transfer (ET) in films of Au_{25}. Indeed, from considerations about the observed β_{film} value we demonstrated that partially interdigitations occurs when the nanoclusters are in the solid state. We estimated a progressively smaller interdigitation with the decrease of the ligand length. For a propanethiolate protected Au_{25} nanocluster we expect a distance between adjacent cores smaller of about 67%.[21] Taking this in consideration we re-calculate the value of *a* (14.76 Å), and so the new main molecular area that resulted

to be 188.62 $Å^2$. This value almost perfectly matches the observed one obtained from the experimental isotherm. This is proof of the formation of a monolayer of Au_{25} nanocluster on the water surface and therefore the efficiency of having even just one hydrophilic group on the surface of the NC.

7.4 Conclusions

Our work has enabled the successful formation of a single monolayer of Au_{25}, showcasing the remarkable impact of a hydrophilic anchoring group in the nanocluster's structure. By introducing a polar moiety onto one of the 18 organic ligands on the organic shell of the Au_{25} nanocluster, we effectively tailored its interfacial properties, rendering it amenable to Langmuir-Blodgett (LB) assembly. This strategic modification facilitated the establishment of a strong anchor between the NC and the water subphase, effectively preventing the formation of islands or multilayers as the barriers were compressed. The achievement of this monofunctionalized Au_{25} cluster was facilitated by our previous studies on ligand exchange reactions under molecular control. Comparing the isotherm of the monofunctionalized Au_{25} nanocluster with that of the non-functionalized counterpart, we were able to discern all the expected phases associated with this type of experiment. We also determined the main molecular area, which aligns perfectly with the theoretical area occupied by a cluster arranged in a hexagonal close-packed lattice, considering ligand interdigitation of 67%. This finding is in line with previous electron transfer (ET) measurements between adjacent nanoclusters in the solid state, further validating our experimental approach.

We strongly believe that this strategy and our findings will serve as a beacon of inspiration for researchers working with nanomaterials that are typically incompatible with the LB technique due to their hydrophobic nature, such as alkanethiolated-protected NCs. By overcoming this hurdle, we have expanded the realm of possibilities for creating molecular films, opening new avenues for the development of innovative devices and applications.

7.5 Experimental

Synthesis and functionalization of Au_{25} nanocusters: The synthesis and characterizations of the studied Au_{25} NC ($Au_{25}(SC_3H_7)_{18}$, $Au_{25}(SC_4H_9)_{18}$, $Au_{25}(SC_{10}H_{21})_{18}$) was made as already explain in section 2.5.1 and 2.5.3. The functionalization of $Au_{25}(SC_3H_7)_{18}$ to obtain the monofunctionalized $Au_{25}(SC_3H_7)_{17}(SPhCH_2COOH)$ was made as already explained comprehensively in Chapter 6, paragraph 6.3.1.1.

LB experiments:

Before starting the experiments, the LB trough (Kibron MicrotroughX) was thoroughly cleaned with acetone and ethanol and filled with Milli-Q water. Typically, 50-200 µL of Au_{25} nanocluster dissolved in 1-2.5 mg/mL solution of dichloromethane was carefully spread on the water surface, by a 100 µL Hemilton siringue, creating small drops that were gently deposited casually on the water surface of the 76050 mm^2 LB bath. After evaporation of the solvent, the barriers were slowly compressed (1mm/m, unless otherwise specified) until the desired surface pressure.

In particular: (i) for $Au_{25}(SC_3H_7)_{18}$ were deposited 3.08×10^{-8} mol. 90 µL of a concentrated solution of Au_{25} NC in DCM (2.3 mg/mL) were gently deposited on the water surface of the Langmuir bath (150 x 507 mm), by a Hamilton syringe. The speed of the barriers was set constant at 1 mm/m. Instead, (ii) for $Au_{25}(SC_3H_7)_{17}(SPhCH_2COOH)$ were deposited 3.14×10^{-8} mol. 200 µL of a concentrated solution of Au_{25} NC in DCM (1.0 mg/mL) were gently deposited in the LB bath (150 x 507 mm). The speed of the barriers was set constant at 1 mm/m.

7.6 Supporting Materials

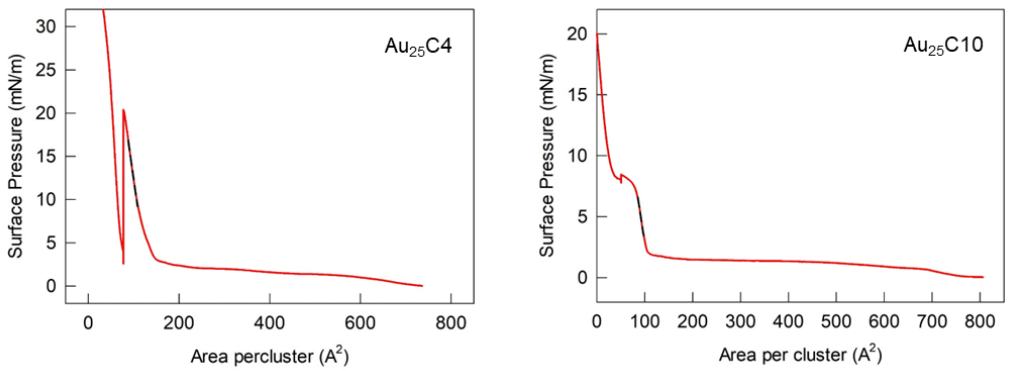

Figure S1 Surface pressure/area isotherm of $Au_{25}(SC_4H_9)_{18}$ (left side) and $Au_{25}(SC_{10}H_{21})_{18}$ (right side) films. Dashed line determines the main molecular area of the molecule at 134 and 111 $Å^2$ respectively,

very far from the theoretical ones (calculated as explained in 7.3.2 section) which should be, respectively, above 177 and above 293 $Å^2$.

7.7 References

1. Oliveira, O. N.; Caseli, L.; Ariga, K. The Past and the Future of Langmuir and Langmuir–Blodgett Films. *Chem. Rev.* **2022**, *122* (6), 6459–6513.
2. Bonacchi, S.; Gobbi, M.; Ferlauto, L.; Stoeckel, M.-A.; Liscio, F.; Milita, S.; Orgiu, E.; Samorì, P. High, Anisotropic, and Substrate-Independent Mobility in Polymer Field-Effect Transistors Based on Preassembled Semiconducting Nanofibrils. *ACS Nano* **2017**, *11* (2), 2000–2007.
3. Swierczewski, M.; Bürgi, T. Langmuir and Langmuir–Blodgett Films of Gold and Silver Nanoparticles. *Langmuir* **2023**, *39* (6), 2135–2151.
4. Ariga, K. Chemistry of Materials Nanoarchitectonics for Two-Dimensional Films: Langmuir–Blodgett, Layer-by-Layer Assembly, and Newcomers. *Chem. Mater.* **2023**, *35* (14), 5233–5254.
5. Ariga, K.; Yamauchi, Y.; Mori, T.; Hill, J. P. 25th Anniversary Article: What Can Be Done with the Langmuir-Blodgett Method? Recent Developments and Its Critical Role in Materials Science. *Adv. Mater.* **2013**, *25* (45), 6477–6512.
6. Brown, J. J.; Porter, J. A.; Daghlian, C. P.; Gibson, U. J. Ordered Arrays of Amphiphilic Gold Nanoparticles in Langmuir Monolayers. *Langmuir* **2001**, *17* (26), 7966–7969.
7. Chen, S. Langmuir Monolayers of Gold Nanoparticles: From Ohmic to Rectifying Charge Transfer. *Anal. Chim. Acta* **2003**, *496* (1–2), 29–37.
8. Acharya, S.; Hill, J. P.; Ariga, K. Soft Langmuir-Blodgett Technique for Hard Nanomaterials. *Adv. Mater.* **2009**, 21, 2959-2981.
9. Micky, S.; Bodik, M.; Micetic, M.; Fetzer, F.; Strienz, M.; Held, V.; Jergel, M.; Schnepf, A.; Schreiber, F.; Siffalovic, P. Multilayer Langmuir Film of Monodisperse Au Nanoclusters: Unusual Growth via Bilayers. *Langmuir*, **2022** *38*(48), 14850-14856.
10. Takeshita, N.; Okuno, M.; Ishibashi, T. Molecular Conformation of DPPC Phospholipid Langmuir and Langmuir–Blodgett Monolayers Studied by Heterodyne-Detected Vibrational Sum Frequency Generation Spectroscopy. *Phys. Chem. Chem. Phys.* **2017**, *19* (3), 2060–2066.
11. Bodik, M.; Jergel, M.; Majkova, E.; Siffalovic, P. Langmuir Films of Low-Dimensional Nanomaterials. *Adv. Colloid Interface Sci.* **2020**, *283*, 102239.
12. Schultz, D. G.; Lin, X.-M.; Li, D.; Gebhardt, J.; Meron, M.; Viccaro, J.; Lin, B. Structure, Wrinkling, and Reversibility of Langmuir Monolayers of Gold Nanoparticles. *J. Phys. Chem. B* **2006**, *110* (48), 24522–24529.
13. Swierczewski, M.; Maroni, P.; Chenneviere, A.; Dadras, M. M.; Lee, L.; Bürgi, T. Deposition of Extended Ordered Ultrathin Films of $Au_{38}(SC_2H_4Ph)_{24}$ Nanocluster Using Langmuir–Blodgett Technique. *Small* **2021**, *17* (27), 2005954.

14. Yokoyama, T.; Hirata, N.; Tsunoyama, H.; Eguchi, T.; Negishi, Y.; Nakajima, A. Vibrational Spectra of Thiolate-Protected Gold Nanocluster with Infrared Reflection Absorption Spectroscopy: Size- and Temperature-Dependent Ordering Behavior of Organic Monolayer. *J. Phys. Chem. C* **2020**, *124* (1), 363–371.

15. Kim, J.; Lee, D. Electron Hopping Dynamics in Au_{38} Nanoparticle Langmuir Monolayers at the Air/Water Interface. *J. Am. Chem. Soc.* **2006**, *128* (14), 4518–4519.

16. Chi, L. F.; Rakers, S.; Hartig, M.; Gleiche, M.; Fuchs, H.; Schmid, G. Monolayers of Nanosized Au55-Clusters: Preparation and Characterization. *Colloids Surf. Physicochem. Eng. Asp.* **2000**, *171* (1–3), 241–248.

17. Chakraborty, P.; Nag, A.; Chakraborty, A.; Pradeep, T. Approaching Materials with Atomic Precision Using Supramolecular Cluster Assemblies. *Acc. Chem. Res.* **2019**, *52* (1), 2–11.

18. Qian, H.; Eckenhoff, W. T.; Zhu, Y.; Pintauer, T.; Jin, R. Total Structure Determination of Thiolate-Protected Au_{38} Nanoparticles. *J. Am. Chem. Soc.* **2010**, *132* (24),

19. Swierczewski, M.; Chenneviere, A.; Lee, L.-T.; Maroni, P.; Bürgi, T. Nanomechanical and Structural Study of Au_{38} Nanocluster Langmuir-Blodgett Films Using Bimodal Atomic Force Microscopy and X-Ray Reflectivity. *J. Colloid Interface Sci.* **2023**, *630*, 28–36.

20. Antonello, S.; Dainese, T.; De Nardi, M.; Perotti, L.; Maran, F. Insights into the Interface Between the Electrolytic Solution and the Gold Core in Molecular Au_{25} Clusters. *ChemElectroChem* **2016**, *3* (8), 1237–1244.

21. Reato, M.; Dainese, T.; Antonello, S.; Maran, F. Electron Transfer in Films of Atomically Precise Gold Nanoclusters. *Chem. Mater.* **2021**, *33* (11), 4177–4187.

8. The Triad: A Step Towards Hierarchical Electroactive Materials

8.1 Abstract

Ligand exchange reactions (LERs) represent a versatile tool for tailoring the surface chemistry of atomically precise metal nanoclusters (NCs), offering the potential to create novel functional materials with tailored properties. One particularly intriguing aspect of LERs is the ability to connect NCs, forming hierarchical structures with enhanced functionalities. However, achieving precise control over LER processes remains challenging, often requiring chromatographic or molecular exclusion columns to separate the desired products from oligomeric byproducts. This work presents a novel triad system composed of two $Au_{25}(SR)_{18}$ clusters connected by a Ru(II) complex coordinated to three bipyridine ligands, one of which bears two $-CH_2SH$ groups, obtained by a novel LER's strategy that cleverly exploited electrostatic driving force between reactants. This gave us the possibility to form this new system, which we called triad, with high yield and completely minimizing the formation of uncontrolled oligomeric structures. The formation of the triad was confirmed by a suite of spectroscopic and electrochemical techniques, including UV-vis absorption spectroscopy, photoluminescence measurements, ESI mass spectrometry, nuclear magnetic resonance (^1H-^{13}C NMR), and cyclic voltammetry (CV) and differential pulse voltammetry (DPV). Intriguingly, the triad exhibited unexpected chemical-physical properties, such as: (i) Efficient energy/electron transfer: The Ru(II) complex emission, when in the triad, resulted quenched, most probably indicating efficient energy (or electron) transfer between the Ru center and the two peripherical Au NCs; and (ii) multi-redox responses: CV and DPV measurements revealed multiple redox processes, also suggesting electronic communication between the two NC cores. These findings demonstrate the potential of the triad system for applications in electroactive materials. The ability to control the electronic communication between the Au NCs and a metal complex through ligand modification provides a new dimension for designing functional materials with enhanced electrochemical activity. This work represents a significant advancement in the field of hierarchical electroactive materials, paving the way for the rational design of complex nanostructured architectures with tailored properties. The formation of the triad

system through a precisely controlled LER approach offers a promising platform for developing next-generation electrocatalysts and sensors devices.

8.2 Introduction

The chemical modification of nanocluster surfaces is a pivotal step in their assembly,[1–5] biomedical applications,[6–14] and in the optimization of their optical and electronic properties.[15–25] Ligand exchange reactions (LERs) stand out as the most versatile and effective method for manipulating the surface chemistry of these nanomaterials (Please see Chapter 6 for LER description). Alongside the widespread interest in the properties and applications of functionalized atomically precise gold nanoclusters (Au NCs), there has been a surge of research exploring their potential as molecular units for assembling larger superstructures, with a particular propensity for the search for dimers. This endeavor has been fueled by the realization that Au NCs can exhibit synergistic properties and functionalities when assembled into organized structures and novel materials.[26] Indeed, the pursuit of novel materials with enhanced functionalities has led to the exploration of alternative building blocks beyond conventional metal nanoparticles (NPs). Moreover, NCs, with their intrinsically ordered structure and perfect monodispersity, have emerged as a promising avenue for creating hierarchical materials with unique collective properties. Unlike NPs, NCs exhibit exceptional thermodynamic stability, enabling controlled size modulation, stoichiometry adjustment, and tailoring of their molecular surface chemistry. This opens the possibility of constructing a vast library of novel molecular units with atomically precise structures and established structure-property relationships. These unique attributes place NCs at the forefront of material science, offering the prospect of designing novel hierarchical materials with unprecedented properties. However, despite the tantalizing promise of self-assembled metal NCs, significant research is required to develop effective tools for controlling their assembly, self-assembly and functionality. The interplay between intercluster interactions, such as covalent bonding, hydrogen bonding, van der Waals forces, electrostatic interactions, π–π stacking, C–H-π interactions, metallophilic forces, and physical/chemical adsorption, dictates the organization of NCs into discrete multimers, 1D, 2D, and 3D architectures. As previously said, a lot of interest grown in the latest years, about the possibility of form dimers of Au NCs, with atomic molecular precision, with the aim of investigating new properties that can derive from having two nanoclusters in proximity and covalently bonded by a molecular bridge. Hakkinen and his collaborators paved the way for exploring this topic, using density functional theory (DFT) calculations.[27] Their study focused on simulating the discrete dimeric species formed by covalently linking anionic $Au_{25}(SR)_{18}$ nanoclusters with a benzene-1,4-dithiol (BDT) molecule (Figure 1).

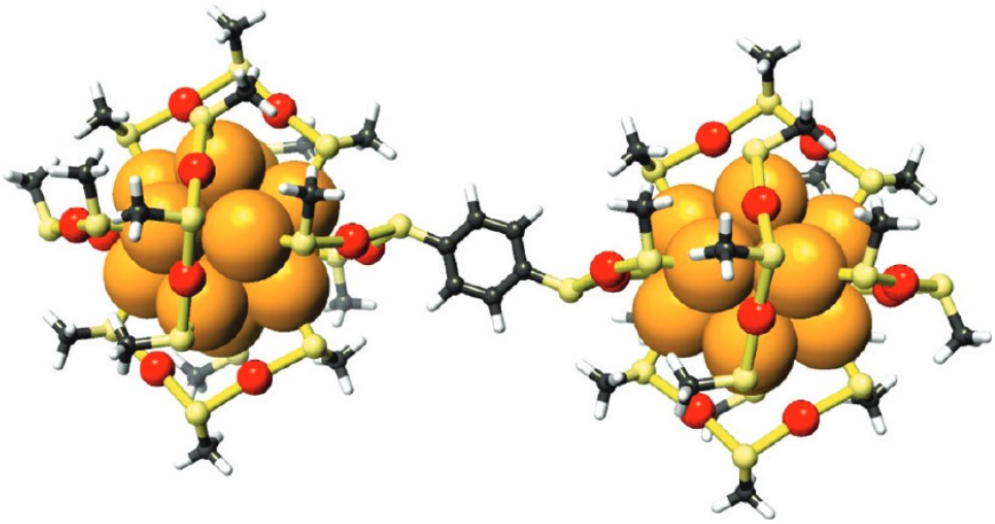

Figure 1 Structure of the relaxed $[Au_{25}(SCH_3)_{17}\text{-BDT-}(SCH_3)_{17}Au_{25}]^{2-}$ dimer. Color code: Au_{core} = orange, Au_{staple} = yellow, S = red, C = black, H = white.[27]

The optimized structure of the Au_{25} dimer revealed that Au_{25} units in the dimer retained their individual electron shell structures after linking with the dithiol ligand. In addition, calculations of the HOMO-LUMO gaps in the gas phase yielded almost identical values, while the density of states was higher for the dimers due to the individual contributions of the two Au_{25} units. This study highlighted the potential of using Au NCs as molecular units for dimers, provided suitable linking methods can be established. Recently, significant progress has been made in utilizing supramolecular chemistry to manipulate the ligand interactions of Au NCs, enabling the formation of intricate and reversible superstructures.[28–30] However, the controlled assembly of Au NCs into well-defined superstructures, with a precise understanding of the atomic-level structure of the resulting materials, remained a challenging endeavor. At this regard, another pioneering study by Hakkinen and colleagues in 2016, actually starts to cover this gap, demonstrating experimentally the covalent coupling of atomically precise Au_{102} and Au_{250} nanoclusters using a dithiol ligand as molecular bridge.[26] Unlike isolated Au NCs, these multimers exhibited hybridized plasmon modes with remarkably large red-shifts, likely arising from electron tunneling through the molecular states of the disulfide bridge. Motivated by these findings, several studies have attempted to synthesize new and well-defined Au NC-based superstructures using a bottom-up approach.[31,32] Among the most important examples it is necessary to mention the works of Burgi and his collaborators. In the recent years they perfectioned the LERs reaction most focusing on the dimerization of Au_{25} NCs, especially by using dithiolated exogenous ligands.[33,34] Indeed, very recently, they published a work about the formation of very stable dimer and trimers of Au_{25} NCs

linked with a very rigid bidentate dithiol.[33] Thanks to MALDI-TOF characterizations they were able to proposed the stoichiometry of the obtained superstructures (Figure 2).

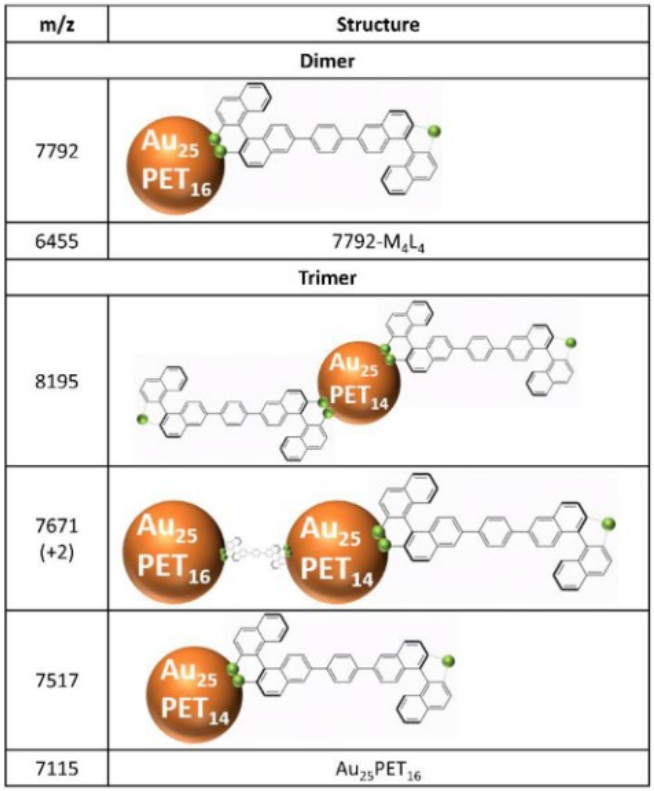

Figure 2 Proposed structures for selected MALDI-TOF MS peaks, obtained from LER using bidentate linker (1R,1'R)-6,6'-(1,4-phenylene)di-1,1'-binaphthyl-2,2'-dithiol. Sulphur atoms are shown in green.[33]

The strategy of using dithiols, that is a ligand that can simultaneously bind to both the initial NCs and the second one during the reaction, as exogenous ligand, is one of the most effective strategies for enhancing the stability of the final superstructures.[31–34] This strategy is particularly advantageous as it allows for the formation of more robust and stable linkages between the NCs, compared to strategies that rely on connecting two differently functionalized NCs. In our previous work (Chapter 6), we attempted to form a dimer by a condensation reaction between an Au_{25} NC with carboxylic acid monofunctionalization (Au_{25}-COOH) and a second Au_{25} with an amine monofunctionalization (Au_{25}-NH_2). Although we successfully detected the formation of this dimer using MALDI-TOF measurements, the stability of the superstructure was not satisfactory. However, while the previous works demonstrates the feasibility of forming stable dimers of metal NCs using rigid molecular-dithiolated bridges, it also highlights the challenges associated with purification and separation of byproducts. Indeed, these LERs often have the tendency of multiple ligand exchange that resulted in polysubstitution and uncontrolled growth of unwanted superstructures, requiring

chromatographic or molecular exclusion columns to separate the desired products from undesired byproducts. Inspired by this observation, we also shifted our focus to using particularly rigid dithiols as exogenous ligand, searching for new strategies with the goal of avoiding intense needed of post synthesis operations. To this regard, another work that significantly influenced our research was the synthesis of the first covalently linked dimer of Ag_{25} NCs by Pradeep et al., using a dithiolated Ru(II) complex as a molecular bridge, again synthesized via LER strategy.[35]

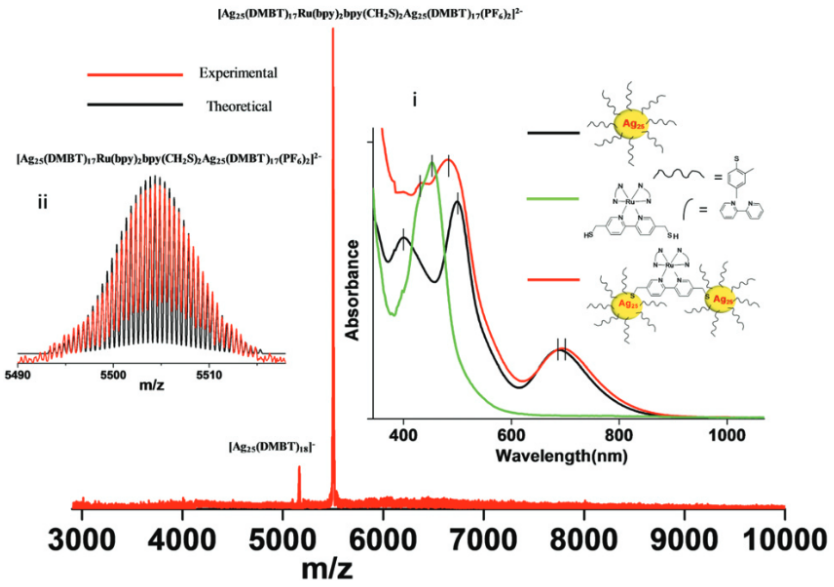

Figure 3 Full range ESI MS in negative ion mode of the Ag_{25} dimer $[Ag_{25}(DMBT)_{17}Ru(bpy)_2bpy(CH_2S)_2Ag_{25}(DMBT)_{17}(PF_6)_2]^{2+}$. Comparison of the optical absorption spectra of Ag_{25}, its dimer and $[Ru(bpy)_2bpy(CH_2SH)_2]^{2+}$ is shown in the inset (i). The experimental isotopic distribution of main peak is compared with the simulated spectrum in the inset (ii).[35]

This produced dimer exhibits minimal changes compared to the parent Ag_{25} cluster, indicating that the core structure remains largely intact. The observed redshift of a 600 nm absorption band and changes around 400 nm are attributed to optical coupling between the Ru(II)-based linker and Ag NCs. In addition to covalent bonding, non-covalent interactions, such as intercluster ligand-ligand van der Waals interactions or π-π interactions between the pyridyl rings in the linker complex and phenyl units in DMBT, are also believed to contribute to the stabilization of this dimeric structure. This work demonstrated the possibility of creating new Au_{25} dimers superstructures which can also house interesting chromophores, both from the point of view, for example, of ECL or photoelectrocatalysis activity, such as complexes of metal ions. Achieving this goal and the desired control over the superstructures formation requires the development of innovative synthetic strategies that can steer the assembly process

towards desired structures. This work presents an innovative strategy that utilizes electrostatic interactions to drive the formation of an insoluble product in the same reaction conditions. In particular, exploited the opposite charges of a Ru(II) complex and of two Au_{25} units, negatively charged, in a polar solvent suitable for charged ions. The formation of a precipitate as products effectively removes byproducts, leading to a completely self-cleaning reaction. This strategy demonstrates the potential for harnessing electrostatic forces to simplify reaction processes, enhance product purity and reduce the need for extensive purification steps, for the synthesis of novel dimeric superstructure based on atomically precise gold nanoclusters.

8.3 Results and Discussion

Synthesis of $Au_{25}(SC_2H_4Ph)_{18}^-$: This nanocluster was synthetized and characterized as detailed in Sections 2.5.1 and 2.5.3. The composition and the monodispersity of the new clusters were assessed by MALDI-TOF mass spectrometry, NMR spectroscopy, and electrochemistry.

Synthesis of dithiolated Ru(II) complex: $Ru(bpy)_2bpy(CH_2SH)_2](PF_6)_2$ was synthesised by an already published procedure.[36,37] 130.9 mg of $Ru(bpy)_2Cl_2$ x $2H_2O$ and 93.0 mg of 5,5´-Bis(mercaptomethyl)-2,2´-bipyridine were dissolved in degassed ethanol (15 mL) under nitrogen and heated to reflux overnight (T = 79-80 °C). After 18 h, the reaction mixture was allowed to cool at room temperature. After that a saturated methanolic solution of ammonium hexafluorophosphate was added. The product was kept in an ice-water bath to promote the precipitation (2 h). The precipitate was collected by filtration and washed with degassed ethanol (2 x 5 mL) and water (2 x 5 mL). The complex was characterized by UV-Vis (Figure 4) and photoluminescene spectroscopy, NMR spectroscopy, and electrochemistry (Please, see the “Supporting materials” section for characterization details). At the end of the reaction a yield of 66 % was calculated.

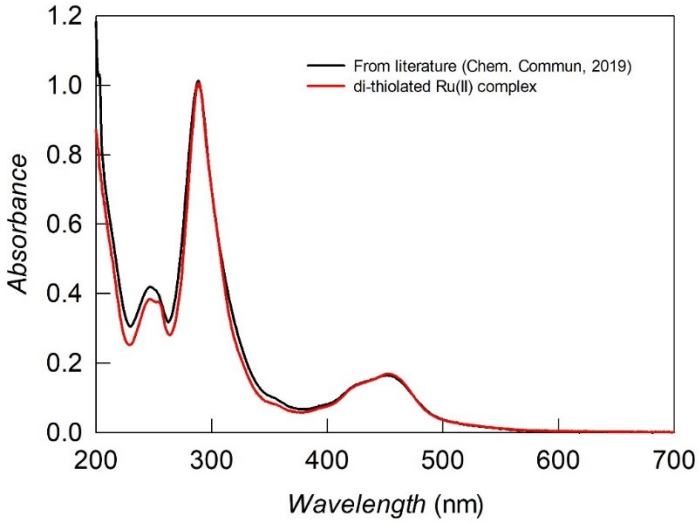

Figure 4 UV–vis absorption spectra of our modified Ru(II) complex (red line) compare with digitalized one (black line) from literature.[35] The matching with the literature spectrum demonstrated the success of the modification. The Ru(II) complex is now bringing two thiols functional groups and can be used as exogenous ligand in a LER. The literature curve was digitalized by CurveSnap Software.

8.3.1 Synthesis of the Novel Triad System via LER Strategy

The synthesis of the novel dimer system was done thanks to a Ligand Exchange Reaction (LER) methodology, using $Au_{25}(SC_2Ph)_{18}^-$ and the above-mentioned modified Ru (II) complex, bearing two anchoring groups (-CH_2SH) as exogenous ligand.

The LER was carried out by mixing 1 eq of Ru (II) complex with 2 eq of Au_{25}^-, in acetonitrile, in the dark, under an inert atmosphere. After 1 h, all the product precipitated in a metal-like black powder and the solution turns almost colorless. All the reactants and the sub-products (PhC_2H_4SH) are soluble in acetonitrile, so the reaction is self-cleaning and doesn't need any further purification. The solvent was eliminated, and the product was further washed several times with MeCN. After several characterizations that we will provide during this Chapter, we found the product to be a dimer of Au_{25}, connected by a Ru(II) complex molecular bridge. From now on this novel system will be called triad. The absence of oxygen during the synthesis was observed to be important for the purity of the reaction product, and so for the final yield (always over 95 %). The singlet oxygen, which can be formed in the presence of light, could affect the stability of the Au_{25}^-, with the results of oxidizing it and compromise the LER.[22] A precise control over the amount (equivalents) of exogenous ligands was observed to be fundamental for the LER result and to have a satisfactory yield. A better understanding of the reaction mechanism is beyond the

goal of this work and has therefore not been investigated in depth. Furthermore, we posit that electrostatic attraction between the reactants, driven by the positive charges of the Ru(II) complex and the negative charges of the Au_{25} NCs, plays a crucial role in facilitating this reaction and resulting in the formation of the unique triad system. This electrostatic driving force serves as a crucial "catalyst" in bringing the two components together, enabling their subsequent bond formation and the creation of this intriguing molecular architecture.

8.3.2 Mass Spectrometry: Triad as a Zwitterionic System

The triad system (the product of the just explained LER) was characterized by high resolution electrospray ionization mass spectrometry (HR ESI-MS). Figure 5 shows the ESI-MS result obtained from a diluted DCM solution, under mild conditions, and detecting the (+) ions by time-of-flight mass spectrometry (for details, see "Supporting materials" section).

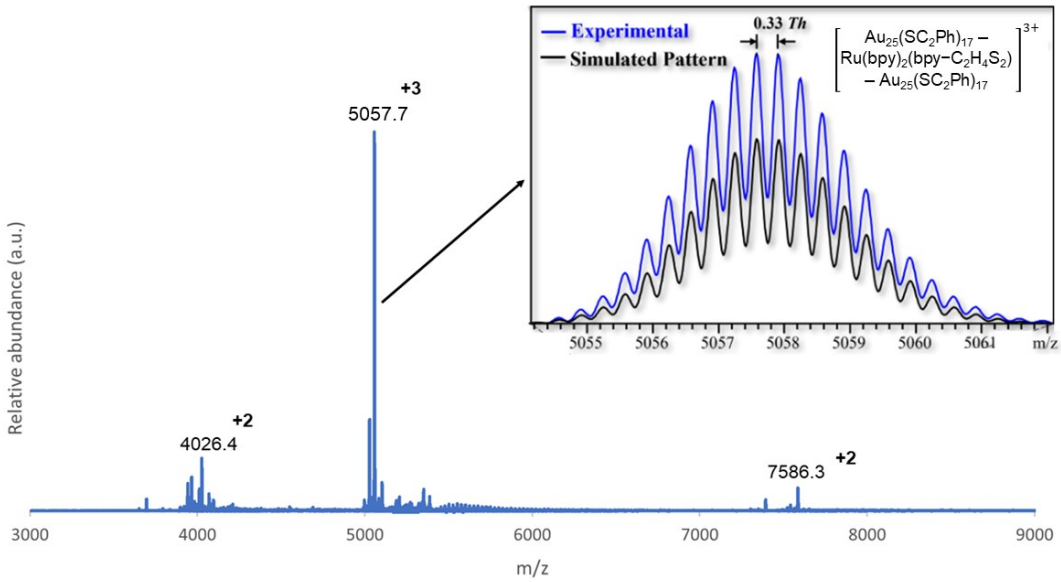

Figure 5 Mass spectrum providing direct evidence for the triad formation. HR ESI-MS (direct infusion positive ESI-MS, see details in the "Supporting materials" section) has been used to obtain the complete mass spectrum (bottom panel) in the m/z 3000-9000 range, wherein the charge states 3+ (5057.7, dominant) and 2+ (7586.3), are assigned in agreement with the molecular formula (mass ~15173 Da) of the putative synthetic product.

The ESI-MS spectra (m/z 3000-9000) display prominent peak centered at 15173 Da (5057.7, 3+), which closely align with the theoretical mass (15174 Da) calculated for the proposed molecular species, $Au_{25}(SC_2Ph)_{17}$ – $Ru(bpy)_2(bpy(CH_2S)_2)$ – $Au_{25}(SC_2Ph)_{17}$. In addition, another secondary signal is observed at 7586.3 m/z value,

referred to a 2+ charge state signal, and so attributable to the same molecular species (triad) which has undergone a different degree of ionization. This data conclusively demonstrate the successful synthesis and isolation of a novel Au_{25} dimer bearing a molecular Ru(II) complex bridge, achieved through a ligand exchange reaction methodology. During the reaction, each cluster exchanged one of its 18 ligands with the exogenous one, resulting in this unique species (Please, notice that the mass spectra considered the loss of two original ligands, as expected). The respective observed and simulated isotopically resolved patterns, with peak-to-peak m/z difference 0.33 Th (inset of Figure 5), agree with the molecular formula within the calibration uncertainty of m/z ± 0.1 unit (Thompson, Th). This represents the first example of a high-purity atomically precise Au_{25} dimer synthesized without the extensive use of chromatographic or size exclusion chromatographic (SEC) columns. The product effectively precipitated upon formation, eliminating the need for multi-exchange reactions, and ensuring the purity of the dimer. Notably, no counterions were detected during the mass measurements, unlike in a similar system with $Ag_{25,}$ presented by Pradeep and co.[35] This observation highlights the complete charge balance of the triad, where the ionic charges of the constituents are fully compensated within the dimer itself. Indeed, the triad could be correctly described as a zwitterion supermolecule. In addition, as you can see from the spectrum in the bottom panel of Figure 5, no additional signals were observed at high m/z value, and so no other superstructures were formed. Instead, the group of signals at about 4000 m/z (+2) are related to various Au_{25} fragmentations. We wanted to stress that no post synthesis separation procedures were used. This evidence demonstrating the efficiency and selectivity of the novel performed LER, which exploited firstly the electrostatic driving force and then a change in solubility of the desired product, which is completely insoluble in the reaction environment, eliminating any possibility of the formation of larger superstructures.

8.3.3 ^{1}H and ^{13}C NMR Spectroscopy and LER Selectivity

^{1}H-NMR spectroscopy provides valuable insights into the monolayer structure capping atomically precise gold nanoclusters, enabling the identification of preferential attachment sites for incoming ligands during LER. Figure 6 compares the ^{1}H-NMR spectra of the triad and the Ru(II) complex, obtained in DCM-d. The triad's ^{1}H-NMR spectrum exhibits three distinct groups of signals. The first group (1), spanning 2.90 to 3.15 ppm, comprises several -CH_2 signals, including the triplet of the

β-CH_2 outer, β-CH_2 inner, and α-CH_2 outer protons. The second group (2) centered at 3.56 ppm corresponds to the α-CH_2 inner ligands. Finally, the third group, extending from 7.00 to 7.20 ppm, represents the aromatic region encompassing all the aromatic signals of the phenyl ligands. All the signals were finely attributed thanks to previous works about the magnetic resonance spectroscopy characterizations of $Au_{25}(SC_2Ph)_{18}^-$.[38] The presence of weak signals associated with the Ru(II) complex ligands is also observed. Importantly, the absence of the triplet signal of the -HS proton at 1.92 ppm in the ^{1}H-NMR spectra of the triad confirms unequivocally the formation of the chemical bond between the S atoms of the Ru(II) complex and the Au atoms of the Au_{25} NCs (inset of Figure 6).

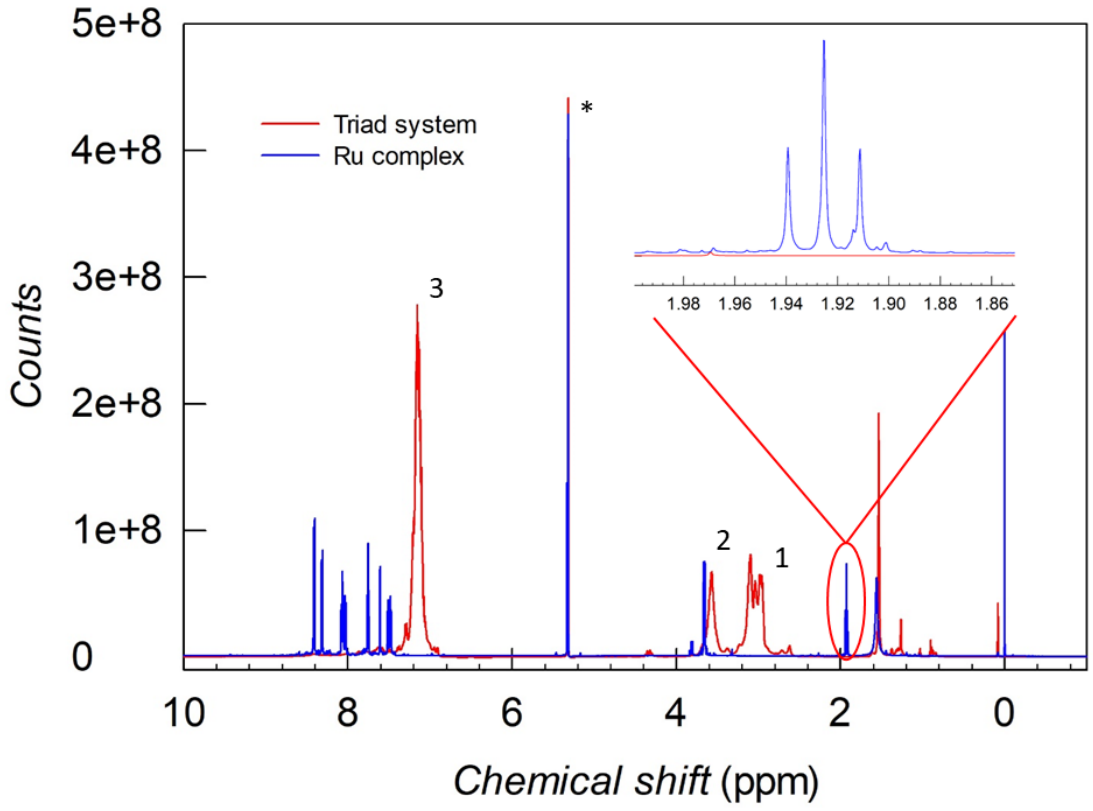

Figure 6 ^{1}H-NMR spectrum of 2 mM triad (red) and 3 mM Ru (II) complex (blue) in DCM-d at 25 °C. For better comparison, the signals of Ru (II) have been enlarged. In the inset the triplet signal of Ru (II), is proof of the formation of the -S-Au bond in the triad system.

Ratio 1:2 of Ru(II) complex and Au_{25} molecules is confirmed by signals integration. Furthermore, no TOA+ signals were detected, in line with what has already been established through ESI-MS characterization. This indicates that the triad presents the two Au_{25} NCs in their anionic form, but they are now neutralized by the two positive charges of the Ru complex, leading to a zwitterionic system (no counterions are required). Specific analyses about that are provided in the “Supporting materials”

section. By calculating the integral of the staple NCs signals (groups 1 and 2) in the triad's ^{1}H-NMR spectrum, insights into the binding position of the ligand during the LER reaction could be obtained. However, this analysis proved challenging due to signal overlap, making it difficult to define the precise ppm range for integration. To further elucidate the positioning of the Ru(II) complex within the NC structures, ^{13}C-NMR spectroscopy was employed. The ^{13}C-NMR spectra of the triad exhibit all staple NCs signals as multiples. This observation suggests that the ligand exchange reaction occurred without any preferential pattern (in-in, in-out, out-in, and out-out positions; Please, see the “Supporting materials” section). This finding appears to contradict previous experimental and computational studies that indicated a preferential attachment site at the inner ligands of each staple.[39,40] However, recent works demonstrated that the trend can be modified increasing the donation reactivity of the substituents on the exogenous ligand, or using ligands that can structurally stabilized the monolayer structure of the final system. In these cases, we can observe not preferentiality over the LER or even a reverse selectivity.[41,42] In addition, it's important to consider that our LER, capable of forming the triad, involves not just a single ligand exchange but a coupled second ligand exchange reaction. As the Ru(II) complex interacts with two different clusters during this process, the second ligand exchange is likely to be significantly influenced by the stability achieved after the formation of the triad. Of course, a reaction involving multiple exchanges of ligands is unpredictable and difficult to rationalize on a mechanistic level, without ad-hoc kinetic studies, but this is beyond the goal of this work and has therefore not been investigated deeply. However, based on these observations, we propose that the first ligand exchange occurs preferentially at the inner ligands, while the second exchange is more random, likely governed by geometric and spatial factors. This could explain the multiplets observed in the ^{13}C-NMR spectrum. In conclusion, NMR spectroscopy gives us information about the selectivity of the performed LER, that resulted to have no preferentiality. In addition, we demonstrated once again the high level of purity of the obtained superstructure since no parasitic signals were observed.

8.3.4 Absorption Optical Properties

The UV-Vis absorption spectra of the triad exhibit striking resemblance to the simulated spectra, closely replicating the individual features of both the Au_{25} clusters and the Ru(II) complex (Figure 7). It is noteworthy that the spectral features attributed to the two Au NCs still reflect the -1 oxidation state, confirming the preservation of the

Au_{25} metal core structure and redox charge state after the ligand exchange reaction (LER).

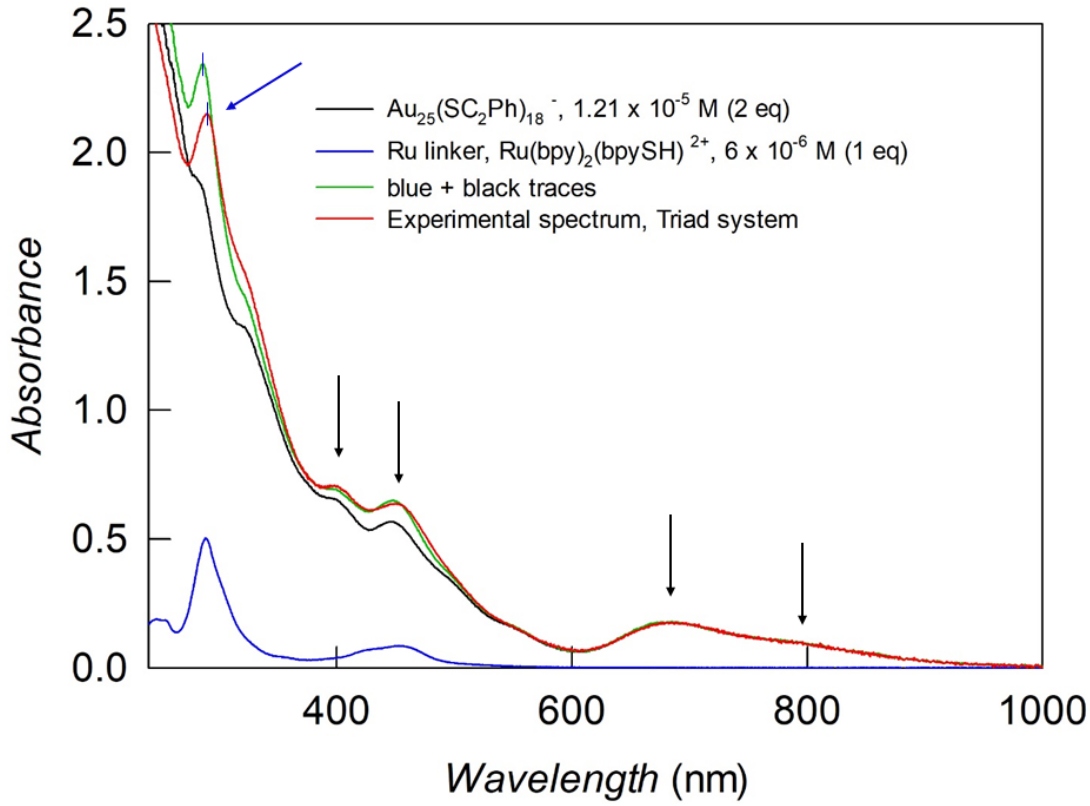

Figure 7 UV–vis absorption spectra of the product compare with the two reactants (blu trace for the Ru(II) complex and black trace for the Au_{25}^{-}) and the theoretical dimer UV-vis absorption spectrum, considering the simply summation of the previous reactants spectra (green trace). The features of Au NC, in the triad, are marked with black arrows, instead of the feature of Ru (II) complex in blue. All the experimental spectra were performed in DCM, at T = 25 °C, in a 10 mm cuvette.

Under 500 nm region, where the Ru(II) complex exhibits minimal absorption, the triad's UV-Vis spectra demonstrate an identical behavior, mirroring the HOMO-LUMO gap, of the Au_{25} cluster in its -1 charge state. This observation strengthens the integrity of the Au_{25} metal core structure. In the region between 500 and 400 nm, the absorption peaks attributed to the Au_{25} clusters become less pronounced due to the presence of the Ru(II) complex's absorption signal in the background. The Ru(II) complex's characteristic signal becomes more evident below 300 nm, where the Au NCs exhibit minimal absorption features. In this wavelength region, the UV-vis spectra reveal a prominent absorption band arising from the ligand-centered transition ($\pi \rightarrow \pi^*$) (Figure 4). Overall, the experimental UV-Vis behavior of the triad closely resembles the simulated/calculated spectra (green line in Figure 7), suggesting a limited degree of communication between the Au_{25} clusters and the Ru(II) complex. However, this

was expected also from DFT calculations on very similar simulated system.[26] The only notable difference lies in a slight red shift observed, especially, at 300 nm, indicating minimal overlapping between the molecular orbitals of the constituent units. This shift was previously attributed to optical coupling between the three components.[35] To further investigate these spectral differences, we calculated the differences between the experimental and simulated spectra, with the goal of obtaining new evidences of electronic coupling between the part constituting the triad. The analysis is shown in figure 8.

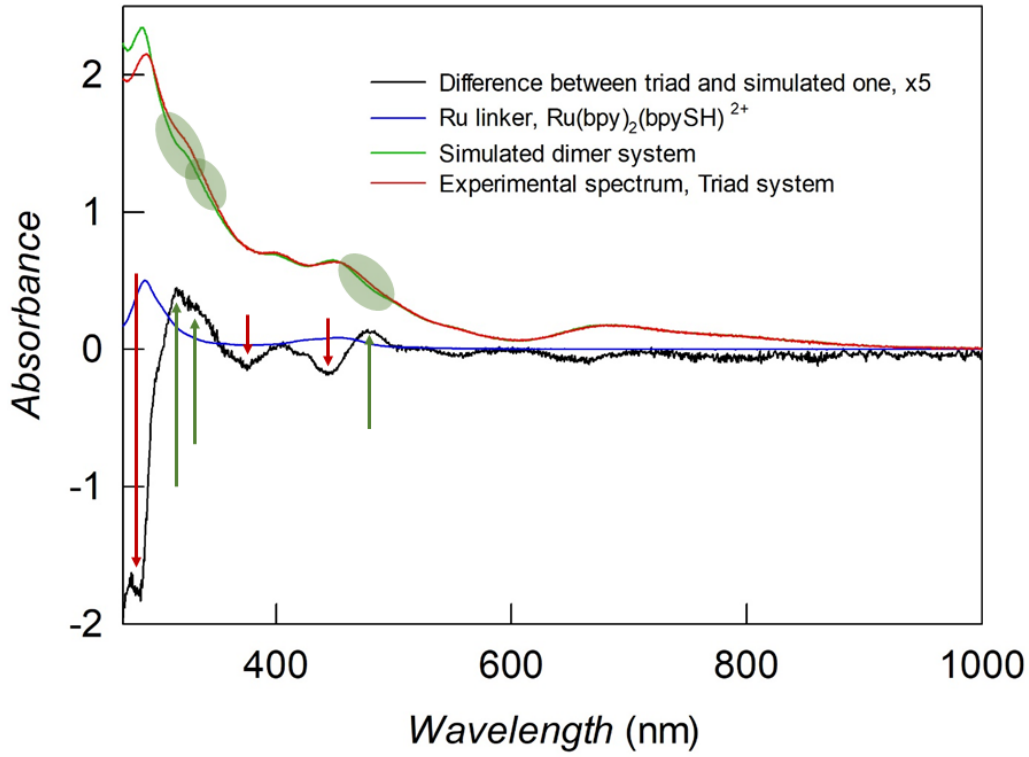

Figure 8 UV-vis spectra of simulated triad system (considering the summation of the three components) (green line) and the experimental spectrum of the triad (red line). In black the difference between the two curves is presented. The difference's signal was arbitrarily scaled by factor 5. In blue the Ru(II) complex is shown. In the Figure the regions where a drop in the optical absorption is observed, is underlined by a red arrow, while the regions where an increase in the absorption happens, green narrows were used. In the inset the zoom of the under 300 region is shown.

This analysis revealed the emergence of new electronic transitions in the UV-Vis region. Notably, a new maximum appears at about 320 nm. These features do not closely resemble the transitions of the individual components, suggesting the possibility of optical coupling between the cores of the Au_{25} clusters. Similar spectral changes have been observed previously in dimers and oligomers of larger clusters. [26] Moreover, all the electronic bands related to the Ru(II) complex, resulted suppressed of a certain degree (red arrow in Figure 8), suggesting, optical coupling

with the two peripheral Au_{25} NCs, which is probably due to the approaching and therefore thickening of the energy levels of the two clusters to the detriment of the orbitals of the metal complex. Finally, the absorption coefficient of the triad, calculated from the experimental UV-Vis spectrum, was determined to be 9.97 x 10^4 $cm^{-1}M^{-1}$. The optical properties of the triad were also monitored from 1000 to 1800 nm, revealing no signals, in agreement with the absence of oligomeric (bigger) superstructures (Please, see "Supporting materials" section).[42]

8.3.5 Photoluminescence

While the absorption properties of the triad suggested a possibility of optical coupling (even if very mild), the emission properties provide definitive evidence of communication between the constituent units. The emission spectra of the triad (Figure 9) unveil almost the same peak position of the Au_{25} at its -1 charge state, confirming one more time the charge state of the Au_{25} NCs inside the triad system.

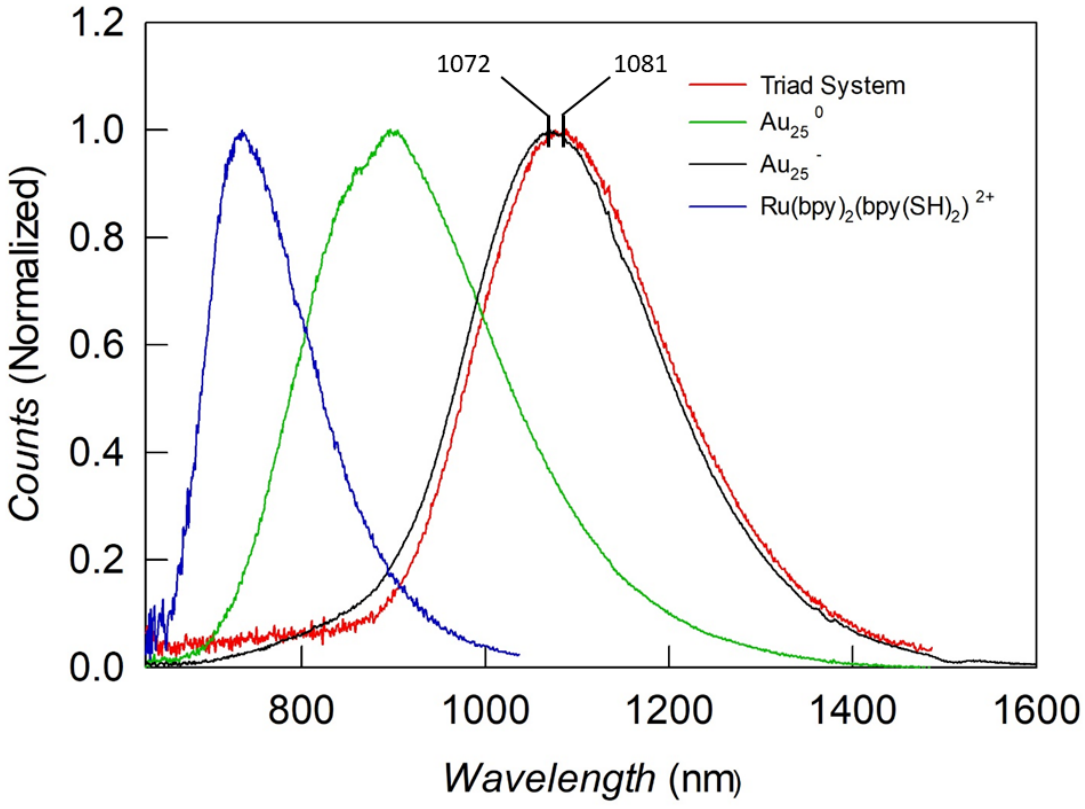

Figure 9 Emission spectra obtained upon excitation at 450 nm of 1 × 10^{-6} M of triad, compared with the two reactants (Ru (II) complex in blue trace and Au_{25}^- in black trace) and the Au_{25} in his 0 charge oxidation state (green trace). The triad, $Au_{25}^-$and the Ru (II) complex was conducted in deuterated DMF, at room temperature, instead Au_{25} (0) was conducted in toluene, at room temperature. The small deformation of the traces at 870 nm is an instrumental artifact related to the photomultiplier and spectral response of the emission grating.

The emission analysis revealed a striking redshift of about 9 nm, attributed to an enhanced energy transfer between the Au_{25} cores and their ligands, likely facilitated by the Ru(II) complex.[43] This observation is further corroborated by the complete absence of any emission signal characteristic of the Ru(II) complex in the triad's emission spectra (see Figure 9, no emission signals under 900 nm). Indeed, we want to stress that the presented spectra are obtained under the same experimental conditions and exciting at the same wavelength. While, in this conditions, the Ru(II) complex presented a very high and characteristic band centered at 740 nm (at higher wavelength respect to reported value[44], because of the detector used) the triad do not. Since we demonstrated the presence of the Ru(II) complex in the structure of the triad, thanks to ESI-MS spectrometry, but also ^{1}H-NMR and UV-Vis spectroscopy, we can conclude that the emission of the Ru(II) is quenched in the triad system, most probably for a high intramolecular energy (or electron) transfer from it to the two peripheral Au_{25} NCs. This also agrees with the observed red-shift on the Au NC emission peak. Indeed, previous works about the formation of triad-like systems demonstrated quenching in the Ru(II) complex emission.[45–49] The mechanism of the observed charge transfer is not fully understood yet, and sometimes was prove to be distance independent[46] and sometimes not.[45] Interesting, regarding superstructures made by NC units, very recently Burgi and collaborator published a work about the formation and isolation of monofunctionalized Au_{25} NC, with a thiol-functionalized terpyridine Ru(II) complex. They also observed a quenching in the emission of the chromophore, that was attributed to energy transfer from him to the NC.[50] When the superstructure became big enough, the supposed coupling, between components, could be also generated by a physiologic disposition of the molecular orbitals arising from the dimer formation itself. Indeed, the orbitals always resulted in being denser and closer together when a superstructure is formed. In this scenario, the excited and ground states of the triad can be better overlapped than before, with the effect of a more probable non-radiative relaxation. In conclusion, this phenomenon is the first proof of how this new species certainly acts as a triad system in which the unity components are collaborating with each other, with the results of modifying the properties of the individual constituents.

8.3.6 Electrochemistry: Evidence of Electronic Communication and Multicomponent Redox Behavior

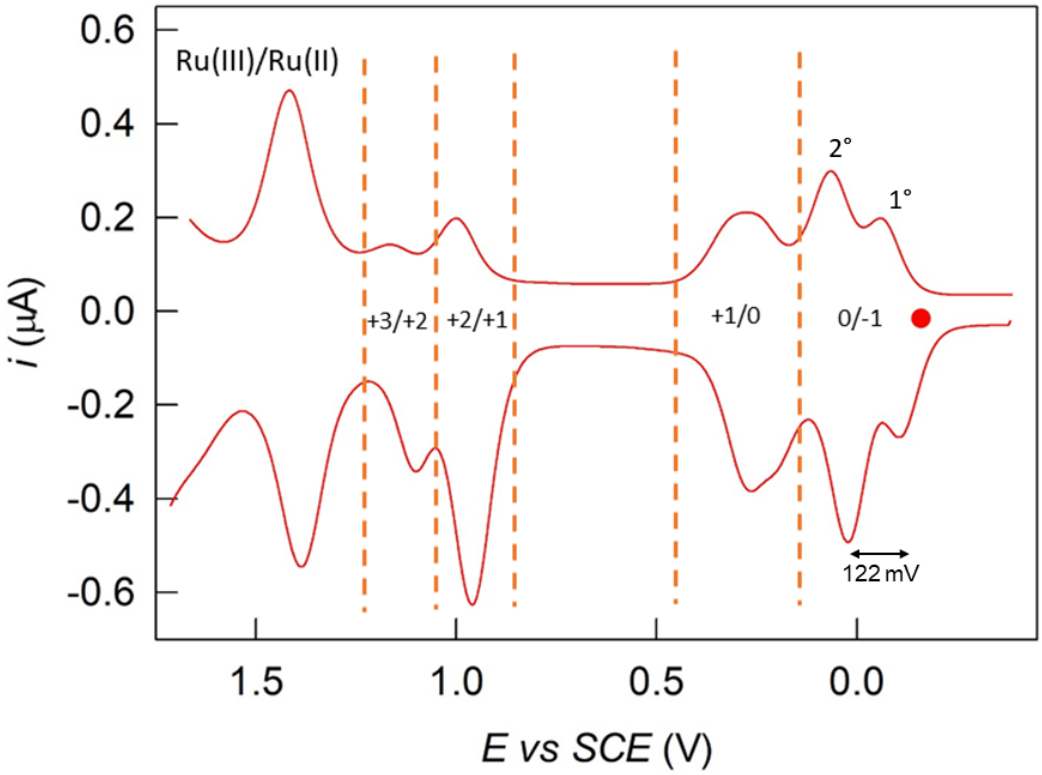

Figure 10 DPV curves in the oxidative region, for 0.6 mM Triad in DCM/0.1 M $TBAPF_6$ at 22 °C. The red circle marks the equilibrium potential. The graph was divided with a orange dot line for better appreciated the redox processes that we observed. The red circles mark the equilibrium potentials.

The electrochemical behavior of the triad, within the oxidative potential window, cannot be simply described as the sum of the redox processes of its constituent units although typical features of them are recognizable. Indeed, four processes related to the oxidation of the two Au_{25} NCs (from -1 to +3 redox-charge states) are observed and underlined in the figure by orange dot lines dividing the potential region where the oxidation is taking place. In addition, at high oxidation potentials, close to +1.4 V vs SCE, the peak related to the oxidation of the Ru(II) complex, (Ru(II) → Ru(III)), is observed. (Please, see the "Supporting materials" section for the complete electrochemical characterizations, also in the reduction potential window). In any case, the most intriguing aspect are the first two oxidation processes of the Au_{25} in the triad system (from -1 to 0 and from 0 to +1 charge-redox state). Indeed, the first oxidation process appears split into two processes (1° and 2° in Figure 10), while the next oxidation processes (from +1/0 onwards) are less affected, since the second oxidation process appears enlarged and the emergence of a shoulder is observed, while the third and the fourth ones seems to be not, or just mildly, affected. This

observation seems to be consistent with a phenomenon determined by the charge state of the system. Indeed, the more we charge the clusters the less the electrochemical behavior is affected. Therefore, the oxidation of the first Au_{25} of the triad affects the electrochemical behavior of the second cluster within the same triad species, disfavoring its oxidation and therefore shifting its equilibrium potential towards higher potentials., This effect is reflected in the DPV behavior, causing the oxidation process of the triad, associated with the first oxidation, to manifest as two separate peaks. In the absence of any kind of communication or interaction between the two clusters the separation between the two peaks should be of 29 mV accounting for a statistical factor and not detectable as two distinct ET events.[51] The measured separation between the two split peaks is 122 mV. The DPV curve of the triad compared to the DPV curves of the two reactants (free Au_{25} and free Ru(II) complex) is shown in Figure 11. This figure clearly illustrates the differences in the electrochemical behavior of the triad and the individual components, revealing its multicomponent redox behavior.

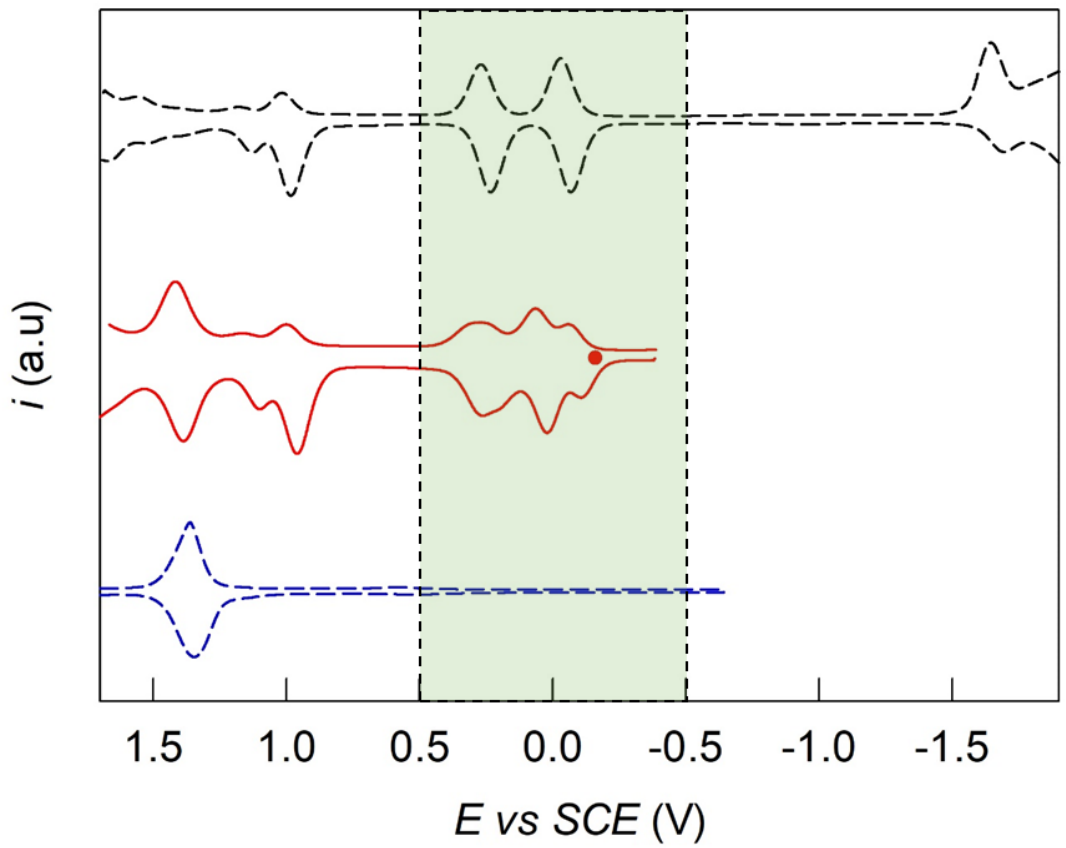

Figure 11 DPV curves for 0.6 mM Triad (red), 1 mM $Au_{25}(SC_2Ph)_{18}$ (black) and 1mM of Ru (II) complex (blue) in DCM/0.1 M TBAH at 22 °C. The DPV behaviors of the Ru (II) complex and of Au_{25}^{-}were been shifted in the y-axe to better visualize the differences. The green region (between -0.5 to 0.5 V vs SCE) shows the splitting of the two reversible peaks of the Au_{25} NC.

The peak position of the very first oxidation process in the triad (1°) is quite similar to that of the Au_{25} "monomer". This suggests that the electronic communication between the three redox centers is limited, which is consistent with the optical measurements. Instead, it reveals that an electrostatic phenomenon is affecting the two Au_{25} clusters.

To further investigate the possible electronic communication between the Au NCs and gaining more information about the single ET process we performed the same electrochemical characterization in a solution 0.1 M of tetrakis(pentafluorinatedphenyl)tetrabutylammonium ([TBA][$B(C_6H_5)_4$]) in DCM. With the use of this electrolyte, we expected a better resolution and a clearer electrochemical picture of multiple redox processes associated with positively charged redox species of the triad.[52–54] Indeed, [$B(C_6F_5)_4$]- is known to be a very bad coordinative anion, thanks to its lower capacity to stabilize positive charges, because of the bigger size of the counter anion (respect to PF_6^-) and the presence of five F atoms for each aromatic rings, thus making the B atom very electron poor. The new electrolyte was synthetized by an ionic exchange between TBACl and [K][$B(C_6F_5)_4$] in dry MeCN (Please, see “Supporting materials” section for synthetic details).[54] Here below (Figure 12) the DPV results, compared with that obtained with $TBAPF_6$, is shown.

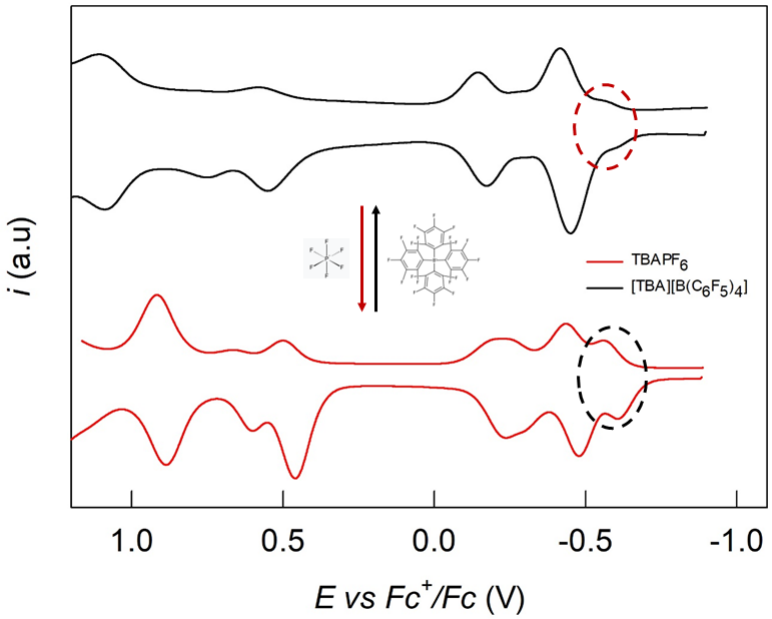

Figure 12 DPV curves for triad, in DCM/0.1 M $TBAPF_6$ (red line), and in DCM/0.1 M [TBA][$B(C_6F_5)_4$] (black line). The DPV behaviors have been shifted in the y-axe to better visualize the differences. The red and black circle underlined the effect of the new electrolyte on the electrochemical behavior, and in the very first ET process (first oxidation). The potentials were calibrated using the Fc^+/Fc couple.

The outcome was quite unexpected, as seems we almost lost electronic communication between the two NCs in the triad structure. Indeed, all the processes resulted shifted at more positive redox potentials, in agreement with the effect of the electrolyte used that destabilize the positive charges, so postponing all the processes in the DPV curve (see, for example, how the oxidation related to the Ru(II) center is shifted of almost 200 mV.) The same situation appears for all the redox processes referring to the two NCs, and the effect is more and more evident with the increase of the positive charge reached, as expected. Indeed, the first process has a shift of about 24 mV, the second one of 60 and the third one of 91 mV. However, the splitting of the first two oxidation processes of the Au_{25} NCs is almost lost. This could indicate that we lost electronic communication, resulting in a single bi-electronic electron transfer process. This result is intriguing but difficult to explain right now. One explanation could be related to the positive charges that are forming during these oxidation processes. Moreover, with the first oxidation event (O1, 1° and 2°) we are oxidizing the two Au_{25}^{-} to Au_{25}^{0}. So, no positive charges are creating in the NCs itself but a net-positive charge (+2) is forming in the triad system, since the two positive charges of Ru(II) complex are no longer balanced. Assuming, as a first approximation, that there is only slight electronic coupling between the components, the counterion, arising from the electrolyte, is acting more importantly on the metal center, probably affecting the possibility of further electronic coupling between the peripheral clusters. In addition, analyzing more in detail the potentials position of the various redox processes, we observed some intriguing potential shifts that cannot be simply ascribed to substitution effects. Briefly, analyzing the Figure 11 we observed that the oxidation peak of the Ru (II) complex (Ru (II) → Ru (III)) is shifted toward more positive potentials, so the oxidation is disadvantaged compared to the compound alone. This agrees with the presence of 3 positive charges in the Au_{25} NCs attached to the Ru (II) complex, when its oxidation takes place. Otherwise, the shifts in the redox processes related to the two $Au25^{-}$ is more difficult to visualize. Anyway, the first reversible redox process is shifted toward more negative potentials, so oxidation is favored. In addition, we measured a gap between the 2nd and the 3rd oxidation process of about 0.708 V, which is quite smaller to the normal separation in Au_{25} system,[23] consistent with a denser density of molecular orbitals.

To obtain information about the hydrodynamic radius of the novel triad system, we analyzed the CVs behavior of the first two reversible redox processes at low scan rates, calculating the diffusion coefficient (D). In particular, we based our analysis on the study of the second peak of the first oxidation process (O1, 2°). The analysis took

advantage of the knowledge of the electrode area and the triad concentration, which was determined accurately also by taking advantage of the constancy of the molar extinction coefficient for these clusters (at 398 nm, $\varepsilon = 9.97 \times 10^4\ M^{-1}cm^{-1}$). The triad radius ($r_{triad}$) is calculated with the Stokes−Einstein equation $D = k_BT/6\pi\eta r_{triad}$, where k_B is the Boltzmann constant and η is the viscosity of the solvent. Of course, the resulting value is just qualitative since the shape of the system is not completely spherical and the number of involved electrons is only approximated to one, but we know, from previous analysis, that the real number is something between 1 and 2, and so the final r value results overestimated. With the approximations, we calculated a D of 1.34 x 10^{-6} $cm^2 \cdot s^{-1}$, and so a hydrodynamic radius of ca. 3.94 nm that is quite in agreement to a chemical species having two Au_{25} (d = 1.88 nm x 2 = 3.76 nm) and one Ru (II) complex (d = 2.2 nm).

To obtain more insight about the oxidation process on the triad system, we performed chemical oxidation using pentafluoro-dibenzoylperoxide ($(ArCO_2)_2$), which is a bifunctional oxidant, already extensively used for this type of goal.[55] $(ArCO_2)_2$ undergoes a two-electron reduction at quite positive potentials (peak potential = 0.50 V vs SCE at 0.1 V s^{-1} in DCM) to form two corresponding benzoate anions. The reaction of the peroxide with every unit of Au_{25} (eq 1 and 2) occurs readily upon mixing.

$$(ArCO_2)_2 + Au_{25}^{-} \rightarrow ArCO2^{-} + ArCO_2^{\bullet} + Au_{25} \quad \textbf{(1)}$$

$$ArCO_2^{\bullet} + Au_{25}^{-} \rightarrow ArCO_2^{-} + Au_{25} \quad \textbf{(2)}$$

The UV-vis absorbance spectra of the triad system were systematically monitored during the chemical oxidation (Please, see “Supporting materials” section for the curves).

The observation of isosbestic points on the UV-Vis spectra, during the titration, indicates the goodness of the oxidation reaction and that the stoichiometry of the reaction remains unchanged during the monitored process. Moreover, the absorbance derivative at the main isosbestic points is particularly sensitive toward changes of the cluster’s redox state. The titration curve (Figure 13) shows how the derivative at 390 nm (isosbestic point) changes upon stepwise addition of the peroxide to a CH_2Cl_2 solution of the cluster.

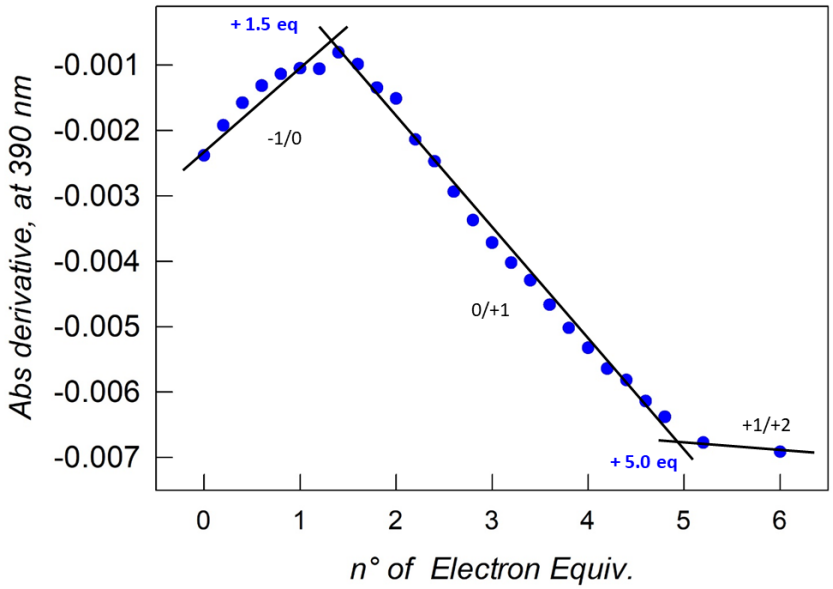

Figure 13 Plot of the absorbance derivative at 390 nm as a function of the electron equivalents (2 times the peroxide ones, since is a two-electron process), until 6 electron equivalents added.

Figure 13 nicely highlights the presence of two breaks. Whereas the first should correspond to full conversion of the two Au_{25}^{-} NCs on the triad system, to Au_{25}^{0}, the second occurs after further addition of ca. 2.5 equiv and is associated with conversion of Au_{25}^{0} into Au_{25}^{+}. The titration curve, focusing on the first segment, shows that the ET reaction is not matching with the theoretical electron equivalents for the conversion of the two Au_{25} from -1 charge state to the neutral form (+2), since a large drop in the absorption derivative was observed just after 1.5 electronic equivalents added. The same experiment, performed with Au_{25} like "monomer", Instead, it resulted in a change of direction of the broken line, just after the addition of 1 electronic equivalent. However, the chemical oxidation of the triad could be influenced by the electronic communication between components affecting the final result in an unpredictable way. The second break is related to the second oxidation, from Au_{25} at 0 charge state to +1. This resulted in being non-quantitative as finished after 5 eq added instead of 4 (theoretical value for full conversion of the two Au NC). After this break point, the addition of more peroxide doesn't have any effect, and after 6 eq the analysis of the titration curve becomes difficult due to the complex interplay between the chemical oxidation and decarboxylation reactions. In conclusion, the overall trend of the titration curve indicates that the ET reaction is influenced by electronic interactions between the components of the triad system. Moreover, the studied system appears to be highly intricate, with oxidation processes being affected by the proximity and possible

orbital overlap between the components. Indeed, further research is needed to fully elucidate the precise oxidation mechanism.

8.4 Conclusions

With this work we successfully synthesized for the first time a precisely atomically-defined Au_{25} "dimer" via a novel ligand exchange strategy employing a dithiolated ligand derived from a modified Ru(II) complex, leveraging an electrostatic driving force between the reactants. The altered solubility characteristics of the desired product within the reaction environment eliminated the need for post-synthetic purification and extraction procedures, transforming the process into a self-cleaning, high-yielding reaction. ESI-MS characterization confirms the formation of a system comprising two covalently linked Au_{25} NCs, each one protected by 17 original ligands and interconnected by a Ru(II) complex molecular bridge.

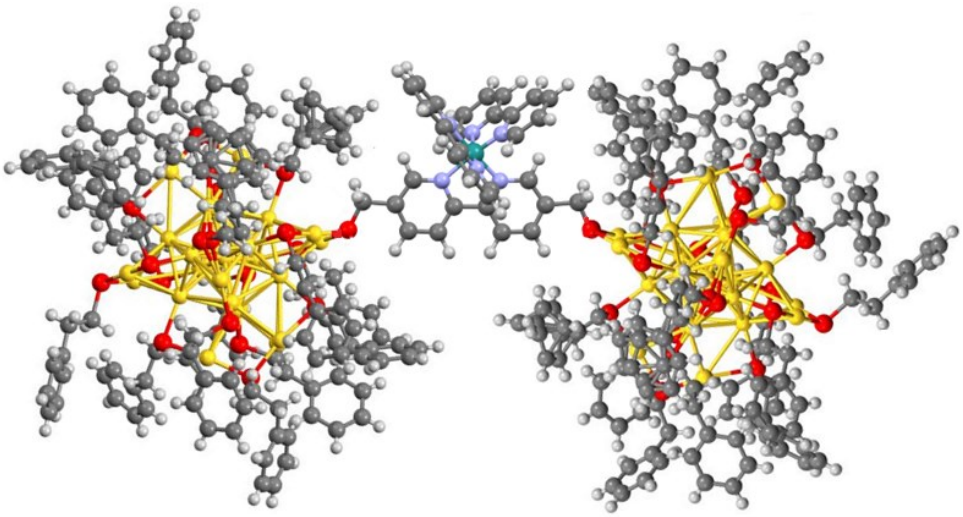

Figure 14 Triad structure. This is not a crystal structure.

ESI-MS further demonstrates the neutrality of the system, with no counterions detected, revealing the zwitterionic nature of the triad. ^{1}H and ^{13}C-NMR spectroscopy substantiates the formation of the -S-Au- bond and identifies a non-preferred site for the ligand exchange reaction (within the monolayer staples). UV-Vis, luminescence spectroscopy, and electrochemical measurements unveil intriguing optical and electrochemical properties of the system. The findings of this study lead to the following conclusions: (i) The system exhibits charge retention, preserving the charge states of its constituent units, as evident from both UV-Vis and emission spectra; (ii) The molecular orbitals of the system closely approximate those of its individual components, reflected by minimal distinctions in UV-Vis behavior and standard potential peak positions; (iii) Upon excitation, the Ru(II) complex emission is quenched, most likely due to an efficient energy transfer between it and the two peripheral Au_{25} NCs. This was further supported by the red-shift of both the dominant

UV-Vis and emission peaks; (iv) The electronic communication between the two Au_{25} clusters is rather weak but present; (v) Electrochemical characterizations (CVs and DPVs analysis) indicate that the novel superstructure behaves as a multicomponent redox species, as the oxidation peaks of the two Au_{25} NCs resulted split. The splitting was observed to be charge-dependent, suggesting that electrostatic effects are also influencing the redox behavior of the system. We tried to gain more insights into these aspects by utilizing a very weak coordinative counterion as electrolyte and analyzing the chemical oxidation (titration followed by UV-Vis spectroscopy) of the triad using a two-electron oxidant. The results pointed to a highly complex yet intriguing system. However, a full understanding of the oxidation mechanism has not yet been achieved. In conclusion, the "dimer" system can be more accurately characterized as a triad system, in which all three components retain their molecular characteristics and exhibit inter-component interactions, including efficient energy transfer from the Ru(II) complex to the Au_{25} clusters as well as electronic communication between the two Au_{25}. This work represents a significant breakthrough in the field of nanomaterial synthesis, paving the way for the creation of intricate materials employing NCs molecular units. Moreover, it demonstrates the potential of incorporating metal complexes into atomically precise nanocluster systems to enhance the properties of individual constituents, offering promising applications in homogeneous catalysis, such as the electrochemical reduction of CO_2.[50]

8.5 Experimental

The synthesis of the LER reactants ($Au_{25}(SC_2H_4Ph)_{18}^-$ and $Ru(II)(bpy)_2(bpy\text{-}C_2H_6S_2)$ were made as explained in the text (Paragraph 8.3).

Emission spectroscopy: Emission spectroscopy measurements were carried out with a near-infrared VARIAN Cary 5000 spectrophotometer with a spectral resolution of 0.5 nm. All the sample were dissolved in DMF-d, using a 10 mm optical-path quartz cuvette; A NIR-sensitive photomultiplier in a nitrogen-flow cooled housing (Hamamatsu R5509-73, spectral response 300–1700 nm) was used as detector. For the emission spectra, the step and dwell time were set at 1 nm and 0.2 s, respectively, and the slit was kept at 5 nm and 10 nm for absorption and emission monochromators, respectively. Experimental errors: absorption maxima, ±2 nm; emission maxima, ±2 nm; excited state lifetimes, ±10%.

UV-Vis spectroscopy, ^{1}H-NMR and ^{13}C-NMR spectroscopy, DPV and CV electrochemical experiments were made as already explained in Section 2.5.3.

HR ESI-MS spectrometry. Mass spectrometry Electrospray ionization mass spectra were acquired on Bruker time-of-flight (microTOF) mass spectrometer or Bruker maXis plus instruments (Bruker Daltronics), operated in the positive ion mode, with the mass-range typically set for m/z 3000-9000. All spectra were acquired by direct infusion out of the neat DCM solution of each sample, diluted to a concentration of 0.1 mg mL^{-1}. The flow rate was 10 µL min^{-1}. *Source:* Nebulizer 0.5 Bar, Focus: Active, Capillary: 5.0 kV, Dry Heater: 220 °C, End Plate Offset: -500 V, Dry Gas: 5.0 l/min, Charging Voltage: 2000 V. *Ion Optics*: Set Funnel 1 and 2 RF: 400:0 and 600.0 Vpp; isCID Energy: 0.0 eV, Set Focus 1-Lens 2, 3: 30.7, -44.0 V; Set Focus 2-Lens 1, 2, 3: 30.0, -48.3, and 24.6 V, respectively; Set Storage and Extraction: 40.0 and 22.0 V; Set Focus 3-Lens 2, 3, 4, 5: 0.0, -105.3, 0.0, and -15.0 V, respectively. *Processing*: Summation: 25895x, Guessed Noise: 200, Peak Width: 5 pts, Average Noise: 1, Guessed Average: 100. *Quadruple*: Ion Energy (MS only): 6.0 eV, Isolation Mass (MS only): *m/z* 2000/800.00, Collision Energy: 5 eV, Collision Cell RF: 2000.0/1200 Vpp, Set Transfer and PrePulseStorage time 120 and 40.0 µs. *TOF*: Corrector Fill: 57.2 V, Corrector Extract: 665.3 V, Corrector Lens: 6055.4 V, Reflector: 2750.0 V Decelerator: 721.8 V, Flight Tube: 9.9 kV, Detector TOF: 1827.6 V.

8.6 Supporting Materials

Modified Ru(II) complex characterizations

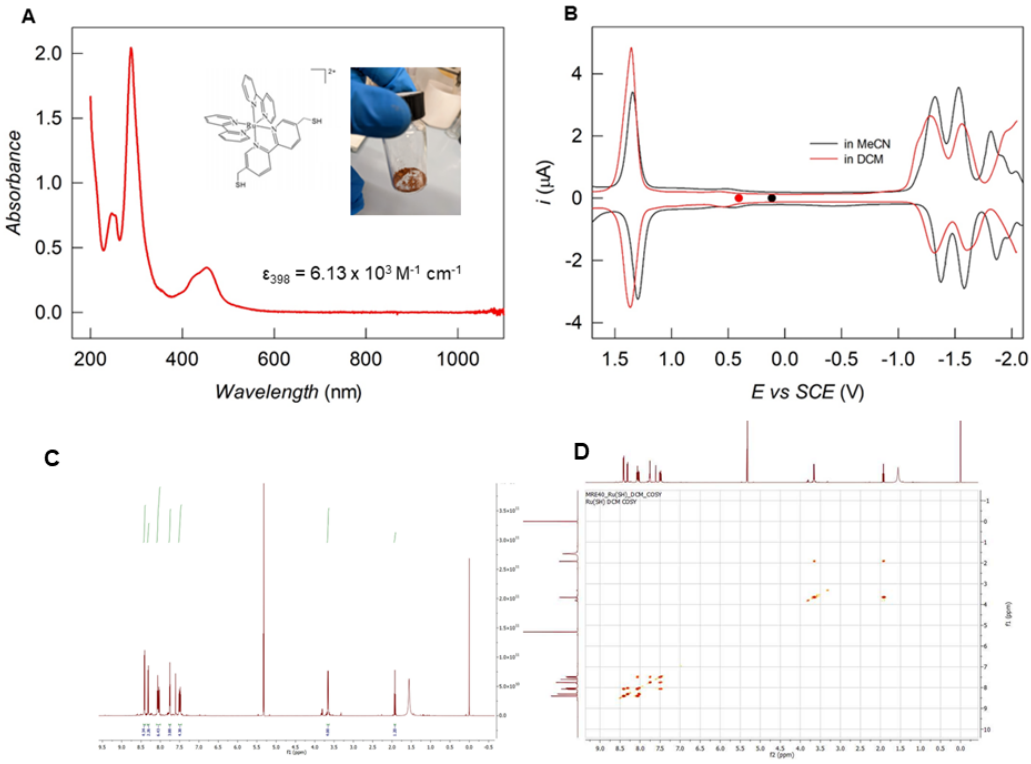

Figure S1 A) UV-Vis absorption of the modified Ru(II) complex, used as dithiolated exogenous ligand in the proposed LER, for the triad formation. The molar extinction coefficient, at 398 nm, was found to be 6.13 x 10^3 $M^{-1}cm^{-1}$; **B)** DPV curves of the same species, in DCM and MeCN/0.1 M $TBAPF_6$ using a GC disc electrode; **C)** ^{1}H-NMR and **D)** COSY (Two-dimensional nuclear magnetic resonance correlation spectroscopy) spectra. Regarding *^{1}H-NMR (600 MHz, Methylene Chloride-d_2) δ 8.41 (d,* J = *8.2 Hz,* 4H, Hbpy-3,3′*), 8.31 (d,* J = *8.4 Hz,* 2H, HbpySH-3,3′*), 8.11 – 7.98 (m, 4H,* Hbpy-4,4′*), 7.75 (dd, 2H,* HbpySH-4,4′*), 7.61 (d, 2H,* HbpySH-6,6′*) 7.54 – 7.45 (m, 4H,* Hbpy5,5′*), 3.66 (dd,* J = *8.4,* 4H, -CH2*), 1.93 (s, 2H, HS-).*

Triad characterizations and analysis

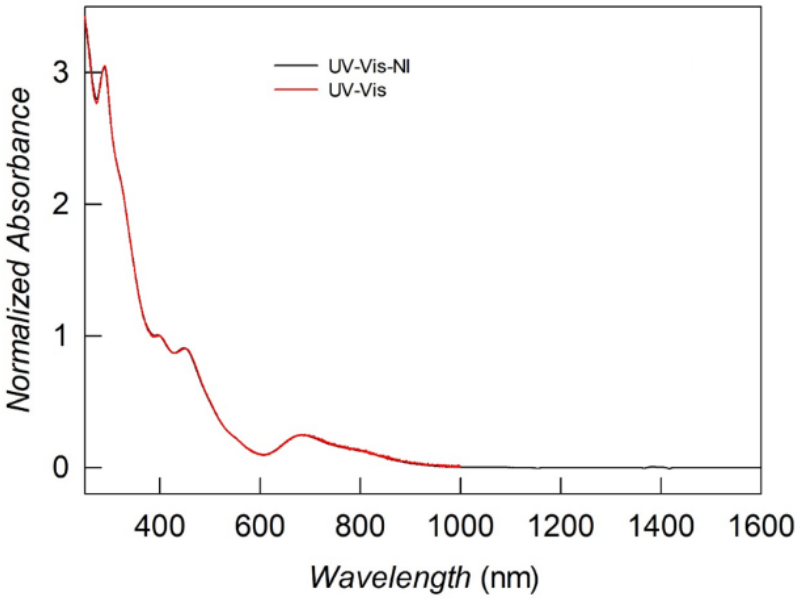

Figure S2 UV-Vis-Ni spectrum of the triad compared to the UV-Vis spectrum show in the "Results and Discussion" section. The First one was done using The Agilent Technologies Cary 5000 UV–vis–NI. The absence of signals in the NI region, further confirm the purity of the sample, and supports the absence of bigger superstructures, which would otherwise have been detected above 1100 nm.

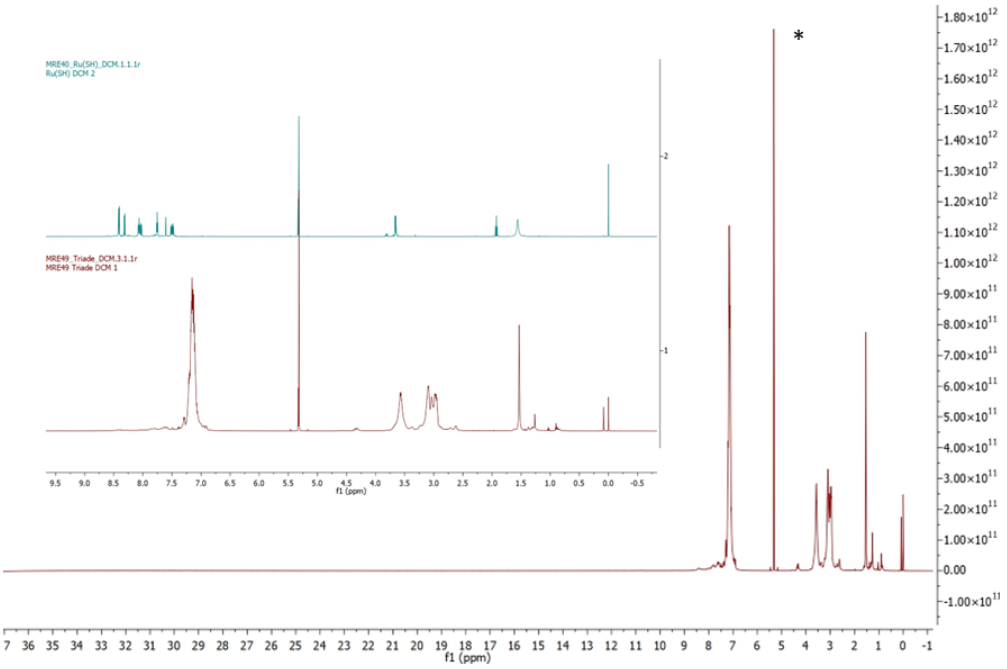

Figure S3 *Full 1H-NMR of the triad and (inset) comparison with the [1]H-NMR of the modified Ru(II) complex. Both in DCM-d, at room temperature.*

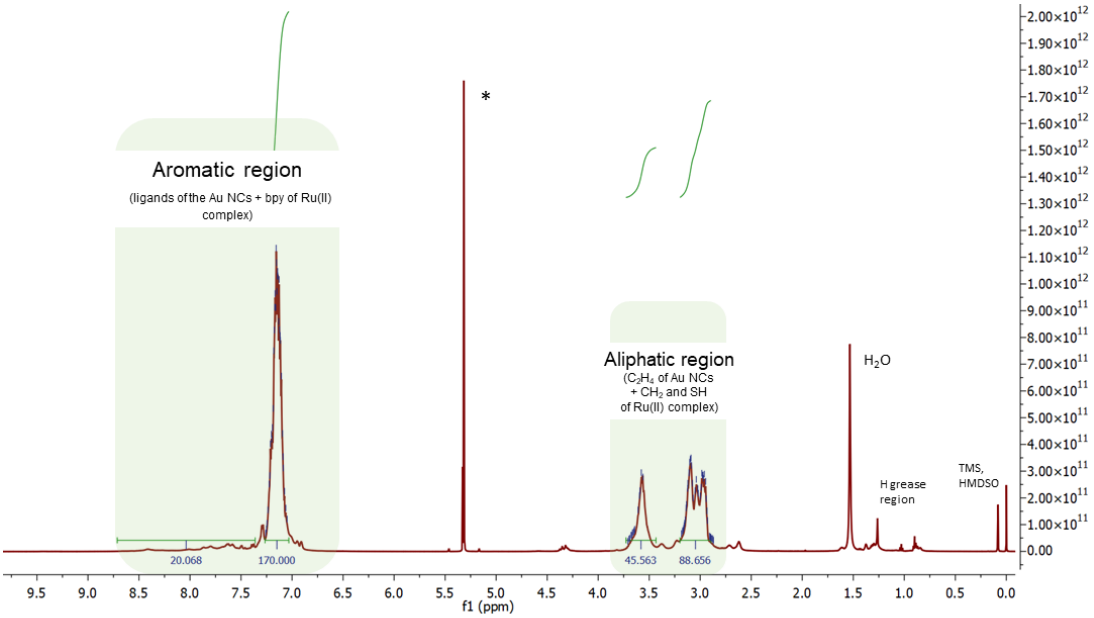

Figure S4 ^{1}H-NMR spectra of the triad with integrals analysis and and assignment of impurities

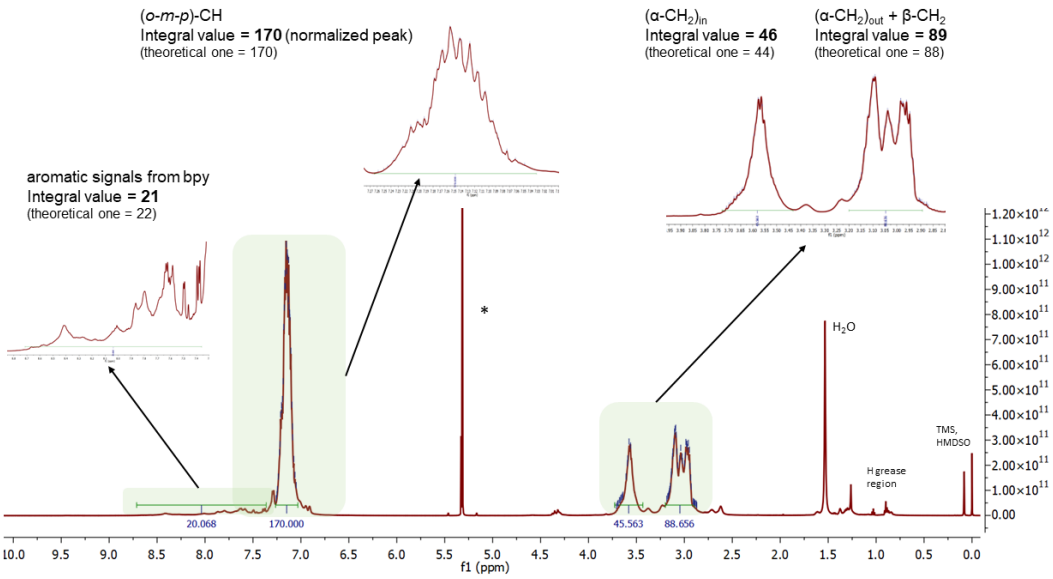

Figure S5 Integration analysis on ^{1}H-NMR spectrum of the triad. The analysis confirms the ratio of 1:2 between Ru (II) complex and Au_{25}, since the experimental integrals almost perfectly match with the theoretical one (the experimental ratio is 0.55), considering one modified Ru(II) complex, every two Au25 NCs. Importantly, no signal related to the S-H triplet was detected (Please see Figure 6), confirming the formation of the bond between the free thiols of the modified Ru(II) complex and the two Au_{25}. Importantly, no evidendes of the presence of TOA^{+} (counterion of the original $Au25^{-}$)was observed, confirming the zwitterion nature of the novel formed system, as the negative charges of the two NCs are now balanced by the two positive charges of the Ru(II) complex. No information about the selectivity over the LER was possible to obtained, because of the overlapping of the signals of the various components which makes the analysis too unreliable.

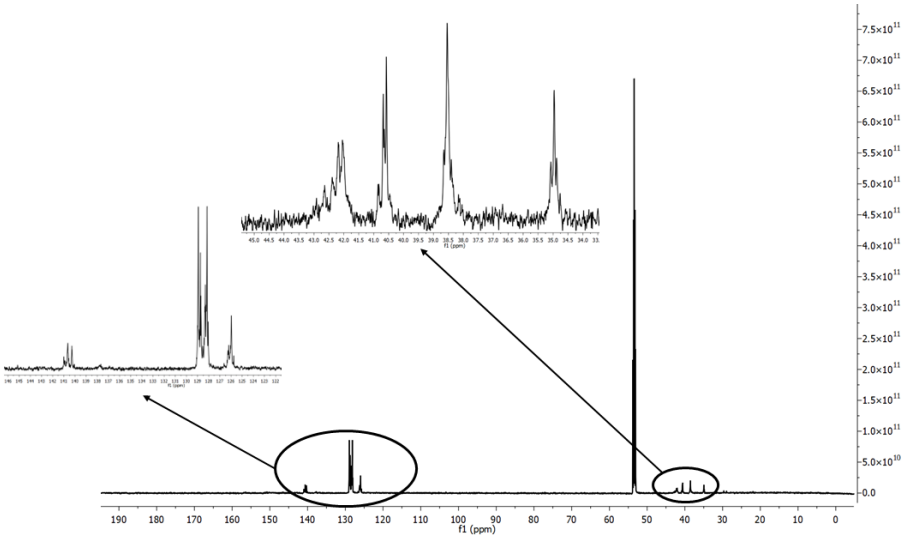

Figure S6 ^{13}C-NMR of triad, in DCM-d. The presence of multiplets pointed to no selectivity over the LER. Therefore, for this reason, the Ru(II) complex has attached in a non-preferential way on the NCs staples, which means that the triad exists as an isomer in which the metal complex has exchanged on the first and second clusters respectively: in-in, out-out, but also in-out way. Having a mixture of isomers maybe is the reason why all attempts to crystallize the compound have failed.

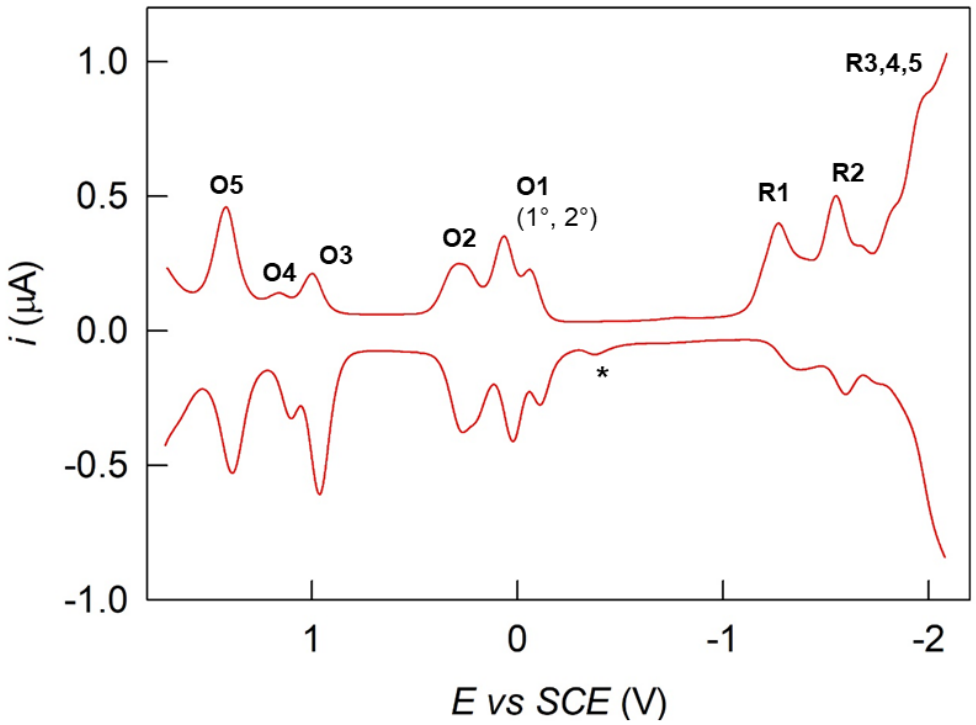

Figure S7 Complete DPV curve, for 0.6 mM Triad in DCM/0.1 M $TBAPF_6$ at 22 °C. The asterisk represents a peak related to the reoxidation of some compounds derived from the bipyridines degradation, after reaching strongly reducing potentials. O5 is referred to the first oxidation process of the Ru (from +2 to +3) in the triad system; The O1 process is splitted into two quasi-monoelectronic processes (Please, see the text for the analysis); The R1 is the first reduction of the Au_{25} in the triad system, while R2 is an overlay between bpy and Au_{25} reduction. At very high reducing potentials some

other reduction processes can be detected (R3,4, and 5), most probably due to the reduction of the bipyidines.

Table S1: $E_{1/2}$ calculated as the half-sum of the anodic and cathodic peaks.

Electrochemical Process	$E_{1/2}$ vs SCE (V)
O1 (1°)	- 0.083
O1 (2°)	+ 0.039
O2	+ 0.273
O3	+ 0.981
O4	+ 1.127
O5	+ 1.400
R1	- 1.325
R2	- 1.571

[TBA][B(C_6F_5)$_4$]) Synthesis: A solutions of TBACl (2.25 g, 1 equiv) in dry MeCN (25 mL) was added into a solution of K[B(C6F5)4] (5.83 g,1 equiv) in dry MeCN (450 mL), in a 3-neck 1-liter round bottom flask under dry argon. Upon mixing, a white precipitate was observed, and the mixture was stirred for 2 h to ensure complete precipitation of KCl. After elimination of KCl, by filtration, the solvent was removed using a rotary evaporating system. The resulting clear oil was further dried under vacuum overnight to yield a white solid. This solid was then dissolved in DCM and layered with hexanes for crystallization. After some days, crystals were collected, dried and recrystallized using the same conditions.

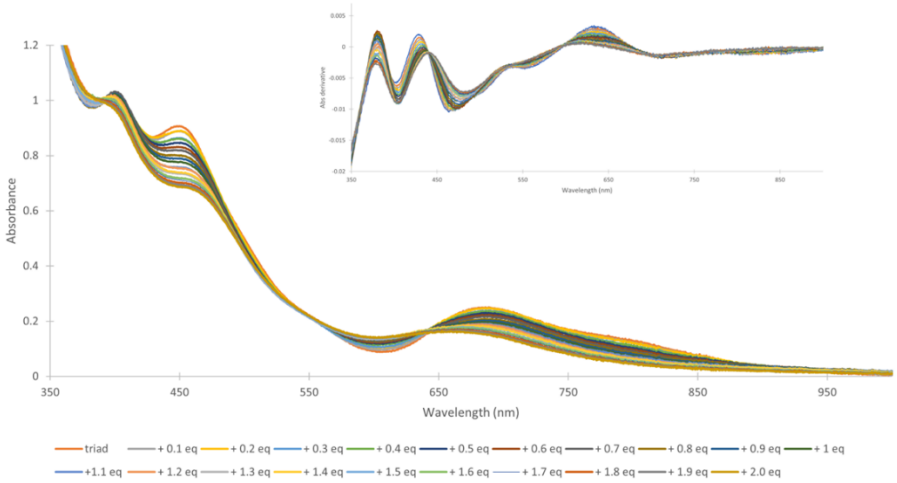

Figure S8 UV-Vis spectra (and his derivative, in the inset) of the chemical oxidation titration on triad, using ($ArCO_2$)$_2$. The observation of isosbestic points on the spectra, during the titration, indicates the goodness of the oxidation reaction and that the stoichiometry of the reaction remains unchanged during the monitored process.

8.7 References

1. Dong, A.; Chen, J.; Vora, P. M.; Kikkawa, J. M.; Murray, C. B. Binary Nanocrystal Superlattice Membranes Self-Assembled at the Liquid–Air Interface. *Nature* **2010**, *466* (7305), 474–477.
2. Sánchez-Iglesias, A.; Rivas-Murias, B.; Grzelczak, M.; Pérez-Juste, J.; Liz-Marzán, L. M.; Rivadulla, F.; Correa-Duarte, M. A. Highly Transparent and Conductive Films of Densely Aligned Ultrathin Au Nanowire Monolayers. *Nano Lett.* **2012**, *12* (12), 6066–6070.
3. Cademartiri, L.; Bishop, K. J. M. Programmable Self-Assembly. *Nat. Mater.* **2015**, *14* (1), 2–9.
4. Zhou, B.; Shi, B.; Jin, D.; Liu, X. Controlling Upconversion Nanocrystals for Emerging Applications. *Nat. Nanotechnol.* **2015**, *10* (11), 924–936.
5. Lin, Q.-Y.; Mason, J. A.; Li, Z.; Zhou, W.; O'Brien, M. N.; Brown, K. A.; Jones, M. R.; Butun, S.; Lee, B.; Dravid, V. P.; Aydin, K.; Mirkin, C. A. Building Superlattices from Individual Nanoparticles via Template-Confined DNA-Mediated Assembly. *Science* **2018**, *359* (6376), 669–672.
6. Chen, L.-Y.; Wang, C.-W.; Yuan, Z.; Chang, H.-T. Fluorescent Gold Nanoclusters: Recent Advances in Sensing and Imaging. *Anal Chem* **2015**, 87, 1, 216–229.
7. Parker, J. F.; Kacprzak, K. A.; Lopez-Acevedo, O.; Häkkinen, H.; Murray, R. W. Experimental and Density Functional Theory Analysis of Serial Introductions of Electron-Withdrawing Ligands into the Ligand Shell of a Thiolate-Protected Au_{25} Nanoparticle. *J. Phys. Chem. C* **2010**, *114* (18), 8276–8281.
8. Gao, P.; Chang, X.; Zhang, D.; Cai, Y.; Chen, G.; Wang, H.; Wang, T. Synergistic Integration of Metal Nanoclusters and Biomolecules as Hybrid Systems for Therapeutic Applications. *Acta Pharm. Sin. B* **2021**, *11* (5), 1175–1199.
9. Gao, P.; Wu, S.; Chang, X.; Liu, F.; Zhang, T.; Wang, B.; Zhang, K.-Q. Aprotinin Encapsulated Gold Nanoclusters: A Fluorescent Bioprobe with Dynamic Nuclear Targeting and Selective Detection of Trypsin and Heavy Metal. *Bioconjug. Chem.* **2018**, *29* (12), 4140–4148.
10. Howes, P. D.; Chandrawati, R.; Stevens, M. M. Colloidal Nanoparticles as Advanced Biological Sensors. *Science* **2014**, *346* (6205), 1247390.
11. Tao, Y.; Li, M.; Ren, J.; Qu, X. Metal Nanoclusters: Novel Probes for Diagnostic and Therapeutic Applications. *Chem. Soc. Rev.* **2015**, *44* (23), 8636–8663.
12. Wu, J.; Wu, Y.; Bian, H.; Peng, Z.; Liu, Y.; Yin, Y.; Du, J.; Lu, X. Fabrication of a Ratiometric Electrochemiluminescence Biosensor Using Single Self-

Enhanced Nanoluminophores for the Detection of Spermine. *Talanta* **2023**, *253*, 123880.

13. Zan, X.; Li, Q.; Pan, Y.; Morris, D. J.; Zhang, P.; Li, P.; Yu, H.; Zhu, M. Versatile Ligand-Exchange Method for the Synthesis of Water-Soluble Monodisperse AuAg Nanoclusters for Cancer Therapy. *ACS Appl. Nano Mater.* **2018**, *1* (12), 6773–6781.

14. Zhu, H.; Zhou, Y.; Wang, Y.; Xu, S.; James, T. D.; Wang, L. Stepwise-Enhanced Tumor Targeting of Near-Infrared Emissive Au Nanoclusters with High Quantum Yields and Long-Term Stability. *Anal. Chem.* **2022**, 94, 38, 13189–13196.

15. Fei, W.; Antonello, S.; Dainese, T.; Dolmella, A.; Lahtinen, M.; Rissanen, K.; Venzo, A.; Maran, F. Metal Doping of $Au_{25}(SR)_{18}^-$ Clusters: Insights and Hindsights. *J. Am. Chem. Soc.* **2019**, *141* (40), 16033–16045.

16. Gunawardene, P.; Martin, J.; Wong, J.; Ding, Z.; Corrigan, J.; Workentin, M. Controlling the Structure, Properties and Surface Reactivity of Clickable Azide-Functionalized $Au_{25}(SR)_{18}$ Nanocluster Platforms Through Regioisomeric Ligand Modifications. *Angew. Chem. Int. Ed*. **2022**, 61, e2022051.

17. Hossain, S.; Kurashige, W.; Wakayama, S.; Kumar, B.; Nair, L. V.; Niihori, Y.; Negishi, Y. Ligand Exchange Reactions in Thiolate-Protected Au_{25} Nanoclusters with Selenolates or Tellurolates: Preferential Exchange Sites and Effects on Electronic Structure. *J. Phys. Chem. C* **2016**, *120* (45), 25861–25869.

18. Jiang, D.; Dai, S. From Superatomic $Au_{25}(SR)_{18}^-$ to Superatomic $M@Au_{24}(SR)_{18}^q$ Core−Shell Clusters. *Inorg. Chem.* **2009**, *48* (7), 2720–2722.

19. Li, Y.; Biswas, S.; Luo, T.-Y.; Juarez-Mosqueda, R.; Taylor, M. G.; Mpourmpakis, G.; Rosi, N. L.; Hendrich, M. P.; Jin, R. Doping Effect on Magnetism of Thiolate-Capped 25-Atom Alloy Nanoclusters. *Chem. Mater.* **2020**, 32, 21, 9238–9244.

20. Walter, M.; Moseler, M. Ligand-Protected Gold Alloy Clusters: Doping the Superatom. *J. Phys. Chem. C* **2009**, *113* (36), 15834–15837.

21. Wang, S.; Li, Q.; Kang, X.; Zhu, M. Customizing the Structure, Composition, and Properties of Alloy Nanoclusters by Metal Exchange. *Acc. Chem. Res.* **2018**, *51* (11), 2784–2792.

22. Agrachev, M.; Fei, W.; Antonello, S.; Bonacchi, S.; Dainese, T.; Zoleo, A.; Ruzzi, M.; Maran, F. Understanding and Controlling the Efficiency of $Au_{24}M(SR)_{18}$ Nanoclusters as Singlet-Oxygen Photosensitizers. *Chem. Sci.* **2020**, *11* (13), 3427–3440.

23. Antonello, S.; Maran, F. Molecular Electrochemistry of Monolayer-Protected Clusters. *Curr. Opin. Electrochem.* **2017**, *2* (1), 18–25.

24. Heinecke, C. L.; Ni, T. W.; Malola, S.; Mäkinen, V.; Wong, O. A.; Häkkinen, H.; Ackerson, C. J. Structural and Theoretical Basis for Ligand Exchange on Thiolate Monolayer Protected Gold Nanoclusters. *J. Am. Chem. Soc.* **2012**, *134* (32), 13316–13322.

25. Wang, Y.; Bürgi, T. Ligand Exchange Reactions on Thiolate-Protected Gold Nanoclusters. *Nanoscale Adv.* **2021**, *3* (10), 2710–2727.

26. Lahtinen, T.; Hulkko, E.; Sokołowska, K.; Tero, T.-R.; Saarnio, V.; Lindgren, J.; Pettersson, M.; Häkkinen, H.; Lehtovaara, L. Covalently Linked Multimers of Gold Nanoclusters Au_{102}(p-MBA)$_{44}$ and $Au_{\sim 250}$(p-MBA)$_n$. *Nanoscale* **2016**, *8* (44), 18665–18674.

27. Akola, J.; Kacprzak, K. A.; Lopez-Acevedo, O.; Walter, M.; Grönbeck, H.; Häkkinen, H. Thiolate-Protected Au_{25}Superatoms as Building Blocks: Dimers and Crystals. *J. Phys. Chem. C* **2010**, *114* (38), 15986–15994.

28. Rival, J. V.; Nonappa; Shibu, E. S. Light-Triggered Reversible Supracolloidal Self-Assembly of Precision Gold Nanoclusters. *ACS Appl. Mater. Interfaces* **2020**, *12* (12), 14569–14577.

29. Nag, A.; Pradeep, T. Assembling Atomically Precise Noble Metal Nanoclusters Using Supramolecular Interactions. *ACS Nanosci. Au* **2022**, 2, 160−178.

30. Qin, Z.; Zhang, J.; Wan, C.; Liu, S.; Abroshan, H.; Jin, R.; Li, G. Atomically Precise Nanoclusters with Reversible Isomeric Transformation for Rotary Nanomotors. *Nat. Commun.* **2020**, *11* (1), 6019.

31. Ho-Wu, R.; Sun, K.; Goodson, T. Synthesis and Enhanced Linear and Nonlinear Optical Properties of Chromophore–Au Metal Cluster Oligomers. *J. Phys. Chem. C* **2018**, *122* (4), 2315–2329.

32. Sokolowska, K.; Hulkko, E.; Lehtovaara, L.; Lahtinen, T. Dithiol-Induced Oligomerization of Thiol-Protected Gold Nanoclusters. *J. Phys. Chem. C* **2018**, *122* (23), 12524–12533.

33. Swierczewski, M.; Cousin, F.; Banach, E.; Rosspeintner, A.; Lawson Daku, L. M.; Ziarati, A.; Kazan, R.; Jeschke, G.; Azoulay, R.; Lee, L.; Bürgi, T. Exceptionally Stable Dimers and Trimers of Au_{25} Clusters Linked with a Bidentate Dithiol: Synthesis, Structure and Chirality Study. *Angew. Chem. Int. Ed.* **2023**, *62* (16), e202215746.

34. Sels, A.; Salassa, G.; Cousin, F.; Lee, L.-T.; Bürgi, T. Covalently Bonded Multimers of Au_{25}(SBut)$_{18}$ as a Conjugated System. *Nanoscale* **2018**, *10* (26), 12754–12762.

35. Bodiuzzaman, M.; Nag, A.; Pradeep Narayanan, R.; Chakraborty, A.; Bag, R.; Paramasivam, G.; Natarajan, G.; Sekar, G.; Ghosh, S.; Pradeep, T. A Covalently Linked Dimer of $[Ag_{25}(DMBT)_{18}]^-$. *Chem. Commun.* **2019**, *55* (34), 5025–5028.

36. Anderson, P. A.; Deacon, G. B.; Haarmann, K. H.; Keene, F. R.; Meyer, T. J.; Reitsma, D. A.; Skelton, B. W.; Strouse, G. F.; Thomas, N. C. Designed Synthesis of Mononuclear Tris(Heteroleptic) Ruthenium Complexes Containing Bidentate Polypyridyl Ligands. *Inorg. Chem.* **1995**, *34* (24), 6145–6157.

37. Bertoncello, P.; Kefalas, E. T.; Pikramenou, Z.; Unwin, P. R.; Forster, R. J. Adsorption Dynamics and Electrochemical and Photophysical Properties of Thiolated Ruthenium 2,2'-Bipyridine Monolayers. *J. Phys. Chem. B* **2006**, *110* (20), 10063–10069.

38. Agrachev, M.; Antonello, S.; Dainese, T.; Gascón, J. A.; Pan, F.; Rissanen, K.; Ruzzi, M.; Venzo, A.; Zoleo, A.; Maran, F. A Magnetic Look into the Protecting Layer of Au_{25} Clusters. *Chem. Sci.* **2016**, *7* (12), 6910–6918.

39. Niihori, Y.; Kikuchi, Y.; Kato, A.; Matsuzaki, M.; Negishi, Y. Understanding Ligand-Exchange Reactions on Thiolate-Protected Gold Clusters by Probing Isomer Distributions Using Reversed-Phase High-Performance Liquid Chromatography. *ACS Nano* **2015**, *9* (9), 9347–9356.

40. Fernando, A.; Aikens, C. M. Ligand Exchange Mechanism on Thiolate Monolayer Protected $Au_{25}(SR)_{18}$ Nanoclusters. *J. Phys. Chem. C* **2015**, *119* (34), 20179–20187.

41. Yan, N.; Xia, N.; Wu, Z. Metal Nanoparticles Confronted with Foreign Ligands: Mere Ligand Exchange or Further Structural Transformation? *Small* **2021**, *17* (27), 2000609.

42. Pengo, P.; Bazzo, C.; Boccalon, M.; Pasquato, L. Differential Reactivity of the Inner and Outer Positions of $Au_{25}(SCH_2CH_2Ph)_{18}$ Dimeric Staples under Place Exchange Conditions. *Chem. Commun.* **2015**, *51* (15), 3204–3207.

43. Chen, J.; Liu, Y.; Mei, L.; Wang, Z.; Fang, M.; Huang, Z. Emission Red Shift and Energy Transfer Behavior of Color-Tunable $KMg_4(PO_4)_3$:Eu^{2+},Mn^{2+} Phosphors. *J. Mater. Chem. C* **2015**, *3* (21), 5516–5523.

44. Bhasikuttan, A. C.; Suzuki, M.; Nakashima, S.; Okada, T. Ultrafast Fluorescence Detection in Tris(2,2'-Bipyridine)Ruthenium(II) Complex in Solution: Relaxation Dynamics Involving Higher Excited States. *J. Am. Chem. Soc.* **2002**, *124* (28), 8398–8405.

45. Borgström, M.; Ott, S.; Lomoth, R.; Bergquist, J.; Hammarström, L.; Johansson, O. Photoinduced Energy Transfer Coupled to Charge Separation in a Ru(II)−Ru(II)−Acceptor Triad. *Inorg. Chem.* **2006**, *45* (12), 4820–4829.

46. Chaignon, F.; Torroba, J.; Blart, E.; Borgström, M.; Hammarström, L.; Odobel, F. Distance-Independent Photoinduced Energy Transfer over 1.1 to 2.3 Nm in Ruthenium Trisbipyridine–Fullerene Assemblies. *New J. Chem.* **2005**, *29* (10), 1272.

47. Collin, J. P.; Guillerez, S.; Sauvage, J. P.; Barigelletti, F.; De Cola, L.; Flamigni, L.; Balzani, V. Photoinduced Processes in Dyads and Triads Containing a

Ruthenium(II)-Bis(Terpyridine) Photosensitizer Covalently Linked to Electron Donor and Acceptor Groups. *Inorg. Chem.* **1991**, *30* (22), 4230–4238.

48. Iengo, E.; Pantoş, G. D.; Sanders, J. K. M.; Orlandi, M.; Chiorboli, C.; Fracasso, S.; Scandola, F. A Fully Self-Assembled Non-Symmetric Triad for Photoinduced Charge Separation. *Chem Sci* **2011**, *2* (4), 676–685.

49. White, T.; Arachchige, S.; Sedai, B.; Brewer, K. Emission Spectroscopy as a Probe into Photoinduced Intramolecular Electron Transfer in Polyazine Bridged Ru(II),Rh(III) Supramolecular Complexes. *Materials* **2010**, *3* (8), 4328–4354.

50. Zhao, J.; Ziarati, A.; Rosspeintner, A.; Bürgi, T. Anchoring of Metal Complexes on Au_{25} Nanocluster for Enhanced Photocoupled Electrocatalytic CO_2 Reduction. *Angew. Chem. Int. Ed.* **2023**, 63, e2023166.

51. Savéant, J. M. Elements of Molecular and Biomolecular Electrochemistry: an Electrochemical Approach to Electron Transfer Chemistry. John Wiley & Sons., **2006.**

52. Diallo, A. K.; Absalon, C.; Ruiz, J.; Astruc, D. Ferrocenyl-Terminated Redox Stars: Synthesis and Electrostatic Effects in Mixed-Valence Stabilization. *J. Am. Chem. Soc.* **2011**, *133* (3), 629–641.

53. Gericke, H. J.; Barnard, N. I.; Erasmus, E.; Swarts, J. C.; Cook, M. J.; Aquino, M. A. S. Solvent and Electrolyte Effects in Enhancing the Identification of Intramolecular Electronic Communication in a Multi Redox-Active Diruthenium Tetraferrocenoate Complex, a Triple-Sandwiched Dicadmium Phthalocyanine and a Ruthenocene-Containing β-Diketone. *Inorganica Chim. Acta* **2010**, *363* (10), 2222–2232.

54. Khan, F. S. T.; Waldbusser, A. L.; Carrasco, M. C.; Pourhadi, H.; Hematian, S. Synthetic, Spectroscopic, Structural, and Electrochemical Investigations of Ferricenium Derivatives with Weakly Coordinating Anions: Ion Pairing, Substituent, and Solvent Effects. *Dalton Trans.* **2021**, *50* (21), 7433–7455.

55. Venzo, A.; Antonello, S.; Gascón, J. A.; Guryanov, I.; Leapman, R. D.; Perera, N. V.; Sousa, A.; Zamuner, M.; Zanella, A.; Maran, F. Effect of the Charge State (z = −1, 0, +1) on the Nuclear Magnetic Resonance of Monodisperse $Au_{25}[S(CH_2)_2Ph]_{18}^{z}$ Clusters. *Anal. Chem.* **2011**, *83* (16), 6355–6362.

9. Ligand Effect on Electrochemical Properties of Superatomic Di-NHC/PPh3-Stabilized Molecular Gold Nanoclusters

9.1 Abstract

The most extensively studied AuNCs are those protected by alkanethiolate ligands where the metal core is surrounded by “staples”, consisting of $[Au(I)_n(R)_m]$ motifs (where R = alkanethiolate), thus stabilizing the cluster core. However, the peculiar staple structure in Au NCs presents some crucial drawbacks for catalytic processes, making communication with the external environment somehow difficult. For this reason, modifying the organic-protecting monolayer with alternative ligand systems is becoming increasingly intriguing. Among many options, the combination of phosphines and N-heterocyclic carbenes complex (NHCs) as ligands is gaining more and more interest in recent years. The physical properties of these nanosystems are far from being exhaustively described and, among these, the electrochemical investigations are rather limited and often affected by significant imprecision. This chapter explores the electrochemical properties of novel Au_{11} and Au_{13} nanoclusters (NCs) protected by phosphines (PR_3) and di-N-heterocyclic carbene (di-NHCs) ligands. Leveraging a diverse library of Au_{11} and Au_{13} NCs with mixed ligands, varying degrees of di-NHCs functionalization, and different substitution patterns on the di-NHCs structure, we gain insights into the influence of ligands on electrochemical properties. This study marks the first systematic investigation of electrochemical properties in sub-nanometer atomically precise NCs. We demonstrate the remarkable tunability of Au NCs redox properties by modifying the NCs surface with di-NHC ligand complexes, influencing reduction and oxidation potentials, stability, and HOMO-LUMO gap. Preliminary evidence of catalytic dichloromethane reduction is also presented. The ability to modulate potential shifts through targeted modifications of di-N-heterocyclic carbene complexes within the metal NC monolayer holds significant promise for a wide range of applications.

9.2 Introduction

Atomically precise gold nanoclusters (Au NCs) and more in general metal NCs with a diameter of less than 1.6 nm are known to exhibit molecular behaviors. They bridge the gap between nanoparticles and molecules, where discrete electronic states form, and distinctive physicochemical properties are observed. Moreover, from the electrochemical point of view, they behave just like a complex redox system.[1,2]

Molecular Au NCs exhibit well-defined, characteristic peaks in their cyclic voltammetry (CV) and differential pulse voltammetry (DPV) patterns which are particularly well-studied for thiolate-ligands protected NCs. Two of the most notable examples are $Au_{25}(SR)_{18}$, which exhibits a well-defined HOMO-LUMO gap (Figure 1), and $Au_{144}(SR)_{60}$, which displays quantized double-layer (QDL) charging behavior.[1,3,4] In QDL charging, each peak corresponds to a single-electron charging event that not necessarily involve orbital at different energy.[5]

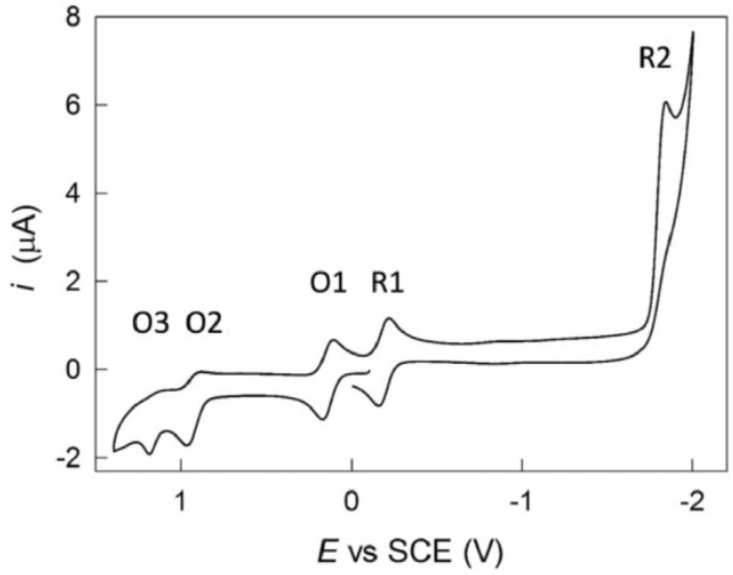

Figure 1 CV of $Au_{25}(SR)_{18}$ ^{0} (in particular, R = C_3H_7) in DCM/0.1 M $TBAPF_6$ at v = 0.1 V s^{-1}.[3]

In these systems the difference between the E° values of the 0/−1 and −1/−2 redox couples is the electrochemical gap, which can be related to the optical HOMO-LUMO gap by subtracting the charging energy. The charging energy is obtained from the difference between the E° values of the +1/0 and 0/−1 redox couples.[6] For alkanethiolate protected Au_{25} nanoclusters, the estimated HOMO-LUMO gap is 1.30 eV, which is in excellent agreement with the optical gap of 1.33–1.35 eV.[3] Interestingly, while inductive effects in ligands and the introduction of oriented dipole moments can affect the E° values of molecular $Au_{25}(SR)_{18}$,[3,7] as well as $Au_{144}(SR)_{60}$,[8]

the actual HOMO-LUMO gap does not change. However, progressive introduction of phenyl chalcogenate ligands into a phenylethanethiolate monolayer has been shown to decrease the electrochemical gap.[9] Figure 2 illustrates the general dependency of the electrochemical gap and the optical HOMO-LUMO gap on the number of Au atoms for a series of thiolate-protected clusters displaying clear-cut electrochemical behaviors.

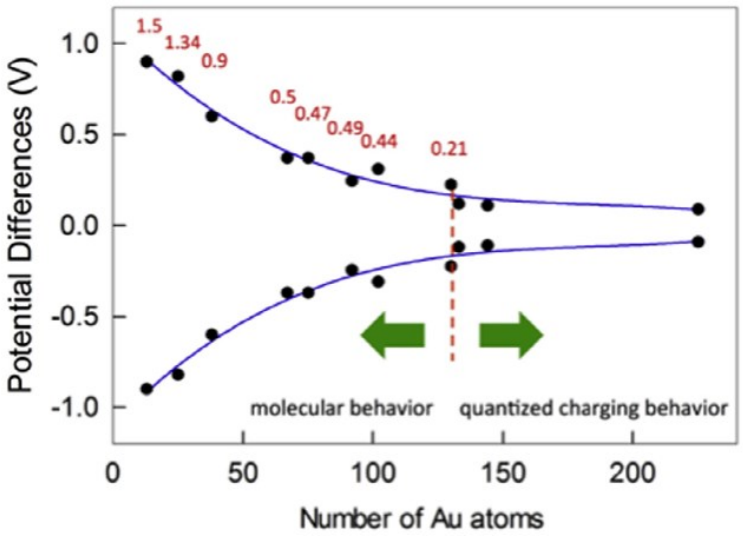

Figure 2 Electrochemical and HOMO–LUMO (in red) gaps as a function of the number of Au atoms. The blue lines are only meant to highlight the general trend.[1]

While the HOMO and LUMO orbitals of molecular clusters span onto the first atoms of the capping ligands,[10,11] the electrochemical behavior is mostly determined by the size and to some extent shape of the metal core. However, the way by which the core communicates with the surroundings is always mediated by the capping monolayer. The ligand shell serves as a crucial interface, often overlooked yet critically important, that mediates the electronic interaction between the nanocluster and its environment, and dictates the physical properties of the nanocluster itself, particularly when the nanocluster size diminishes (fewer gold atoms), and ligands exert a more direct influence on the core.

Chen and Murray, in 2002 and 2006 respectively, were the first to publish electrochemical characterizations of sub-nanometer Au nanoclusters (Au NCs) with fewer than 18 gold atoms.[12,13] However, the synthetic strategies and characterization techniques employed at the time were not optimized for atomically precise nanoclusters, leading to approximate results, particularly due to the difficulty in separating different NC species. Despite these limitations, they were able to evaluate the effect of ligand substitutions. In both cases, the nanoclusters were protected by

mixed ligands, consisting of linear alkanethiolates and phosphines. Both electrochemical and optical measurements support the molecule-like electronic energy structure of these nanoclusters (in a similar way to the bigger ones), arising from their ultrasmall core dimensions and resulting in a substantial bigger HOMO-LUMO gap, ranging from 1.4 to 1.8 eV. Moreover, through CV and DPV measurements, they demonstrated that the effect of ligand fields, and consequently the surface chemistry of the nanoclusters, plays a crucial role in determining the electronic energy structure of the system, particularly the HOMO-LUMO energy gap. For this reason, modifying the organic-protecting monolayer with alternative ligand systems is becoming increasingly intriguing. Among many options, the combination of phosphines and N-heterocyclic carbenes complex (NHCs) as ligands is gaining more and more interest in recent years.

Following these pioneering works, significant advances have been made in both synthesis and electrochemical characterizations. However, the physical properties of these nanosystems are far from being fully elucidated, and among these, electrochemical investigations are rather limited and often hindered by significant imprecisions.[14–16]

This chapter focuses on the electrochemical properties of novel, ultra-small Au NCs with 13 or fewer gold atoms, protected by mixed ligands (phosphines, and di-NHCs). We address two main issues concerning the electron transfer properties of these NCs: firstly, the definition of the HOMO-LUMO gap and its correlation with cluster size and/or ligand properties; and secondly, the elucidation of how carbene ligands can influence redox properties in terms of reduction and oxidation potentials, stability, and additivity factors. The results of this work demonstrate that ligands can exert a significant influence on the electrochemical properties of sub-nanometer atomically precise gold nanoclusters. These results open new possibilities for the design and synthesis of nanoclusters with desired electrochemical properties.

9.3 Results and Discussion

All the clusters that we will present in this work were prepared by Dott. Matteo Bevilacqua, working in the Chemical Sciences Department, University of Padova, under the supervision of Prof. Andrea Biffis. They all have an $[Au_{11}]^{3+}$ or $[Au_{13}]^{5+}$ core and were obtained from direct synthesis (using phosphine or di-NHC complexes as reactants) or by ligand exchange reaction (LER), starting from $[Au_{11}(PPh_3)_8Cl_2]Cl$ nanocluster.

Au_{11} is the most well-known and investigated sub-nanometer nanocluster. It is composed of an 11-atom incomplete icosahedral kernel, which is derived from the icosahedral Au_{13} synthon through etching and removal of two gold atoms.[17]

Four types of new nanoclusters were analyzed, with different gold core (Au_{11} or Au_{13}), number of di-NHC ligands (different degrees of substitution), and charge state.

Type 1: $[Au_{11}(di\text{-}NHC)(PPh_3)_6Cl_2]Cl$

Type 2: $[Au_{13}(di\text{-}NHC)_2(PPh_3)_4Cl_4]Cl$

Type 3: $[Au_{13}(di\text{-}NHC)_3(PPh_3)_3Cl_3]Cl_2$

Type 4 (benchmark): $[Au_{13}(di\text{-}NHC)_5Br_2]Br_3$

All the NCs were purified by column chromatography, using DCM/MeOH (9/1) as eluent, and characterized by UV-Vis spectroscopy, ESI-MS spectrometry and photoluminescence measurements. The ligands used to protect and stabilize the metal cores are presented in Figure 3.

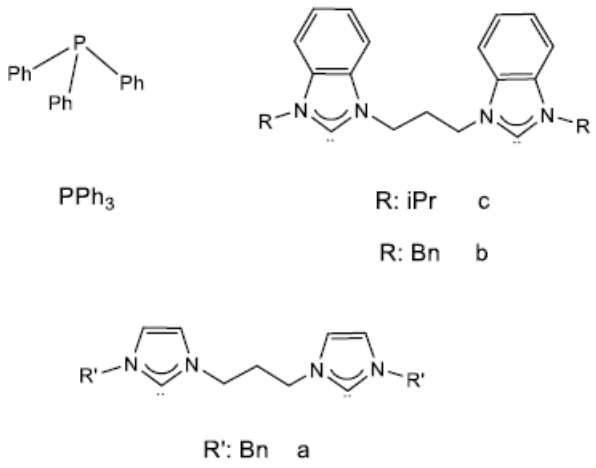

Figure 3 di-NHC and phosphine ligands used in this work as protecting ligands for Au_{11} and Au_{13} NCs.

The list of samples is reported as follows:

Au_{11}

$[Au_{11}(PPh_3)_8Cl_2]Cl$, **11**

$[Au_{11}($**di-NHC^c**$)(PPh_3)_6Cl_2]Cl$, **11-1_c**

Au_{13}

$[Au_{13}($**di-NHC^b**$)_5Br_2]Br_3$, **13-5_b**

$[Au_{13}($**di-NHC^a**$)_2(PPh_3)_4Cl_4]Cl$, **13-2_a**

$[Au_{13}($**di-NHC^a**$)_3(PPh_3)_3Cl_3]Cl_2$, **13-3_a**

$[Au_{13}($**di-NHC^b**$)_2(PPh_3)_4Cl_4]Cl$, **13-2_b**

$[Au_{13}($**di-NHC^b**$)_3(PPh_3)_3Cl_3]Cl_2$, **13-3_b**

For each cluster Cyclic Voltammetry (CV) and Differential Pulse Voltammetry (DPV) behaviors were analyzed. DPV characterization was needed because of the low amount of material available (due to purification difficulties) since this technique suppresses background currents much more effectively than CV.

9.3.1 Electrochemical Characterization of $Au_{11}(PPh_3)_8$ and his HOMO-LUMO gap

The ET behavior of $Au_{11}(PPh_3)_8$ was studied on 0.22 mm glassy carbon (GC) disk electrode, in dichloromethane (DCM) and acetonitrile (MeCN) containing 0.1 M $TBAPF_6$. More details will be provided in the “Experimental” section.

The CV obtained in DCM is illustrated in Figure 4 which shows three irreversible peaks.

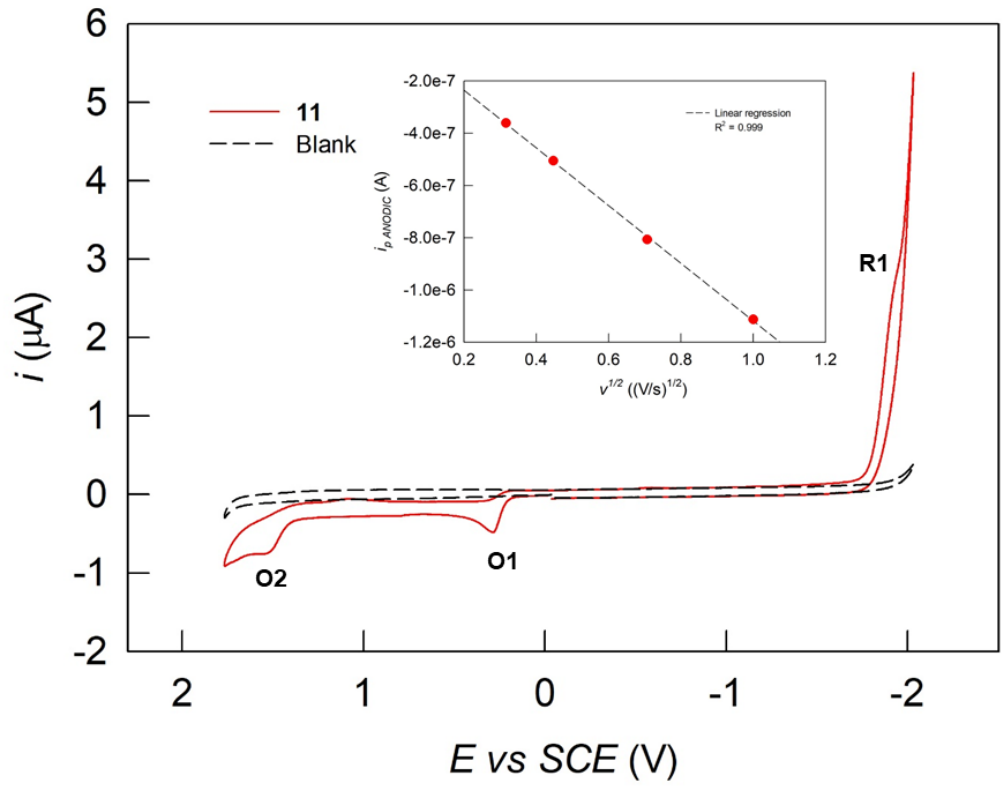

Figure 4 CV of 0.6 mM $[Au_{11}(PPh_3)_8Cl_2]Cl$ in DCM containing 0.1 M $TBAPF_6$. Conditions: v = 0.2 Vs^{-1}, GC electrode, 25 °C. In the inset, the analysis of the $i_{p\ ANODIC}$ peak of O1 process as the function of the $v^{1/2}$.

The first one, at 0.284 V vs SCE, is related to the first oxidation (O1) of the nanoclusters; the first reduction (R1) starts at about -1.73 V vs SCE, demonstrating very high stability towards reduction, while the second oxidation (O2) lies at about 1.55 V vs SCE. While the first reduction and the first oxidation are certainly referred to the cluster, the second oxidation, given the much larger shape, could be due to the oxidation of one of the ligands. Moreover, the behavior of this peak is not reproducible, presumably arising also from the breakdown of the cluster. The irreversibility of the processes is consistent with the possible chemical changes in the clusters upon both reduction and oxidation. Indeed, no reversibility was observed neither at high scan rates nor low temperature (down to - 40 °C). The first reduction peak appears to correspond to a multiple-electron reduction since its peak has a much higher intensity than expected for a monoelectronic process. This was attributed to a redox catalysis process that we will discuss later in the chapter. Analyzing the behavior of the peak current i_p of the O1 process up to 500 mV/s, we observed a linear dependance on the square root of scan rate, indicating that the electroactive species are diffusing nanoclusters in solution (inset of Figure 4). As we move from DCM to MeCN, some differences are evident. First of all, the available reduction potential window is much

larger, and this allows us to observe a larger number of reductive process involving the NC. After that, a second important point is the smaller separation between the peaks, both O2-O1 and O1-R1. In details, the separation between O1 and R1 decreases of about 164 mV (Figure 5).

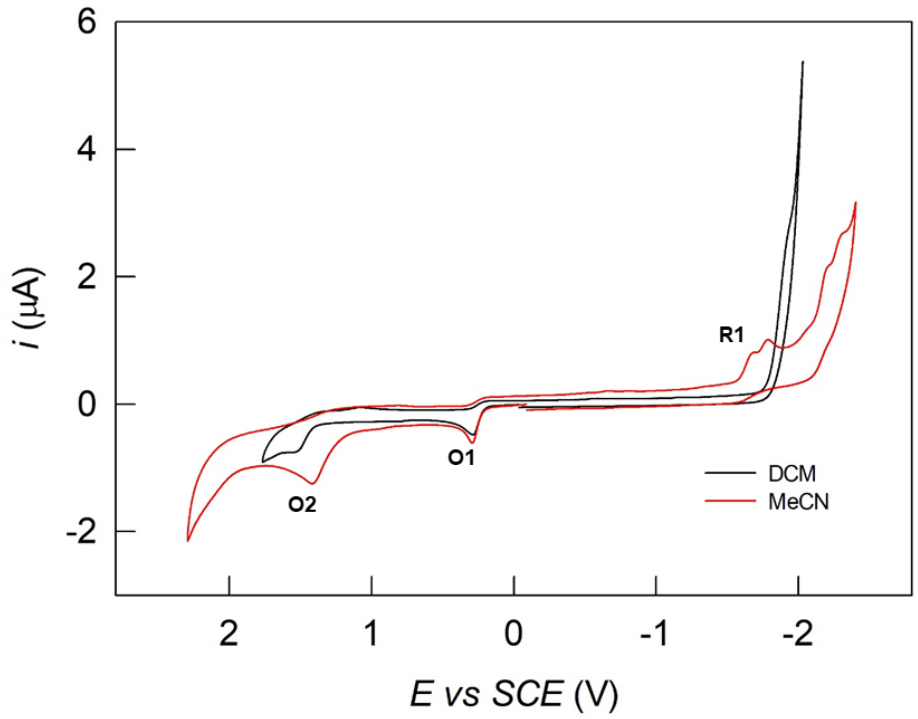

Figure 5 CV of 0.6 mM $[Au_{11}(PPh_3)_8Cl_2]Cl$ in DCM (black line) and MeCN (red line) containing 0.1 M $TBAPF_6$. Conditions: v = 0.2 Vs^{-1}, GC electrode, 25 °C.

This is in keeping with the expected effect exerted by switching to a more polar environment.[6] Moreover, no catalysis curve in the reduction region was observed in MeCN. Given this last observation, we can assume that the current increase that characterizes the R1 peak in DCM is due to a catalytic reduction reaction of the DCM itself, caused by the reduced nanocluster species. Some more details about this process will be given later. Unfortunately, the diffusion coefficient (D) and the hydrodynamic radius (r) could not be calculated due to the high uncertainty on the concentration of the investigated sample due to the purification problems and their limited stability even in standard conditions.[18]

Giving a better look at the CV from O1 and R1 (Figure 6), we assessed the electrochemical HOMO-LUMO gap of the nanocluster.

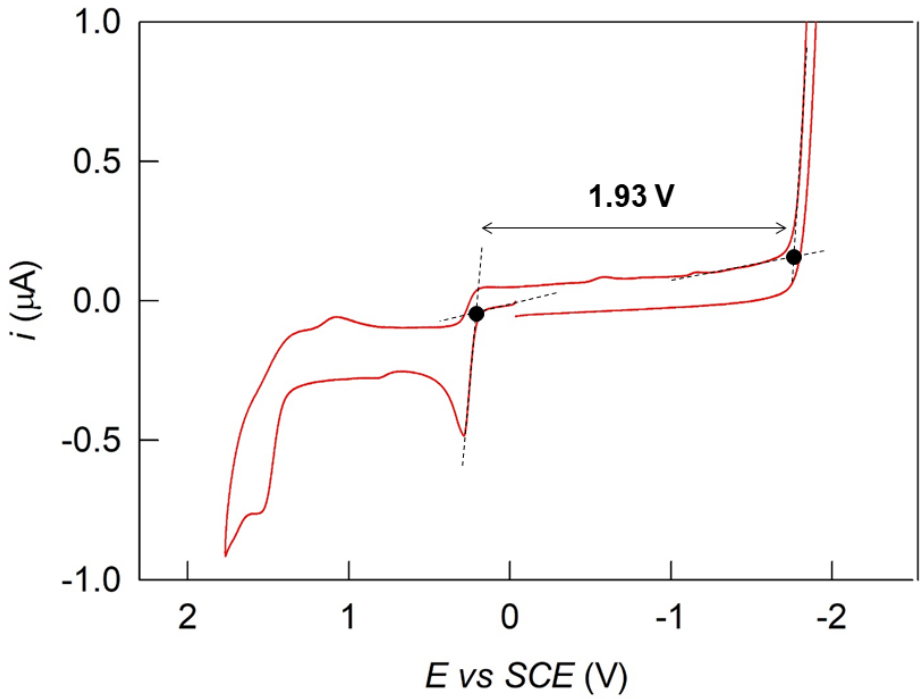

Figure 6 CV of 0.6 mM $[Au_{11}(PPh_3)_8Cl_2]Cl$ in DCM containing 0.1 M $TBAPF_6$. Conditions: v = 0.2 Vs^{-1}, GC electrode, 25 °C. In the curve the calculated HOMO-LUMO gap is underlined.

Considering the potential's onset of the first oxidation and reduction peaks processes we calculated an electrochemical HOMO-LUMO gap of 1.93 eV. This value should represent an overestimation of the gap since we didn't subtract the charging energy contribution, since we cannot obtain estimation of its value from the CV in DCM. Anyway, the overestimation is in part compensated by using the onset potential of the peak in place of the *E*° of the process. Indeed, the obtained value is in good agreement with that derived from the UV-Vis spectral data (583 nm absorption peak, see the "Supporting materials" section) by extrapolation to zero absorbance, that is 2.13 eV. The HOMO-LUMO value of the same Au_{11} nanocluster was previously evaluated via DFT calculations, by Hakkinen and co. revealing a value of 1.95 eV,[19] in excellent agreement with the experimental one obtained by us by CV. Moreover, the measured HOMO-LUMO gap of 1.93 eV is perfectly consistent with the graph showed in the "Introduction" section of this chapter, which shows how the electrochemical HOMO-LUMO gap changes as the number of gold atoms in the NCs increases.[1,20] Here below (Figure 7), the same graph, with the gap value found for Au_{11} (green dots) is presented.

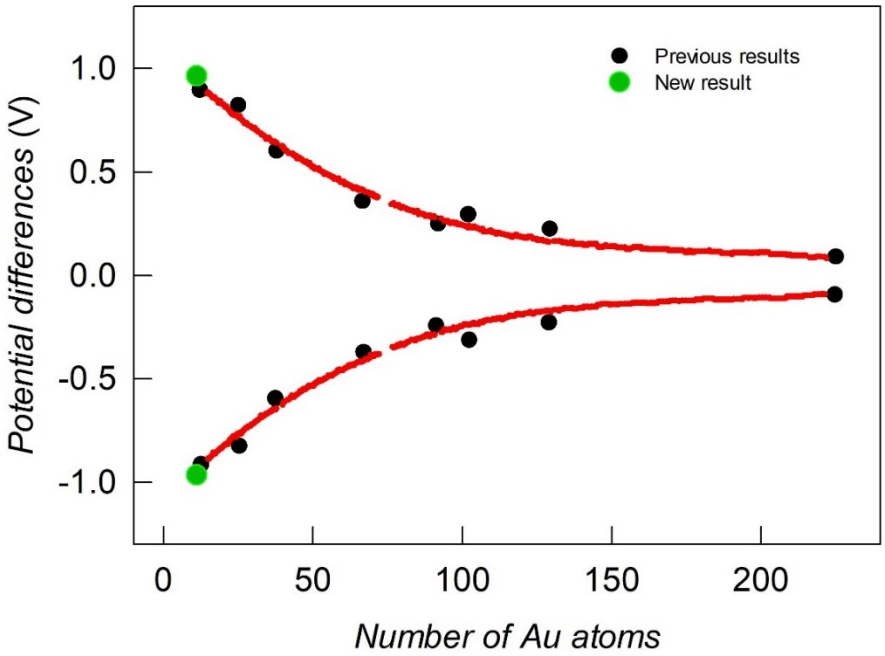

Figure 7 Electrochemical gaps as function of the number of Au atoms. The red lines are only meant to highlight the general trend. The green circle represents the new result (1.95 eV) about $[Au_{11}(PPh_3)_8Cl_2]Cl$.

With the goal of increasing the current/background ratio and better comparing the results with literature data, the DPV characterization was also performed, with no different outcomes (See "Supporting materials" section). The DPV in MeCN reveals a larger number of redox processes. In the oxidation potential region four processes are observed with $E_{1/2}$ value of 0.246, 0.72, 1.10, and 1.34 V vs SCE (calculated as the half-sum of the anodic and cathodic peaks). In the reduction region, 4 processes were found ($E_{1/2}$ = -1.66, -1.76, -2.07, and -2.18 V vs SCE). The electrochemical HOMO-LUMO gap (again without subtraction of the charging energy), in MeCN (more reliable, because of the absence of the electrocatalytic current at the first reduction peak) is 1.91 eV (please, see Figure in the "Supporting materials" section). We can approximate the charging energy of the nanolcluster from the gap between R1 and R2 (charging process of the HOMO orbital). Considering this correction (R1-R2 gap of 105 mV), the HOMO-LUMO gap is 1.8 eV.

9.3.2 The Effect of the Single di-Carbene Ligand on the Electrochemical Properties of Au_{11} Nanocluster

The di-NHC substituted Au_{11} NCs were synthetized via ligand exchange reaction (LER). by substitution of two endogenous phosphine ligand out of the 8 originals. Having a monofunctionalized nanocluster gives us the opportunity to finely

understand the effect of the di-NHC on the electrochemical properties of the nanocluster. The CV behavior was found out to be essentially the same of the non-substituted nanocluster, both in DCM (Figure 8) and MeCN, but shifted towards less positive potentials.

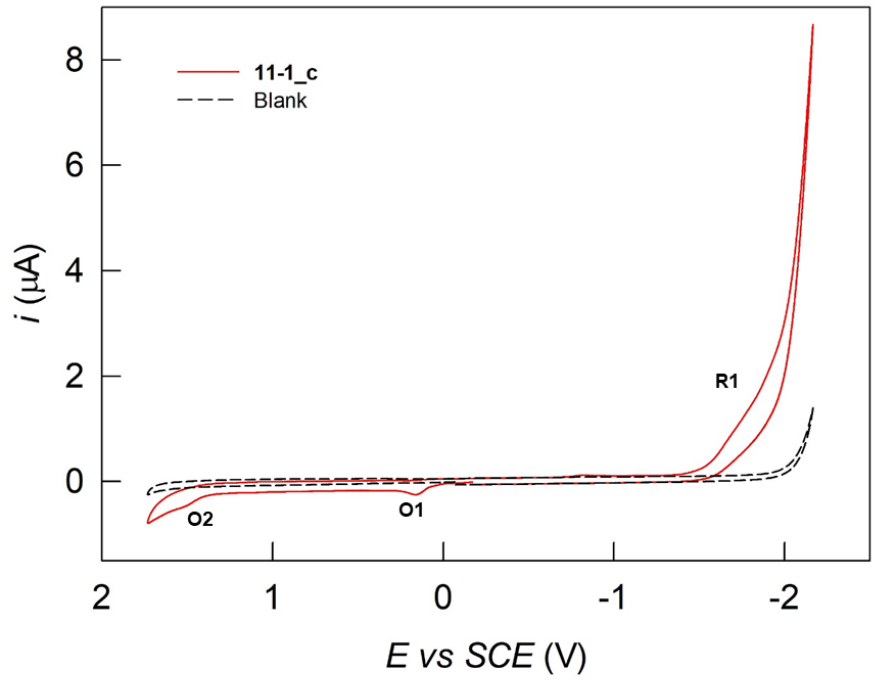

Figure 8 CV of 0.6 mM $[Au_{11}(PPh_3)_6(di\text{-}NHC^c)Cl_2]Cl$ in DCM containing 0.1 M $TBAPF_6$. Conditions: v = 0.2 Vs^{-1}, GC electrode, 25 °C.

In details, the CV shows three irreversible redox processes. The first oxidation (O1) lies at 0.160 V vs SCE; the first reduction (R1) starts at about -1.520 V vs SCE, while the second oxidation (O2) at about 1.511 V vs SCE. No reversibility was observed either at high scan rates or low temperature (down to - 40 °C). As for the Au_{11} non-substituted nanocluster, R1 appears to be a catalytic peak. In Figure 9 the overlay of the DPVs highlights the effect of the presence of the carbene ligand on Au_{11}.

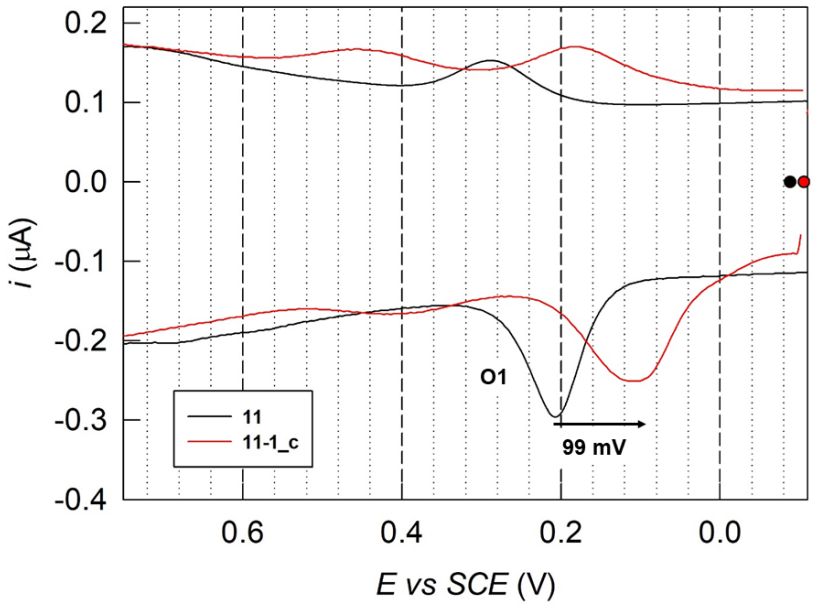

Figure 9 DPV redox peak related to O1 process of unsubstituted Au_{11} (black line) and monosubstituted with one di-NHC^c (red line), measured in MeCN. In the curve, the shift of about 99 mV is underlined.

A substantial shift towards negative potentials was observed for all the redox processes. This demonstrates that one carbene complex in the structure has the effect of favoring the oxidation of the cluster, in agreement with carbene complexes reactivity. In general, the electron donating effect of carbene complexes is higher than that of phosphine ligands.[21,22] This means that now the ligands are donating electrons to the nanocluster core more efficiently, with the effect of better stabilizing the positive charges. For this reason, the redox process consisting in the oxidation from +1 to +2 (O1) is anticipated, demonstrating the effect of the di-NHC complexes on the nanocluster structure. The presence of a di-carbene complex on the system also has the effect of upshift the LUMO, resulting in a larger HOMO-LUMO gap respect to the non-substituted one of about 0.30 eV (See Figure in the “Supporting materials” section). This observation agrees with previous results[13,23] that were attributed to the stronger bonding of Au-NHC compared to that of Au-P (Cl),[21,22] which is aligned to ligand-field effects on the splitting of the electronic energy of coordinated complexes.[23]

9.3.3 Manipulating the Physicochemical Properties of Au_{13}: The Effect of Modifying the Ligand Properties

The influence of ligand composition on the physicochemical properties of Au_{13} sub-nanometer nanoclusters will be explored in the following paragraphs. A series of mixed-ligand Au_{13} nanoclusters were synthesized using ligand exchange reactions, starting from $[Au_{11}(PPh_3)_8Cl_2]Cl$. This approach allows for a more comprehensive understanding of how di-NHC complexes impact the Au_{13} nanocluster's electrochemical properties. While detailed electrochemical characterizations are presented in the "Supporting materials" section, these next paragraphs will primarily focus on significant insights.

In the previous paragraph we demonstrated that the replacing of two phosphines ligands with one di-NHC complex, as the effect of favoring the oxidation of the nanocluster, in agreement with carbene complexes reactivity. Here we wanted to analyze the effect of having in the Au_{13} nanocluster's structure, the same number of di-carbene ligands, but with different substitution at the back of the five-member ring. We compared the electrochemical behavior of **13-2_a** and **13-2_b**, characterized by the same Au_{13} core and the same number (2) of di-NHC ligands, but with different chemical structure (ligands **a** and **b** in Figure 3). In particular, the "b" complex is a di-NHC bringing an aromatic group on the back of the five rings (benzimidazole carbene ligand), linked from the edge of the rings. Figure 10 shows the comparison between the DPV behavior of the two clusters in MeCN (the complete electrochemical characterization is presented in the "Supporting materials" section).

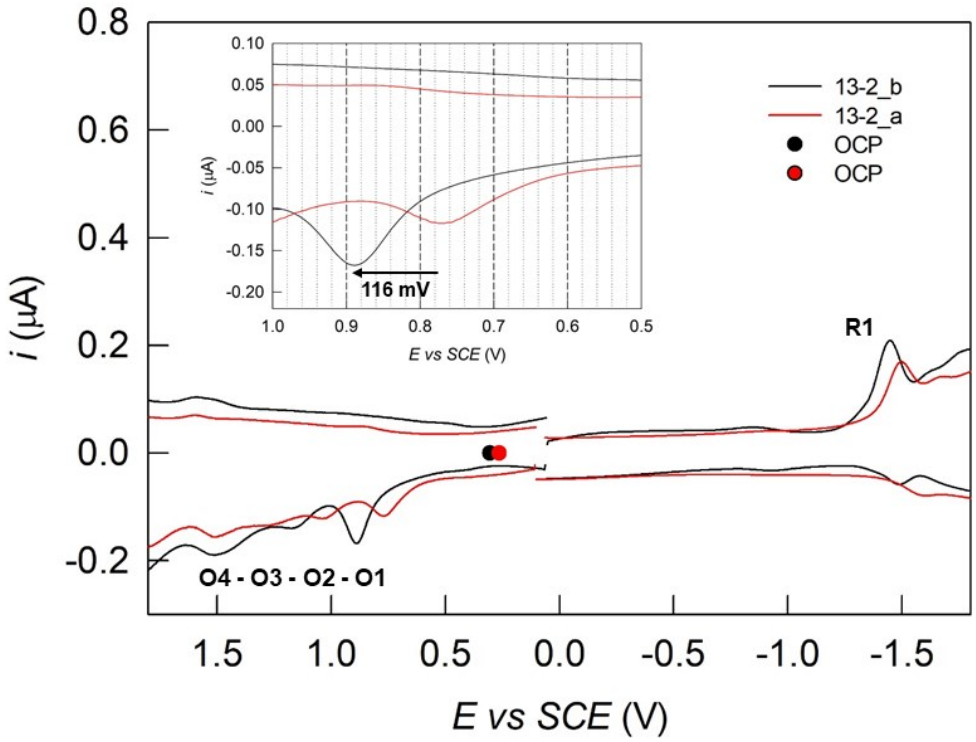

Figure 10 DPV behavior of **13-2_b** (0.4 mM) (black line) and **13-2_a** (0.3 mM) (red line) in MeCN. The effect of the different di-NHC is shown by the potential shift toward less positive values. In the inset the redox peaks related to O processes is showed. In the curve, the shift of about 116 mV is underlined.

The electrochemical behavior is quite similar with the same sequence of peaks that are observed in the two DPVs. However, the presence of benzimidazole carbene ligand (black line) induces a positive shift in the peaks potential values respect the ligand without the condensed aromatic ring. This result agrees with the expectation, indeed, the benzimidazole ligand can better delocalize electrons on its aromatic back ring and lower the cluster LUMO energy. On the other side, the oxidation process is less favorable. Comparable energy shifts are observed for both the HOMO and the LUMO orbitals, resulting in no significant variation of the HOMO-LUMO gap (2.32 eV for **13-2_a** and 2.36 eV for **13-2_b**). This means that the HOMO_LUMO gap could be affected by the nature of the Au-ligand bond but not much by eventual inductive effects of the organic moiety.

9.3.4 Manipulating the Physicochemical Properties of Au_{13}: The Effect of the Number of di-NHC Ligands

The availability of a library of Au_{13} nanoclusters with different degrees of carbene complex substitution, gave us the opportunity to deeper explore the ligand composition effect on the electrochemical properties. In particular, the possibility of

analyzing the Au_{13} nanocluster completely protected and stabilized by carbene complexes (five di-NHC^c and two bromide anions) allows us to use it as a benchmark. Figure 11 shows its DPV behavior in MeCN.

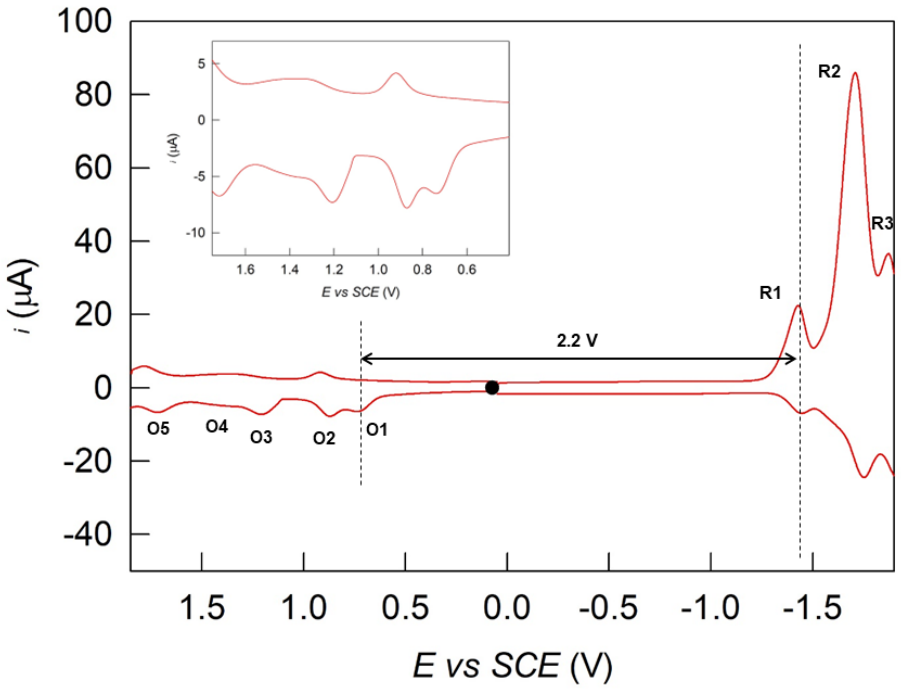

Figure 11 DPV of 1 mM $[Au_{13}(di\text{-}NHC^c)_5Br_2]Br_3$ in MeCN containing 0.1 M $TBAPF_6$. In the inset, the zoom of the oxidative region is magnified.

From the DPV behavior here above (Figure 11), we can observe at least seven redox processes (that resulted to be irreversible in CV curve). From the first oxidation (O1) at 0.738 V vs SCE and the first reduction (R1) at -1.438V vs SCE we can estimate an electrochemical HOMO-LUMO gap of 2.2 eV (without considering the charging energy correction), in very good agreement with the optical one, obtained from the on-set of the first signal (560 nm, corresponding to an energy of 2.22 eV). In addition, there are three further oxidative processes (E°(O2) = 0.895 V, E°(O3) = 1.272 V, E_p(O4) = 1.379 V, and E_p(O5) = 1.721 V vs SCE), and two more reduction processes (E°(R2) = -1.730 V, and E°(R3) = -1.890 V vs SCE). The second reduction (R2), is characterized by a much larger current intensity respect the other peaks but it is not easy to explain this behavior: it could be due to multielectrons reduction processes involving the ligands or arising from the dissociative ET mechanism as happens for thiolate-protected clusters.[24] Indeed, the irreversibility of the processes is consistent with the possible chemical changes in the clusters upon both reduction and oxidation. Moreover, no reversibility was observed either at high scan rates or low temperature (down to - 40 °C). In addition, passivation of the electrode was observed every time

the reduction window was spanned, most probably due to the production of some insoluble products at the R2 process. Serving as a benchmark, this sample facilitates a more in-depth assessment of how the number of di-NHC complexes affects the nanocluster electrochemical properties. In the following section, a comparison of Au_{13} nanoclusters with three and five di-NHC complexes is presented (Detailed electrochemical characterizations are provided in the "Supporting materials" section). In Figure 12 the DPV behavior in MeCN of sample **13-5_b** and **13-3_b** is presented.

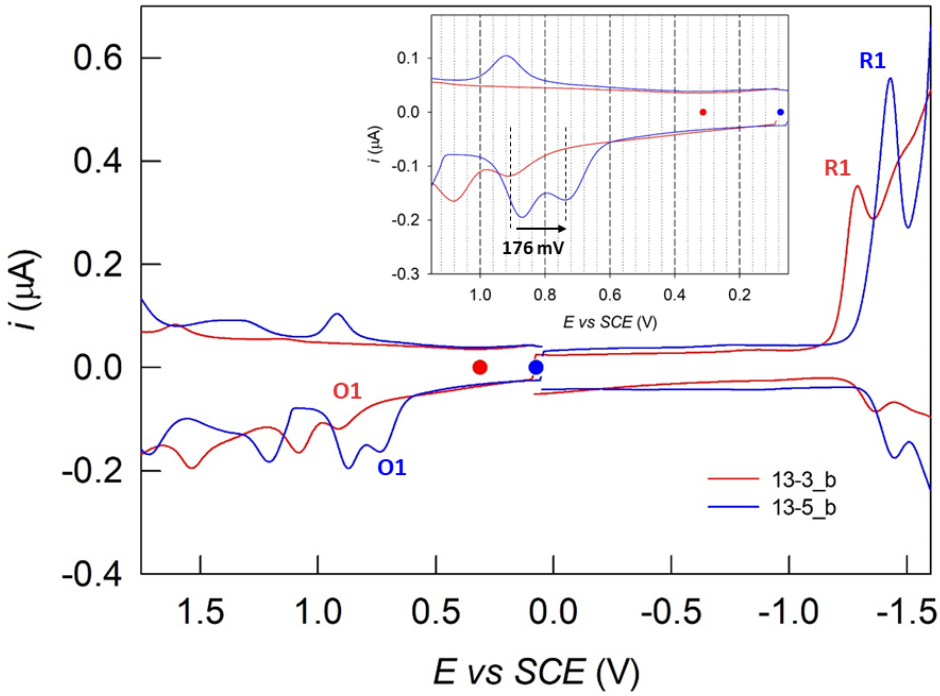

Figure 12 DPV behavior of **13-3_b** (0.6 mM) (red line) and **13-5_b** (1 mM) (blue line), in MeCN. The effect of the number of di-NHC is shown by the potential shift toward less positive values (anticipating the oxidation processes). In the inset the redox peaks related to O1 processes are shown. In the curve, the shift of about 176 mV is underlined.

The two DPV curves show a similar pattern for the two Au_{13} nanoclusters. However, a significant potential shift was observed in all the redox processes of the two species. The presence of two additional carbene ligands in **13-5_b** respect **13-3_b** induces a general shift of the peak towards negative potentials in line with the sigma-donating effect that characterizes these ligands. In the inset of Figure 12 the effect on the first oxidation process (O1) is highlighted. Increasing the number of di-NHC complexes ligands it is then possible to better stabilize positive charges resulting in anticipating the oxidation potentials, and, at the same time, delay the reduction processes. This effect is also observed from the equilibrium potentials (OCP) of the two samples (red and blue circles on the DPV). Indeed, the OCP value of **13-5_b** is really anticipated

and now close to 0 V vs SCE, demonstrating that the carbene ligands are mitigating the positive charges of the cores, that actually is formally an $[Au_{13}]^{+5}$ ("superatoms" theory).[25]

9.3.5 Catalysis of Dichloromethane Reduction Reaction

In our previous studies (please, see the 10.3.1 paragraph) we demonstrated that all investigated nanoclusters (NCs) exhibit catalytic currents in dichloromethane (DCM) within the reduction region. Specifically, the Faradic current undergoes a substantial increase corresponding to the first reduction peak/process of the investigated nanoclusters. This observation is attributed to the catalysis of DCM reduction by the reduced nanoclusters. A representative catalytic current is depicted in Figure 13.

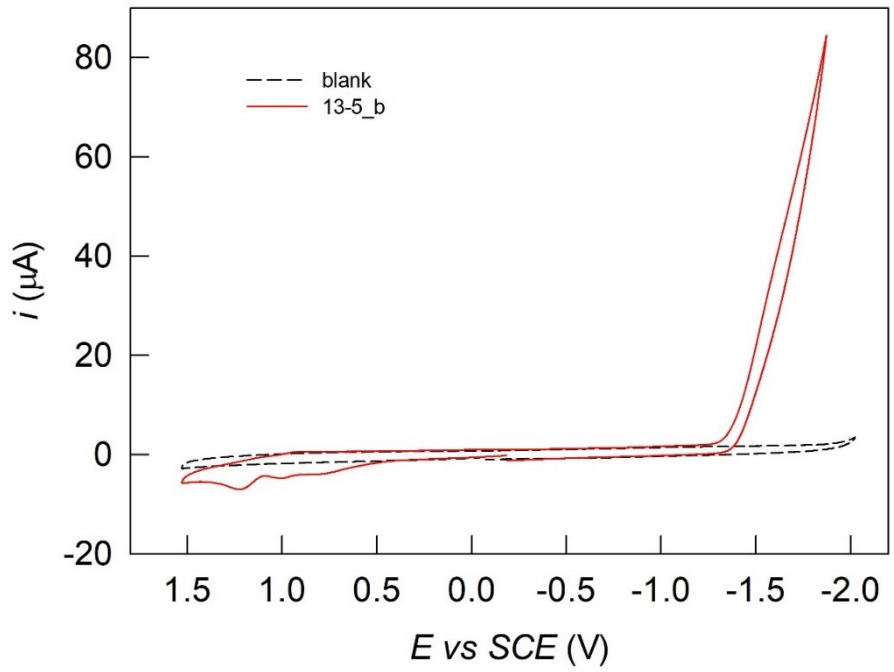

Figure 13 CV of 1 mM $[Au_{13}(di\text{-}NHC^c)_8Br_2]Br_3$ in DCM containing 0.1 M $TBAPF_6$. Conditions: v = 0.2 Vs^{-1}, GC electrode, 25 °C. At potentials lower than -1.4 V vs SCE, a catalysis current starts to increase.

This phenomenon was observed in all the seven investigated samples, suggesting its independence from the type/dimension of the core (Au_{11} or Au_{13}) and by the type of ligands. Catalysis was consistently observed in mixed nanoclusters, as well as in those completely protected by phosphines or di-NHC complexes. Typically, the organic ligands forming the monolayer act as insulators for the NC's core and the surrounding environment. However, in this scenario the dynamism of the monolayer becomes crucial for the reactivity of the NC, which is the reason why the LER strategies have proven to be highly effective with NCs.[26] The ligands, especially when

the cluster is in solution, are never stationary in their position but are constantly in motion even if always anchored. During their movement, they can expose the core to the external environment. However, this is not our case, because the structure of these sub-nanometer NCs does not consist of a conventional monolayer, since all the ligands are directly bonded to the metal core. In this second scenario, the core appears to be much more exposed, especially to small organic molecules that can penetrate more easily between the binders. This exposure could be the reason for the observed catalytic current arising from the reduction of DCM on the almost naked surface of the core. The catalytic current appears at the first reduction process, suggesting that the reduced NC is the active species. The following is the suggested scheme of reactions:

R1: $AuNC + 1e^- (electrode) \rightarrow AuNC^-$

CAT: $AuNC^- + CH_2Cl_2 \rightarrow AuNC + CH_2Cl^{\bullet} + Cl^-$

New R1: $AuNC + 1e^- (electrode) \rightarrow AuNC^-$

The regeneration of the original Au NC through the DCM catalysis reaction (**CAT**) triggers a subsequent reduction reaction at the electrode (**New R1**), thereby amplifying the cluster reduction current, as depicted in Figure 13. To qualitatively assess the catalytic efficiency of these Au NCs, we compared the current intensities of distinct samples, aiming to evaluate the relative catalytic performances. This involved extracting the current intensity at the inflection, through the minimum signals in the first derivative of the CVs current of each AuNC and normalizing it to the actual concentration at the time of measurement. The results are presented in Figure 14.

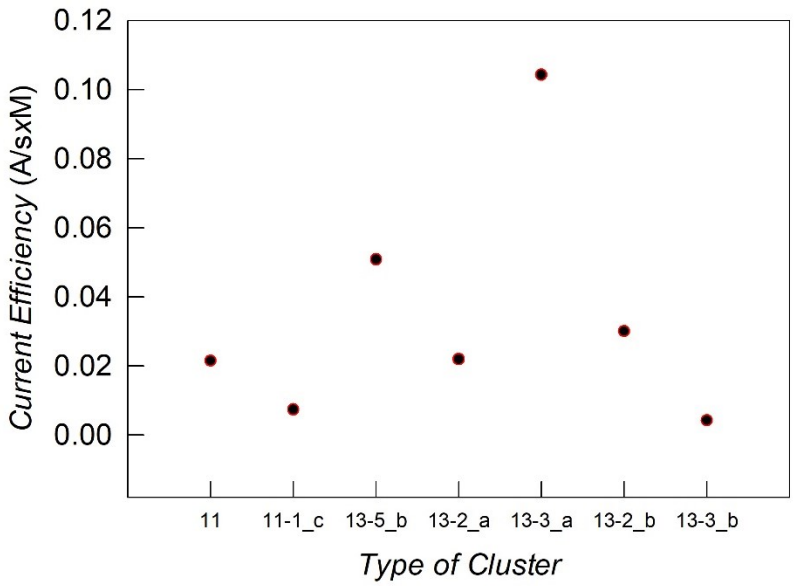

Figure 14 Graph showing the catalytic efficiency of each NCs, evaluated as the current intensity at the first inflection of the current in the reduction potential region.

No trend was observed. This topic needs to be better studied with more systematic measurements, investigating all the parameters that can be important in this intriguing but also inexplicable catalysis reaction.

9.4 Conclusions

The presented study explores the influence of ligands, particularly di-carbene complexes, on the electrochemical properties of sub-nanometer nanoclusters (Au_{11} and Au_{13} NCs). The findings reveal that all tested nanoclusters exhibit redox activity and remarkable stability against oxidation and reduction reactions. Intriguingly, these nanoclusters demonstrate electrocatalytic activity towards the reduction of dichloromethane. The incorporation of carbene complexes as ligands significantly alters the electrochemical characteristics of the nanoclusters, inducing shifts towards more positive potentials. Notably, the redox potential can be effectively modulated by tailoring the carbene complex, showcasing a stronger influence on the NC's core compared to conventional alkanethiol ligands. To visualize the effect of di-NHC ligands on potential shifts and HOMO-LUMO gaps, we plotted the O1 and R1 processes of all investigated nanoclusters in a single graph (Figure 15). It is crucial to note that these results are primarily intended for comparisons between similar clusters and do not account for the carbene position within the structure, especially when multiple complexes are introduced. As demonstrated by Crudden and co., the carbene position can modulate the HOMO-LUMO gap by up to 0.17 eV, either positively or negatively.[19]

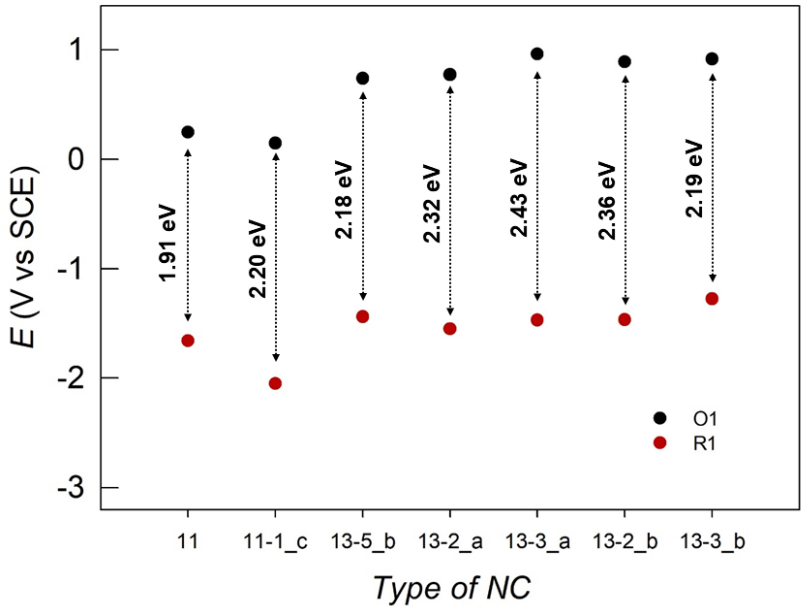

Figure 15 Summary of the first reduction potentials (R1, marked with red) and the first oxidation potentials (O1, marked with black) of Au_{11} and Au_{13} nanoclusters, taken from DPV curves, in MeCN. The calculated electrochemical HOMO-LUMO gap, is highlighted.

The ability to fine-tune the electrochemical properties of nanomaterials through ligand modification, particularly with carbene complexes, holds promising potential for diverse future applications.

9.5 Experimental

The electrochemical experiments were carried out in DCM (MeCN) containing 0.1 M TBAPF6, under an Ar atmosphere, in a glass cell thermostatted at $25\ (\pm 1)$ °C (unless otherwise specified). A 0.22 mm-radius glassy carbon disk prepared and activated as already described,[27] was the working electrode, whereas a Pt wire was the counter electrode. An Ag wire was used as the quasi-reference electrode. At the end of each experiment, the potential of the latter was calibrated against the ferricenium/ferrocene redox couple (in DCM/0.1 M TBAH, E0 = 0.460 V against the KCl saturated calomel electrode, SCE). To minimize the ohmic drop between the working and the reference electrodes, careful feedback correction was applied. The DPV experiments were carried out under the same conditions. The experimental parameters were a peak amplitude of 50 mV, pulse width of 0.025 s, 4 mV increments per cycle, and pulse period of 0.05 s.

9.6 Supporting Materials

In this section, all the electrochemical characterizations (the CVs shown were obtained at 0.2 V/s), plus some other characterizations necessary for the aim of the Chapter will be presented.

11, $[Au_{11}(PPh_3)_8Cl_2]Cl$

Electrochemical characterizations:

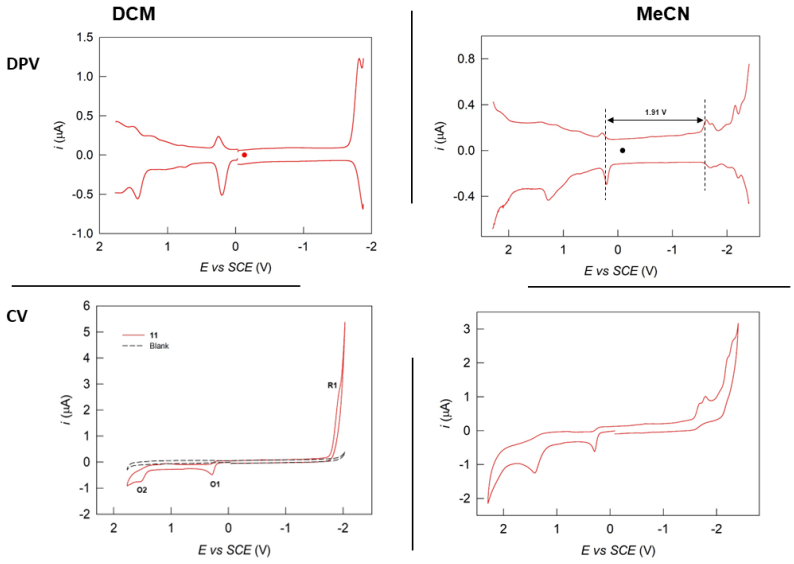

Optical characterizations and optical HOMO-LUMO gap:

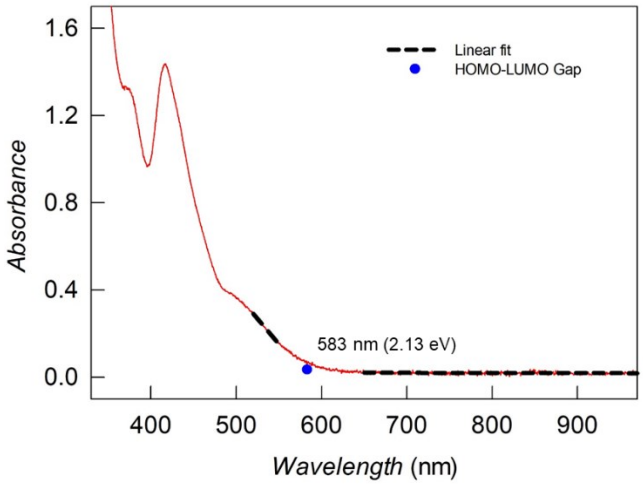

11-1_c, $[Au_{11}(\textbf{di-NHC}^{c})(PPh_3)_6Cl_2]Cl$

Electrochemical characterizations:

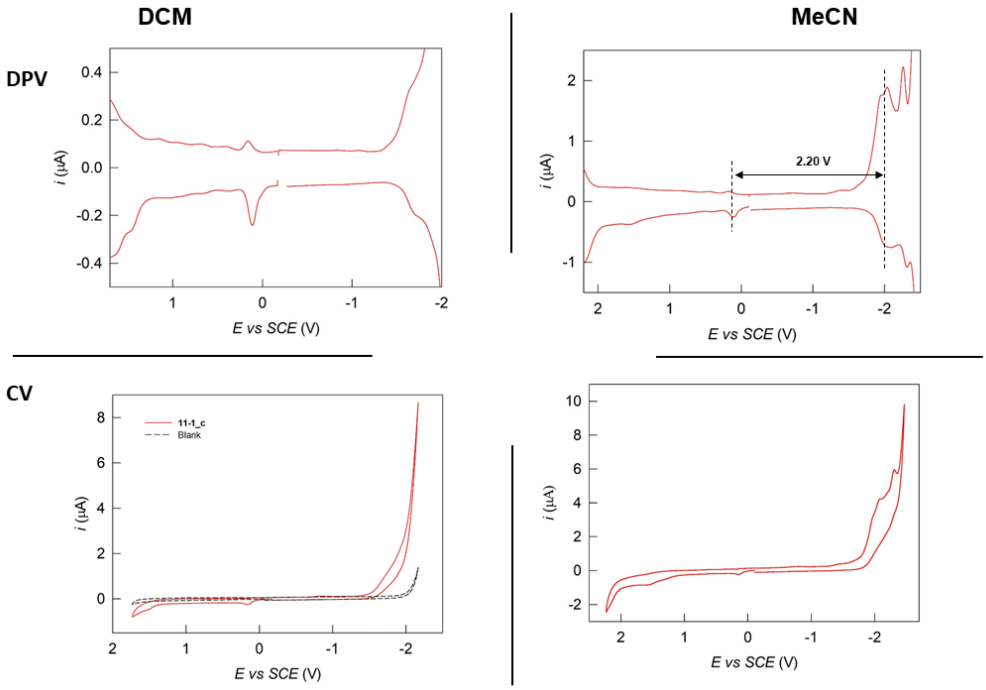

13-5_b, $[Au_{13}(\textbf{di-NHC}^{b})_5Br_2]Br_3$

Electrochemical characterizations:

(This is the only sample studied using a 0.93 mm-radius glassy carbon disk*)*

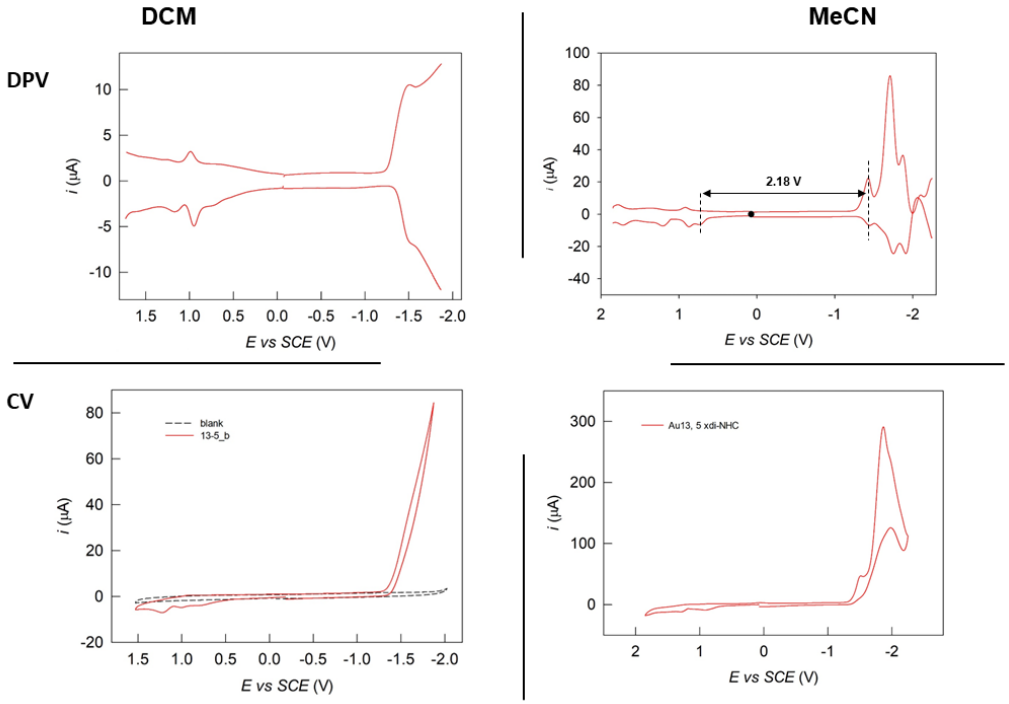

13-2_a, $[Au_{13}(\textbf{di-NHC}^{a})_2(PPh_3)_4Cl_4]Cl$

Electrochemical characterizations:

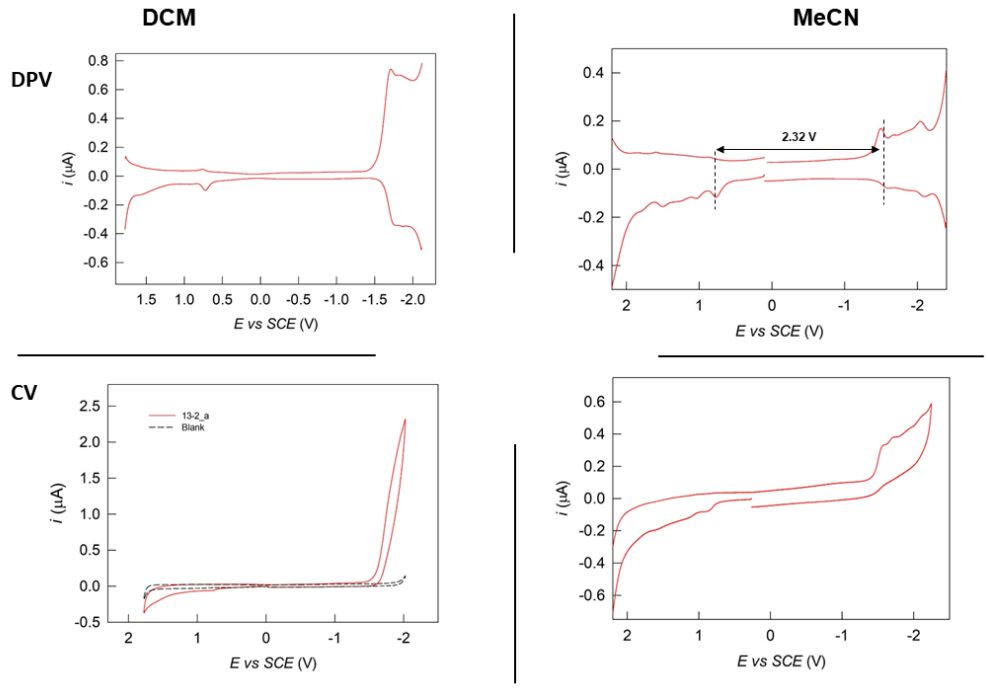

13-3_a, $[Au_{13}(\textbf{di-NHC}^{a})_3(PPh_3)_3Cl_3]Cl_2$

Electrochemical characterizations:

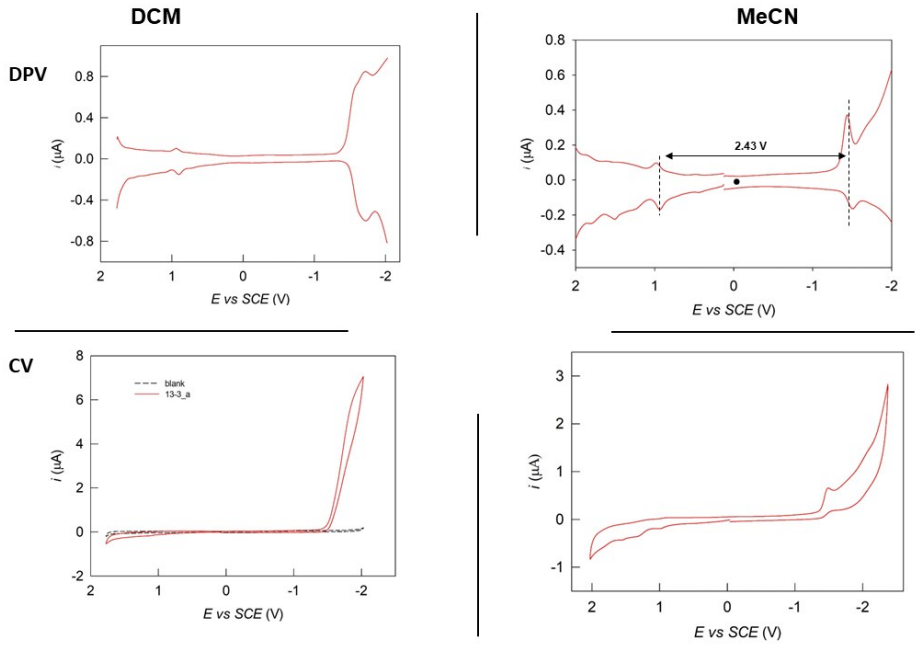

13-2_b, $[Au_{13}(\textbf{di-NHC}^{b})_2(PPh_3)_4Cl_4]Cl$

Electrochemical characterizations:

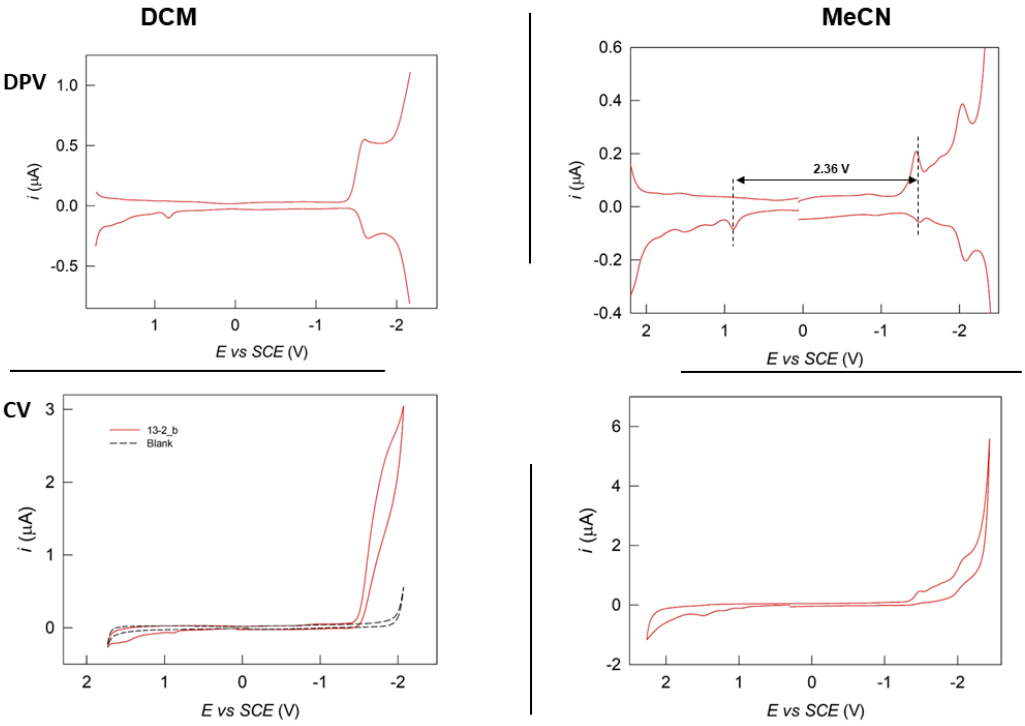

13-3_b, $[Au_{13}(\textbf{di-NHC}^{b})_3(PPh_3)_3Cl_3]Cl_2$

Electrochemical characterizations:

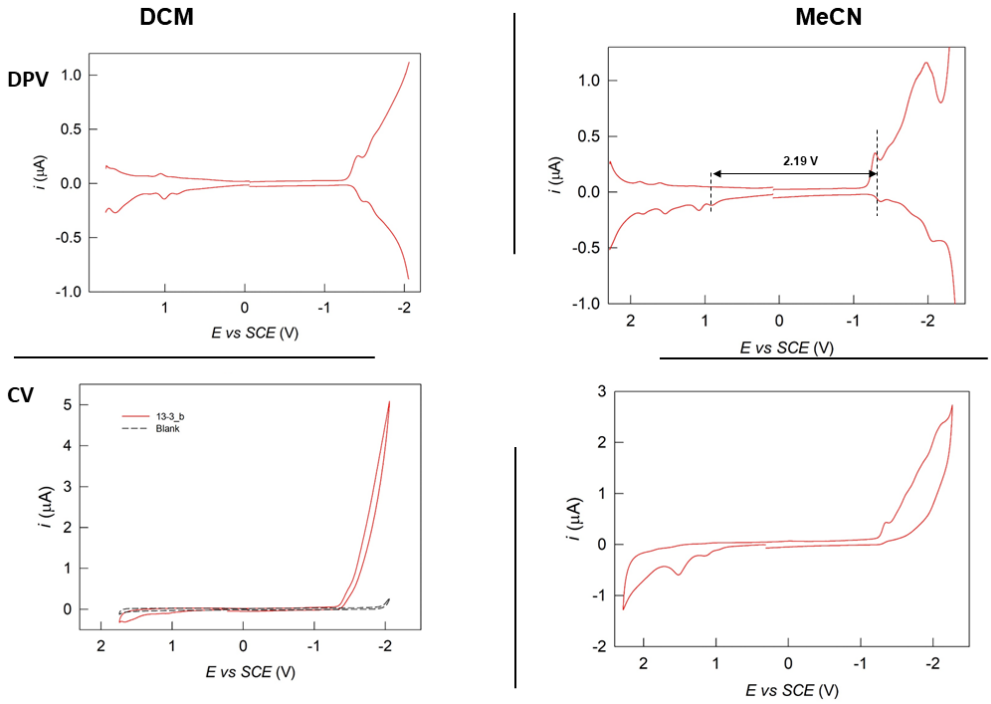

9.7 References

1. Antonello, S.; Maran, F. Molecular Electrochemistry of Monolayer-Protected Clusters. *Curr. Opin. Electrochem.* **2017**, *2* (1), 18–25.

2. Agrachev, M.; Ruzzi, M.; Venzo, A.; Maran, F. Nuclear and Electron Magnetic Resonance Spectroscopies of Atomically Precise Gold Nanoclusters. *Acc. Chem. Res.* **2019**, *52* (1), 44–52.

3. Antonello, S.; Dainese, T.; De Nardi, M.; Perotti, L.; Maran, F. Insights into the Interface Between the Electrolytic Solution and the Gold Core in Molecular Au_{25} Clusters. *ChemElectroChem* **2016**, *3* (8), 1237–1244.

4. Antonello, S.; Arrigoni, G.; Dainese, T.; De Nardi, M.; Parisio, G.; Perotti, L.; René, A.; Venzo, A.; Maran, F. Electron Transfer through 3D Monolayers on Au_{25} Clusters. *ACS Nano* **2014**, *8* (3), 2788–2795.

5. Quinn, B. M.; Liljeroth, P.; Ruiz, V.; Laaksonen, T.; Kontturi, K. Electrochemical Resolution of 15 Oxidation States for Monolayer Protected Gold Nanoparticles. *J. Am. Chem. Soc.* **2003**, *125* (22), 6644–6645.

6. Lee, D.; Donkers, R. L.; Wang, G.; Harper, A. S.; Murray, R. W. Electrochemistry and Optical Absorbance and Luminescence of Molecule-like Au_{38} Nanoparticles. *J. Am. Chem. Soc.* **2004**, *126* (19), 6193–6199.

7. Guo, R.; Murray, R. W. Substituent Effects on Redox Potentials and Optical Gap Energies of Molecule-like $Au_{38}(SPhX)_{24}$ Nanoparticles. *J. Am. Chem. Soc.* **2005**, *127* (34), 12140–12143.

8. Holm, A. H.; Ceccato, M.; Donkers, R. L.; Fabris, L.; Pace, G.; Maran, F. Effect of Peptide Ligand Dipole Moments on the Redox Potentials of Au_{38} and Au_{140} Nanoparticles. *Langmuir* **2006**, *22* (25), 10584–10589.

9. Hossain, S.; Kurashige, W.; Wakayama, S.; Kumar, B.; Nair, L. V.; Niihori, Y.; Negishi, Y. Ligand Exchange Reactions in Thiolate-Protected Au_{25} Nanoclusters with Selenolates or Tellurolates: Preferential Exchange Sites and Effects on Electronic Structure. *J. Phys. Chem. C* **2016**, *120* (45), 25861–25869.

10. Venzo, A.; Antonello, S.; Gascón, J. A.; Guryanov, I.; Leapman, R. D.; Perera, N. V.; Sousa, A.; Zamuner, M.; Zanella, A.; Maran, F. Effect of the Charge State (z = −1, 0, +1) on the Nuclear Magnetic Resonance of Monodisperse Au_{25} $[S(CH_2)_2Ph]_{18}^{z}$ Clusters. *Anal. Chem.* **2011**, *83* (16), 6355–6362.

11. Agrachev, M.; Antonello, S.; Dainese, T.; Gascón, J. A.; Pan, F.; Rissanen, K.; Ruzzi, M.; Venzo, A.; Zoleo, A.; Maran, F. A Magnetic Look into the Protecting Layer of Au_{25} Clusters. *Chem. Sci.* **2016**, *7* (12), 6910–6918.

12. Chen, S. Langmuir Monolayers of Gold Nanoparticles: From Ohmic to Rectifying Charge Transfer. *Anal. Chim. Acta* **2003**, *496* (1–2), 29–37.

13. Menard, L. D.; Gao, S.-P.; Xu, H.; Twesten, R. D.; Harper, A. S.; Song, Y.; Wang, G.; Douglas, A. D.; Yang, J. C.; Frenkel, A. I.; Nuzzo, R. G.; Murray, R. W. Sub-Nanometer Au Monolayer-Protected Clusters Exhibiting Molecule-like Electronic Behavior: Quantitative High-Angle Annular Dark-Field Scanning Transmission Electron Microscopy and Electrochemical Characterization of Clusters with Precise Atomic Stoichiometry. *J. Phys. Chem. B* **2006**, *110* (26), 12874–12883.

14. Hirano, K.; Takano, S.; Tsukuda, T. Ligand Effects on the Structures of $[Au_{23}L_6(C{\equiv}CPh)_9]^{2+}$ (L = N-Heterocyclic Carbene vs Phosphine) with Au_{17} Superatomic Cores. *J. Phys. Chem. C* **2021**, *125* (18), 9930–9936.

15. Shen, H.; Wu, Q.; Malola, S.; Han, Y.-Z.; Xu, Z.; Qin, R.; Tang, X.; Chen, Y.-B.; Teo, B. K.; Häkkinen, H.; Zheng, N. N-Heterocyclic Carbene-Stabilized Gold Nanoclusters with Organometallic Motifs for Promoting Catalysis. *J. Am. Chem. Soc.* **2022**, *144* (24), 10844–10853.

16. Wang, X.; Liu, R.; Tian, L.; Bao, J.; Zhao, C.; Niu, F.; Cheng, D.; Lu, Z.; Hu, K. Highly Luminescent NHC-Stabilized Au_{13} Clusters as Efficient Excited-State Electron Donors. *J. Phys. Chem. C* **2022**, *126* (43), 18374–18382.

17. McKenzie, L. C.; Zaikova, T. O.; Hutchison, J. E. Structurally Similar Triphenylphosphine-Stabilized Undecagolds, $Au_{11}(PPh_3)_7Cl_3$ and $[Au_{11}(PPh_3)_8Cl_2]Cl$, Exhibit Distinct Ligand Exchange Pathways with Glutathione. *J. Am. Chem. Soc.* **2014**, *136* (38), 13426–13435.

18. Qin, Z.; Zhao, D.; Zhao, L.; Xiao, Q.; Wu, T.; Zhang, J.; Wan, C.; Li, G. Tailoring the Stability, Photocatalysis and Photoluminescence Properties of Au $_{11}$ Nanoclusters *via* Doping Engineering. *Nanoscale Adv.* **2019**, *1* (7), 2529–2536.

19. Narouz, M. R.; Osten, K. M.; Unsworth, P. J.; Man, R. W. Y.; Salorinne, K.; Takano, S.; Tomihara, R.; Kaappa, S.; Malola, S.; Dinh, C.-T.; Padmos, J. D.; Ayoo, K.; Garrett, P. J.; Nambo, M.; Horton, J. H.; Sargent, E. H.; Häkkinen, H.; Tsukuda, T.; Crudden, C. M. N-Heterocyclic Carbene-Functionalized Magic-Number Gold Nanoclusters. *Nat. Chem.* **2019**, *11* (5), 419–425.

20. Murray, R. W. Nanoelectrochemistry: Metal Nanoparticles, Nanoelectrodes, and Nanopores. *Chem. Rev.* **2008**, *108* (7), 2688–2720.

21. Herrmann, W. A. N-Heterocyclic Carbenes: A New Concept in Organometallic Catalysis. *Angew. Chem. Int. Ed.* **2002**, *41* (8), 1290–1309.

22. Hopkinson, M. N.; Richter, C.; Schedler, M.; Glorius, F. An Overview of N-Heterocyclic Carbenes. *Nature* **2014**, *510* (7506), 485–496.

23. Yang, Y.; Chen, S. Surface Manipulation of the Electronic Energy of Subnanometer-Sized Gold Clusters: An Electrochemical and Spectroscopic Investigation. *Nano Lett.* **2003**, *3* (1), 75–79.

24. Antonello, S.; Perera, N. V.; Ruzzi, M.; Gascón, J. A.; Maran, F. Interplay of Charge State, Lability, and Magnetism in the Molecule-like $Au_{25}(SR)_{18}$ Cluster. *J. Am. Chem. Soc.* **2013**, *135* (41), 15585–15594.

25. Jena, P.; Sun, Q. Super Atomic Clusters: Design Rules and Potential for Building Blocks of Materials. *Chem. Rev.* **2018**, *118* (11), 5755–5870.

26. Wang, Y.; Bürgi, T. Ligand Exchange Reactions on Thiolate-Protected Gold Nanoclusters. *Nanoscale Adv.* **2021**, *3* (10), 2710–2727.

27. Meneses, B. A.; Antonello, S.; Arévalo, M. C.; Maran, F. Double-Layer Correction for Electron-Transfer Kinetics at Glassy Carbon and Mercury Electrodes in N,N-Dimethylformamide. *Electroanalysis*, **2006**, *18*(4), 363-370.